A Rigorous Analysis of Diffraction Stress Formalism

Mehmet Hazar Şeren

Submitted in partial fulfillment of the
requirements for the degree of
Doctor of Philosophy
under the Executive Committee
of the Graduate School of Arts and Sciences

COLUMBIA UNIVERSITY

2021

Abstract

A Rigorous Analysis of Diffraction Stress Formalism

Mehmet Hazar Şeren

Diffraction strain/stress analysis has been widely used in the determination of residual and applied stresses in the surface layers and bulk volumes of materials for a long time. The technique has been used for almost 100 years. However, there are still issues that have not been yet addressed.

In this dissertation, we address these issues. The basic theory of diffraction strain/stress analysis is extensively reviewed and the weaknesses of the analysis are explained carefully. The current definitions that have been used for describing residual stresses are unified under this expanded analysis. In addition, the homogeneous continuum analysis is extended to the polycrystalline materials under various loading types.

To search for answers to the questions asked in this dissertation, finite element modeling. was used. This approach provides both local and global stress and strain information at all locations of a virtual specimen.

The results show that St. Venant regions such as edges, voids, or geometric constraints cause local inhomogeneous strain/stress distribution which can cause deviations from linear deformation theory. Even if the far-field load region is sampled by X-rays, the representative volume element should be determined by preliminary experiments because almost all single-phase polycrystalline materials (with the exception of tungsten) are composite materials within which variations of elastic moduli are observed along with sample directions. In the multiphase

polycrystalline materials, this problem becomes more serious due to the differential deformation of each phase with respect to each other. Therefore, an experimenter needs to be careful during the experiment, in acquiring representative data; this requires significant preparation and material characterization.

With the findings of the dissertation, a set of rules are written for users and experimenters to apply during or before the experiments to collect accurate and representative data.

Table of Contents

List of Figures ix

List of Tables xx

List of Symbols xxxv

Acknowledgments xlii

Dedication xliv

1- INTRODUCTION AND BASIC THEORY 45

1.1- Analysis of Residual Stress Fields 45

1.2- Residual Stress Definitions 49

1.2.1- Process-Based Definitions 49

1.2.1.1- Thin-Film Residual Stresses 51

1.2.2- Solid Mechanics Based Definitions 51

1.2.2.1- Scale Based Definitions 55

1.2.2.2- Effect of Sample Geometry and St. Venant's Principle 57

1.3- Residual Stress Measurement Methods 59

1.3.1- Diffraction Strain/Stress Analysis 60

1.3.2- Computation of Strains from Regular " $d_{\phi\psi}$" vs. $sin^2\,\psi$ Data 62

1.3.3- Computation of Stresses from Regular " $d_{\phi\psi}$" $vs. sin^2\,\psi$ Data in Homogeneous Materials 64

1.3.3.1- Biaxial Stress Analysis 66

1.3.3.2- Triaxial Stress Analysis 67

1.3.3.2.1- Analysis of Linear $d_{\phi\psi}$ vs. $sin^2\,\psi$ Data 67

1.3.3.2.2- Analysis of Split in $d_{\phi\psi}$ vs. $sin^2\,\psi$ Data 68

1.3.4- Non-regular "$d_{\phi\psi}$" vs. $sin^2\,\psi$ Data 69

1.3.5- Methods Proposed to Analyze Oscillatory Behavior of "$d_{\phi\psi}$" vs. $sin^2\,\psi$ 70

1.3.5.1- Greenough Model 70

1.3.5.2- The Marion-Cohen Method 71

1.3.5.3- Dölle-Hauk Method (Oscillation-free Reflections) 74

1.3.5.4- X-ray Integral Methods (Löde and Peiter) 75

1.3.5.4.1- ψ-integral Method 76

1.3.5.4.2- ϕ-integral Method 77

1.3.5.5- The Crystallite-group Method 77

1.3.5.6- The Glancing Angle Technique 79

1.3.5.7- Fixed Crystal Orientation Technique 81

1.3.5.8- The Generalized $\sin^2\psi$ (Matrix) Method 83

1.3.5.9- Other Methods 85

1.3.6- Summary 86

1.4- Problems and Questions 86

2- EXPANDED ANALYSIS AND DEFINITIONS 89

2.1- Residual Stresses in Homogeneous Materials 89

2.1.1- Homogeneous Stress/Strain Fields and Far-field Stresses 91

2.1.2- St. Venant Stress/Strain Fields 92

2.2- Residual Stresses/Strains in Polycrystalline Materials 93

2.2.1- Polycrystalline Materials – Homogeneous Far-field Stress 94

2.2.2- Polycrystalline Materials – St. Venant Regions 96

2.3- Residual Stresses/Strains: Effects of Plastic Flow 97

2.3.1- Effects of Plastic Flow – Homogeneous Materials 98

2.3.1.1- Regions with Uniform Far-field Stresses 98

2.3.1.2- Regions with St. Venant Stresses 99

2.3.2- Effects of Plastic Flow – Polycrystalline Materials 100

2.3.2.1- Regions with Homogeneous Far-field Stresses 100

2.3.2.2- Polycrystalline Regions with St. Venant Stresses 102

2.4- Revised Definitions for Diffraction Stress Analysis 102

2.4.1- Microstress 103

2.4.2- Macrostress 104

2.5- Representative Volume Definition for Diffraction Techniques 106

2.5.1- Oscillatory ε'_{33} vs. $sin^2\psi$ Plots and Pseudo-Macro Stresses 107

2.6- Summary 109

3- MODELING PROCEDURE 111

3.1- Introduction 111

3.2- St. Venant's Stresses in a Homogeneous Isotropic Sample 112

3.3- Thermal Expansion of Single and Multiphase Materials under Constraint 115

3.3.1- Grain Definition and Mesh Geometry 115

3.3.2- Definition of Grain Orientations 117

3.3.3- Material Constants Calculations 125

4- ST. VENANT AND FAR-FIELD STRESS FIELDS IN AN IDEAL SYSTEM 133

4.1- Material Definition 133

4.2- General Analytical Solution of Spherical Eshelby Inclusion in a Finite Spherical Shell 135

4.2.1- Force Balance at Overall Volume 140

4.2.2- Effect of Geometry and Material on the Critical Length (r^*) 141

4.3- FEM Analysis vs. Analytical Computations 143

4.3.1- Strain Energy Approach for Critical Radius Determination 148

4.3.2- Effect of Shell Geometry 151

4.4- Implications of the MMC Stress Distribution for Diffraction Strain/Stress Measurements 154

4.4.1- Local vs. Average Stress Values 154

4.4.2- Representative Volume Element Definition 156

4.4.3- Effect of Beam Size and Position on $d_{\phi\psi}\ vs.\ sin^2\psi$ 156

4.4.4- Classification of Local and Average Stress Distributions 161

4.5- Distribution of Applied Stresses in a SICS Systems 162

4.5.1- Uniaxially Loaded SICS Model 164

4.5.2- Biaxially Loaded SICS Model 166

4.6- Summary 168

5- STRESSES UNDER THERMAL EFFECTS IN IDEAL POLYCRYSTALLINE THIN FILMS 170

5.1- Materials Selection 171

5.2- Modelling Approach 173

5.3- Results and Discussion 178

5.3.1- Free Thermal Expansion of Single-phase W & Cu Films 178

5.3.2- Heating Single-phase W & Cu Films under Bi-axial Boundary Constraint .. 179

5.3.2.1- Heating Single-phase W Films under Bi-axial Boundary Constraint 180

5.3.2.2- Heating of Cu Thin Films under Biaxial Constraint 184

5.3.2.2.1- Edge-constrained Cu Film at Incipient Plastic Flow 188

5.3.2.2.2- Stress Distribution in Sample Coordinates 191

5.3.2.2.3- Diffraction Strain/Stress Analysis 196

5.3.2.3- Pervasive Plastic Deformation..... 200

5.3.2.3.1- Stress Distribution in Sample Coordinates..... 202

5.3.2.3.2- Diffraction Strain/Stress Analysis 205

5.3.2.3.2.1- Determination of Oscillations in $\langle \varepsilon'_{11,\psi} \rangle_{i,\psi}$ vs. $\sin^2 \psi$..... 208

5.3.3- Free Expansion of Cu – W Virtual Sample 209

5.3.3.1- State of Stress in Sample Coordinates..... 210

5.3.3.1.1- Phase-average Stress Components in Sample Coordinates Selected by Diffraction……216

5.3.3.2- Diffraction Stress Analysis..... 220

5.4- Summary 224

6- FAR-FIELD MECHANICAL STRESSES IN IDEAL POLYCRYSTALLINE SYSTEMS……...226

6.1- Materials Selection..... 227

6.2- Model Definition and Meshing 228

6.3- Loading Geometry..... 230

6.4- Results..... 234

6.4.1- Uniaxial Tension of Single-phase W Bar..... 234

6.4.1.1- Analysis of Gage Section of W Bar..... 236

6.4.1.2- Analysis of Grip Sections of W Bar 239

6.4.1.2.1- Stress Distributions in Sample Coordinates 240

6.4.1.2.2- Diffraction Strain/Stress Analysis of the Grip Regions..... 243

6.4.2- Uniaxial Tension of Single-phase Cu Bar 247

6.4.2.1- Uniaxial Tension of Single-phase Cu Bar at Elastic Regime..... 248

6.4.2.1.1- Stress Distributions in Sample Coordinates 249

6.4.2.1.2- Diffraction Strain/Stress Analysis 253

6.4.2.2- Determination of Diffraction Elastic Constants for Single-phase W & Cu .. 258

6.4.2.2.1- Diffraction Determination of DECs for Single-phase W 258

6.4.2.2.2- Diffraction Determination of DECs for Single-phase Cu 259

6.4.2.3- Uniaxial Tension of Single-phase Cu Bar at Plastic Regime 268

6.4.2.3.1- Stress Distributions in Sample Coordinates 270

6.4.2.3.2- Diffraction Strain/Stress Analysis 272

6.4.2.4- Single-phase Cu Bar at Zero External Load after Tensile Plastic Flow..... 280

6.4.2.4.1- Stress Distributions in Sample Coordinates 281

6.4.2.4.2- Diffraction Strain/Stress Analysis 285

6.4.2.5- Partitioning of Internal Stresses/Strains in a Two-phase, Cu – W sample 290

6.4.2.6- Determination of Diffraction Elastic Constants for Two-phase Cu – W Sample……..294

6.4.2.6.1- Determination of Diffraction Elastic Constants for W Phase..... 294

6.4.2.6.2- Determination of Diffraction Elastic Constants for Cu Phase..... 296

6.4.2.7- Uniaxial Tension of Cu – W Bar at Plastic Regime..... 301

6.4.2.7.1- Stress Distribution in Sample Coordinates..... 302

6.4.2.7.1.1- Phase-averaged Stress Components in Sample Coordinates Selected by Diffraction……307

6.4.2.7.2- Diffraction Stress/Strain Analysis..... 310

6.4.2.8- Two-phase Cu – W Bar at Zero External Load after Tensile Plastic Flow... 318

6.4.2.8.1- Stress Distribution in Sample Coordinates..... 320

6.4.2.8.1.1- Phase-averaged Stress Components in Sample Coordinates Selected by Diffraction……...324

6.4.2.8.2- Diffraction Stress/Strain Analysis..... 327

6.4.2.9- Deformation Distributions of Virtual Cu Sample..... 334

6.4.2.10- Effect of Sampling on Results of Two-phase Cu – W Simulations..... 338

6.5- Summary..... 343

7- CONCLUSIONS & FUTURE WORK..... 345

References..... 351

List of Figures

Figure 1.1: a) Schematic description of the normal shot-peening process. b) Free body deformation of the surface and bulk layers without mutual constraint (b) and with mutual constraint (c) of a hypothetical shot-peened specimen. 46

Figure 1.2: Distribution of the in-plane stress along the x_3 direction in a virtual specimen shot peened on both sides. 48

Figure 1.3: Homogeneous, isotropic solid bar elastically deformed with the distributed load. ... 52

Figure 1.4: A body subjected to arbitrary forces, F_1, F_2, and F_3. 53

Figure 1.5: Schematical depiction of residual stresses of the first, second and, third types [3]. .. 56

Figure 1.6: Stress profile around an internal void [28]. 58

Figure 1.7: a) Certain grains (hkl) satisfy Bragg's Law and diffract beam at a 2θ value which depends on the spacing of the hkl planes which is affected by stresses. Once the specimen is tilted, diffraction occurs from other grains $(hkl)_2$ but the same set of planes. b) Since the normal stress component for $(hkl)_1$ is different than $(hkl)_2$, the interatomic spacing will be different as will the diffraction angle…… 60

Figure 1.8: Definition of the angles ϕ and ψ and orientation of the laboratory coordinate system, $\vec{L}_i$, with respect to the sample coordinate system, $\vec{S}_i$, and the measurement direction, $\vec{S}_\phi$…….. 62

Figure 1.9: Regular $d_{\phi\psi}$ vs. $sin^2\,\psi$ plots. Linear behavior is predicted when shear strains normal to the surface (along $\vec{S}_3$), ε_{13}, and ε_{23}, are zero. If either or both of these terms are finite, the $d_{\phi\psi}$ vs. $sin^2\,\psi$ plot "splits" into two branches for $\mp\psi$ [1]……...64

Figure 1.10: Non-regular " $d_{\phi\psi}$" vs. $sin^2\,\psi$ plots; a) curved and b) oscillatory behavior..... 69

Figure 1.11: Model of polycrystalline aggregate. P is the applied stress, A is the cross-sectional area of each grain, and T_1, T_2… Tr are the stresses in the crystals of orientations 1, 2, … r. 71

Figure 1.12: Specimen geometry and the definition of α and β in the Marion-Cohen method. ... 73

Figure 1.13: Definition of the glancing angle Seemann-Bohlin geometry. The diffracting plane normal ($\vec{L}_3$) makes an angle ψ with the surface normal ($\vec{S}_3$). The incidence angle α is a function of the tilt angle ψ and the diffraction angle θ……. 81

Figure 1.14: Schematic of a tensile test sample and volumes defined during a diffraction experiment and mechanical testing. 87

Figure 2.1: Formation of the residual stress in the homogeneous bar constrained by a c-shape clamp [99]. 90

Figure 2.2: Free-body diagrams corresponding to the different regions of the ideal cylinder. Regions FBD-1 and FBD-3 represent the St. Venant regions where end-effects and geometry modulate the stress fields. The stress/strain field in the central region, FBD-2, is homogeneous…… 91

Figure 2.3: FBD-2 of a single-phase polycrystalline cylinder of uniform cross-section A_0 loaded in tension. 94

Figure 2.4: Stress vs. strain curve of a homogeneous isotropic solid showing perfect plasticity (no strain hardening)……... 100

Figure 2.5: Transformation of a random polycrystalline FBD (a) composed of anisotropic grains with moduli, C_{ijkl}, (c), A collection of such grains yield a representative volume element, RVE with moduli E, ν (b), and a collection of RVE form the FBD of the equivalent isotropic material (EIM). In both the RVE and the EIM the stresses, elastic strains, and elastic

moduli are homogeneous; and RVE in the polycrystalline FBD is represented by a point in the EIM……... 106

Figure 3.1: Schematic diagrams of the FEM model for r_{Inc} = 5 mm and R_{Mat} = 50 mm (The different mesh sizes are delineated by color)..... 114

Figure 3.2: Top view of ABAQUS mesh containing 400 anisotropic grains with isotropic edge (and corner) grains..... 116

Figure 3.3: Step-wise thermal loading and unloading of the numerical model. 117

Figure 3.4: Illustration of a general unit cell with three basis vectors, a, b and c. 118

Figure 3.5: The relationship between basis vectors and cartesian crystal coordinates. 119

Figure 3.6: Hypothetical material consisting of grains whose crystal axes are parallel to the sample coordinates. 121

Figure 3.7: The relationship between grain, sample and, crystal coordinate systems. 122

Figure 3.8: a) Schematic of diffraction geometry with a) the sample axes b) laboratory axes. . 124

Figure 3.9: Stereographic projection of the 200 grains placed in the mesh of finite element modeling. 125

Figure 3.10: Phase and grain distributions for the copper-tungsten virtual composite. For the phase distribution, red indicates copper; blue indicates tungsten. 129

Figure 4.1: Spherical Eshelby inclusion in a finite spherical shell. 134

Figure 4.2: Representation of spherical coordinates in the composite system. 137

Figure 4.3: a) Hydrostatic stress state of the 5 mm inclusion with different shell radius and b) the surface tangential stress at the different shell radius in Al – Fe system ($\Delta\alpha_{Al-Fe}$ = 11.1E-06). 144

Figure 4.4: Radial stress distribution of three different systems in 5 mm inclusion with 50 mm matrix (For all three systems, the differences between FEM and closed-form solutions are less than 0.1%, $\Delta\alpha_{Cu-W}$=12.9E-06, $\Delta\alpha_{Al-Fe}$=11.1E-06 and $\Delta\alpha_{Al-W}$=19.2E-06). 145

Figure 4.5: Tangential stress distribution of three different systems in 5 mm inclusion with 50 mm shell (For all three systems, FEM and quantification of the difference between them is less than 0.1%). 145

Figure 4.6: Critical lengths, r*, for 15 different Fe shells encapsulating a 5 mm Al inclusion ($\Delta\alpha_{Al-Fe}$=11.1E-06). The top abscissa and right ordinate show the volume fraction, f, corresponding to a given shell radius, and $\Delta r = r^*_{FEM} - r^*_{Analytical}$, respectively. 146

Figure 4.7: Variation of radial (a) and tangential (b) stresses with the position in three inclusion-shell systems with $\frac{r_{Inc}}{R_{Mat}} = 0.67$. In this case, f=0.3 while the maximum inclusion volume fraction required to achieve Γ=0.03, computed from Eq. (4-23) is 0.016. 147

Figure 4.8: The calculated ratio of critical length to the radius of inclusion vs. radius of inclusion in the Al – Fe system. The volume fraction of the inclusion to the shell is kept constant. 147

Figure 4.9: Strain energy for 5 mm inclusion and 50 mm shell in Al – Fe system. The log-scale inset shows the difference between the two types of decay. 150

Figure 4.10: a) Spherical inclusion-in-cubic shell b) Variation of tangential and radial stresses with the position in shell and cube models. 152

Figure 4.11: Eight spherical inclusion-in-cubic shell (SICS) units stacked in a 2x2x2 arrangement to form a metal-matrix composite (MMC) system. 152

Figure 4.12: Variation of radial and tangential stresses within two neighboring SICS of the MMC as a function of position for four different cubic-shell dimensions. For all cases, the inclusion radius is 5 mm. The cube edge lengths are a) 200 mm, b) 72 mm, c) 40 mm, and d) 30 mm, respectively..... 153

Figure 4.13: Variation of stress components over the central cross-section of a 2x2x2 MMC. For (a) the MMC is constructed of eight Fe Shell-Al inclusion SICS, with 200 mm edges. For (b) The SICS have edge lengths of 30 mm. In all cases, the inclusions have 5 mm radii. .. 155

Figure 4.14: Variation of stress components over the representative volume of the central cross-section of a 2x2x2 MMC having a 200 mm edge. 157

Figure 4.15: Variation of σ_{12} over the representative volume of the central cross-section of a 2x2x2 MMC having 200 mm edge. Three directions, 1, 2, and 3 are shown with dashed lines. 158

Figure 4.16: Average stresses calculated along 1,2 and 3 directions in sample coordinate system for different beam sizes..... 159

Figure 4.17: a) Position (shown in purple square box) of the 5 mm beam on the matrix along three directions on the representative volume, b) the $(\varepsilon'_{11})\ vs.\ sin^2\psi$ plots belong to experiment performed in different beam positions. 160

Figure 4.18: Metal matrix composite system with different sampling volumes..... 162

Figure 4.19: Variation of stress components over the central cross-section of a uniaxially loaded SICS. The SICS is constructed of Fe Shell-Al inclusion with 100 mm edges..... 165

Figure 4.20: Variation of $\left(\sigma_{ij}^{SV}\right)_{x,y,z}$ across the uniaxially loaded SICS along the x-axis..... 166

Figure 4.21: Variation of stress components over the central cross-section of a biaxially loaded SICS. The SICS is constructed of Fe Shell-Al inclusion with 100 mm edges..... 167

Figure 4.22: Variation of $\left(\sigma_{ij}^{SV}\right)_{x,y,z}$ across the biaxially loaded SICS along the x-axis..... 168

Figure 5.1: a) X-ray diffraction pattern of Cu – W sample containing 50% Cu – 50% W, and b) binary phase diagram of Cu and W [130]..... 173

Figure 5.2: Distribution of (200), (222) & (420) reflections for the single-phase W finite element mesh. 174

Figure 5.3: Scattering geometry for a single grain of the FEM mesh, oriented for diffraction at ψ=0 into the hkl reflection. In this figure, the [hkl] direction is coincident with the $\vec{S}_3$ sample axis, and $\vec{S}_3$ is in coplanar with the incident and diffracted beam vectors k_i, k_d^{hkl}, respectively. 175

Figure 5.4: Computed $\langle \varepsilon'_{11,\psi} \rangle_{i,\psi}$ vs. $sin^2\psi$ plots for all reflections of W (a) and Cu (b) models heated 100 °C without boundary constraint. Lattice strains, $\langle \varepsilon'_{11,\psi} \rangle_{i,\psi}$, are identical for all grains diffracting into all reflections. 179

Figure 5.5: Grain averaged stress values in sample coordinates, $\langle \sigma_{22} \rangle_{i,\psi} = \langle \sigma_{33} \rangle_{i,\psi}$ (a) and $\langle \sigma_{11} \rangle_{i,\psi}$ (b) for the ψ -ensembles diffracting into the 200 reflection. At each ψ there are N_ψ^{200} identical stress values. Plots for the 222 and 420 reflections were identical. 182

Figure 5.6: $\langle \varepsilon'_{11,\psi} \rangle_{i,\psi}^{W}$ $vs. sin^2\psi$ plot computed from the strain output of the W model subjected to a 75 °C temperature increase with its in-plane edges constrained. At each ψ there are N_ψ^{200} identical strain values..... 183

Figure 5.7: Young's modulus and Poisson's ratio distribution for Cu with reflections hkl = 200, 222, 420 at different ψ angles..... 187

Figure 5.8: ψ-volume averages of plastic strain values in sample coordinates, $\langle \varepsilon_{11}^{pl} \rangle_{\psi}^{hkl}$ (a) and $\langle \varepsilon_{33}^{pl} \rangle_{\psi}^{hkl}$ (b) for the ψ -ensembles diffracting into the 200, 222 & 420 reflections..... 190

Figure 5.9: The grain stress averaged values along in-plane (a, c, e) and normal (b, d, f) sample axes; $\langle \sigma_{33} \rangle_{i,\psi}, \langle \sigma_{11} \rangle_{i,\psi}$, respectively, for all reflections as a function of $\sin^2\psi$..... 195

Figure 5.10: $\langle \varepsilon'_{11,\psi} \rangle_{i,\psi}^{Cu}\ vs.\ sin^2\psi$ (a, c, e) and $\langle \varepsilon'_{11,\psi} \rangle_{i,\psi}^{*-Cu}\ vs.\ sin^2\psi$ (b, d, f) plots for studied reflections of the edge constrained Cu film at incipient plastic flow. 197

Figure 5.11: ψ-volume averages of plastic strain values in sample coordinates, $\langle \varepsilon_{11}^{pl} \rangle_{\psi}^{hkl}$ (a) and $\langle \varepsilon_{33}^{pl} \rangle_{\psi}^{hkl}$ (b) for the ψ -ensembles diffracting into the 200, 222 & 420 reflections..... 202

Figure 5.12: The grain stress averaged values along in-plane (a, c, e) and normal (b, d, f) sample axes; $\langle \sigma_{33} \rangle_{i,\psi}, \langle \sigma_{11} \rangle_{i,\psi}$, respectively, for all reflections as a function of $\sin^2\psi$..... 204

Figure 5.13: $\langle \varepsilon'_{11,\psi} \rangle_{i,\psi}^{Cu}\ vs.\ sin^2\psi$ (a, c, e) and $\langle \varepsilon'_{11,\psi} \rangle_{i,\psi}^{*-Cu}\ vs.\ sin^2\psi$ (b, d, f) plots for studied reflections of the Cu mesh under plastic loading..... 206

Figure 5.14: The phase-average, Cu (a, c, e) and W (b, d, f), grain stress values along in-plane sample axis; $\langle \sigma_{33} \rangle_{i,\psi}$, , respectively, for all reflections as a function of $\sin^2\psi$. 218

Figure 5.15: The phase-average, Cu (a, c, e) and W (b, d, f), grain stress values along out-of-plane sample axis; $\langle \sigma_{11} \rangle_{i,\psi}$, , respectively, for all reflections as a function of $\sin^2\psi$..... 219

Figure 5.16: $\langle \varepsilon'_{11,\psi} \rangle_{i,\psi}^{Ph}\ vs.\ sin^2\psi$ plots for studied reflections of each phase in Cu – W mesh under the thermal loading. 221

Figure 6.1: Refined and Experimental Stress-Strain Curve of a) Cu, b) W. The experimental data is collected from the Atlas of Stress-Strain Curves [131]..... 228

Figure 6.2: Schematic of the virtual sample used in FEpX. ParaView software was used for visualization. 229
Figure 6.3: Distribution of Grain Volumes in W and Cu mesh. 229
Figure 6.4: Grain average stress values in sample coordinates, $\langle\sigma_{33}\rangle_{i,\psi}$ along z a) between 0 to 3 b) between 0.5 and 2.25. 232
Figure 6.5: Variation of $\langle\sigma_{ij}^{N}\rangle_{i,\psi}$ with position for five different tensile loads in the isotropic bar. 233
Figure 6.6: Schematic free-body diagram of W bar extended along L_3 direction. The gage and grip sections are defined and they have equal volume fractions. 235
Figure 6.7: Grain average stress values in sample coordinates, $\langle\sigma_{ij}\rangle_{i,\psi}$ a) sorted with respect to z b) for ψ -ensembles diffracting into all reflections. At each ψ there are N_{ψ}^{hkl} identical stress values. Plots for the individual reflections were identical. 237
Figure 6.8: $\langle\varepsilon'_{11,\psi}\rangle_{i,\psi}^{W}\ vs.\ sin^2\psi$ plot computed from the strain output of the W model extended along the z-direction. At each ψ, there are N_{ψ}^{110} identical strain values 238
Figure 6.9: The grain stress average values a) $\langle\sigma_{11}\rangle_{i,\psi}$, b) $\langle\sigma_{22}\rangle_{i,\psi}$, c) $\langle\sigma_{33}\rangle_{i,\psi}$ d) shear stresses, for all grains as a function of $\sin^2\psi$..... 241
Figure 6.10: $\langle\varepsilon'_{11,\psi}\rangle_{i,\psi}^{W}\ vs.\ sin^2\psi$ plots for studied reflections of the grip section of uniaxially loaded W bar. 244
Figure 6.11: a) global average stress vs. applied stress b) global average lattice strain vs. applied strain. 248
Figure 6.12: The grain stress average values a) $\langle\sigma_{11}\rangle_{i,\psi}$, b) $\langle\sigma_{22}\rangle_{i,\psi}$, c) $\langle\sigma_{33}\rangle_{i,\psi}$ d) shear stresses, for all grains diffracting into 420 reflection as a function of $\sin^2\psi$. 252

Figure 6.13: $\langle \varepsilon'_{11,\psi} \rangle_{i,\psi}^{Cu}\ vs.\ sin^2\psi$ plots for all reflections of gage section of Cu bar uniaxially loaded to 169.5 MPa. 255

Figure 6.14: $\langle \varepsilon'_{11,\psi} \rangle_{i,\psi}^{*-Cu}\ vs.\ sin^2\psi$ plots for all reflections of gage section of Cu bar uniaxially loaded to 169.5 MPa. 256

Figure 6.15: Variation of I_{hkl} and m_{hkl} with respect to $\sigma_{33}^{Ap.}$ for all reflections in the gage section of W. 259

Figure 6.16: $\langle \varepsilon'_{11,\psi} \rangle_{i,\psi}^{Cu}\ vs.\ sin^2\psi$ plot for the Cu 220 reflection of the combined model at $\sigma_{33}^{App.} = 113$ MPa. Strain values from all 417 grains of the 220 reflection in the gage section are plotted..... 262

Figure 6.17: Variation of $I_{hkl}\ and\ m_{hkl}$ with respect to $\sigma_{33}^{App.}$ for all reflections in the gage section of combined Cu sample 264

Figure 6.18: $\langle \varepsilon'_{11,\psi} \rangle_{i,\psi}^{Cu}\ vs.\ sin^2\psi$ plot for the Cu 220 reflection of the combined model at $\sigma_{33}^{App.} = 113$ MPa. Strain values from all 3710 grains in the gage section are plotted. 268

Figure 6.19: ψ-volume averages of equivalent plastic strain values in sample coordinates, $\langle \varepsilon^{eqpl} \rangle_{\psi}^{hkl}$ for the ψ -ensembles diffracting into the 111, 200, 220, 311 & 420 reflections. 270

Figure 6.20: The grain stress average values a) $\langle \sigma_{11} \rangle_{i,\psi}$, b) $\langle \sigma_{22} \rangle_{i,\psi}$, c) $\langle \sigma_{33} \rangle_{i,\psi}$ d) shear. stresses, for all grains diffracting into 420 reflection as a function of $\sin^2\psi$.. 272

Figure 6.21: $\langle \varepsilon'_{11,\psi} \rangle_{i,\psi}^{Cu}\ vs.\ sin^2\psi$ plots for all reflections of gage section of Cu bar uniaxially loaded to 334.5 MPa. 273

Figure 6.22: $\langle \varepsilon'_{11,\psi} \rangle_{i,\psi}^{*-Cu}\ vs.\ sin^2\psi$ plots for all reflections of gage section of Cu bar uniaxially loaded to 334.5 MPa. 274

Figure 6.23: The grain stress average values a) $\langle\sigma_{11}\rangle_{i,\psi}$, b) $\langle\sigma_{22}\rangle_{i,\psi}$, c) $\langle\sigma_{33}\rangle_{i,\psi}$ d) shear stresses, for all grains as a function of $\sin^2\psi$..... 282

Figure 6.24: $\langle\varepsilon'_{11,\psi}\rangle_{i,\psi}^{Cu}\ vs.\ sin^2\psi$ plots for all reflections of the gage section of Cu bar at zero external load after plastic flow..... 286

Figure 6.25: $\langle\varepsilon'_{11,\psi}\rangle_{i,\psi}^{Cu}\ vs.\ sin^2\psi$ plot for all grains in the gage section of unloaded Cu bar..... 290

Figure 6.26: Refined stress-strain curve of the Cu – W by using single-phase compliances, yield response, and modified Voce parameters of the individual phases. 293

Figure 6.27: Variation of I_{hkl} and m_{hkl} with respect to $\sigma_{33}^{App.}$ for all W reflections in the gage section of two-phase Cu – W specimen..... 295

Figure 6.28: Variation of I_{hkl} and m_{hkl} with respect to $\sigma_{33}^{App.}$ for all Cu reflections in the gage section of Cu – W sample..... 298

Figure 6.29: The phase-averaged grain stress values a) $\langle\sigma_{11}\rangle_{i,\psi}^{Cu}$, b) $\langle\sigma_{22}\rangle_{i,\psi}^{Cu}$, c) $\langle\sigma_{33}\rangle_{i,\psi}^{Cu}$ d) the shear stresses, for all grains as a function of $\sin^2\psi$. 308

Figure 6.30: The phase-averaged grain stress values a) $\langle\sigma_{11}\rangle_{i,\psi}^{W}$, b) $\langle\sigma_{22}\rangle_{i,\psi}^{W}$, c) $\langle\sigma_{33}\rangle_{i,\psi}^{W}$ d) the shear stresses, for all grains as a function of $\sin^2\psi$. 309

Figure 6.31: $\langle\varepsilon'_{11,\psi}\rangle_{i,\psi}^{Cu}\ vs.\ sin^2\psi$ plots for studied reflections of the Cu phase in the Cu – W mesh after plastic flow..... 311

Figure 6.32: $\langle\varepsilon'_{11,\psi}\rangle_{i,\psi}^{W}\ vs.\ sin^2\psi$ plots for studied reflections of the W phase in the Cu – W mesh after plastic flow..... 312

Figure 6.33: Unloading portion of the tensile plot in Fig. 6.26. We observe significant reverse yielding for far-field stresses, σ_{33}^{o}, below 350 MPa..... 320

Figure 6.34: The phase-averaged grain stress values a) $\langle\sigma_{11}\rangle_{i,\psi}^{Cu}$, b) $\langle\sigma_{22}\rangle_{i,\psi}^{Cu}$, c) $\langle\sigma_{33}\rangle_{i,\psi}^{Cu}$ d) the shear stresses, for all grains as a function of $\sin^2\psi$. 325

Figure 6.35: The phase-averaged grain stress values a) $\langle\sigma_{11}\rangle_{i,\psi}^{W}$, b) $\langle\sigma_{22}\rangle_{i,\psi}^{W}$, c) $\langle\sigma_{33}\rangle_{i,\psi}^{W}$ d) the shear stresses, for all grains as a function of $\sin^2\psi$. 326

Figure 6.36: $\langle\varepsilon'_{11,\psi}\rangle_{i,\psi}^{Cu}\ vs.\ sin^2\psi$ plots for studied reflections of the Cu phase of the unloaded the Cu – W model. 328

Figure 6.37: $\langle\varepsilon'_{11,\psi}\rangle_{i,\psi}^{W}\ vs.\ sin^2\psi$ plots for studied reflections of the W phase of the unloaded the Cu – W model. 329

Figure 6.38: The distribution of a) the trace and b) Von Mises stresses of 3 elastic loadings for virtual Cu. Trace and Von Mises stresses are normalized by the applied stress to aid in plotting. 335

Figure 6.39: The distribution of a) the trace and b) Von Mises stresses of seven elastoplastic loading steps for the single-phase Cu model. Trace and Von Mises stresses are normalized by the applied stress. 336

List of Tables

Table 1.1: Some sources of process-based residual stresses [3]. 50

Table 3.1: Mechanical and thermal properties of the components along the loading axis. The mechanical parameters of steel, aluminum alloy, copper, and tungsten were obtained from the Metals Handbook, [111, 112]. 114

Table 4.1: Mechanical and thermal properties of the components along the loading axis. The mechanical parameters of steel, aluminum alloy, copper and tungsten were obtained from the Metals Handbook, [111, 112]. 134

Table 4.2: The critical lengths, r*, for 3 different metallurgies, with all systems consisting of a 5 mm radius inclusion surrounded by a 50 mm radius spherical shell. 148

Table 4.3: Fitted strain energy for 3 different couplings having 5 mm radius of inclusion and 50 mm radius shell. 151

Table 5.1: The Zener index, stiffness, and compliance constants for selected crystals and coefficients of thermal expansion of Cu and W [129]. 173

Table 5.2: The color coding of each ψ angle for each reflection in the finite element mesh. 175

Table 5.3: Stress and strain tensor for the edge-constrained W thin film model heated to 75°C, computed using various approaches. The XRD values are the reflection averages of the stress and strain terms. 181

Table 5.4: Diffraction elastic constants of W calculated from the W stiffness tensor using various approaches [1, 56]. These values are independent of reflection since W is isotropic.... 183

Table 5.5: Stress and strain tensors for the edge-constrained Cu thin film model heated from 25°C obtained from Eqs. (5-4 & 5) and the finite element model. The terms in parentheses denote standard deviations. 189

Table 5.6: Plastic and elastic strain tensors for the highest deformed grains in the edge-constrained Cu thin film model. The grain in the last row is fully elastic and is included for comparison. 191

Table 5.7: Reflection average stress tensors, $\langle \sigma_{ij} \rangle^{hkl}$, for the 200, 222, and 420 reflections. The terms in parentheses denote standard deviations. 194

Table 5.8: Diffraction Elastic Constants of non-textured polycrystalline Cu at various limits.. 198

Table 5.9: The average stresses obtained from simulated diffraction analysis of the plots shown in Fig. 5.10. 198

Table 5.10: The average strains in sample coordinates obtained from simulated diffraction analysis of the plots shown in Fig. 5.10. The averages for the reflection-ensembles in real space are also included, along with the model averages. 200

Table 5.11: Stress and strain tensors for the edge-constrained Cu thin film model heated from 25°C obtained from Eqs. (5-4 & 5) and the finite element model. The terms in parentheses denote standard deviations. 201

Table 5.12: Reflection average stress tensors,$\langle \sigma_{ij} \rangle^{hkl}$, for the 200, 222, and 420 reflections. The terms in parentheses denote standard deviations. 203

Table 5.13: The average stresses obtained from simulated diffraction analysis of the plots shown in Fig. 5.14. 207

Table 5.14: The average strains in sample coordinates obtained from simulated diffraction analysis of the plots shown in Fig. 5.14. The averages for the reflection-ensembles in real space are also included, along with the model averages. 208
Table 5.15: The average stresses obtained from simulated diffraction analysis of the plots shown in Fig. 5.14 after removal of the first two ψ-ensemble points. 209
Table 5.16: Global average stress tensor of the entire Cu – W film heated to 90°C and its dispersion parameters. The model contains 676 grains, 352 Cu, and 324 W. All values are in MPa. 211
Table 5.17: Average lattice strain tensor of the entire Cu – W film heated to 90°C and its dispersion parameters. All values are in microstrain (με). 211
Table 5.18: Average stress tensor for the Cu phase of the Cu – W film heated to 90°C and its dispersion parameters. This phase contains 352 grains. All values are in MPa. 213
Table 5.19: Average lattice strain tensor for the Cu phase of the Cu – W film heated to 90°C and its dispersion parameters. All values are in microstrain (με). 213
Table 5.20: Average plastic strain tensor for the Cu phase of the Cu – W film heated to 90°C and its dispersion parameters. All values are in microstrain (με). 214
Table 5.21: Average stress tensor for the W phase of the Cu – W film heated to 90°C and its dispersion parameters. This phase contains 324 grains. All values are in MPa. 215
Table 5.22: Average lattice strain tensor for the W phase of the Cu – W film heated to 90°C and its dispersion parameters. All values are in microstrain (με). 215

Table 5.23: Reflection average stress tensors for the Cu and W phases of the Cu – W film heated to 90°C. The phase-average stress tensor is also included for ease of comparison. All values are in MPa. 217

Table 5.24: Slopes and intercepts of lines fitted to $\langle \varepsilon'_{11,\psi} \rangle_{i,\psi}^{Ph}$ $vs. sin^2 \psi$ data and the corresponding reflection average strain tensors for the Cu phase. The corresponding real space averages are also included. All values are in microstrain (με). 223

Table 5.25: Slopes and intercepts of lines fitted to $\langle \varepsilon'_{11,\psi} \rangle_{i,\psi}^{Ph}$ $vs. sin^2 \psi$ data and the corresponding reflection average strain tensors for the W phase. The corresponding real space averages are also included. All values are in microstrain (με). 223

Table 5.26: The computed reflection average stresses from the average strain tensors listed in Tables 5.24 & 25, and isotropic Hooke's law..... 224

Table 5.27: The reflection-specific stress terms, $\langle \sigma_{33}^{D} - \sigma_{11}^{D} \rangle^{Ph-hkl}$ obtained from the slopes of the $\langle \varepsilon'_{11,\psi} \rangle_{i,\psi}^{Ph}$ $vs. sin^2 \psi$ 224

Table 6.1: Refined Voce hardening parameters of Cu and W. 227

Table 6.2: The population number for each ψ-ensemble N_{ψ}^{hkl} , and its volume fraction, f_{ψ}^{hkl} in finite element mesh of Cu sample..... 230

Table 6.3: The population number for each ψ-ensemble N_{ψ}^{hkl} , and its volume fraction, f_{ψ}^{hkl} in finite element mesh of Wsample. 230

Table 6.4: Global average stress tensor of the entire W bar loaded to 989 MPa and its dispersion parameters. The model contains 1500 grains. All values are in MPa. 234

Table 6.5: Average lattice strain tensor of the entire W bar loaded to 989 MPa and its dispersion parameters. The model contains 1500 grains. All values are in microstrain (με). 235

Table 6.6: Stress and strain tensor for the gage section of the extended W model, computed using various approaches. The XRD values are the reflection averages of the stress and strain terms. 237

Table 6.7: Stress and strain tensor for the grip section of the extended W model, computed using various approaches. The XRD values are the reflection averages of the stress and strain terms (terms in parentheses are STD values, not errors). 240

Table 6.8: ψ-ensemble average stress tensors, $\langle \sigma_{ij} \rangle_{\psi}^{hkl}$, for the 110, 200, 211, 220, and 310 reflections. 242

Table 6.9: Reflection average stress tensors, $\langle \sigma_{ij} \rangle^{hkl}$, for the 110, 200, 211, 220, and 310 reflections. The components of these tensors were obtained by averaging the particular average stress components, $\langle \sigma_{ij} \rangle_{i,\psi}$, (in the sample coordinates) of all grains for all ψ–tilts for each reflection. 243

Table 6.10: The average stresses, $\langle \sigma_{33}^{D} \rangle^{Cu-hkl}$, obtained from simulated diffraction analysis of the plots shown in Fig. 6.10. 245

Table 6.11: The average strains in sample coordinates obtained from simulated diffraction analysis of the plots shown in Fig. 6.10. The averages for the reflection-ensembles in real space are also included, along with the model averages. 246

Table 6.12: Stress and strain tensor for the gage section of the extended Cu model, computed using various approaches. The XRD values are the reflection averages of the stress and strain terms. 249

Table 6.13: The population number for each ψ-ensemble N_{ψ}^{hkl} in the gage section of the Cu sample. 250

Table 6.14: Reflection average stress tensors, $\langle\sigma_{ij}\rangle^{hkl}$, for the 111, 200, 220, 311 and 420 reflections. The components of these tensors were obtained by averaging the particular average stress components, $\langle\sigma_{ij}\rangle_{i,\psi}$, (in the sample coordinates) of all grains for all ψ–tilts for each reflection. 252

Table 6.15: The average stresses, $\langle\sigma_{33}^{D}\rangle^{Cu-hkl}$, obtained from simulated diffraction analysis of the plots shown in Fig. 6.14. 257

Table 6.16: The average strains in sample coordinates obtained from simulated diffraction analysis of the plots shown in Fig. 6.14. The averages for the reflection-ensembles in real space are also included, along with the model averages. 257

Table 6.17: m_{hkl}, and I_{hkl} of the $\langle\varepsilon'_{11,\psi}\rangle_{i,\psi}^{W}$ $vs.\, sin^2\psi$ plots for the loads, 198, 396, 594, 792, 990 MPa. 258

Table 6.18: Diffraction elastic constants, S_1^{SP-Sim} and $\frac{S_2}{2}^{SP-Sim}$, obtained from the FEA analysis of the gage section of single-phase W. Values computed from single-elastic compliances at the Voigt. Reuss, Neerfeld-Hill and Kröner limits are also shown. 259

Table 6.19: Diffraction elastic constant, S_1^{SP-Sim}, obtained from the FEA analysis of the gage section of single-phase Cu. Values are computed from single-elastic compliances at the Voigt, Reuss, Neerfeld-Hill and Kröner limits. % Deviation of simulated S_1^{SP-Sim} from Kröner was also shown. 261

Table 6.20: Diffraction elastic constant, $\frac{S_2}{2}^{SP-Sim}$, obtained from the FEA analysis of the gage section of single-phase Cu. Values are computed from single-elastic compliances at the Voigt,

Reuss, Neerfeld-Hill and Kröner limits. % Deviation of simulated $\frac{S_2}{2}^{SP-Sim}$ from Kröner was also shown. 261

Table 6.21: Population distribution of grains in the gage section of the combined model. 263

Table 6.22: Slopes, m_{hkl}, and intercepts, I_{hkl} ,of regression fits of $\langle \varepsilon'_{11,\psi} \rangle_{i,\psi}^{Cu}$ $vs. sin^2\psi$ plots for applied loads, 56.5, 113, 159.5 MPa for the gage section of the combined sample. 264

Table 6.23: Diffraction elastic constant, S_1^{SP-Sim}, obtained from the FEA analysis of the gage section of combined Cu sample. Values are computed from single-elastic compliances at the Voigt, Reuss, Neerfeld-Hill and Kröner limits. % Deviation of simulated S_1^{SP-Sim} from Kröner was also shown. 265

Table 6.24: Diffraction elastic constant, $\frac{S_2}{2}^{SP-Sim}$, obtained from the FEA analysis of the gage section of combined Cu sample. Values are computed from single-elastic compliances at the Voigt, Reuss, Neerfeld-Hill and Kröner limits. % Deviation of simulated $\frac{S_2}{2}^{SP-Sim}$ from Kröner was also shown. Young's Modulus, E^{hkl}, and Poisson's ratio, ν^{hkl}, are calculated from S_1^{SP-Sim} and $\frac{S_2}{2}^{SP-Sim}$ values. 265

Table 6.25: DEC values for each model used in the combined analysis, their averages, and $\frac{-\nu}{E}$ and $\frac{1+\nu}{E}$ values computed from macroscopic values. All values are in TPa^{-1}.. 267

Table 6.26: DEC values for the combined model computed using the full data set from all reflections at each ψ. Young's Modulus, E, and Poisson's ratio, ν, are calculated from DEC values. 267

Table 6.27: Stress and strain tensor for the gage section of the extended Cu model, computed using various approaches. The XRD values are the reflection averages of the stress and strain terms. 269

Table 6.28: Reflection average stress tensors, $\langle\sigma_{ij}\rangle^{hkl}$, for the 111, 200, 220, 311, and 420 reflections. The components of these tensors were obtained by averaging the particular average stress components, $\langle\sigma_{ij}\rangle_{i,\psi}$, (in the sample coordinates) of all grains for all ψ–tilts for each reflection. 271

Table 6.29: The average stresses, $\langle\sigma_{33}^{D}\rangle^{Cu-hkl}$, obtained from simulated diffraction analysis of the plots shown in Fig. 6.19. For comparison, $\bar{\sigma}_{ij} = 351\ MPa.$ 275

Table 6.30: The average stresses obtained from simulated diffraction analysis of the plots shown in Fig. 6.21 after removal of first two ψ-ensemble points. 276

Table 6.31: The average strains in sample coordinates obtained from simulated diffraction analysis of the plots shown in Fig. 6.21. The averages for the reflection-ensembles in real space are also included, along with the model averages. 277

Table 6.32: Global strain tensors from the isotropic equation, model average, and for the reflections in the model. 278

Table 6.33: The computed reflection average stresses from the average strain tensors listed in Table 6.32 and (1) E^{hkl}, ν^{hkl}, (2) E, ν. 279

Table 6.34: Global average stress tensor of the gage section of Cu bar at zero external load after plastic flow and its dispersion parameters. All values are in MPa. 280

Table 6.35: Average lattice strain tensor of the gage section of Cu bar at zero external load after plastic flow and its dispersion parameters. All values are in microstrain (με). 281

Table 6.36: ψ-ensemble average stress tensors, $\langle\sigma_{ij}\rangle_{\psi}^{hkl}$, for the 111, 200, 220, 311, and 420 reflections..... 284

Table 6.37: Reflection average stress tensors, $\langle\sigma_{ij}\rangle^{hkl}$, for the 111, 200, 220, 311 and 420 reflections. The components of these tensors were obtained by averaging the particular average stress components, $\langle\sigma_{ij}\rangle_{i,\psi}$, (in the sample coordinates) of all grains for all ψ–tilts for each reflection.. 285

Table 6.38: The average stresses, $\langle\sigma_{33}^{D}\rangle^{Cu-hkl}$, obtained from simulated diffraction analysis of the plots shown in Fig. 6.19. For comparison, $\bar{\sigma}_{ij} = 0\ MPa$. 287

Table 6.39: The average stresses obtained from simulated diffraction analysis of the plots shown in Fig. 6.24 after removal of first two ψ-ensemble points..... 287

Table 6.40: The average strains in sample coordinates obtained from simulated diffraction analysis of the plots shown in Fig. 6.24. The averages for the reflection-ensembles in real space are also included, along with the model averages..... 288

Table 6.41: The computed reflection average stresses from the average strain tensors listed in Table 6.32 and (1) E^{hkl}, ν^{hkl}, (2) E, ν. 289

Table 6.42: The population number and volume fraction for each ψ-ensemble N_{ψ}^{hkl} for the Cu phase in the gage section of the Cu – W sample..... 292

Table 6.43: The population number and volume fraction for each ψ-ensemble N_{ψ}^{hkl} for the W phase in the gage section of the Cu – W sample..... 292

Table 6.44: Young's Modulus, E, Poisson's ratio, v, and yield strength of the two-phase Cu – W sample, computed from Fig 6.36 and Vegard's Law 293

Table 6.45: Slopes, m_{hkl}, and intercepts, I_{hkl} ,of regression fits of $\langle \varepsilon'_{11,\psi} \rangle_{i,\psi}^{W}$ $vs. sin^2\psi$ plots for applied loads, 9.5, 19, 28.5, 38, 47.5 MPa. 295

Table 6.46: Diffraction elastic constants obtained from the FEA analysis of W phase for the gage section of two-phase Cu – W specimen. Values computed from single-elastic compliances at the Voigt. Reuss, Neerfeld-Hill and Kröner limits are also shown. Young's Modulus, E^{hkl}, and Poisson's ratio, ν^{hkl}, are calculated from S_1^{TP-Sim} and $\frac{S_2}{2}^{TP-Sim}$ values. 296

Table 6.47: Slopes, m_{hkl}, and intercepts, I_{hkl} ,of regression fits of $\langle \varepsilon'_{11,\psi} \rangle_{i,\psi}^{Cu}$ $vs. sin^2\psi$ plots for applied loads, 9.5, 19, 28.5, 38, 47.5 MPa 297

Table 6.48: Diffraction elastic constant, S_1^{TP-Sim}, obtained from the FEA analysis of Cu phase for the gage section of two-phase Cu – W specimen. Values are computed from single-elastic compliances at the Voigt, Reuss, Neerfeld-Hill and Kröner limits. % Deviation of simulated S_1^{TP-Sim} from S_1^{SP-Sim} was also shown. 299

Table 6.49: Diffraction elastic constant, $\frac{S_2}{2}^{TP-Sim}$, obtained from the FEA analysis of Cu. phase for the gage section of two-phase Cu – W specimen. Values are computed from single-elastic compliances at the Voigt, Reuss, Neerfeld-Hill and Kröner limits. % Deviation of simulated $\frac{S_2}{2}^{TP-Sim}$ from $\frac{S_2}{2}^{SP-Sim}$ was also shown. 299

Table 6.50: Diffraction elastic constants obtained from the FEA analysis of Cu phase for the gage section of single-phase Cu and two-phase Cu – W specimen. 300

Table 6.51: Young's moduli, E^{hkl}, and Poisson's ratios, ν^{hkl}, computed from DECs of Cu phase in Cu – W shown in Table 6.50. 300

Table 6.52: Applied stress tensor and global average stress tensor of the entire Cu – W and each Cu and W phase elastically loaded. All values are in MPa. 301
Table 6.53: Global average stress tensor of the gage section of Cu – W bar extended 3 % and its dispersion parameters. The model contains 1252 grains, 610 Cu and, 642 W. All values are in MPa. 303
Table 6.54: Global average lattice strain tensor of the gage section of Cu – W bar extended 3 % and its dispersion parameters. The model contains 1252 grains, 610 Cu and, 642 W. All values are in microstrain (με). 303
Table 6.55: Average stress tensor for the Cu phase of the gage section of Cu – W bar extended 3 % and its dispersion parameters. This phase contains 610 grains. All values are in MPa. 304
Table 6.56: Average lattice strain tensor for the Cu phase of the gage section of Cu – W bar extended 3 % and its dispersion parameters. This phase contains 610 grains. All values are in microstrain (με). 304
Table 6.57: Average equivalent plastic strain for the Cu phase of the gage section of Cu – W bar extended 3 % and its dispersion parameters. This phase contains 610 grains. All values are in microstrain (με). 305
Table 6.58: Average stress tensor for the W phase of the gage section of Cu – W bar extended 3 % and its dispersion parameters. This phase contains 642 grains. All values are in MPa. 306

Table 6.59: Average lattice strain tensor for the W phase of the gage section of Cu – W bar extended 3 % and its dispersion parameters. This phase contains 642 grains. All values are in microstrain (με). 306

Table 6.60: Average equivalent plastic strain for the W phase of the gage section of Cu – W bar extended 3 % and its dispersion parameters. This phase contains 642 grains. All values are in microstrain (με). 307

Table 6.61: Reflection average stress tensors for the Cu and W phases of the gage section of the Cu – W bar extended 3 %. The phase-average stress tensor is also included for ease of comparison. All values are in MPa. 310

Table 6.62: The average stresses, $\langle \sigma_{33}^{D} \rangle^{Cu-hkl}$, obtained from simulated diffraction analysis of the plots shown in Fig. 6.31. For comparison, $\bar{\sigma}_{ij} = 1019\ MPa$..... 313

Table 6.63: The average stresses, $\langle \sigma_{33}^{D} \rangle^{W-hkl}$, obtained from simulated diffraction analysis of the plots shown in Fig. 6.31. For comparison, $\bar{\sigma}_{ij} = 1019\ MPa$..... 314

Table 6.64: The average stresses obtained from simulated diffraction analysis of the plots shown in Figs. 6.31 & 32 after removal of first two ψ-ensemble points. 314

Table 6.65: Slopes and intercepts of lines fitted to $\langle \varepsilon'_{11,\psi} \rangle_{i,\psi}^{Ph}\ vs.\ sin^2\psi$ data and the corresponding reflection average strain tensors for the Cu phase. The corresponding real space averages are also included. All values are in microstrain (με). 315

Table 6.66: Slopes and intercepts of lines fitted to $\langle \varepsilon'_{11,\psi} \rangle_{i,\psi}^{Ph}\ vs.\ sin^2\psi$ data and the corresponding reflection average strain tensors for the W phase. The corresponding real space averages are also included. All values are in microstrain (με). 316

Table 6.67: The computed reflection average stresses from the average strain tensors listed in Tables 6.65 & 66 and E^{hkl}, ν^{hkl}. 317
Table 6.68: Average equivalent plastic strain for the Cu phase of the gage section of Cu – W bar unloaded after extended 3 % and its dispersion parameters. This phase contains 610 grains. All values are in microstrain (με). 319
Table 6.69: Average equivalent plastic strain for the W phase of the gage section of Cu – W bar unloaded after extended 3 % and its dispersion parameters. This phase contains 642 grains. All values are in microstrain (με). 319
Table 6.70: Global average stress tensor of the gage section of Cu – W bar unloaded after extended 3 % and its dispersion parameters. The model contains 1252 grains, 610 Cu, and 642 W. All values are in MPa. 321
Table 6.71: Global average lattice strain tensor of the gage section of Cu – W bar unloaded after extended 3 % and its dispersion parameters. The model contains 1252 grains, 610 Cu, and 642 W. All values are in microstrain (με). 321
Table 6.72: Average stress tensor for the Cu phase of the gage section of Cu – W bar unloaded after extended 3 % and its dispersion parameters. This phase contains 610 grains. All values are in MPa. 322
Table 6.73: Average lattice strain tensor for the Cu phase of the gage section of Cu – W bar unloaded after extended 3 % and its dispersion parameters. This phase contains 610 grains. All values are in microstrain (με). 322

Table 6.74: Average stress tensor for the W phase of the gage section of Cu – W bar unloaded after extended 3 % and its dispersion parameters. This phase contains 642 grains. All values are in MPa. 323

Table 6.75: Average lattice strain tensor for the W phase of the gage section of Cu – W bar unloaded after extended 3 % and its dispersion parameters. This phase contains 642 grains. All values are in microstrain (με). 323

Table 6.76: Reflection average stress tensors for the Cu and W phases of the gage section of the Cu – W bar unloaded after extended 3 %. The phase-average stress tensor is also included for ease of comparison. All values are in MPa. 327

Table 6.77: The average stresses, $\langle \sigma_{33}^{D} \rangle^{Cu-hkl}$, obtained from simulated diffraction analysis. of the plots shown in Fig. 6.35. For comparison, $\bar{\sigma}_{ij} = 9\ MPa$. 330

Table 6.78: The average stresses, $\langle \sigma_{33}^{D} \rangle^{W-hkl}$ obtained from simulated diffraction analysis of the plots shown in Fig. 6.36. For comparison, $\bar{\sigma}_{ij} = 9\ MPa$..... 330

Table 6.79: The average stresses obtained from simulated diffraction analysis of the plots shown in Figs. 6.31 & 32 after removal of first two ψ-ensemble points. 331

Table 6.80: Slopes and intercepts of lines fitted to $\langle \varepsilon'_{11,\psi} \rangle_{i,\psi}^{Ph}\ vs.\ sin^2\psi$ data and the corresponding reflection average strain tensors for the Cu phase. The corresponding real space averages are also included. All values are in microstrain (με). 332

Table 6.81: Slopes and intercepts of lines fitted to $\langle \varepsilon'_{11,\psi} \rangle_{i,\psi}^{Ph}\ vs.\ sin^2\psi$ data and the corresponding reflection average strain tensors for the W phase. The corresponding real space averages are also included. All values are in microstrain (με). 333

Table 6.82: The computed reflection average stresses from the average strain tensors listed in Tables 6.80 & 81 and E^{hkl}, ν^{hkl}. 334

Table 6.83: The population distribution for the Cu phase in the gage section of the Cu – W sample. 339

Table 6.84: The population distribution for the W phase in the gage section of the Cu – W sample. 340

Table 6.85: Diffraction elastic constants obtained from the FEA analysis of W phase for the gage section of the combined model. % Deviation of simulated $S_1^{TP-Sim-Com.}$ & $\frac{S_2}{2}^{TP-Sim-Com.}$ from S_1^{TP-Sim} & $\frac{S_2}{2}^{TP-Sim}$ was also shown. 341

Table 6.86: Diffraction elastic constant, $S_1^{TP-Sim-Com.}$, obtained from the FEA analysis of Cu phase for the gage section of the combined model. % Deviation of simulated $S_1^{TP-Sim-Com.}$ from S_1^{TP-Sim} was also shown. 341

Table 6.87: Diffraction elastic constant, $\frac{S_2}{2}^{TP-Sim-Com.}$, obtained from the FEA analysis of Cu phase for the gage section of the combined model. % Deviation of simulated $\frac{S_2}{2}^{TP-Sim-Com.}$ from $\frac{S_2}{2}^{TP-Sim}$ was also shown. 341

Table 6.88: Global average stress tensor of the gage section of the Cu – W bar extended 3 % and its dispersion parameters. The model contains 6260 grains, 3050 Cu, and 3210 W. All values are in MPa. 342

Table 6.89: Global average lattice strain tensor of the gage section of the Cu – W bar extended 3 % and its dispersion parameters. The model contains 6260 grains, 3050 Cu, and 3210 W. All values are in microstrain (με). 342

List of Symbols

ε_{ij}^{p}	plastic strain tensor
$\left(\sigma_{ij}\right)_{x,y,z}$	local stress tensor
$\left(\varepsilon_{ij}\right)_{x,y,z}$	local stress tensor
$\langle\bar{\sigma}_{ij}\rangle_{ROI}$	average stress tensor at the region of interest
$\langle\bar{\varepsilon}_{ij}\rangle_{ROI}$	average strain tensor at the region of interest
σ_{ij}^{o}	far-field stress tensor
$\left(C_{ijkl}\right)_{x,y,z}$	local stiffness tensor
$\langle\bar{C}_{ijkl}\rangle_{ROI}$	average stiffness tensor at the region of interest
C_{ijkl}^{o}	far-field stiffness tensor
V_{RVE}	representative volume element
$\langle\bar{C}_{ijkl}\rangle_{RVE}$	average stiffness tensor at representative volume element
$\langle\bar{\sigma}_{ij}\rangle_{RVE}$	average stress tensor at representative volume element
$\langle\bar{\varepsilon}_{ij}\rangle_{RVE}$	average strain tensor at representative volume element
$\langle\bar{\sigma}_{ij}^{T}\rangle_{V_0}$	total stress tensor at a volume, V_o

$\langle \bar{\varepsilon}_{ij}^{T} \rangle_{V_0}$ total strain tensor at a volume, V_o

d_{hkl} lattice spacing for a plane, (hkl).

$\vec{S}_i$ sample coordinate system, i = 1,2, and 3

$\vec{L}_i$ laboratory coordinate system, i = 1,2, and 3

a_{ij} direction cosines

$(\varepsilon'_{33})_{\phi\psi}$ strain measured within the diffraction volume at laboratory coordinate system

S'_{ijkl} compliance tensor at laboratory coordinate system

σ'_{kl} stress tensor at laboratory coordinate system

$\frac{1+\nu}{E}\left(\frac{S_2}{2}\right), -\frac{\nu}{E}(S_1)$ diffraction elastic constants

$\langle \bar{\sigma}_{ij} \rangle_{VM}$ average stress tensor for any measurement volume

$\langle \bar{\sigma}_{ij} \rangle_{FBD}$ average stress tensor for the free-body diagram

$\langle \bar{\varepsilon}_{ij} \rangle_{FBD}$ average strain tensor for the free-body diagram

$\langle \bar{C}_{ijkl} \rangle_{FBD}$ average stiffness tensor for the free-body diagram

$\left(\sigma_{ij}^{SV}\right)_{x,y,z}$ St. Venant stress tensor

$\left(\varepsilon_{ij}^{SV}\right)_{x,y,z}$ St. Venant strain tensor

σ_{ij}^{*} interaction stress tensor arises to maintain material continuity along a given vector across grain boundaries of grains with different elastic moduli

ε_{ij}^{*} interaction strain tensor arises to maintain material continuity along a given vector across grain boundaries of grains with different elastic moduli

$\left(\sigma_{ij}^{SV}\right)_{x,y,z}^{P}$ total stress at any point, P, in the St. Venant region

$\left(\varepsilon_{ij}^{SV}\right)_{x,y,z}^{P}$ total strain at any point, P, in the St. Venant region

σ_{ij}^{**} local heterogeneous stress tensor due to differential yielding

ε_{ij}^{**} local heterogeneous strain tensor due to differential yielding

$\left(\sigma_{ij}^{R}\right)_{x,y,z}$ local residual stress tensor after relaxation of applied load

$\langle\bar{\sigma}_{ij}^{R}\rangle_{V_{SV}}$ average residual stress tensor after relaxation of applied load at St. Venant regions

$\sigma_{ij}^{\sharp}$ stress tensor due to load transfers caused by plastic flow

$\sigma_{ij}^{\sharp\sharp}$ local residual stress tensor balanced between grains with different plastic strains after unloading

V_{ψ} the volume of the set of grains selected at ψ-tilt

$FBD_{V_{\psi}}^{hkl}$ the free-body diagram of the representative volume element for a particular V_{ψ}

$\langle\bar{\varepsilon}_{ij}^{p}\rangle_{hkl}$ average plastic strain tensor at a reflection, hkl

$\vec{G}_{i}$ grain coordinate system

$\vec{k}_o$	incident beam vectors
$\vec{k}_t$	transmitted beam vectors
$\vec{k}_d$	diffracted beam vectors
θ_B	Bragg angle
S^s_{ijkl}	compliance tensor in sample coordinate system
ν	Poisson's ratio
E	Young's modulus
g_0	initial slip system strength
g_1	reference value of saturation strength
$\dot{\gamma}$	fixed-state strain rate scaling coefficient
$\dot{\gamma}_s$	saturation strength strain rate scaling coefficient
h_0	strength hardening rate coefficient
$\vec{R}_{ij}$	rotation matrix
σ_y	yield stress
$\langle\sigma_{ij}\rangle_{Inc}$	average stress tensor in the inclusion
$\langle\sigma_{ij}\rangle_{Shell}$	average stress tensor in the matrix
σ_{rr}^{Inc}	radial stress in the inclusion

$\sigma_{\theta\theta}^{Inc}$	tangential stress in the inclusion
σ_{rr}^{Shell}	radial stress in the shell
$\sigma_{\theta\theta}^{Shell}$	tangential stress in the shell
f	fraction of the inclusion in the shell-inclusion system
Γ	threshold ratio
$r*$	critical length
r_{Inc}	radius of the spherical inclusion
R_{Shell}	radius of the spherical shell
$\left(\sigma_{ij}^{M}\right)_{x,y,z}$	local stress tensor of the matrix
$\langle\bar{\sigma}_{ij}\rangle_{M}$	average stress tensor of the matrix
σ_{ij}^{I}	local stress tensor of the inclusion
η_{Z}	Zener index
$\langle\varepsilon'_{11,\psi}\rangle_{i,\psi}$	measured strain for the i^{th} grain within a given ψ-volume
$\langle\varepsilon_{ij}\rangle_{i,\psi}$	average strain tensor for the i^{th} grain within a given ψ-volume
$\langle\sigma_{ij}\rangle_{i,\psi}$	average stress tensor for the i^{th} grain within a given ψ-volume
$\langle\sigma_{ij}^{D}\rangle^{hkl}$	reflection average stress tensor computed from $\langle\varepsilon'_{11,\psi}\rangle_{i,\psi}$ vs. $\sin^2\psi$
N_{ψ}^{hkl}	population number for each ψ-ensemble

f_{ψ}^{hkl}	fraction of each ψ-ensemble
$(E_i)_{\psi}^{hkl}$	effective Young's modulus of a grain
$(E)_{\psi}^{hkl}$	ψ-ensemble average of the elastic modulus
$\langle E \rangle^{hkl}$	reflection average of the elastic modulus
$\bar{E}$	bulk average of the elastic modulus
$(\nu_i)_{\psi}^{hkl}$	effective Poisson's ratio of a grain
$(\nu)_{\psi}^{hkl}$	ψ-ensemble average of Poisson's ratio
$\langle \nu \rangle^{hkl}$	reflection average of Poisson's ratio
$\bar{\nu}$	bulk average of Poisson's ratio
$\langle \sigma_{ij} \rangle_i$	grain average stress tensor
$\langle \sigma_{ij} \rangle_{\psi}^{hkl}$	ψ-ensemble average stress tensor
$\langle \sigma_{ij} \rangle^{hkl}$	reflection average stress tensor
$\bar{\sigma}_{ij}$	global average stress tensor
$\langle \sigma_{ij} \rangle_{\psi}^{*-hkl}$	ψ-ensemble average interaction stress tensor
$\langle \varepsilon_{ij}^{D} \rangle^{hkl}$	reflection average strain tensor computed from $\langle \varepsilon'_{11,\psi} \rangle_{i,\psi}$ vs. $\sin^2 \psi$
$\langle \varepsilon_{ij}^{pl} \rangle_{\psi}^{hkl}$	ψ-ensemble average plastic strain tensor

$\langle \varepsilon'_{11,\psi} \rangle_{i,\psi}^{Ph}$ measured strain for the i^{th} grain within a given ψ-volume of specific phase

$\langle \varepsilon_{ij}^{D} \rangle^{Ph-hkl}$ reflection average strain tensor computed from $\langle \varepsilon'_{11,\psi} \rangle_{i,\psi}$ vs. $\sin^2 \psi$ of specific phase

$\sigma_{ij}^{App.}$ applied stress tensor

$\langle \varepsilon^{eqpl} \rangle_{\psi}^{hkl}$ ψ-ensemble average equivalent plastic strain

$S_1^{SP-Sim}, \frac{S_2}{2}^{SP-Sim}$ Diffraction elastic constants for the simulated single-phase sample

$S_1^{MP-Sim}, \frac{S_2}{2}^{MP-Sim}$ Diffraction elastic constants for the specific phase of simulated multiphase sample

$S_1^{MP-Sim-Com}, \frac{S_2}{2}^{MP-Sim-Com}$ Diffraction elastic constants for the specific phase of simulated multiphase combined sample

E^{hkl} Young's modulus of particular reflection

ν^{hkl} Poisson's ratio of particular reflection

$tr(\sigma_{ij})$ trace of the stress tensor

σ_{VM} Von Mises stress

Acknowledgments

I would like to express my deepest appreciation and gratitude to my advisor, Prof. İsmail Cevdet Noyan, in the first place for his guidance and support at all stages of my graduate studies at Columbia University. I learned a lot of lessons from him not just about my professional life but also about my personal life. I am sure that I will keep enlightened by him in the future. I count myself very lucky to have such a great advisor who is involved in each step of the research passionately and willingly.

I am indebted to our collaborators for their financial and technical support. This thesis would not have been completed without their effort. I could not perform some of the derivations included in this thesis without the help of Dr. Conal Murray. Dr. Ercan Çakmak helped me a lot with my studies and made possible publications for the first time in my academic life. Likewise, Dr. Thomas R. Watkins worked with me patiently and explained a lot about residual stress and mechanical testing. Moreover, I would not be able to perform most of the computations presented in this thesis without help from Prof. Darren Pagan.

I would like to thank Dr. Seung-Yub Lee for his efforts to teach me finite element modeling and being a mentor. I am grateful to Dr. Shangmin Xiong for her support and patience while I was complaining about my models. I would like to express my appreciation to Prof. Pat Mooney for her thoughtful comments.

I am fortunate to be a member of the Department of Applied Physics and Applied Mathematics at Columbia University. I would like to thank Stella Lau, Christina Rohm, Kristen Henlin, David Barrera, Adrian Chitu, Constantine Chernyavsky for their efforts to make mine and

all graduate students life easier. I am grateful to Svitlana Samoilina for her friendship and countless great conversations.

I would like to express my wholehearted and deepest gratitude to my best friend and the brother that I never had, Dr. Mustafacan Kutsal, for being present, showing his support when I was having bad days. I would like to give my special thanks to Dr. Lütfi Ağartan, Dr. Onur Denizhan, Shmuel Kampner, Brian Minevich, Dr. Tuğba Turnaoğlu, Songsheng Tao, Ma'ayan Malter, Ashley Culver, Elena Lomako, Dr. Can Ağca, Dr. Halil Levent Tekinalp, and Nathan Fritz for their invaluable friendship.

Lastly, I want to thank my mother, Sema Şeren, my father, Ahmet Şeren, my sister, Hazal Şeren Köle, my brother in law, Emre Köle, my nephew, Patila, and my companion, Hazelnut for keeping their supports by all means. It is a pleasure to have a family like you and know that you are always with me. Thank you for making me the person that I am.

Dedication

To my beloved family,

“Sema Şeren, Ahmet Şeren & Hazal Şeren Köle”,

Whose support, affection, and love make me able to achieve

such success and honor

1- INTRODUCTION AND BASIC THEORY

1.1- Analysis of Residual Stress Fields

Residual stresses are self-equilibrating internal stresses existing in a free body that has no external forces acting on its boundary [2]. In such bodies the net sums of resultant forces and moments must be zero over the entire volume:

$$\int_{V_{Material}} \sigma_{ij} dV_{Material} = 0 \qquad \text{Eq. (1-1-a)}$$

$$\int_{V_{Material}} \sigma_{ij} x_j dV_{Material} = 0 \qquad \text{Eq. (1-1-b)}$$

Residual stresses in engineering components can be generated during service life and/or manufacturing processes. These stresses arise from the elastic response of the material to an inhomogeneous distribution of non-elastic strains within the component. In other words, residual stresses will be created by elastic deformation of surrounding material to preserve dimensional continuity [3].

Three main mechanisms causing residual stresses are:

a) Non-uniform plastic deformation: occurs in the manufacturing process that changes the dimensions of the body including forging, extrusion, drawing, and during service life as in railway rails.

b) Surface modification: occurs in surface processing operations such as machining, grinding, polishing, carburizing, and shot peening and, during service life, as corrosion.

c) Material phase and/or density changes: occur during manufacturing, heat treatment, and service life in the presence of large thermal gradients. Examples are welding, casting, quenching, annealing, precipitation hardening in alloys, and polymerization in plastics. Local corrosion can also cause density changes in the corroded volume. Also, grain scale anisotropic thermal expansion will cause residual stresses, as well.

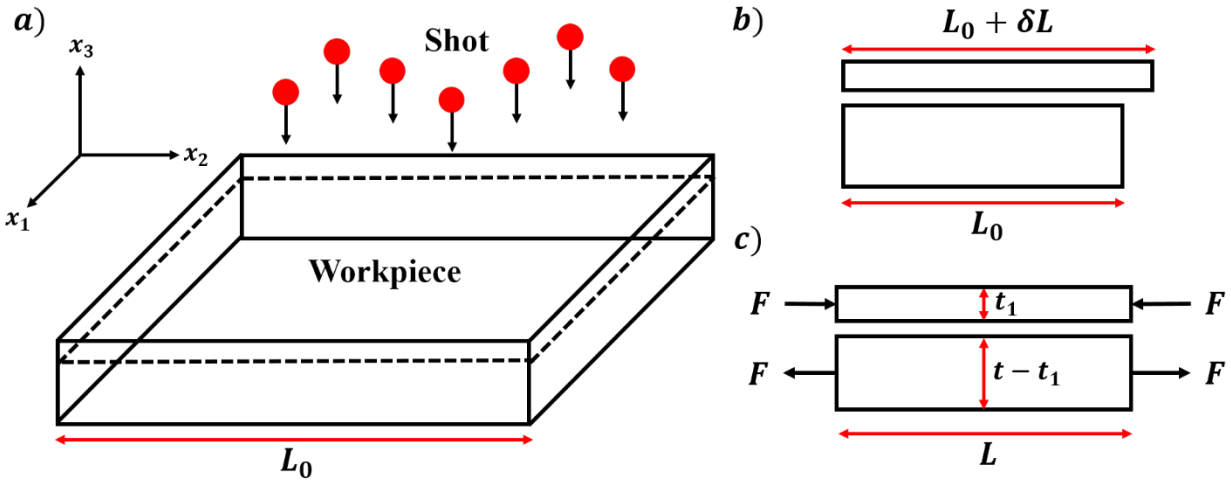

Figure 1.1: a) Schematic description of the normal shot-peening process. b) Free body deformation of the surface and bulk layers without mutual constraint (b) and with mutual constraint (c) of a hypothetical shot-peened specimen.

One of the best examples of the formation of residual stresses is shot peening. This is a surface modification process where spherical balls (shot) randomly impact the surface of a flat workpiece (of dimensions L_0 in the x_1 and x_2 directions and initial thickness t_0) and plastically deform the material close to the surface layers, (Fig. 1.1-a). For a homogeneous, isotropic material

that is peened with a large number of shots impinging randomly on the surface, the plastic strain tensor, ε_{ij}^{p}, in the surface layer can be written as:

$$\varepsilon_{ij}^{p} = \begin{bmatrix} \varepsilon_{11}^{p} & 0 & 0 \\ 0 & \varepsilon_{22}^{p} & 0 \\ 0 & 0 & \varepsilon_{33}^{p} \end{bmatrix} \quad \text{Eq. (1-2)}$$

In the direction of x_3, a compressive plastic strain, ε_{33}^{p} , is produced due to the force exerted by impinging shot. From the conservation of volume, tensile plastic flow, $\frac{\varepsilon_{11}^{p}=\varepsilon_{22}^{p}=-\varepsilon_{33}^{p}}{2}$, will also occur in the direction of x_1 and x_2. The plastic strain terms, ε_{11}^{p}, ε_{22}^{p} and ε_{33}^{p} imply length and thickness changes in the surface layers. Due to the random nature of the deformation process, the distribution of plastic flow is homogeneous in the plane of surface layers.

Let us assume that the surface layer, of initial length L_0 and thickness t_1^0 ($t_1^0 \ll t_0$) can be peened separately from the rest of the sample. The final dimensions of the surface layer become:

$$L' = L_0 + \int \varepsilon_{11}^{p} dx_1 = L_0 + \delta L \quad \text{Eq. (1-3-a)}$$

$$t_1' = t_1^0 + \int \varepsilon_{33}^{p} dx_3 = t_1^0 + \delta t \quad \text{Eq. (1-3-b)}$$

where it is assumed that the plastic deformation is constant within the surface layer (Fig. 1.1-b). If this layer is placed back on the top of the bulk, the lateral dimensions will not match since the bulk of the sample did not undergo any plastic deformation and is still of length L_0. To match the sample dimensions, forces must be applied on the ends of both parts such that the final length L, $L' > L > L_0$, of bulk and the surface layer will be equal (Fig. 1.1-c). Consequently, residual stress fields of opposite signs in the surface and bulk volumes will be formed after the layers are glued together

and the applied forces, F are relaxed. Fig. 1.2 shows the variation of the residual stresses in the workpiece after reattachment.

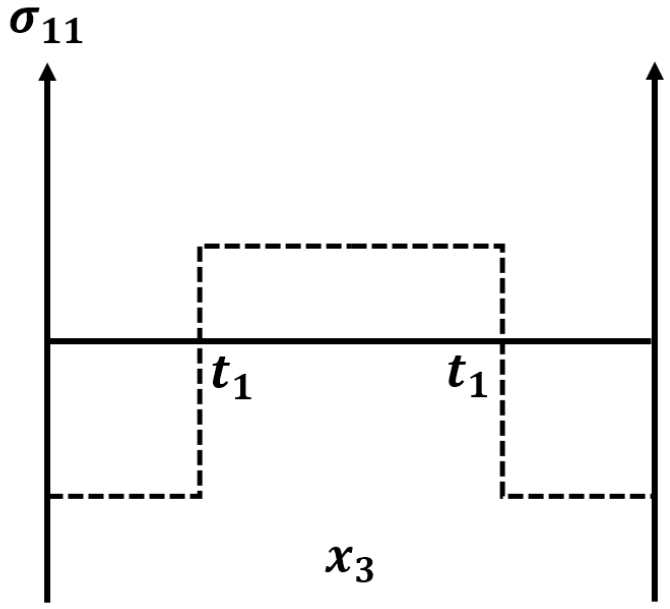

Figure 1.2: Distribution of the in-plane stress along the x_3 direction in a virtual specimen shot peened on both sides.

The residual stress state of a component can have a significant impact on its service life and reliability. Consequently, there have been many efforts to measure and categorize these stresses. However, at this point, there is no consensus among the scientific community about such definitions. In what follows, we will review definitions of residual stress currently in use.

1.2- Residual Stress Definitions

1.2.1- Process-Based Definitions

Almost all processes used to manufacture components and to modify their properties can cause deformation gradients which, in turn, result in the formation of manufacturing residual stresses. Thus, many definitions identify the residual stress state in a component by the type of the manufacturing process. For example, in a multiphase component, phases having different coefficients of thermal expansion will constrain each other during heating and cooling. This phenomenon will cause **thermal residual stresses** due to the constrained expansion/contraction [4, 5]. Differential deformation of a component during machining and forming will cause **mechanical residual stresses** [4]. Volumetric change due to shrinkage of resin during the curing process of thermosetting resin composites forms **chemical residual stresses** [6].

In polymers, two special kinds of residual stresses are defined. First, due to the viscoelastic nature of the polymeric melt, **flow-induced residual stresses** will be formed during the filling, packaging, and holding stages during the manufacture of polymer components. Second, due to the rapid increase of rigidity of the polymer as it passes the glass transition region, if each point in the material solidifies at different times, differential contraction will cause the formation of **thermally-induced residual stresses** [5].

Table 1.1: Some sources of process-based residual stresses *[4]*.

Main Groups	Sub Groups
Machining residual stresses	Grinding Turning Milling Threading Drilling
Joining residual stresses	Welding Soldering Brazing Adhering Riveting
Casting residual stresses	
Forming residual stresses	Rolling Drawing Forging Pressing Spinning Peening Molding
Heat-treating residual stresses	Quenching Transformation Hardening Case Hardening Nitriding
Coating residual stresses	Cladding Spraying Electroplating Plating Galvanizing

1.2.1.1- Thin-Film Residual Stresses

Thin film structures are extensively used in modern technology such as transistors and solar panels etc. Researchers at different disciplines working on thin films have used a different set of definitions. Residual stresses, introduced during processing are separated into two categories. Incompatibility of displacements caused by coefficient of thermal expansion mismatch between the film and substrate are termed **extrinsic residual stresses**. On the other hand, all film stresses introduced during the deposition process are classified as **intrinsic residual stresses** [7]. Due to the locked-in nature of residual stresses, two other definitions were also proposed: **Interlayer residual stresses** are formed due to the mutual elastic constraint of the film and its substrate. These stresses are balanced between the film and the substrate. All processes which cause unequal dimensional changes within either the film or the substrate will form **intralayer residual stresses** within these volumes [8]. The formation of intralayer stresses will also cause interlayer stresses between the film and the substrate.

1.2.2- Solid Mechanics Based Definitions

Solid Mechanics based definitions are more comprehensive than process-based ones described above. Any definition based on the processing technique can be described with the mechanics-based definitions in which residual stresses are categorized by the length scale over which the stress field is assumed to act. The equations written for mechanics-based definitions usually treat stress and strain components as tensor quantities. All such definitions assume, usually implicitly, that the material under investigation is homogeneous, and use Hooke's Law to link stress and strain tensors at a geometric point. These tensors are, then, extrapolated to volumes of

relevant scale. In what follows we review some definitions of basic solid mechanics used in these definitions, after which the definitions, themselves, are presented.

A homogeneous material is a material that has uniform properties at every point in its volume [9]. An **isotropic solid** is a homogeneous material that possesses non-direction-dependent physical properties as opposed to anisotropy, where the material properties are identical at all points but are direction-dependent [10].

Let's assume that a homogeneous isotropic solid bar with a cross-sectional area, A_0 and volume, V_0 is axially loaded with a force, F, distributed over A_0 in elastic compression as shown in Fig. 1.3.

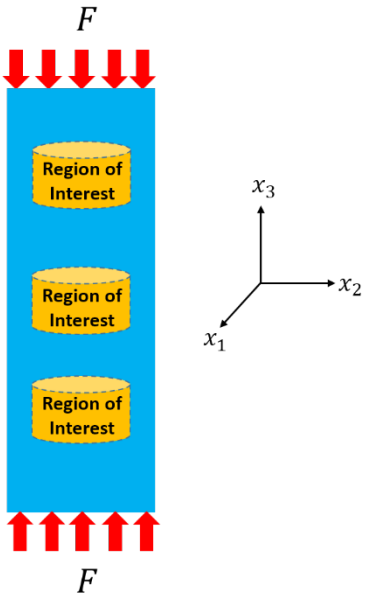

Figure 1.3: Homogeneous, isotropic solid bar elastically deformed with the distributed load.

The stress field can be defined as the distribution of normalized internal forces in a body that balances a given set of external forces/tractions[1]. To determine the internal stress field, the experimenter needs to choose **the region of interest (ROI)** which is the area or the volume centered at a position x_{ROI}, y_{ROI}, z_{ROI}. Stresses/strains existing at a point are called **local stresses/strains** ($(\sigma_{ij})_{x,y,z}$, $(\varepsilon_{ij})_{x,y,z}$).

In practice, we would not define stress/strain at a point because the body of interest is finite in engineering problems. However, modeling of the body of interest containing infinitesimal points forming a continuum allows us to use mathematical tools of continuous functions. To illustrate this, let's assume a body subjected to arbitrary forces, F_1, F_2, and F_3 as shown in Fig. 1.4.

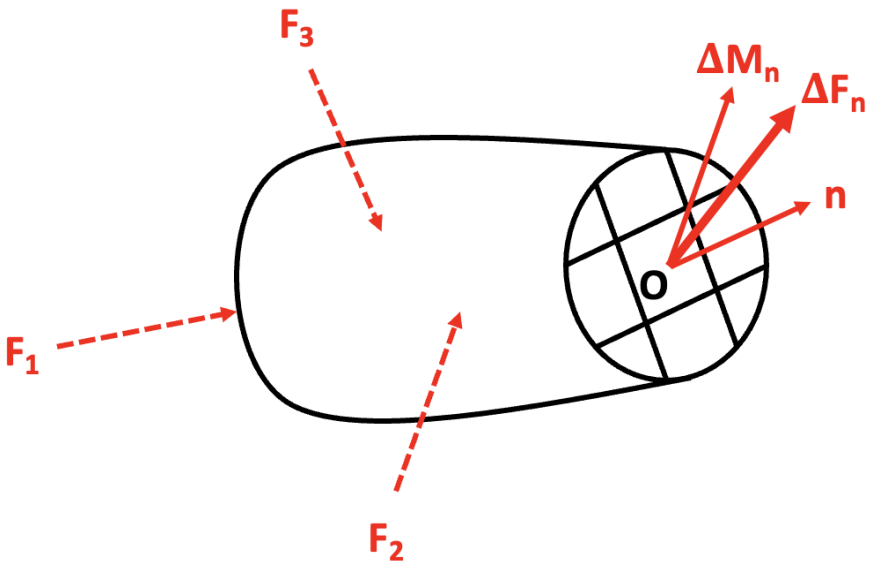

Figure 1.4: A body subjected to arbitrary forces, F_1, F_2, and F_3.

[1] The residual stress fields balance each other within the material volume.

To keep the body in equilibrium, the load, ΔF_n, over the point O in the squared region of ΔA with a normal vector, $\vec{n}$, will have a moment, ΔM_n. This is because ΔF_n by itself is a distributed force over the area, ΔA, and therefore, it is equivalent to the addition of a point load and a moment. As long as, ΔF_n exerts on a finite area, the moment will exist. To be able to define the stress uniquely, the moment has to be zero. This is possible if and only if ΔA goes to zero. Thus, we can define stress vector as $\vec{S}_n = \lim_{\Delta A \to 0} \frac{\Delta Fn}{\Delta A}$. From this vector, components of stress tensor can be derived.

The stress field within the sample of uniform cross-section caused by a statically equivalent system of forces distributed uniformly over the relevant surfaces is called **far-field stress $\left(\boldsymbol{\sigma_{ij}^0}\right)$.** For all measurement locations, the far-field stress can be considered constant and equivalent to a distributed force applied at the boundary of the appropriate free-body section containing the measurement locations. At all points within ROI, the **average stress ($\langle \bar{\sigma}_{ij} \rangle_{ROI}$)** and **average strain ($\langle \bar{\varepsilon}_{ij} \rangle_{ROI}$)** will be equal to the local stresses/strains for a homogeneous bar.

$$\sigma_{ij}^0 = \langle \bar{\sigma}_{ij} \rangle_{ROI} = \left(\sigma_{ij}\right)_{x,y,z} = \begin{pmatrix} 0 & 0 & 0 \\ 0 & 0 & 0 \\ 0 & 0 & \frac{F}{A_0} \end{pmatrix} \quad \text{Eq. (1-4)}$$

In addition, stiffness tensor at a point which links strain and stress tensor is equal to the average stiffness tensor.

$$\langle \bar{C}_{ijkl} \rangle_{ROI} = \left(C_{ijkl}\right)_{x,y,z} = C_{ijkl}^o \quad \text{Eq. (1-5)}$$

A heterogeneous material is a material in which properties vary with the position [11]. Polycrystalline materials, which consist of grains (crystallites), grain boundaries, etc. are

heterogeneous. In general, the **global** stress/strain response of polycrystalline materials is treated using some simplifying assumptions. The most common treatment of polycrystalline materials assumes that the material is **quasi-homogeneous:** that is, the material is homogeneous at a macroscopic level and heterogeneous at the microscale [12]. The local and global stress/strain fields will be different due to local heterogeneity. Therefore, we can define a **representative volume element** ($\boldsymbol{V_{RVE}}$) such that, within its volume, V_{RVE}, the following relationships hold:

a) The average elastic moduli are equal to the bulk moduli for the material:

$$\langle \bar{C}_{ijkl} \rangle_{RVE} = \frac{\int_{V_{RVE}} (C_{ijkl})_{x,y,z} dV}{V_{RVE}} = C^0_{ijkl} \qquad \text{Eq. (1-6-a)}$$

b) The average stresses/strains are equal to the far-field values:

$$\sigma^0_{ij} = \langle \bar{\sigma}^T_{ij} \rangle_{V_0} = \langle \bar{\sigma}_{ij} \rangle_{RVE} = \frac{\int_{V_{RVE}} (\sigma_{ij})_{x,y,z} dV}{V_{RVE}} \qquad \text{Eq. (1-6-b)}$$

$$\varepsilon^0_{ij} = \langle \bar{\varepsilon}^T_{ij} \rangle_{V_0} = \langle \bar{\varepsilon}_{ij} \rangle_{RVE} = \frac{\int_{V_{RVE}} (\varepsilon_{ij})_{x,y,z} dV}{V_{RVE}} \qquad \text{Eq. (1-6-c)}$$

c) The addition of any random volume to the RVE does not change these average values.

$$\sigma^0_{ij} = \langle \bar{\sigma}^T_{ij} \rangle_{RVE+\Delta V} = \frac{\int_{V_{RVE+\Delta V}} (\sigma_{ij})_{x,y,z} dV}{V_{RVE+\Delta V}} = \langle \bar{\sigma}^T_{ij} \rangle_{V_0} = \begin{pmatrix} 0 & 0 & 0 \\ 0 & 0 & 0 \\ 0 & 0 & \frac{F_3}{A_0} \end{pmatrix} \qquad \text{Eq. (1-6-d)}$$

1.2.2.1- Scale Based Definitions

Due to the scale dependency of the stress/strain fields in polycrystalline materials yet another set of definitions were formulated. These are briefly reviewed below.

a) Macherauch classified residual stresses in polycrystalline materials into three categories (Fig. 1.5): **Type I** residual stresses are nearly homogeneous across large scales, several grains, of a material and are equilibrated with respect to the whole component. **Type II** residual stresses are nearly homogeneous across a grain or part of a grain of the material and are equilibrated across a sufficient number of grains. Finally, **type III** residual stresses are inhomogeneous across submicroscopic small areas, several atomic distances within a grain, and are equilibrated across small parts of the grain [4]. In these definitions, homogeneous means "constant in magnitude and direction" [13].

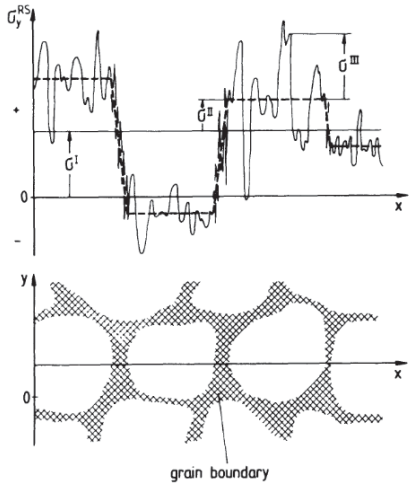

Figure 1.5: Schematical depiction of residual stresses of the first, second and, third types *[4]***.**

b) Cullity first classified residual stresses into two categories and later defined a third category [14]. **Macrostress** is a type of residual stress which is reasonably constant in magnitude, sign, and direction over a fairly large distance (many grain diameters). **Microstress** fields

act over small distances (one grain diameter or less). Then **pseudo-macrostress** [15] (fictitious stresses [16], anomalous stresses [17]) were defined as a special kind of **average** microstress field. Pseudo-macrostresses are constant over large volumes, similar to macrostress, however, they do not satisfy the equations of equilibrium applicable to macrostresses. In addition, pseudo-macrostress fields were detected by diffraction and magnetic methods whereas mechanical relaxation methods failed to reveal their presence [18, 14]. The definition by Cullity captures both aspects of such residual stress fields.

c) Noyan and Cohen defined **macrostress and microstress** similar to Cullity and Macherauch. However, they define **pseudo-macrostress** as the average microstress within a large number of grains selected by diffraction for a given reflection [19].

d) Baczmanski provided three different kinds of residual stress. **First order** stress was defined as the average stress over a sample volume containing a large number of grains. The difference in the behavior of grains with varying lattice orientations will introduce **second order** stresses which are the deviation from first order one. **Third order** stress was defined to characterize stress heterogeneity around defects of the crystal lattice in grain [20]

1.2.2.2- Effect of Sample Geometry and St. Venant's Principle

It is well known that even in homogeneous materials geometric features such as voids, corners, surfaces, etc. as well as point applied loads, can cause position-dependent elastic strain and stress fields (Fig. 1.6). These effects were originally discussed by Barre de Saint Venant, who defined his principle as "The difference between the effects of two different but statically

equivalent loads become very small at sufficiently large distances from load" [21]. In addition, the different versions of the principle with further clarifications [22], [23], [24], [25] were described.

Many authors had efforts to solve and quantify St. Venant's principle to obtain critical length (r^*) for certain applications by finding the position dependency of stress, strain, and strain energy density in various geometries [24], [26], [27], [28]. However, an exact solution that is valid for all linear elastic bodies is not currently available.

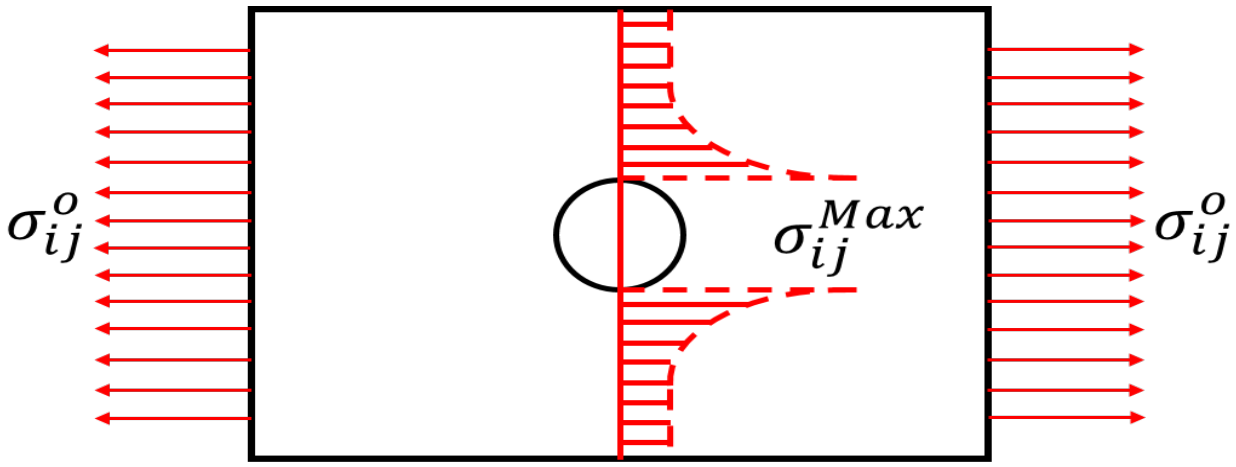

Figure 1.6: Stress profile around an internal void *[29]*.

For this thesis, we will define position-dependent elastic stresses which arise in a material with homogeneous elastic properties due to finite size effects, point loading, changes in cross-section, local voids, etc., as "St. Venant stresses". Stresses arising in and around inclusions will be termed "Eshelby stresses" because the stress field inside inclusions are uniform. In this case,

even if the matrix and inclusion possess homogeneous elastic properties, the overall material is a heterogeneous composite.

From the discussion presented so far, one can conclude that *a priori* knowledge of the type and dimensionality of the stress/strain fields existing in a given sample will be important in choosing the stress measurement technique for the particular system. For example, for a two-phase material, one might wish to determine the stress carried by the individual phases. In what follows, we will present a brief overview of available techniques, followed by an extensive discussion on diffraction-based stress determination methods which are the main thrust of this thesis.

1.3- Residual Stress Measurement Methods

Various methods can be used to determine the residual stresses existing in a manufactured part. Those methods can be separated into destructive and non-destructive categories. Mechanical relaxation methods such as hole-drilling [30], sectioning [31, 32], slitting [33, 34], or the contour technique utilize the dimensional changes induced in the sample by material sectioning and/or removal to determine the initial stress state. Other methods, such as magnetic [35, 36], ultrasonic [37, 38], thermoelastic [39], photoelastic [40], and indentation [41] methods, measure changes in a given property (such as magnetic susceptibility, the velocity of sound, refractive index, and hardness) and relate it to the stress state of the region under investigation. Diffraction techniques, which utilize laboratory or synchrotron x-rays, electrons, or thermal neutrons, measure atomic plane spacings in diffracting volumes and relate these to stresses. These are widely used due to their non-destructive and phase-sensitive nature; this enables the measurement of lattice strain the calculation of stress in different phases in multiphase crystalline materials [19, 42, 43, 44].

1.3.1- Diffraction Strain/Stress Analysis

The lattice plane spacing, "d_{hkl}" of the reflection, hkl, can be obtained from the angular position, θ, of the appropriate diffraction peak through Bragg's Law, $\lambda = 2d \sin\theta$, where λ is the wavelength of the incoming beam [43]. Almost all diffraction techniques utilize, "d_{hkl}", of a crystalline material as an internal strain gage. The "d_{hkl}" of grains aligned at various angles to the surface of the polycrystalline samples will deviate from their unstressed values proportional to the resolved stress normal to them. By measuring the plane spacings of grains at different orientations (termed different ψ-tilts) one can compute the stress state acting on the aggregate (Fig. 1.7). For this purpose, the material is assumed to be homogeneous (isotropic or anisotropic as the case might be) and two coordinate systems are defined as shown in Fig. 1.8. Here the sample coordinate system axes $\vec{S}_i$ define the surface of the specimen, with $\vec{S}_1$ and $\vec{S}_2$ in the surface plane.

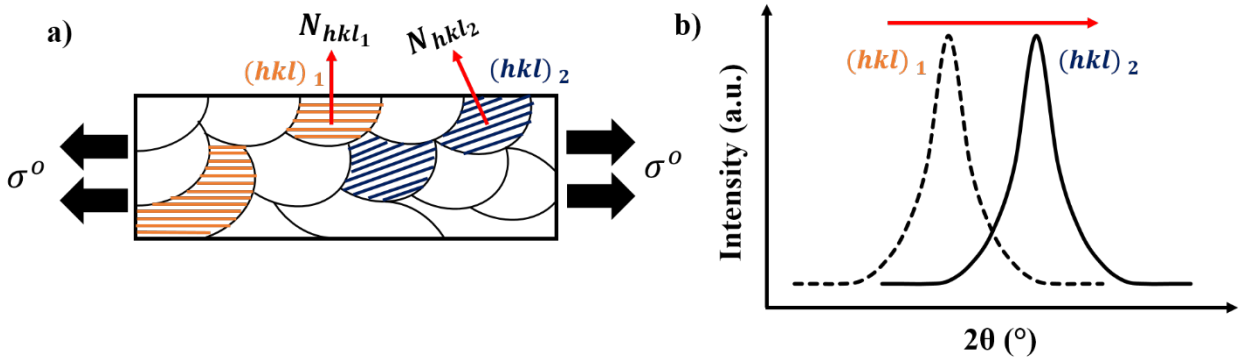

Figure 1.7: a) Certain grains (hkl) satisfy Bragg's Law and diffract beam at a 2θ value which depends on the spacing of the hkl planes which is affected by stresses. Once the specimen is tilted, diffraction occurs from other grains $(hkl)_2$ but the same set of planes. b) Since the normal stress component for $(hkl)_1$ is different than $(hkl)_2$, the interatomic spacing will be different as will the diffraction angle.

The axes of the laboratory coordinate system, $\vec{L}_i$, are defined such that $\vec{L}_3$ ($\vec{L}_{\phi\psi}$) is in the direction of the normal to the family of crystallographic planes (hkl) whose spacing is measured by diffraction. The angle between $\vec{L}_3$ and $\vec{S}_2$ is termed ψ. $\vec{L}_2$ is in the plane defined by $\vec{S}_1$ and $\vec{S}_2$ and makes an angle ϕ with $\vec{S}_2$ [45, 46, 47, 48]. From this point on, tensor quantities referred to the laboratory coordinate system $\vec{L}_i$ will be denoted with primes. Unprimed quantities are referred to the sample coordinate system $\vec{S}_i$ [49].

Once "$d_{\phi\psi}$" in the direction of any $\left(\vec{\mathrm{L}}_3\right)_{\phi\psi}$ is measured, the strain $\left[(\varepsilon'_{33})_{\phi\psi}\right]_{V_{Diff.}}$ within the diffraction volume can be obtained from:

$$\left[(\varepsilon'_{33})_{\phi\psi}\right]_{V_{Diff.}} \equiv (\varepsilon'_{33})_{\phi\psi} = \frac{d_{\phi\psi}-d_0}{d_0} \qquad \text{Eq. (1-8)}$$

where d_0 is the unstressed lattice spacing for the material under investigation. Since the measured strain is a tensor quantity, the second-rank tensor transformation rule can be used to express the measured strain in terms of the strains in the sample coordinate system [50]. Furthermore, Hooke's law links the stresses with strains in both sample and laboratory coordinate systems. As a result, the stresses/strains in both coordinate systems can be expressed in terms of each other. These relationships are described below:

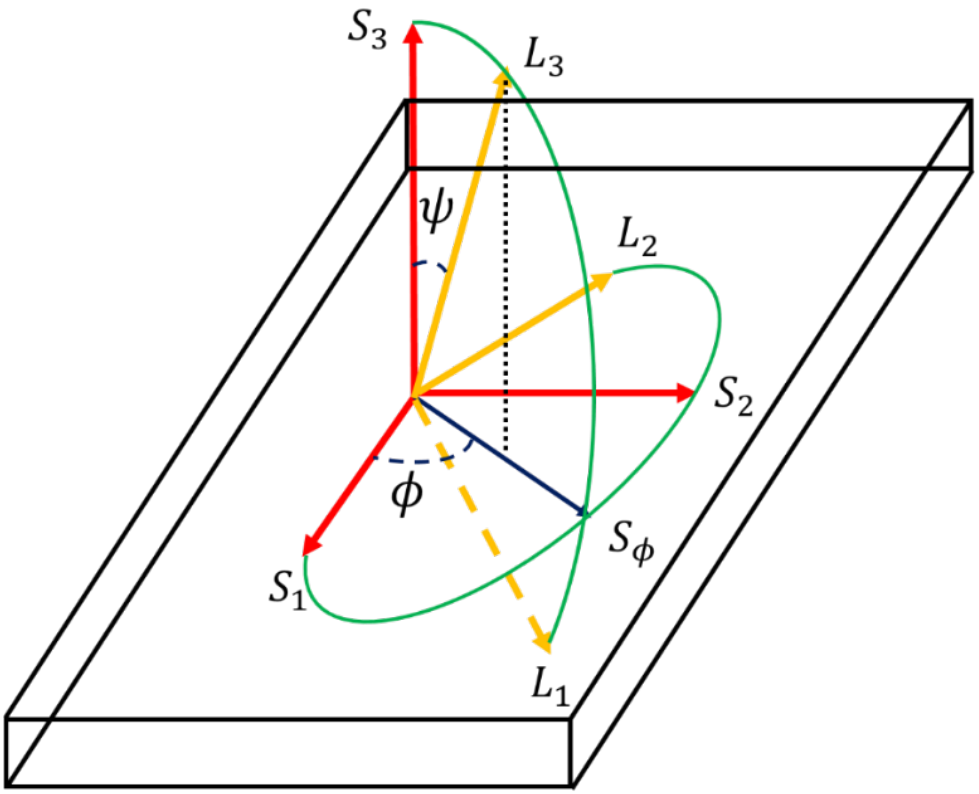

Figure 1.8: Definition of the angles ϕ and ψ and orientation of the laboratory coordinate system, $\vec{L}_i$, with respect to the sample coordinate system, $\vec{S}_i$, and the measurement direction, $\vec{S}_\phi$.

1.3.2- Computation of Strains from Regular "$d_{\phi\psi}$" vs. $sin^2\,\psi$ Data

The strain, $(\varepsilon'_{33})_{\phi\psi}$, computed from the measured plane spacing, $d_{\phi\psi}$, via Eq. 1.8 can be expressed in terms of strains ε_{kl} in the sample coordinate system using the second-rank tensor transformation rule:

$$(\varepsilon'_{33})_{\phi\psi} = a_{3k}a_{3l}\varepsilon_{kl}\,,(k,l=1,3) \qquad \text{Eq. (1-9)}$$

Here a_{3k} and a_{3l} are components of the direction cosine matrix linking coordinate systems $\vec{S}_i$ and $\vec{L}_i$, which :

$$a_{3l} = \begin{bmatrix} \cos\phi\cos\psi & \sin\phi\cos\psi & -\sin\psi \\ -\sin\phi & -\cos\phi & 0 \\ \cos\phi\sin\psi & \sin\phi\sin\psi & \cos\psi \end{bmatrix} \quad \text{Eq. (1-10)}$$

By substituting the direction cosine terms into Eq. (1-9), we obtain:

$$(\varepsilon'_{33})_{\phi\psi} = \frac{d_{\phi\psi}-d_0}{d_0} = [\varepsilon_{11}\cos^2\phi + \varepsilon_{12}\sin 2\phi + \varepsilon_{22}\sin^2\phi - \varepsilon_{33}]\sin^2\psi + [\varepsilon_{13}\cos\phi + \varepsilon_{23}\sin\phi]\sin 2\psi + \varepsilon_{33} \quad \text{Eq. (1-11)}$$

Two different regular $d_{\phi\psi}$ vs. $\sin^2\psi$ behavior can be predicted by Eq. (1-11) predicts two types of dependencies of the "measured" strain $(\varepsilon'_{33})_{\phi\psi}$ on the tilt-angle . (1) When ε_{13} and ε_{23} are zero, Eq. (14) predicts a linear " $d_{\phi\psi}$" vs. $\sin^2\psi$ (Fig. 1.9-a); (2) When either or both of these components are non-zero, the measured spacing, " $d_{\phi\psi}$", will be different at positive and negative ψ tilts (Fig. 1.9-b). The reason for this phenomenon, called ψ-splitting, is that $\sin 2\psi$ is an odd function, which causes a split in the "$d_{\phi\psi}$" vs. $\sin^2\psi$ [49, 51]. Following Noyan, we term these two predicted dependencies "regular" $d_{\phi\psi}$ vs. $\sin^2\psi$ behavior. We note that when the measured strain data has a regular dependency on $\sin^2\psi$, we can conclude, with high certainty, that the strains in the two coordinate systems, $\vec{S}_i$ and $\vec{L}_i$, are linked by Eq. (1-9). Thus, by determining six or more independent strain values in $\vec{L}_i$ coordinates, one can determine all terms of the strain tensor in the $\vec{S}_i$ coordinate system.

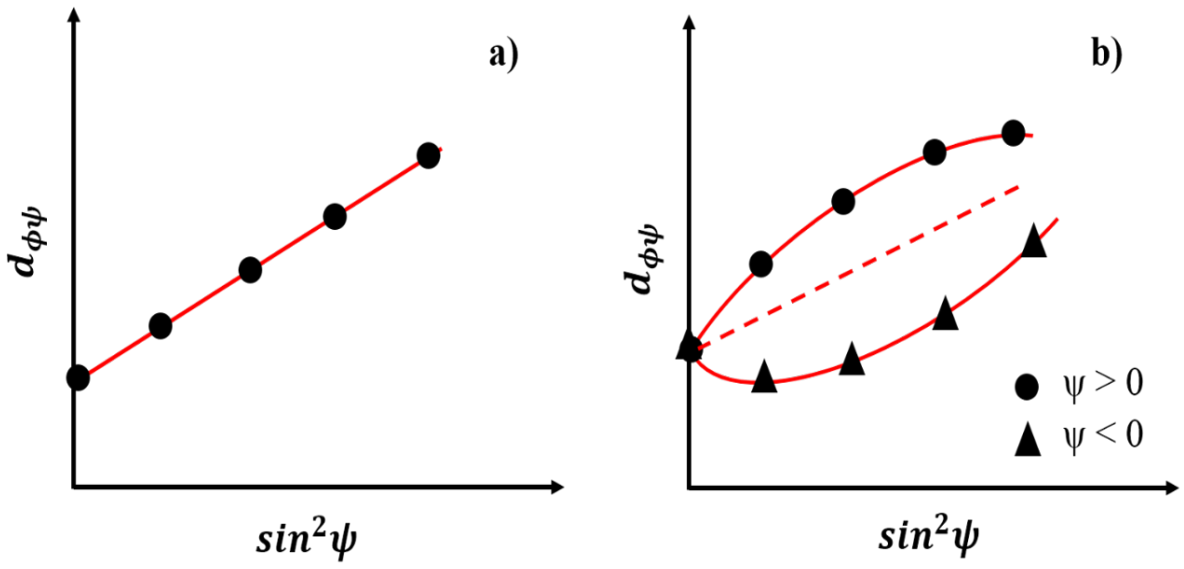

Figure 1.9: Regular $d_{\phi\psi}$ vs. $sin^2\psi$ plots. Linear behavior is predicted when shear strains normal to the surface (along $\vec{S}_3$), ε_{13}, and ε_{23}, are zero. If either or both of these terms are finite, the $d_{\phi\psi}$ vs. $sin^2\psi$ plot "splits" into two branches for $\mp\psi$ *[1]*.

1.3.3- Computation of Stresses from Regular " $d_{\phi\psi}$" vs. $sin^2\psi$ Data in Homogeneous Materials

Hooke's Law can be written for the strains/stresses in laboratory coordinate system as:

$$\varepsilon'_{ij} = S'_{ijkl}\sigma'_{kl} \qquad \text{Eq. (1-12)}$$

Where S'_{ijkl} is the compliance tensor in the laboratory coordinate system. Einstein notation, indicating summation over repeated indices is used. Through the transformation rule, stresses in laboratory coordinate system can also be expressed in terms of the stresses in the sample coordinate system:

$$\sigma'_{kl} = a_{km}a_{ln}\sigma_{mn} \qquad \text{Eq. (1-13)}$$

To link the strains along the diffraction vector $\vec{L}_3$ and to the stresses along $\vec{S}_i$, Eqs. (1-12 & 13) can be combined:

$$\varepsilon'_{33} = S'_{33kl} a_{km} a_{ln} \sigma_{mn} \quad \text{Eq. (1-14)}$$

This equation can be expanded and used for homogeneous materials, with arbitrary stress states. The generalized version is given below:

$$\varepsilon'_{33} = (S'_{3333} - S'_{3311})[\sigma_{11}\cos^2\phi + \sigma_{12}\sin 2\phi + \sigma_{22}\sin^2\phi - \sigma_{33}]\sin^2\psi + (S'_{3333} - S'_{3311})\sigma_{33} + S'_{3311}(\sigma_{11} + \sigma_{22} + \sigma_{33}) + (S'_{3333} - S'_{3311})[\sigma_{13}\cos\ \phi + \sigma_{23}\sin\phi]\sin 2\psi \quad \text{Eq. (1-15)}$$

In the case of an isotropic material, Eq. (1-15) can be significantly simplified:

$$\varepsilon'_{33} = \left(\frac{1+v}{E}\right)[\sigma_{11}\cos^2\phi + \sigma_{12}\sin 2\phi + \sigma_{22}\sin^2\phi - \sigma_{33}]\sin^2\psi + \left(\frac{1+v}{E}\right)\sigma_{33} - \left(\frac{v}{E}\right)(\sigma_{11} + \sigma_{22} + \sigma_{33}) + \left(\frac{1+v}{E}\right)[\sigma_{13}\cos\phi + \sigma_{23}\sin\phi]\sin 2\psi \quad \text{Eq. (1-16)}$$

Here *E* is Young's modulus and *v* is Poisson's ratio of the (isotropic) material. It can be seen from Eq. (1-16) that only four type of stress states can yield linear "$d_{\phi\psi}$" vs. $sin^2\psi$ behavior (Fig. 1.9-a). The stress tensors for these cases are shown below:

$$\begin{pmatrix} \sigma_{11} & \sigma_{12} & 0 \\ \sigma_{12} & \sigma_{22} & 0 \\ 0 & 0 & 0 \end{pmatrix}; \begin{pmatrix} \sigma_{11} & 0 & 0 \\ 0 & \sigma_{22} & 0 \\ 0 & 0 & 0 \end{pmatrix} \quad \text{Eq. (1-17-a \& b)}$$

$$\begin{pmatrix} \sigma_{11} & 0 & 0 \\ 0 & \sigma_{22} & 0 \\ 0 & 0 & \sigma_{33} \end{pmatrix}; \begin{pmatrix} \sigma_{11} & \sigma_{12} & 0 \\ \sigma_{12} & \sigma_{22} & 0 \\ 0 & 0 & \sigma_{33} \end{pmatrix} \quad \text{Eq. (1-17-c \& d)}$$

In such cases, the components of the stress tensor can be determined using various data reduction techniques. These are described below.

1.3.3.1- Biaxial Stress Analysis

If the stress state is biaxial, Eq. (1-16) will become:

$$\varepsilon'_{33} = \frac{d_{\phi\psi} - d_0}{d_0} = \left(\frac{1+\nu}{E}\right)\sigma_\phi \sin^2\psi - \left(\frac{\nu}{E}\right)(\sigma_{11} + \sigma_{22}) \quad \text{Eq. (1-18)}$$

Here σ_ϕ is the stress component along $\vec{S}_\phi$ direction, which can be written in two different forms depending on whether the in-plane shear stress (σ_{12}) is finite or zero:

$$\sigma_\phi = \sigma_{11}\cos^2\phi + \sigma_{12}\sin 2\phi + \sigma_{22}\sin^2\phi \quad \text{Eq. (1-19)}$$

$$\sigma_\phi = \sigma_{11}\cos^2\phi + \sigma_{22}\sin^2\phi \quad \text{Eq. (1-20)}$$

Eq. (1-18) predicts a linear variation of " $d_{\phi\psi}$" vs. $sin^2\psi$ for both cases. From the slope of a least square fit to " $d_{\phi\psi}$" vs. $sin^2\psi$ data, the stress in $\vec{S}_\phi$ direction can be obtained, if the elastic constants (E and ν) and unstressed lattice spacing, " d_0" are known. The terms $\frac{1+\nu}{E}$ and $-\frac{\nu}{E}$ in Eq. (1-18) are known as diffraction elastic constants in the literature [52, 53, 54]. For most of the materials, experimentally measured diffraction elastic constants for the commonly used reflections can be found in the literature [55]. If measured values are not available the constants can be calculated from single crystal elastic constants [2, 56]. Moreover, for biaxial stress states, the lattice spacing measured at $\psi = 0$ can be used as " d_0" without introducing too much error since it is a multiplicand in Eq. (1-18) [19].

1.3.3.2- Triaxial Stress Analysis

1.3.3.2.1- Analysis of Linear $d_{\phi\psi}$ vs. $\sin^2\psi$ data

If the stress tensor within the diffraction volume can be described by Eq. (1.17-c,d) the $d_{\phi\psi}$ vs. $sin^2\,\psi$ plot will still be linear. In this case, Eq. (1-16) becomes:

$$\varepsilon'_{33} = \frac{d_{\phi\psi}-d_0}{d_0} = \left(\frac{1+v}{E}\right)[\sigma_{11}\cos^2\phi + \sigma_{12}\sin 2\phi + \sigma_{22}\sin^2\phi - \sigma_{33}]\sin^2\psi + \left(\frac{1+v}{E}\right)\sigma_{33} - \left(\frac{v}{E}\right)(\sigma_{11}+\sigma_{22}+\sigma_{33}) \quad \text{Eq. (1-21)}$$

Comparing Eq. (1-18) and Eq. (1-21), we observe that, since σ_{33} is finite within the penetration volume, there will be an extra σ_{33} term in the stress term σ_ϕ. For such cases, the following analysis is used [57]: First, strain data, $\frac{d_{\phi\psi}-d_0}{d_0}$, are collected over a set of ψ-angles for two different ϕ tilts, $\phi = \phi_A \; and \; \phi = \phi_A + 90°$ where ϕ_A is an arbitrary angle. The slopes of the corresponding ε'_{33} vs. $sin^2\,\psi$ plots (m_{ϕ_A} , $m_{\phi_{A+90°}}$) are:

$$m_{\phi_A} = \left(\frac{1+v}{E}\right)[\sigma_{11}\cos^2\phi + \sigma_{12}\sin 2\phi + \sigma_{22}\sin^2\phi - \sigma_{33}] \quad \text{Eq. (1-22-a)}$$

$$m_{\phi_A} = \left(\frac{1+v}{E}\right)[\phi_A - \sigma_{33}] \quad \text{Eq. (1-22-b)}$$

$$m_{\phi_{A+90°}} = \left(\frac{1+v}{E}\right)\left[\begin{matrix}\sigma_{11}\cos^2(\phi_A+90°) + \sigma_{12}\sin 2(\phi_A+90°) + \\ \sigma_{22}\sin^2(\phi_A+90°) - \sigma_{33}\end{matrix}\right] \quad \text{Eq. (1-22-c)}$$

$$m_{\phi_{A+90°}} = \left(\frac{1+v}{E}\right)[\phi_{A+90°} - \sigma_{33}] \quad \text{Eq. (1-22-d)}$$

The sum of the slopes is:

$$m_{\phi_{A+90^\circ}} + m_{\phi_A} = \left(\frac{1+v}{E}\right)[\sigma_{11}+\sigma_{22} - 2\sigma_{33}] \quad \text{Eq. (1-23)}$$

The intercept (I) of " $d_{\phi\psi}$" vs. $sin^2\,\psi$ does not depend on ϕ:

$$I = \left(\frac{1+v}{E}\right)\sigma_{33} - \frac{v}{E}[\sigma_{11}+\sigma_{22}+\sigma_{33}] \quad \text{Eq. (1-24)}$$

To obtain σ_{33}, first, σ_{11} and σ_{22} are computed from Eq. (1-22-b) and Eq. (1-22-d), and then Eq. (1-23) and Eq. (1-24) are solved together to obtain σ_{33}.

1.3.3.2.2- Analysis of Split in $\mathbf{d_{\phi\psi}}$ vs. $\mathbf{\sin^2\psi}$ data

If the measurement volume is in a general tri-axial stress state, with stress tensor:

$$\begin{pmatrix} \sigma_{11} & \sigma_{12} & \sigma_{13} \\ & \sigma_{22} & \sigma_{23} \\ & & \sigma_{33} \end{pmatrix} \quad \text{Eq. (1-25)}$$

The terms, a_1 and a_2 are defined for use in the analysis [49]:

$$a_1 = \left\{\frac{d_{\phi\psi+}+d_{\phi\psi-}}{2}\right\} = \left(\frac{1+v}{E}\right)[\sigma_{11}\cos^2\phi + \sigma_{12}\sin 2\phi + \sigma_{22}\sin^2\phi - \sigma_{33}]\sin^2\psi + \left(\frac{1+v}{E}\right)\sigma_{33}$$

$$-\left(\frac{v}{E}\right)(\sigma_{11}+\sigma_{22}+\sigma_{33}) \quad \text{Eq. (1-26-a)}$$

$$a_2 = \left\{\frac{d_{\phi\psi+}-d_{\phi\psi-}}{2}\right\} = \left(\frac{1+v}{E}\right)[\sigma_{13}\cos\phi + \sigma_{23}\sin\phi]\sin 2\psi \quad \text{Eq. (1-26-b)}$$

These terms are linear in $\sin^2\psi$ and $\sin 2\psi$, respectively. Consequently, stresses σ_{11}, σ_{12}, σ_{22} and σ_{33} may be obtained from the slopes and intercepts of regression-fitted a_1 vs. $\sin^2\psi$ plots for $\phi = 0°, 45°, 90°$. Shear stresses σ_{13}, σ_{23} are obtained from the slopes of regression-fitted a_2 vs. $\sin|2\psi|$ plots for $\phi = 0°, 90°$, respectively.

1.3.4- Non-regular " $d_{\phi\psi}$" vs. $sin^2\psi$ Data

For polycrystalline samples, there are two further categories of $d_{\phi\psi}$ vs. $\sin^2\psi$ plots reported in the literature (in addition to the regular responses discussed above). Parabolic (curved) " $d_{\phi\psi}$" vs. $\sin^2\psi$ variation with no ψ–splitting (Fig. 1.10-a) are usually taken as the indication of the presence of strain or concentration gradients along the surface normal $\vec{S}_3$ [1]. While such strain distributions cannot be analyzed with current formalisms, (Fig. 1.10-a) various modifications, based on the different penetration depths of the x-rays at different ψ −tilts, etc. have been proposed [1]. These approaches can predict such plots without adjustable parameters and are considered reliable. On the other hand, there is no consensus on the analysis of oscillatory " $d_{\phi\psi}$ " vs. $\sin^2\psi$ (Fig. 1.10-b). Such data can be neither predicted nor analyzed by Eq. (1-11) or its rigorous extensions. The cause of these oscillations has been investigated in many articles and various explanations have been provided [58, 46, 49, 59, 60, 61, 62, 63, 64, 53] [65, 66]. In what follows, we will present a brief overview of these approaches.

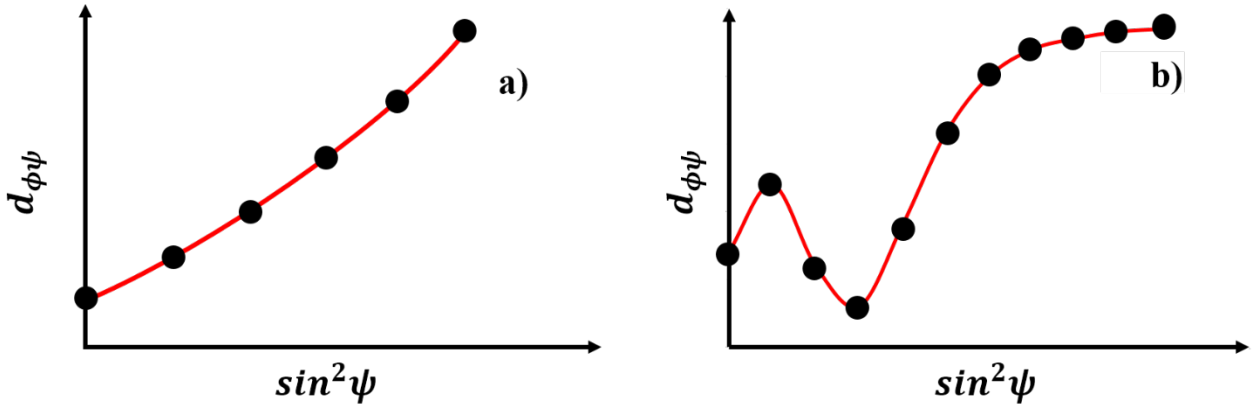

Figure 1.10: Non-regular " $d_{\phi\psi}$" *vs.* $sin^2\psi$ plots; a) curved and b) oscillatory behavior.

1.3.5- Methods Proposed to Analyze Oscillatory Behavior of " $d_{\phi\psi}$ " vs. $\sin^2\psi$

The simplest approach to oscillatory $d_{\phi\psi}$ vs. $\sin^2\psi$ data has been to ignore the oscillations, fit the data with a straight line, and use the traditional analysis presented above. In extreme cases of this "approach" $d_{\phi\psi}$ data are acquired at only two, arbitrary, $\psi-$ angles, avoiding any oscillations which might be present, and a straight line is fitted to the data. This approach is termed the "two-tilt" method and is quite popular with industrial users.

More serious approaches from research groups are described below.

1.3.5.1- Greenough Model

The first scientist that attempted to explain oscillations in " $d_{\phi\psi}$ " vs. $\sin^2\psi$ was Greenough [67]. In this model, the polycrystalline aggregate was replaced by some elastically isotropic and plastically anisotropic single crystals of an equal cross-section but random orientations. The crystals were all parallel, (Fig. 1.11). Once the loading starts, some of the grains exceed the yield point much faster and the strain on these grains is no longer completely elastic. After plastically deforming all grains, the load is removed and let the grains contract elastically. The grains deformed first will be under compression by the grains that have a higher yield point. The possible plastic deformation because of compression is neglected. By using Taylor's plasticity analysis and Schmid equation for the resolved shear stress, the residual lattice strain is calculated.

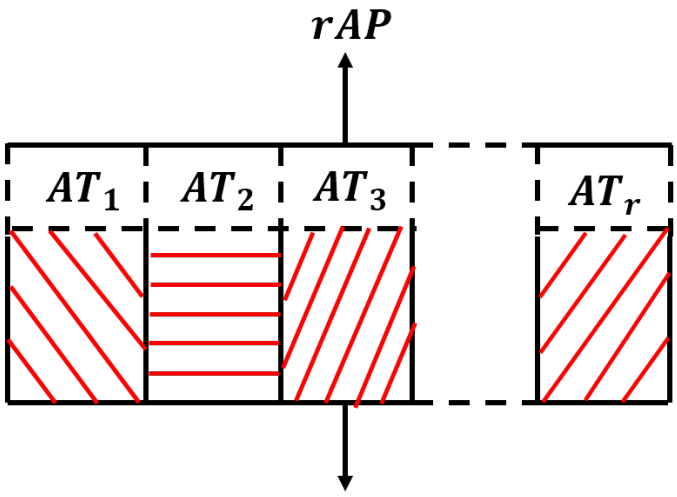

Figure 1.11: Model of polycrystalline aggregate. P is the applied stress, A is the cross-sectional area of each grain, and T_1, T_2… Tr are the stresses in the crystals of orientations 1, 2, … r.

Several experiments were performed to validate the model by comparing the experimental curves with simulated curves [68, 69]. It was shown that the calculated lattice strains did not possess the same angular dependence on ψ exhibited by the measured strains. Also, the values were smaller by a factor of 10 [70, 71]. The biggest source of error in this is that the transverse stresses are neglected.

1.3.5.2- The Marion-Cohen Method

In this method, dynamic recovery of dislocation-poor crystallite regions (plastic deformation followed by localized elastic recovery) is assumed to be the reason for oscillations. To utilize the method, the following assumptions were made [72, 73, 68]:

a) Only crystal regions with a small amount of dislocation density contribute to the maximum of a diffraction peak.

b) The regions of small dislocation density are initially under compressive stress state in a material subjected to plastic deformation (because of expansion in dislocation-rich regions).

c) Some of the dislocation-poor crystallite regions will adjust themselves by rotating in the direction of slip during deformation to be in a more energetically favorable position (A orientation and A regions) relative to the deformation geometry. The compressive stress will be relieved and there will be an increase in lattice spacing. Thus, the lattice parameter of A regions, $d_A = d_{Max}$, has higher values than other regions (B orientation and B regions) whose dislocation density is also small and those crystallites cannot relieve the compressive stresses due to an unfavorable orientation to the applied load.

d) The lattice constant measured by X-rays possesses a maximum "d_{Max}" for each orientation (hkl) of the sample under investigation. From this maximum value, the lattice constant varies with the orientation of the sample according to a distribution function.

With these assumptions, the relationship between lattice spacing and orientation may be expressed as follows:

$$d = (d_{Max} - d_B) f(\alpha, \beta) + d_B \qquad \text{Eq. (1-27)}$$

Here $f(\alpha, \beta)$ is the distribution function of a particular (hkl) plane relative to the sample coordinates and α and β are defined in Fig. 1.12.

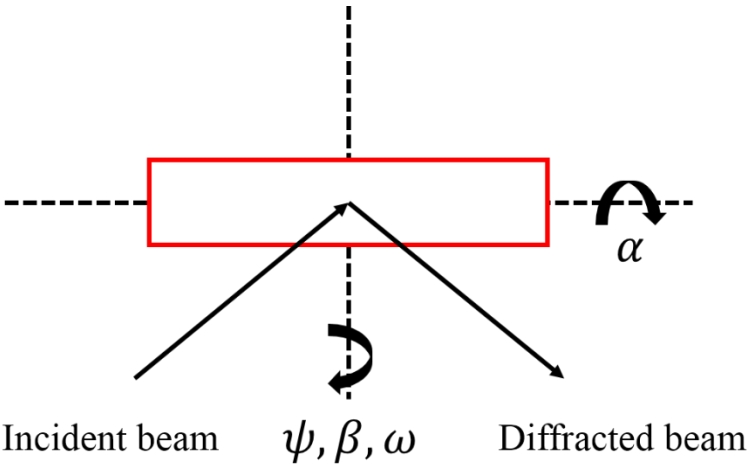

Figure 1.12: Specimen geometry and the definition of α and β in the Marion-Cohen method.

If there is also a macroscopic stress field in the material in addition to the microstrain distribution, Eq. (1-27) becomes:

$$d_{\phi\psi} = (d_{Max} - d_B) f(\alpha, \beta) + d_B + d_0 \frac{1+\nu}{E} \sigma_\phi \sin^2 \psi \qquad \text{Eq. (1-28)}$$

where it is assumed that the macrostress contribution to σ_ϕ yields a linear $d_{\phi\psi}$ vs. $\sin^2 \psi$ dependence. Therefore, elastic interaction strains are assumed to be zero.

The unknowns, d_{Max}, d_B and σ_ϕ in Eq. (1-28) can be solved by curve-fitting techniques, if $f(\alpha, \beta)$ and $d_{\phi\psi}$ are measured as a function of ψ for a particular ϕ. This method predicts that oscillations in "$d_{\phi\psi}$" vs. $\sin^2 \psi$ and $f(\alpha, \beta)$ vs. $\sin^2 \psi$ will have the same form. However, it was proven that this is not always the case [72]. Depending on the ψ-range, the assumption that the maximum range in oscillations is observed in a given measurement can fail. The method assumes that elastic

interaction effects are negligible. This assumption is not true especially for stress relieved textured materials [60].

1.3.5.3- Dölle-Hauk Method (Oscillation-free Reflections)

In this method, it was proposed that oscillations in " $d_{\phi\psi}$ " vs. $\sin^2\psi$ are primarily due to elastic anisotropy [53, 60]. Since grains with different orientations are sampled at ψ and ϕ tilts, the diffraction elastic constants can vary with different tilts in strongly-textured materials. The relation between interplanar spacing " $d_{\phi\psi}$ " and applied stress is:

$$\frac{d_{\phi\psi}-d_0}{d_0} = \langle\varepsilon'_{33}\rangle = \langle\left(S'_{33ij} + t'_{33ij}\right)\sigma_{ij}\rangle \qquad \text{Eq. (1-29)}$$

where S'_{33ij} are the single-crystal elastic compliances in laboratory coordinate system $\vec{L}_i$, and t'_{33ij} are the elastic interaction terms of a grain and its surrounding matrix ("elastic susceptibility"). The brackets in Eq. (1-29) indicate that the average is taken over all the diffracting crystallites. This equation neglects the inhomogeneous microstrain distributions due to an inhomogeneous distribution of plastic deformation. The proposed solution to solve Eq. (1-29) simplifies the system even further by assuming the Reuss limit to describe the stress state in the material. Then S'_{33ij} are calculated in the Reuss limit and σ_{ij} can be determined from a non-linear least-squares solution. The diffraction elastic constants in the Reuss limit is given as below:

$$S_1^R(hkl) = \tilde{S}_{1122} + \tilde{S}_0\Gamma \text{ and } \frac{1}{2}S_2^R(hkl) = \tilde{S}_{1111} - \tilde{S}_{1122} - 3\tilde{S}_0\Gamma$$

$$\tilde{S}_0 = \tilde{S}_{1111} - \tilde{S}_{1122} - 2\tilde{S}_{1212} \text{ and } \Gamma = \frac{h^2k^2+h^2l^2+k^2l^2}{(h^2+k^2+l^2)^2} \qquad \text{Eq. (1-30)}$$

The method predicts no oscillations for (h00) and (hhh) type reflections in cubic materials since the calculated diffraction elastic constants are equal to the isotropic elastic constants. In other words, for these reflections, the anisotropic crystal behaves like isotropic material [49]. It was concluded that if one switches (h00) and (hhh) reflections once oscillations in " $d_{\phi\psi}$ " vs. $\sin^2\psi$ in another (hkl) reflection was observed one should obtain regular " $d_{\phi\psi}$ " vs. $\sin^2\psi$ which can be analyzed with current formalism.

Experiments were performed to check the theory of oscillation-free reflections, and it was summarized that the theory does not work owing to using the Reuss model approximation in which all interaction stresses and strains are assumed to be zero [74]. As a result, it does not satisfy compatibility conditions and would cause the formation of voids at boundaries between grains that have different crystallographic orientations with respect to the applied load axis. In a textured material, non-random inhomogeneous solids, interactions cannot be assumed to be zero.

1.3.5.4- X-ray Integral Methods (Löde and Peiter)

In this method, it was claimed that the reason for oscillations in " $d_{\phi\psi}$ " vs. $\sin^2\psi$ are non-monotonic stress gradients with depth [75]. Since X-ray penetration depth changes at each ψ-tilt, the net average stress affecting individual ψ-tilts will change sign and it will cause oscillations in " $d_{\phi\psi}$ " vs. $\sin^2\psi$.

Two methods were proposed and both are based on a strain field analysis in a thin layer, the developments of the local displacements in a $\langle\varepsilon_{\phi\psi}\rangle$ Taylor's series and the weighting of the measured values [76].

$$\langle \varepsilon_{\phi\psi} \rangle = \frac{\int_0^{z_1} \varepsilon_{\phi\psi} e^{-z/z_0}\, dz}{\int_0^{z_1} e^{-z/z_0}\, dz} \qquad \text{Eq. (1-31)}$$

where z is the penetration depth which is a function of ψ, z_0 is the maximum penetration depth and z_1 is the limit of integration. The integration should be performed over the region illuminated by the beam; the depth of penetration can be computed for the particular geometry utilizing the photoelectric absorption coefficient of x-rays of the selected (monochromatic) radiation for the material under investigation [62]. From this point, two different methods can be used for evaluation:

1.3.5.4.1- ψ-integral Method

The form of $\langle \varepsilon_{\phi\psi} \rangle$ can be expressed as a trigonometric polynomial:

$$\langle \varepsilon_{\phi\psi} \rangle = B_0 + B_2 \cos 2\psi + A_2 \sin 2\psi + B_4 \cos 4\psi + A_4 \sin 4\psi \qquad \text{Eq. (1-32)}$$

In this equation, the coefficients depend on local displacement values and can be evaluated by integrating Eq. (1-32) between $\psi = -45°$ and $\psi = 45°$.

$$\begin{matrix} A_k \\ B_k \end{matrix} = \frac{2}{\pi} \int_{-45}^{45} \langle \varepsilon_{\phi\psi} \rangle \begin{matrix} \sin k\psi \\ \cos k\psi \end{matrix} d\psi \qquad \text{Eq. (1-33)}$$

From these coefficients, one can obtain the strains and the stresses from the appropriate form of Hooke's Law.

1.3.5.4.2- ϕ-integral Method

This method is similar to the ψ-integral method with two exceptions. The strain $\langle \varepsilon_{\phi\psi} \rangle$ is expressed as a polynomial in terms of ϕ and integrated over ϕ from $\phi = 0°$ to $\phi = 360°$ to obtain the coefficients from which the strains are evaluated.

$$\langle \varepsilon_{\phi\psi} \rangle = \frac{B_0}{2} + B_1 \cos\phi + A_1 \sin\phi + B_2 \cos^2\phi + A_2 \sin^2\phi \qquad \text{Eq. (1-34)}$$

These techniques are not popular: The ϕ-integral method is time-consuming. However, its results are in excellent agreement with $\sin^2\psi$ method for homogeneous stress/ strain distributions. The biggest advantage of this technique over $\sin^2\psi$ method is having same x-ray (depth) average at all ϕ rotations because the variation of ϕ does not alter the penetration depth of x-rays [77, 78]. On the other hand, ψ-integral technique is not reliable due to ill-conditioned matrix coefficients. These magnify experimental error, causing large errors in final stress values [79]. Both of these methods were developed for oscillations due to macrostress gradients in the direction of the surface normal and therefore, they should not be used unless it is known that the reason for oscillations is caused by a macrostress gradient.

1.3.5.5- The Crystallite-group Method

The Crystallite-group method was proposed for strongly textured materials. It was first introduced for drawn wires, and then further improved for rolled materials and fiber texture [80, 81, 82, 83]. This method treats all crystallites with the same orientation as one crystal. It is assumed that the stresses within all crystals belonging to a particular crystallite group are the same. Also in strong textured materials, diffraction intensities are much lower for reflections that are not oriented

in the direction of texture, the measuring directions are chosen with respect to texture [84]. Once the strains are determined for a crystallite group, its stress state can be evaluated as follows:

$$\varepsilon_{\bar{m}} = \left[S_{12} + S_0(\alpha^2\alpha_i^2 + \beta^2\beta_i^2 + \gamma^2\gamma_i^2) + \frac{1}{2}S_{44}(\alpha\alpha_i + \beta\beta_i + \gamma\gamma_i)^2\right]\sigma_i \qquad \text{Eq. (1-35)}$$

with $S_0 = S_{11} - S_{12} - \frac{1}{2}S_{44}$

where $\varepsilon_{\bar{m}}$ is the measured strain in the direction $\bar{m}$ and $\alpha_i, \beta_i, \gamma_i$ are the components of the transformation matrix which gives the relationship between crystal and sample coordinate system. The measuring directions are given in the form of α, β and γ where

$\alpha = \cos\phi \sin\psi$, $\beta = \sin\phi \sin\psi$ and $\gamma = \cos\psi$.

The strain measured in $\bar{m}$ direction is the average of individual strain values of all crystallites having the reflection (hkl) under study, oriented perpendicular to $\bar{m}$. And the strains measured should be weighed by the frequency of the orientation distribution function. The main assumption in this method is that all influences of other crystallites which have different (hkl) but still diffracts in $\bar{m}$ direction are neglected. In other words, the strain and stress were determined from only one reflection (in general, corresponds to texture axis) and this calculated local stress is assumed to be macroscopic stress in the material [84]. This method neglects interaction strains between grains. This assumption, alongside the assumption of constant stress within crystallite groups is weak argument in need of systematic investigation.

1.3.5.6- The Glancing Angle Technique

In " $d_{\phi\psi}$ " vs. $\sin^2\psi$ technique, the penetration depth of the beam varies with ψ angle during the measurement, with the penetration depth decreasing with the tilt angle. While this is not an issue for homogeneous strain/stress fields in the depths sampled, this is not always the case: In very thin coatings with steep strain gradients, measurement of residual stress with $d_{\phi\psi}$ vs. $\sin^2\psi$ technique yields an average which does not represent the true stress state. Further, diffraction may occur in the substrate as well, complicating the interpretation and analysis of the diffraction pattern [85, 86, 87]. Usage of the Seemann-Bohlin geometry with the glancing angle technique was proposed to overcome this problem [85, 87]. As shown in Fig. 1.13, this technique uses low-angle-of-incidence (glancing) incident beams. During the measurement, the glancing angle "α" should be fixed in order to keep the penetration depth constant, and multiple (hkl) reflections are measured at different ψ angles. In this model, the penetration depth is shallower and thus, the strain data collected from this technique is limited to layers very close to the film surface.

In this technique, small changes in "α" due to alignment produces a larger error in the measured data. Therefore, a correction should be done by using a zero-stress polycrystalline powder sample. Any measured stress from the powder sample is due to errors in the alignment of the instrument. Once the correction is made, the strain component, ε_σ for the condition where $\sigma_{11} = \sigma_{22} = \sigma$ and $\sigma_{33} = 0$ can be written as:

$$\varepsilon_\sigma = \left(2S_1 + \frac{1}{2}S_2\right)\sigma\left(1 - \frac{\frac{1}{2}S_2}{2S_1+\frac{1}{2}S_2}\cos^2\psi\right) \qquad \text{Eq. (1-36)}$$

where S_1 and $\frac{S_2}{2}$ are the diffraction elastic constants (DEC). From the slope of ε_σ vs. $\cos^2\psi$ graph, stress value can be evaluated if DECs are known.

Since theoretical analysis showed that this model will not work for thin films that have texture, a combined model was developed to analyze the ε_σ vs. $\cos^2\psi$ for textured materials [88]. In this model, the mechanical response of the material is assumed to be a weighted average of the Reuss and Voigt model.

$$\varepsilon_{\phi\psi} = \varepsilon'_{33} = \left[x f_{ij} + (1-x)\omega_{3k}\omega_{3l}S^V_{klij}\right]\sigma_{ij} \qquad \text{Eq. (1-37)}$$

Here x is the "fraction" of the Reuss response and f_{ij} represents DECs based on the Reuss model which can be computed by calculating the weighted average of the single crystal elastic moduli over all the crystal orientations that can diffract. S^V_{klij} is the compliance tensor in Voigt model. $\omega_{3k}\omega_{3l}$ are the direction cosines which enable the transformation of strains from sample to laboratory system [88].

Another complication encountered in the usage of the technique is the accuracy of the peak positions at low 2θ angles. A considerable amount of error in strain/stress values can result from the analysis of these peaks [1]. Calculating overall stress or strain tensor from multiple reflections can be deceiving because all stress/strain tensor is assumed to be the same for all reflections.

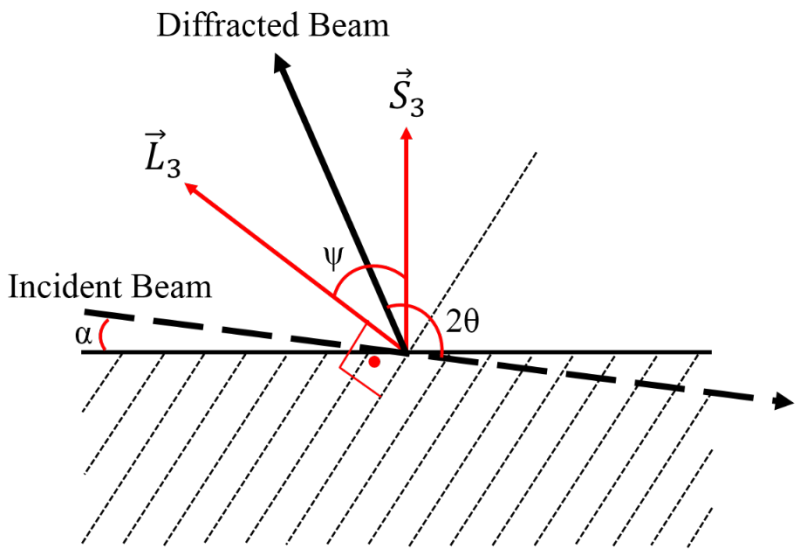

Figure 1.13: Definition of the glancing angle Seemann-Bohlin geometry. The diffracting plane normal ($\vec{L}_3$) makes an angle ψ with the surface normal ($\vec{S}_3$). The incidence angle α is a function of the tilt angle ψ and the diffraction angle θ.

Although it was stated that the compound model gives a better fit for textured materials, the model has no physical meaning. In other words, the "x" value can be any number between 0 and 1, depending on the stress state of the material. More importantly, the method does not take the interaction strains between grains into account.

1.3.5.7- Fixed Crystal Orientation Technique

Fixed crystal orientation technique was introduced to measure residual macroscopic stresses in textured materials [89]. If crystallites of a cubic material have lattice planes ($h_1k_1l_1$) preferentially oriented parallel to the substrate surface, the (h'k'l') lattice planes of these crystallites make an angle ψ with the surface of the substrate shown as:

$$\psi = \cos^{-1}\frac{h_1h' + k_1k' + l_1l'}{\left[\left(h_1^2 + k_1^2 + l_1^2\right)\left(h'^2 + k'^2 + l'^2\right)\right]^{1/2}} \quad \text{Eq. (1-38)}$$

The relation between ψ and the incident angle (θ_I) between incident beam and surface of the substrate can be written as:

$$\psi = \theta - \theta_I \quad \text{Eq. (1-39)}$$

It should be noted that the incident angle is not constant in this method. In order to determine ψ angles from Eq. (1-38), it was assumed that the texture of the material is invariant under the rotation of the sample around its surface normal. This method is claimed to be superior over glancing angle and $\sin^2\psi$ technique in textured materials and thin films. A good signal-to-noise ratio can be obtained for the reflections that are not oriented along the texture axis. For thin films, although the incident angle in this method is not small like in glancing angle, the signal to noise ratio is still strong for all reflections.

If the material is considered as homogeneous and in a biaxial stress state, the relation between lattice parameter, *a*, and stress can be written as:

$$a = \sigma a_0 f(\psi) + a_0 \text{ where } f(\psi) = \frac{1}{2}S_2^{hkl}\sin^2\psi + 2S_1^{hkl} \text{ and } a = \frac{d}{h^2+k^2+l^2} \quad \text{Eq. (1-40)}$$

S_1^{hkl} and S_2^{hkl} are DECs. Stress can be determined by least-square fitting from the plot of a vs. $f(\psi)$.

In this method, it was claimed that the problems observed in " $d_{\phi\psi}$ " vs. $\sin^2\psi$ technique due to elastic incompatibility between grains with a different orientation do not occur because the stress is determined using different reflections from one family of grains [86]. However, the

possibility of obtaining data from other grains which satisfy the Bragg condition in the measurement volume may cause measuring elastic incompatibility strains. In addition to this, there is a chance that the calculated stress is not purely residual macrostress because it is not known for sure that the effect of interaction strains due to elastic incompatibility are averaged to zero. Moreover, only a limited number of grains contribute to diffraction thus, employing this technique affects the grain statistics.

1.3.5.8- The Generalized $\sin^2\psi$ (Matrix) Method

The most recent method developed to help us understand oscillations in " $d_{\phi\psi}$ " vs. $\sin^2\psi$ is called the generalized $\sin^2\psi$ or matrix method [90, 91]. In this method, instead of using traditional $\frac{\phi}{\psi}$ angles, any distribution of measurement points ($\frac{\phi}{\psi}$) can be employed. In addition, performing each pole figure measurement with a linear detector yields 2θ positions of various (hkl) reflections (nearly full diffractogram) at a great number of measurement directions which can be defined by $\frac{\phi}{\psi}$ pair [92]. Almost the whole orientation sphere with densely distributed measurement directions can be scanned. The theoretical basis for this method starts with a modified form of the Dölle-Hauk equation (a special form of Hooke's law) [49]:

$$\varepsilon(\phi,\psi,hkl) = F_{ij}(\phi,\psi,hkl)\sigma_{ij} \qquad \text{Eq. (1-41)}$$

where $\varepsilon(\phi,\psi,hkl)$ is the measured average strain from a particular reflection that contributes the diffraction and $F_{ij}(\phi,\psi,hkl)$ is called X-ray elastic factors and given in the same coordinate

system with stress, σ_{ij}. Eq. (1-42) can be simplified by defining a vector ($\vec{r}$) for the measurement direction instead of $\frac{\phi}{\psi}$.

$$\begin{pmatrix} r_1 \\ r_2 \\ r_3 \end{pmatrix} = \begin{pmatrix} \cos\phi \sin\psi \\ \sin\phi \sin\psi \\ \cos\psi \end{pmatrix} \quad \text{Eq. (1-42)}$$

The relations among $\vec{r}$ and$\frac{\phi}{\psi}$ can be implemented to Eq. (1-41) and the resultant equation is given:

$$\varepsilon(\vec{r}, hkl) = F_{ij}(\vec{r}, hkl)\sigma_{ij} \quad \text{Eq. (1-43)}$$

It was stated that if the coordinate system changes, all of the quantities must be kept the same. In other words, the only way to keep all quantities unchanged is to accept that $\varepsilon(\vec{r}, hkl)$ is a scalar quantity. As a result, $F_{ij}(\vec{r}, hkl)$ must be tensor [93]. For biaxial stress state, this equation becomes:

$$a(\phi, \psi, hkl) = a_0 + F_{11}(\phi, \psi, hkl)a_0\sigma_{11} + F_{22}(\phi, \psi, hkl)a_0\sigma_{22} + F_{12}(\phi, \psi, hkl)a_0\sigma_{12} \quad \text{Eq.(1-44)}$$

Here $a(\phi, \psi, hkl)$ is the lattice parameter and calculated from the measured interplanar spacing $d(\phi, \psi, hkl)$. With enough measurements, a system of linear equations can be obtained and solved together for the unknowns. All d-values are going to be used in the solutions however, not all equations are going to contribute equally. Depending on the standard deviations (calculated the using counting statistics, the background level, the peak line width etc.) of the corresponding measurements, the weights are introduced [93].

The provided proof shows that the claim of the x-ray stress factor being a tensor quantity is not accurate because the measured strains are not tensor quantities that must obey the appropriate

transformation rules and both sets of tensor quantities (original and transformed one) represent the same physical quantity [50].

Other problems of this method: (1) Materials having a strong stress gradient cannot be analyzed. (2) Eq. (1-43) assumes that inhomogeneous micro-strain distribution due to inhomogeneous distribution of plastic deformation is negligible. This second assumption is not very reliable and may invalidate the approach in presence of plastic flow.

1.3.5.9- Other Methods

There are three recent methods that are claimed to be capable of analyzing both regular and non-regular $d_{\phi\psi}$ vs. $\sin^2\psi$ data. These methods are:

- The g method (Grazing Incidence X-ray Diffraction) [94, 95].
- The $\cos^2\theta$ method [96].
- The $\cos\alpha$ method [97].

While these approaches use different tilt and rotation schemes, they are still based on the measurement of lattice strains through diffraction which is then used, along with the appropriate elastic moduli in Hooke's law for stress computation. Consequently, they have the same limitations as all of the previously mentioned techniques did.

1.3.6- Summary

All stress determination techniques discussed above are based on the measurement of lattice strains through diffraction which are then transformed into the (sample) coordinate system of interest. These transformed strains are used, along with the appropriate elastic moduli, in Hooke's law for stress computation[2]. These equations are strictly valid at geometric points. Their utilization in analyzing data using strains measured over "volumes" is possible only when the material, and the stress state within the data acquisition volume, are homogeneous. Ascribing the stress/strain fields obtained from a measurement volume to a given specimen requires assuming further that the material and the stress/strain state within the sample volume are homogeneous.

These requirements show that extension of the diffraction formalisms to strain/stress determination in polycrystalline materials is not straightforward since strain information is obtained only from subsets of grains for each orientation due to the orientation selectivity of Bragg's law. Strictly speaking, even a single-phase polycrystalline material (with the exception of tungsten) is a composite material within which variations of elastic moduli are observed along with sample directions. As a result, there are several issues which need to be addressed when applying diffraction-based stress determination techniques to such systems.

1.4- Problems and Questions

Consider the case where a polycrystalline dog-bone tensile test sample is loaded in tension, and diffraction analysis is used to measure $d_{\phi\psi}$ vs. $\sin^2\psi$ data (Fig. 1.14). Generally, the volume

[2] While the discussion was presented for the analysis of strains obtained by diffraction, any technique which would yield strains along six or more independent $\vec{L}_3(\vec{L}_{\phi\psi})$ directions (Fig. 1.8) could be used with Eqs. (1-8 to 1-25).

of interest, the measurement volume, and the diffraction volume are not the same. Since only certain grains which satisfy Bragg's condition diffract at each ψ-tilt, and these grains are not necessarily next to each other [98], the experiment is performed over discontinuous volumes. Thus, there are several questions which must be answered before one links the (measured) lattice strains to the applied stresses:

a) What is the distribution of stresses and strains within the sampled grains in the measurement volume?

b) How many grains over how many ψ–tilts, and how many reflections need to be sampled for the diffraction measurement to yield the applied stress?

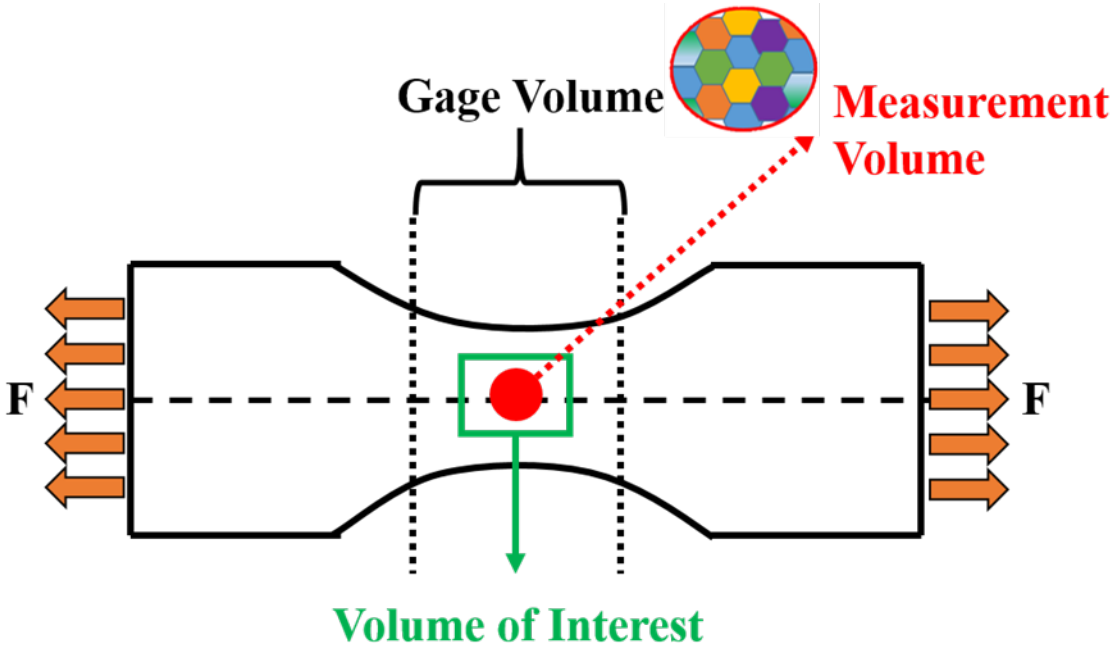

Figure 1.14: Schematic of a tensile test sample and volumes defined during a diffraction experiment and mechanical testing.

c) How do plastic flow and the attendant stress/strain re-distribution change the stress obtained from XRD measurements?

d) Once the applied load is relaxed to zero after plastic deformation, what is the stress/strain distribution in the sample?

In addition, based on our review of the past literature, the following questions need to be answered to provide a rigorous theoretical basis for diffraction-based stress analysis formalisms:

e) What are the origins of oscillations in $d_{\phi\psi}$ vs. $\sin^2\psi$ data?

f) Is it possible to rigorously link oscillations in $d_{\phi\psi}$ vs. $\sin^2\psi$ data to a unique stress state in the material?

g) How do the answers to the above questions change for multiphase polycrystalline materials?

Answering these questions in a statistically meaningful way through experiments requires the measurement of stress and strain within many individual grains of a polycrystalline sample. Such experiments would be quite hard to conduct at this point. In the rest of the thesis, we will try to answer these questions through rigorous finite-element modeling. First, however, we will try to illustrate the issues described above using a simple model and provide a more appropriate set of definitions based on solid mechanics.

2- EXPANDED ANALYSIS AND DEFINITIONS

2.1- Residual Stresses in Homogeneous Materials

An ideal model system with a simple residual stress state is depicted in Fig. 2.1, where a homogeneous solid cylinder (the sample) of initial length, L_0, and cross-section, A_0 , is elastically compressed by a C-clamp to a final length, $L_F = L_0 - \Delta L$. In this model, the compressive residual stresses in the sample are balanced by the tensile residual stresses in the clamp, and the system is at static equilibrium; the effect of the clamp on the free-body diagram sample can be represented by two-point loads[3]. In the following discussion, we will only focus on the elastic strain/stress distributions in the sample induced by these point loads. As can be seen from the photo-elastic stress contours, the stress field within the cylinder can be classified into two distinct types. In the central region (Region 2) we observe a homogeneous stress distribution. In both end regions (Regions 1 and 3) the internal stress depends on the position. Thus, for ease of stress analysis, the cylinder can be represented with three additional free-body diagrams (Fig. 2.2) representing these regions. We will utilize these free-body diagrams to define the stress fields in the cylinder.

[3] Even though the clamp will exert distributed forces over the finite contact surfaces since these areas are assumed to be much smaller than the cylinder's cross-section we represent the clamp forces as point loads for simplicity. This yields the classical *Boussinesq-Cerruti problem* in the theory of elasticity, where the stresses vary as the inverse of the distance from the loaded point.

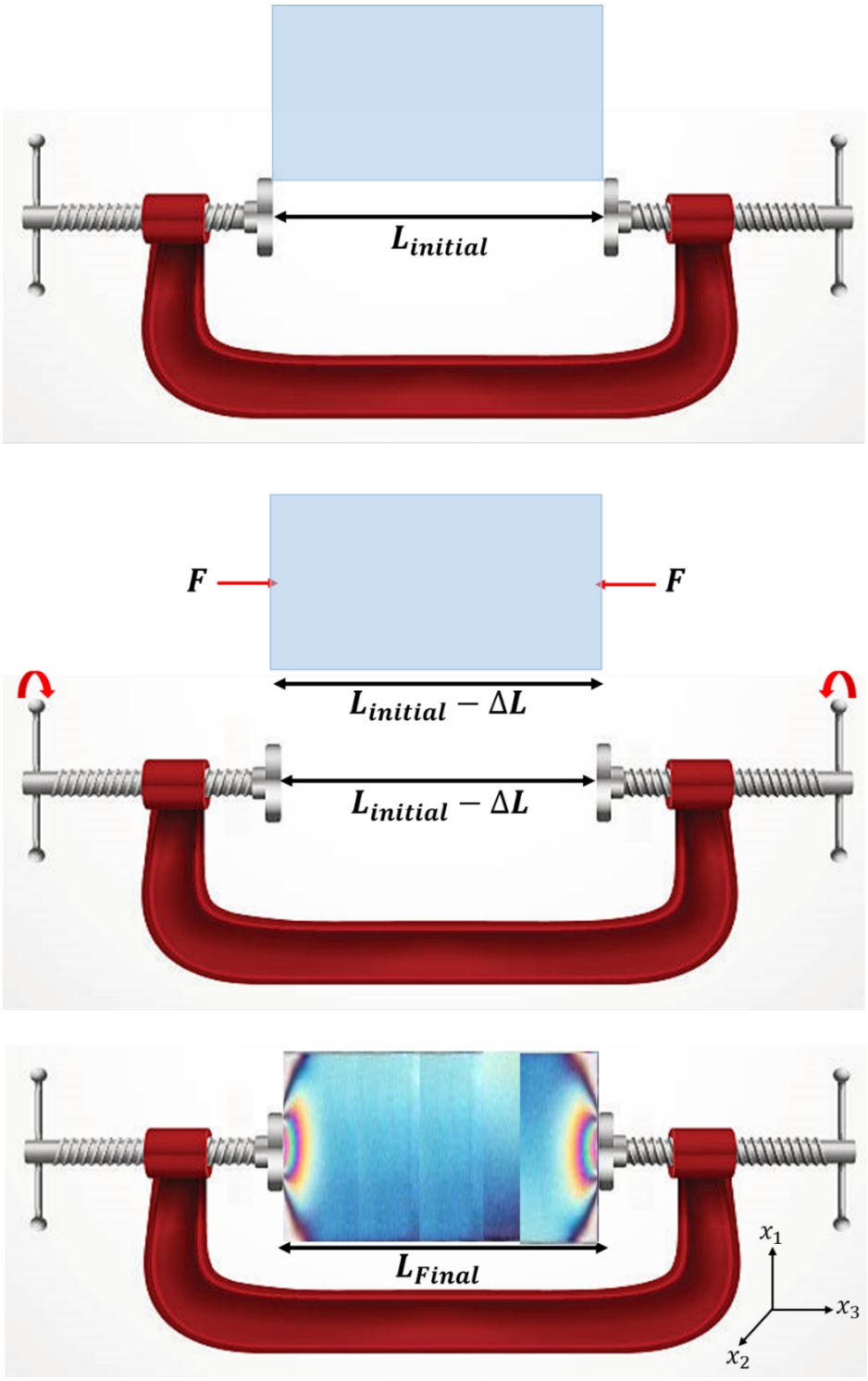

Figure 2.1: Formation of the residual stress in the homogeneous bar constrained by a c-shape clamp *[99]*.

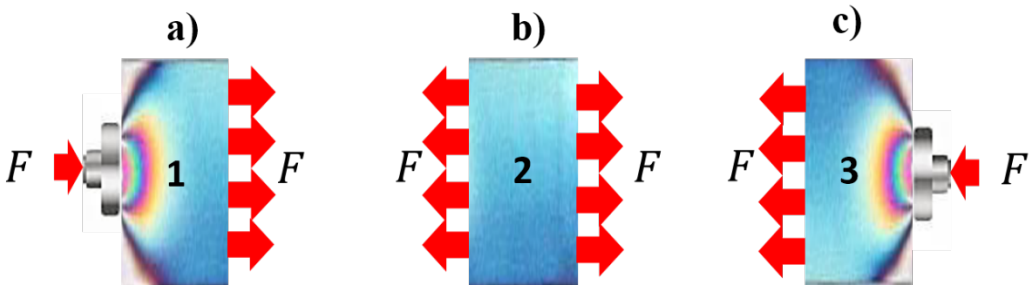

Figure 2.2: Free-body diagrams corresponding to the different regions of the ideal cylinder. Regions FBD-1 and FBD-3 represent the St. Venant regions where end-effects and geometry modulate the stress fields. The stress/strain field in the central region, FBD-2, is homogeneous.

2.1.1- Homogeneous Stress/Strain Fields and Far-field Stresses

Consider free-body diagram for region 2 (FBD-2) first. In this region the **stress field,** i.e. the distribution of normalized internal forces which balance the forces/tractions at the boundary, is homogeneous. Thus, the **local stresses,** $(\boldsymbol{\sigma_{ij}})_{x,y,z}$, are independent of position, and the **average stress** for any measurement volume, $\langle\bar{\sigma}_{ij}\rangle_{V_M}$, or within any region of interest (ROI), including the total FBD-2 volume, will be equal to the local stress:

$$\langle\bar{\sigma}_{ij}\rangle_{V_M} = \langle\bar{\sigma}_{ij}\rangle_{ROI} = \langle\bar{\sigma}_{ij}\rangle_{FBD-2} = (\sigma_{ij})_{x,y,z} = \begin{pmatrix} 0 & 0 & 0 \\ 0 & 0 & 0 \\ 0 & 0 & \sigma_{33}^0 = \frac{F}{A_0} \end{pmatrix} \qquad \text{Eq. (2-1)}$$

Here σ_{33}^0 is a component of the **far-field stress tensor**, σ_{ij}^0, which we define as the stress field within the free body caused by a statically equivalent system of forces distributed uniformly over its relevant boundaries. The elastic strains within FBD-2 are also homogeneous, with equal local and global strain tensors:

$$\langle \bar{\varepsilon}_{ij} \rangle_{V_M} = \langle \bar{\varepsilon}_{ij} \rangle_{ROI} = \langle \bar{\varepsilon}_{ij} \rangle_{FBD-2} = \left(\varepsilon_{ij}\right)_{x,y,z} = \begin{pmatrix} \varepsilon_{11}^0 & 0 & 0 \\ 0 & \varepsilon_{22}^0 & 0 \\ 0 & 0 & \varepsilon_{33}^0 \end{pmatrix} \quad \text{Eq. (2-2)}$$

Stress and strain tensors are linked via the same stiffness tensor for all length scales:

$$\langle \bar{C}_{ijkl} \rangle_{V_M} = \langle \bar{C}_{ijkl} \rangle_{ROI} = \langle \bar{C}_{ijkl} \rangle_{FBD-2} = \left(C_{ijkl}\right)_{x,y,z} \quad \text{Eq. (2-3)}$$

This line of reasoning has two consequences:

a) Any <u>average</u> strain tensor measured within any volume subset of FBD-2 can be transformed to an arbitrary new coordinate system using the second-rank tensor transformation rule[4], Eq. (1-9);

b) Stress/strain analysis in the homogeneous region, FBD-2, is scale and location-independent; <u>measured average strains</u> can be linked to the <u>far-field stresses</u> using Hooke's law:

$$\sigma_{ij}^0 = C_{ijkl} \langle \bar{\varepsilon}_{kl} \rangle_{V_M} \quad \text{Eq. (2-4)}$$

2.1.2- St. Venant Stress/Strain Fields

In the free-body diagrams representing the end regions, FBD-1, FBD-3, (Fig. 2.2-a & c) the local stress and strain tensors, $\left(\sigma_{ij}\right)_{x,y,z}$, $\left(\varepsilon_{ij}\right)_{x,y,z}$ are tri-axial [100, 101, 102] and depend on position due to the boundary conditions associated with point loading. We term these tensors St. Venant stresses and strains respectively:

[4] It was assumed that a homogeneous cylinder has a cubic symmetry.

$$\left(\sigma_{ij}^{SV}\right)_{x,y,z} = \begin{pmatrix} \sigma_{11}^{SV} & \sigma_{12}^{SV} & \sigma_{13}^{SV} \\ \sigma_{21}^{SV} & \sigma_{22}^{SV} & \sigma_{23}^{SV} \\ \sigma_{31}^{SV} & \sigma_{32}^{SV} & \sigma_{33}^{SV} \end{pmatrix};\ \left(\varepsilon_{ij}^{SV}\right)_{x,y,z} = \begin{pmatrix} \varepsilon_{11}^{SV} & \varepsilon_{12}^{SV} & \varepsilon_{13}^{SV} \\ \varepsilon_{21}^{SV} & \varepsilon_{22}^{SV} & \varepsilon_{23}^{SV} \\ \varepsilon_{31}^{SV} & \varepsilon_{32}^{SV} & \varepsilon_{33}^{SV} \end{pmatrix} \quad \text{Eq. (2-5)}$$

For all points (x,y,z), these tensors are linked via Hooke's law: $\left(\sigma_{ij}\right)_{x,y,z} = C_{ijkl}\ (\varepsilon_{kl})_{x,y,z}$. Thus, if local strains could be measured at a point, the local stress at that point could be calculated. Average stresses, strains for a given region of interest, $\langle\bar{\sigma}_{ij}\rangle_{ROI}, \langle\bar{\varepsilon}_{ij}\rangle_{ROI}$, will also be functions of the volume and position of the ROI, and/or the measurement volume within the ROI. In general, we cannot assume, a priori, that the average stress tensor, $\langle\bar{\sigma}_{ij}\rangle_{ROI}$, for a given region-of-interest is equal to the far-field or nominal stress tensor. Consequently, $\sigma_{ij}^{0} \neq C_{ijkl}\langle\bar{\varepsilon}_{kl}\rangle_{ROI}$; in such regions, one cannot obtain the far-field stresses only from Hooke's law or measure the actual stiffness tensor of the material by correlating the nominal applied stress and (measured) average strains.

2.2- Residual Stresses/Strains in Polycrystalline Materials

We now expand the treatment given above to polycrystalline materials by substituting a single-phase, polycrystalline material with very small, equiaxed, grains for the homogeneous material of our cylindrical sample (Fig. 2.1). For consistency, we will assume that the chemistry of the material remains the same, with the same stiffness/compliance tensors, while the microstructure is transformed. In this case, the (residual) stress applied by the clamp will cause local stress perturbations around grain boundaries due to elastic moduli variations between grains along a given sample direction. These will be superposed on the elastic strain/stress distributions for the homogeneous material cause by the clamp stresses and boundary conditions. For simplicity, we will treat the case for FBD-2 first, and extend the discussion to FBD-1 and FBD-3.

2.2.1- Polycrystalline Materials – Homogeneous Far-field Stress

Fig. 2.3 depicts the FBD-2 of the polycrystalline cylinder which has compressive forces, $\vec{F}_3$, uniformly distributed on its horizontal faces. We assume the system is in the elastic loading regime. The stress/strain tensors at any position can be expressed as:

$$\left(\sigma_{ij}^{T}\right)_{x,y,z} = \begin{pmatrix} 0 & 0 & 0 \\ 0 & 0 & 0 \\ 0 & 0 & \sigma_{33}^{0} = \frac{F}{A_0} \end{pmatrix} + \begin{pmatrix} \sigma_{11}^{*} & \sigma_{12}^{*} & \sigma_{13}^{*} \\ \sigma_{21}^{*} & \sigma_{22}^{*} & \sigma_{23}^{*} \\ \sigma_{31}^{*} & \sigma_{32}^{*} & \sigma_{33}^{*} \end{pmatrix} \qquad \text{Eq. (2-6-a)}$$

$$\left(\varepsilon_{ij}^{T}\right)_{x,y,z} = \begin{pmatrix} \varepsilon_{11}^{0} & 0 & 0 \\ 0 & \varepsilon_{22}^{0} & 0 \\ 0 & 0 & \varepsilon_{33}^{0} \end{pmatrix} + \begin{pmatrix} \varepsilon_{11}^{*} & \varepsilon_{12}^{*} & \varepsilon_{13}^{*} \\ \varepsilon_{21}^{*} & \varepsilon_{22}^{*} & \varepsilon_{23}^{*} \\ \varepsilon_{31}^{*} & \varepsilon_{32}^{*} & \varepsilon_{33}^{*} \end{pmatrix} \qquad \text{Eq. (2-6-b)}$$

The interaction stresses and strains, σ_{ij}^{*}, ε_{ij}^{*}, respectively, arise to maintain material continuity (compatibility) along a given vector across grain boundaries of grains with different elastic moduli. These stresses/strains are proportional to the far-field stress and the distribution of elastic moduli around the point of interest.

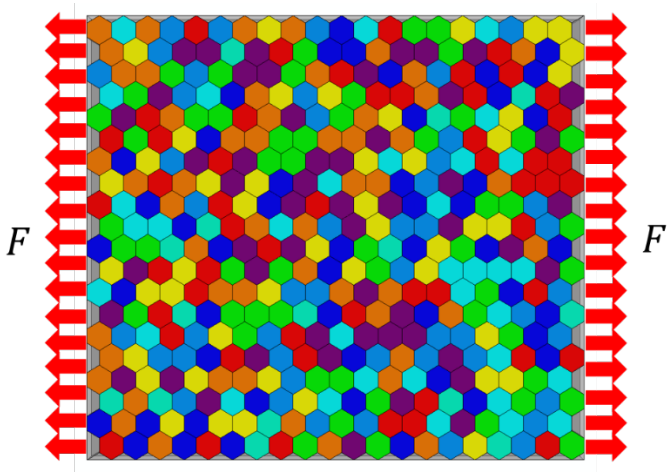

Figure 2.3: FBD-2 of a single-phase polycrystalline cylinder of uniform cross-section A_0 loaded in tension.

Due to equations of equilibrium, and boundary conditions, the interaction stress/strain field is self-equilibrating and will yield a null value when integrated over the entire FBD-2.

$$\sigma_{ij}^{0} = \langle \bar{\sigma}_{ij}^{T} \rangle_{V_0} = \frac{\int_{V_0} \left(\sigma_{ij}^{T}\right)_{x,y,z} dV}{V_0} = \begin{pmatrix} 0 & 0 & 0 \\ 0 & 0 & 0 \\ 0 & 0 & \sigma_{33}^{0} = \frac{F}{A_0} \end{pmatrix} \quad \text{Eq. (2-7)}$$

The average stress/strain for any random volume subset, V, of FBD-2 will yield the volume-weighted average of the stress field within V:

$$\langle \bar{\sigma}_{ij}^{T} \rangle_{V} = \frac{\int_{V} \left(\sigma_{ij}^{T}\right)_{x,y,z} dV}{V} \quad \text{Eq. (2-8-a)}$$

$$\langle \bar{\varepsilon}_{ij}^{T} \rangle_{V} = \frac{\int_{V} \left(\varepsilon_{ij}^{T}\right)_{x,y,z} dV}{V} \quad \text{Eq. (2-8-b)}$$

Within FBD-2, we can define a **representative volume element (V_{RVE})** such that, within its volume, V_{RVE}, the following relationships hold as it was mentioned in Chapter 1.2.2:

a) The average elastic moduli are equal to the bulk moduli for the material:

$$\langle \bar{C}_{ijkl} \rangle_{RVE} = \frac{\int_{V_{RVE}} \left(C_{ijkl}\right)_{x,y,z} dV}{V_{RVE}} = C_{ijkl}^{0} \quad \text{Eq. (2-9-a)}$$

b) The average stresses/strains are equal to the far-field values:

$$\sigma_{ij}^{0} = \langle \bar{\sigma}_{ij}^{T} \rangle_{V_0} = \langle \bar{\sigma}_{ij} \rangle_{RVE} = \frac{\int_{V_{RVE}} \left(\sigma_{ij}\right)_{x,y,z} dV}{V_{RVE}} = \begin{pmatrix} 0 & 0 & 0 \\ 0 & 0 & 0 \\ 0 & 0 & \sigma_{33}^{0} = \frac{F}{A_0} \end{pmatrix} \quad \text{Eq. (2-9-b)}$$

$$\varepsilon_{ij}^{0} = \langle \bar{\varepsilon}_{ij}^{T} \rangle_{V_0} = \langle \bar{\varepsilon}_{ij} \rangle_{RVE} = \frac{\int_{V_{RVE}} \left(\varepsilon_{ij}\right)_{x,y,z} dV}{V_{RVE}} = \begin{pmatrix} \varepsilon_{11}^{0} & 0 & 0 \\ 0 & \varepsilon_{22}^{0} & 0 \\ 0 & 0 & \varepsilon_{33}^{0} \end{pmatrix} \quad \text{Eq. (2-9-c)}$$

c) The addition of any random volume to the RVE does not change these average values.

Measurements are performed over volumes larger than V_{RVE} will yield identical stress and strain tensors, independent of the center of location of the particular V_{RVE} within the sample volume. Thus, the material can be considered as quasi-homogeneous for measurement volumes, $V_M > V_{RVE}$. The stress/strain tensors for $V_M < V_{RVE}$ will be heterogeneous. In addition, if $V_M < V_{RVE}$, the relationship between the average strains and stresses existing in V_M cannot be described by the theoretical stiffness/compliance tensors for the material.

2.2.2- Polycrystalline Materials – St. Venant Regions

If the material in the free-body diagrams representing the end regions, FBD-1, FBD-3, (Fig. 2.2-a & c) is polycrystalline, interaction stresses/strains will also arise around grain boundaries, so that the total stress/strain tensors at any point can be written as:

$$\left(\sigma_{ij}^{SV}\right)_{x,y,z}^{P} = \begin{pmatrix} \sigma_{11}^{SV} & \sigma_{12}^{SV} & \sigma_{13}^{SV} \\ \sigma_{21}^{SV} & \sigma_{22}^{SV} & \sigma_{23}^{SV} \\ \sigma_{31}^{SV} & \sigma_{32}^{SV} & \sigma_{33}^{SV} \end{pmatrix} + \begin{pmatrix} \sigma_{11}^{*} & \sigma_{12}^{*} & \sigma_{13}^{*} \\ \sigma_{21}^{*} & \sigma_{22}^{*} & \sigma_{23}^{*} \\ \sigma_{31}^{*} & \sigma_{32}^{*} & \sigma_{33}^{*} \end{pmatrix} \quad \text{Eq. (2-10-a)}$$

$$\left(\varepsilon_{ij}^{SV}\right)_{x,y,z}^{P} = \begin{pmatrix} \varepsilon_{11}^{SV} & \varepsilon_{12}^{SV} & \varepsilon_{13}^{SV} \\ \varepsilon_{21}^{SV} & \varepsilon_{22}^{SV} & \varepsilon_{23}^{SV} \\ \varepsilon_{31}^{SV} & \varepsilon_{32}^{SV} & \varepsilon_{33}^{SV} \end{pmatrix} + \begin{pmatrix} \varepsilon_{11}^{*} & \varepsilon_{12}^{*} & \varepsilon_{13}^{*} \\ \varepsilon_{21}^{*} & \varepsilon_{22}^{*} & \varepsilon_{23}^{*} \\ \varepsilon_{31}^{*} & \varepsilon_{32}^{*} & \varepsilon_{33}^{*} \end{pmatrix} \quad \text{Eq. (2-10-b)}$$

In the St. Venant regions, the interaction stresses/strains arising to maintain compatibility across grain boundaries will be proportional to the St. Venant stress field at that point, as well as the distribution of the elastic moduli around the point. Consequently, defining a representative volume element becomes problematic, especially in regions with steep St. Venant stress/strain gradients. That is, even if one defines an RVE which yields quasi-homogeneous elastic moduli, the interaction stresses within such RVEs will be heterogeneous due to the heterogeneity of the St.

Venant stresses within. We expect that, when materials consisting of highly anisotropic grains are point loaded with large forces, the resulting interaction stresses could be quite high, and comparable in magnitude to the St. Venant stresses. Finally, the interaction stresses in the St. Venant regions are also self-equilibrating and will integrate out to zero if the integral is taken over the entire free-body volume.

2.3- Residual Stresses/Strains: Effects of Plastic Flow

Plastic flow within the sample under load has two major consequences with regards to residual or applied stress/strain fields. First, plastic flow limits stresses within the yield point, σ_Y, of the material. Second, if the distribution of plastic flow within the sample volume is heterogeneous, the load is transferred from the plastically deformed regions to the undeformed regions. Consequently, the elastic stress/strain fields in these regions will be different. If the far-field load on such a system is relaxed subsequent to the (heterogeneous) plastic flow, the mutual constraint of the regions with different amounts of plastic flow will cause a heterogeneous residual stress field to form within the material. These points are discussed in more detail below.

2.3.1- Effects of Plastic Flow – Homogeneous Materials

2.3.1.1- Regions with Uniform Far-field Stresses

Consider an infinitely long homogeneous isotropic solid cylinder with cross-sectional area A_0, and volume V_0 axially loaded in tension, without boundary constraints, to its yield point[5], σ_Y and deformed to total (elastic plus plastic) strain ε_2 (Fig. 2.4). It is assumed that the material is ideally plastic. For total strain between ε_1 and ε_2, the local and average stress/ elastic strain tensors for any point within the volume can be written as

$$\left(\sigma_{ij}\right)_{x,y,z} = \bar{\sigma}_{ij} = \begin{pmatrix} 0 & 0 & 0 \\ 0 & 0 & 0 \\ 0 & 0 & \boldsymbol{\sigma_Y} \end{pmatrix} \qquad \text{Eq. (2-11-a)}$$

$$\left(\varepsilon_{ij}\right)_{x,y,z} = \bar{\varepsilon}_{ij} = \begin{pmatrix} -\nu\varepsilon_{33} & 0 & 0 \\ 0 & -\nu\varepsilon_{33} & 0 \\ 0 & 0 & \varepsilon_{33} \cong \frac{\boldsymbol{\sigma_Y}}{E} \end{pmatrix} \qquad \text{Eq. (2-11-b)}$$

Since all points within the ideal elastoplastic solid bar undergo identical plastic flow, all points and all ROIs within the material volume will be stress/elastic strain-free when it is unloaded from $(\sigma_Y, \varepsilon_2)$ to zero load all points:

$$\left(\sigma_{ij}\right)_{x,y,z} = \langle\bar{\sigma}_{ij}\rangle_V = 0\ ;\ \left(\varepsilon_{ij}\right)_{x,y,z} = \langle\bar{\varepsilon}_{ij}\rangle_V = 0 \qquad \text{Eq. (2-12)}$$

[5] The tensile force acting on the cylinder is $F^{\#}$.

2.3.1.2- Regions with St. Venant Stresses

If geometric stress concentrations (Fig. 2.2) exist, local (heterogeneous) yielding can occur before the homogeneous regions reach the yield point. Such differential yielding will modify the stress distributions in the St. Venant regions.

$$\left(\sigma_{ij}\right)_{x,y,z} = \begin{pmatrix} \sigma_{11}^{SV} & \sigma_{12}^{SV} & \sigma_{13}^{SV} \\ \sigma_{21}^{SV} & \sigma_{22}^{SV} & \sigma_{23}^{SV} \\ \sigma_{31}^{SV} & \sigma_{32}^{SV} & \sigma_{33}^{SV} \end{pmatrix} + \begin{pmatrix} \sigma_{11}^{**} & \sigma_{12}^{**} & \sigma_{13}^{**} \\ \sigma_{21}^{**} & \sigma_{22}^{**} & \sigma_{23}^{**} \\ \sigma_{31}^{**} & \sigma_{32}^{**} & \sigma_{33}^{**} \end{pmatrix} \quad \text{Eq. (2-13)}$$

Where σ_{ij}^{**} represents the local heterogeneous stresses due to differential yielding. Furthermore, upon full relaxation of the applied load, neighboring regions with different plastic strains can mutually constraint each other from achieving their unconstrained (rest) dimensions, resulting in local residual stress fields balanced between these regions:

$$\left(\sigma_{ij}^{R}\right)_{x,y,z} = \begin{pmatrix} \sigma_{11}^{***} & \sigma_{12}^{***} & \sigma_{13}^{***} \\ \sigma_{21}^{***} & \sigma_{22}^{***} & \sigma_{23}^{***} \\ \sigma_{31}^{***} & \sigma_{32}^{***} & \sigma_{33}^{***} \end{pmatrix} \quad \text{Eq. (2-14)}$$

These stresses are self-equilibrating over the relevant FBD volume:

$$\langle \bar{\sigma}_{ij}^{R} \rangle_{V_{SV}} = \frac{\int_{V_{SV}} \left(\sigma_{ij}^{R}\right)_{x,y,z} dV}{dV_{SV}} = 0 \quad \text{Eq. (2-15)}$$

The final magnitude and distribution of this residual stress field at zero applied load will depend on the sample and loading geometries as well as the magnitude and distribution of plastic flow.

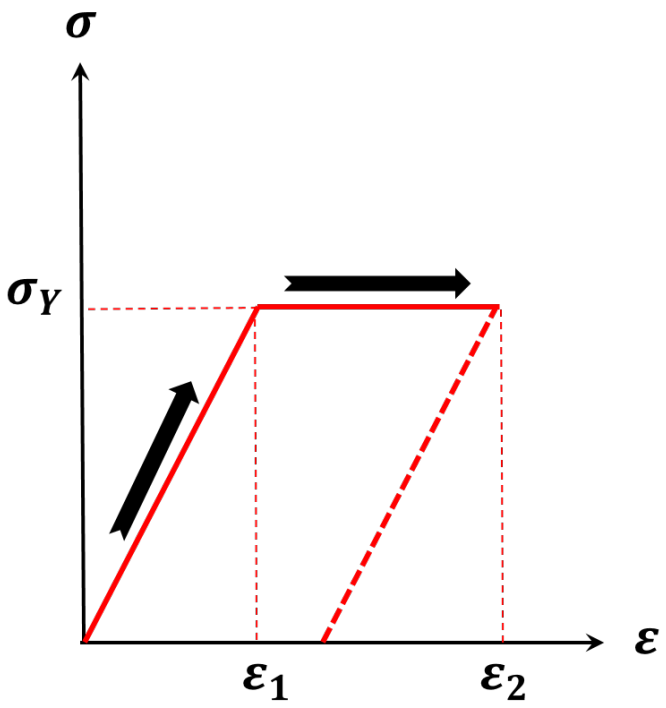

Figure 2.4: Stress vs. strain curve of a homogeneous isotropic solid showing perfect plasticity (no strain hardening).

2.3.2- Effects of Plastic Flow – Polycrystalline Materials

2.3.2.1- Regions with Homogeneous Far-field Stresses

Plastic deformation (slip) in a single crystal occurs most easily on slip systems comprising of close-packed atomic planes along with close-packed crystal directions. Thus, in a polycrystalline solid subjected to a far-field load those grains favorably aligned for slip, with the maximum resolved shear stress acting on an active slip system, will yield first, causing local stress re-distribution. This will modify the local stress distribution such that the total stress tensor at a point can be written as:

$$\left(\sigma_{ij}^{T}\right)_{x,y,z} = \begin{pmatrix} 0 & 0 & 0 \\ 0 & 0 & 0 \\ 0 & 0 & \frac{F\#}{A_0} \end{pmatrix} + \begin{pmatrix} \sigma_{11}^{*} & \sigma_{12}^{*} & \sigma_{13}^{*} \\ \sigma_{12}^{*} & \sigma_{22}^{*} & \sigma_{23}^{*} \\ \sigma_{13}^{*} & \sigma_{32}^{*} & \sigma_{33}^{*} \end{pmatrix} + \begin{pmatrix} \sigma_{11}^{\#} & \sigma_{12}^{\#} & \sigma_{13}^{\#} \\ \sigma_{12}^{\#} & \sigma_{22}^{\#} & \sigma_{23}^{\#} \\ \sigma_{13}^{\#} & \sigma_{23}^{\#} & \sigma_{33}^{\#} \end{pmatrix} \quad \text{Eq. (2-16)}$$

Here $\sigma_{ij}^{\#}$ is the stress tensor due to load transfers caused by plastic flow. At static equilibrium, this tensor is also self-equilibrating over the relevant free-body diagram. If the plastic deformation is randomly distributed among grains, which would be the case for a non-textured solid, the average stresses measured over a volume should tend to the far-field stresses acting on the boundaries of the FBD once the measurement volume equals or exceeds that of the appropriate RVE.

$$\sigma_{ij}^{0} = \langle \bar{\sigma}_{ij} \rangle_{RVE^{\#}} = \frac{\int_{V_{RVE^{\#}}} \left(\sigma_{ij}\right)_{x,y,z} dV}{V_{RVE^{\#}}} = \begin{pmatrix} 0 & 0 & 0 \\ 0 & 0 & 0 \\ 0 & 0 & \frac{F^{\#}}{A_0} \end{pmatrix} \quad \text{Eq. (2-17)}$$

Heterogeneous distribution of plastic strain among constituent grains of a polycrystalline material will also cause an extra residual stress field to form since undeformed grains will constrain plastically deformed grains from achieving their "rest" dimensions. The magnitude of this stress field, which we denote with $\sigma_{ij}^{\#\#}$, will increase during unloading as σ_{ij}^{0} decreases, and can cause reverse yielding in most of the material before the material is fully unloaded to $\sigma_{ij}^{0} = 0$. The Bauschinger effect, the lowering of elastic limit in compression observed in materials deformed in tension beyond the elastic limit, is due to such residual stresses [103].

Once the system is unloaded, local residual stresses balanced between grains with different plastic strain fields will exist:

$$\left(\sigma_{ij}\right)_{x,y,z} = \begin{pmatrix} \sigma_{11}^{\#\#} & \sigma_{12}^{\#\#} & \sigma_{13}^{\#\#} \\ \sigma_{12}^{\#\#} & \sigma_{22}^{\#\#} & \sigma_{23}^{\#\#} \\ \sigma_{13}^{\#\#} & \sigma_{23}^{\#\#} & \sigma_{33}^{\#\#} \end{pmatrix} \quad \text{Eq. (2-18)}$$

In the fully unloaded case, stresses averaged over the total volume of the sample, over the appropriate V''_{RVE} if the sample volume is large enough, as well as averaged across any sample cross-section, must be equal to zero.

2.3.2.2- Polycrystalline Regions with St. Venant Stresses

This configuration results in the most complicated residual distribution. Due to the presence of end effects and/or stress concentrators such as cracks or voids, the applied stress distribution is inhomogeneous in the sample volume. In addition, the heterogeneous distribution of elastic moduli will cause a heterogeneous distribution of interaction residual stresses. The superimposition of these stress fields, coupled with the heterogeneous distribution of active slip systems will cause a complicated distribution of local yielding and resultant load shedding. During unloading a self-equilibrated residual stress field will be set up between the yielded and unyielded regions. The final magnitude and distribution of this residual stress field at zero applied load will depend on the sample and loading geometries, size and orientation distribution of the grains, as well as the magnitude and distribution of plastic flow.

2.4- Revised Definitions for Diffraction Stress Analysis

The discussion so far has shown that heterogeneous distribution of elastic and/or plastic strains within a region of interest can cause complicated residual stress/strain profiles. While the residual stress tensor can be obtained for all cases from Hooke's law *if* the elastic lattice strains at a geometric point could be obtained, this approach might not always be feasible if the measured strains are averages that are taken over volumes which contain non-monotonic stress/strain

gradients. If the volume over which such an average taken is systematically selective-such as diffraction where only grains satisfying Bragg's law are sampled-obtaining the stress tensor in the ROI from measured average strains becomes complicated. In such cases selection of a useful measurement volume within an ROI requires, in addition to the averaging process employed by the particular measurement technique, *a priori* knowledge of the stress distribution such as those caused by end effects, plus the representative volume element for the microstructure of the material under investigation. The average stresses reported from such ROI must be defined in a manner that conveys information about these factors. In what follows we provide a set of revised definitions for this purpose.

2.4.1- Microstress

Strictly defined microstresses are **total stresses acting <u>at a point</u> within an ROI**. In terms of diffraction based measurements, these stresses are computed from strains measured from or within a single grain. Thus, **x-ray diffraction based microstresses are average stresses**. For homogeneous samples, such as a large single crystal, we assume the diffraction volume is much smaller than the size of the ROI, and the ROI size is small compared to the steepness of the stress gradients within the specimen. For polycrystalline specimens, it is assumed that the grain size is much smaller than the size of the specimen. For both cases, the volume from which lattice strains are obtained has homogeneous elastic moduli, C_{ijkl} , such that the stress tensor can be computed

from Hooke's law. The average microstress tensor reported for such small domains might contain contributions from all possible sources such as end effects and/or **Heyn stresses[6].**

2.4.2- Macrostress

We define **macrostresses** as the **average stresses within a measurement volume wherein the measurement technique has sampled sufficient volume so that all self-equilibrating stresses (i.e. Heyn stresses) have been averaged out.** Consequently, the macrostress tensor will tend to the far-field stresses acting on the boundaries of the free-body diagram of the ROI.

For ROIs which are homogeneous with respect to material properties and stress distributions, the residual macrostress tensor for all volume subsets, $V_i \geq V_{ROI}$, will be equal to the far-field stress tensor:

$$\langle \sigma_{ij}^{M} \rangle_{V_i} = \sigma_{ij}^{0} \qquad \text{Eq. (2-19)}$$

For polycrystalline materials with no preferred orientation, macrostresses are defined for volumes which are equal to or larger than the representative volume elements[7] within the ROI. Consequently, the material within the FBD is assumed to be an **equivalent isotropic material**

[6] We use the term **Heyn stresses and strains**, to denote self-equilibrating heterogeneous stress/strain fields arising from all causes discussed previously.

[7] For smaller volumes, the interaction stresses due to heterogeneous distribution of elastic constants and/or plastic deformation will be finite.

with (effective) Young's Modulus and Poisson's ratio, $\bar{E}$ and $\bar{\nu}$, respectively[8]. Representative volume elements in the free-body diagram of the real system are mapped onto points within the equivalent isotropic material (Fig. 2.5). In this case, the standard elasticity analysis described in Chapter 2 for isotropic materials with homogeneous strain and stress fields, can be used directly:

$$(\varepsilon'_{33})_{\phi\psi} = \frac{d_{\phi\psi}-d_0}{d_0} = [\varepsilon_{11}\cos^2\phi + \varepsilon_{12}\sin 2\phi + \varepsilon_{22}\sin^2\phi - \varepsilon_{33}]\sin^2\psi + [\varepsilon_{13}\cos\phi + \varepsilon_{23}\sin\phi]\sin 2\psi + \varepsilon_{33} \quad \text{Eq. (2-20)}$$

$$\varepsilon'_{33} = \frac{d_{\phi\psi}-d_0}{d_0} = \left(\frac{1+\nu}{E}\right)[\sigma_{11}\cos^2\phi + \sigma_{12}\sin 2\phi + \sigma_{22}\sin^2\phi - \sigma_{33}]\sin^2\psi + \left(\frac{1+\nu}{E}\right)\sigma_{33} - \left(\frac{\nu}{E}\right)(\sigma_{11}+\sigma_{22}+\sigma_{33}) \quad \text{Eq. (2-21)}$$

Thus, for such averages, strains obtained from diffraction data for various tilt angles, ε'_{kl} vs. $sin^2\psi$, should exhibit regular behavior (Figs. 2-6-a & b) and the stress terms can be obtained using the formalisms discussed before.

[8] These terms are obtained from averaging single crystal elastic constants over all crystal orientations.

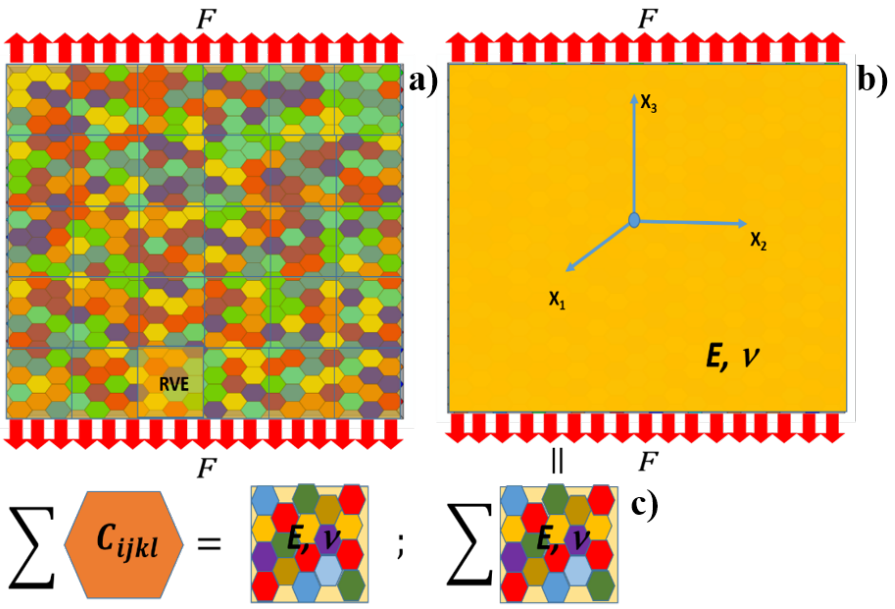

Figure 2.5: Transformation of a random polycrystalline FBD (a) composed of anisotropic grains with moduli, C_{ijkl}, (c), A collection of such grains yield a representative volume element, RVE with moduli E, ν (b), and a collection of RVE form the FBD of the equivalent isotropic material (EIM). In both the RVE and the EIM the stresses, elastic strains, and elastic moduli are homogeneous; and RVE in the polycrystalline FBD is represented by a point in the EIM.

2.5- Representative Volume Definition for Diffraction Techniques

In the case of diffraction techniques which utilize Eqs. (2-20 & 21) definition of the RVE is complicated. Due to the selectivity of diffraction, a different set of grains are selected at each ψ–tilt. Following [74], we term these ***ψ*–volumes**, $\boldsymbol{V_\psi}$. For Eq. (2-20) to apply, the average strains in the sample coordinate system, $\bar{\varepsilon}_{ij}$, must be identical in each and every V_ψ utilized in the experiment**.** For this case, a necessary (but not always sufficient) condition is the equality of average elastic moduli of all V_ψ**.** A schematic free-body diagram of the representative-volume element for a particular V_ψ of a particular reflection *hkl,* $FBD_{V_\psi}^{hkl}$, extracted from the irradiated

volume of the random polycrystalline specimen is shown in Fig. 2.5. The distributed stresses acting on the boundary of the $FBD_{V_\psi}^{hkl}$ are assumed to be the same as the far-field stresses acting on the random polycrystalline FBD. Since all of the grains in $FBD_{V_\psi}^{hkl}$, diffract into the hkl reflection at the particular ψ–tilt, they all have one member of the <hkl> family of directions parallel to the laboratory axis $L_3 \equiv L_{\phi,\psi}$. Thus the elastic moduli along this direction can be computed from single crystal elastic moduli. The crystallographic orientations of the grains in the plane normal to <hkl>: along L_1, L_2 at the particular tilt and rotation angles, ϕ, ψ, are not specified by diffraction. For all $FBD_{V_\psi}^{hkl}$ extracted from a non-textured polycrystalline solid, it is reasonable to assume that all crystallographically allowable directions are equally represented. Consequently, we can assume that, for such conditions, the elastic moduli of all V_ψ will be identical, including at $\phi = 0, \psi = 0$ where the sample and diffraction coordinate systems coincide. If the average elastic moduli of all V_ψ are identical, Hooke's law requires that all $\bar{\varepsilon}_{ij}$ are also identical, and a diffraction measurement will yield regular ε'_{33} vs. $sin^2\psi$ plots.

2.5.1- Oscillatory ε'_{33} vs. $sin^2\psi$ Plots and Pseudo-Macro Stresses

If the average strains in the sample coordinates vary non-monotonically with ψ–tilt oscillations in ε'_{33} vs. $sin^2\psi$ plots will occur. In the absence of St. Venant stress fields, which is the case we are examining here, such variation can occur for several reasons:

1) The same far-field stress acts on all grains for the V_ψ, but the elastic moduli of individual V_ψ are different due to texture or incomplete sampling, the $\bar{\varepsilon}_{ij}$ for elastically stiff V_ψ will

be different than those for more compliant ψ–volumes, resulting in oscillatory ε'_{33} vs. $sin^2\psi$ plots.

2) Consider an RVE with no far-field stress, unloaded after suffering plastic flow. In this case, the grains belonging for a particular V_ψ might have suffered more plastic deformation compared to other grains within the RVE this might be due to the favorable orientation of their slip systems for the particular ψ–tilt. Consequently, this population would have higher elastic constraints from surrounding undeformed or less deformed grains, and the average stresses in the sample coordinates, $\bar{\varepsilon}_{ij}$, will be different for different V_ψ . This will also result in oscillatory ε'_{33} vs. $sin^2\psi$ plots.

We note that there might be cases where all V_ψ sampled during a diffraction experiment might possess comparable average plastic strain fields, $\langle\bar{\varepsilon}^P_{ij}\rangle_{hkl}$, where this plastic strain is different than the plastic strains in grains scattering into other reflections. In this case, the average elastic strains arising to constrain the heterogeneous plastic flow in the RVE will be equal to $\langle\bar{\varepsilon}^{\#}_{ij}\rangle_{hkl}$within all V_ψ of the particular reflection. This will result in regular (linear or ψ –split) ε'_{33} vs. $sin^2\psi$ plots. In this case the stresses are balanced between grains of different reflections and/or different phases (for a multiphase alloy) and mechanical sectioning of the RVE would yield no macro-residual stresses. Consequently, we define **pseudo-macro stresses for a reflection *hkl*** as the stress state where: (1) There is no far-field stress; (2) The ε'_{33} vs. $sin^2\psi$ plots exhibit regular (linear or ψ –split) for ψ –tilts used in the experiment. The presence of pseudo-macro stresses for one reflection *hkl* does not imply that all reflections have pseudo-macro stresses. The overall stress state might be balanced by other grains or grain boundary regions. The pseudo-macro stress field

is NOT a stress field in Cartesian space. It refers to diffraction selected volumes, V_{ψ}^{hkl}, which are discontinuous in real space. Consequently, such "stresses" do not have to obey the standard equations of equilibrium since one cannot draw a continuous cross-section through the RVE such that it only contains cross-sections of V_{ψ}^{hkl} .

2.6- Summary

Based on solid mechanics, three kinds of stresses were defined:

a) **Local stresses:** The total stress tensor which exists at a point. Local stresses will have contributions from applied loads and Heyn stresses arising from elastic and plastic incompatibility. If the sample has stress concentrators such as void or cross-sectional changes, the far-field stress field which would exist in an equivalent homogeneous sample will be modified. These modified stresses are called **St. Venant stresses**.

b) **Average stresses:** These are averages of local stresses over a given volume. Their value depends on the size and type of the sampling volume. Diffraction measurements always yield average lattice strain/stress values. Linking these to the stress state existing in an ROI requires **a priori knowledge** of the microstructure of the material and its previous deformation history.

c) **Pseudo-macro stresses:** These are a particular type of average stresses. They cannot be referred to as a continuous volume in Cartesian space even though they yield regular ε'_{33} vs. $sin^2\psi$ plots.

The Bragg selectivity of the diffraction process makes the separation of these various stress types very complicated. Decomposing experimental values into the particular stress types and identifying the volumes to which they refer is an ill-conditioned inverse problem [104]. We decided to use finite element analysis for a rigorous simulation of such decomposition since our previous attempts [105, 106, 74] were not comprehensive. This effort is discussed in the remaining chapters. We will start by describing the modeling procedures we used.

3- MODELING PROCEDURE

3.1- Introduction

Our discussion in the previous sections showed that continuum elasticity assumptions are not necessarily satisfied in polycrystalline aggregates analyzed by diffraction methods. This is due to the selective nature of the diffraction: not all possible grain orientations are present in the measurement volume and different measurement volumes may yield different results even in utilizing the same reflections [107]. The transformation of the average strains measured in the laboratory coordinate system into stresses in the sample coordinate system is not a trivial task and requires a lot of assumptions whether the experimenter uses stress or strain as a starting point of the transformation. In cases where the experimenter wants to determine the strain/stress state of a particular grain (**microstresses)**, average strains should be measured from individual grains and utilized with elastic moduli to compute stresses using Hooke's law. This can be accomplished using 3D diffraction imaging where strain from individual grains can be collected however, this method is time-consuming, complicated, and requires expensive purpose-built optical and software systems [108, 109].

To search for answers to the questions asked at the end of chapter two, we used finite element modeling. This approach provides both local and global stress and strain information at all locations of a virtual specimen. Thus, we avoid dealing with only average strain quantities and the associated inverse problem. In literature, there have been some efforts to simulate a diffraction experiment on a virtual specimen under different loading regimes [74, 106, 105]. However, these efforts were limited and did not answer a lot of the key issues.

In this study, we employed two state-of-the-art finite element codes, ABAQUS CAE [110] and Finite Element Polycrystal Plasticity (FEpX) [111] for different kinds of numerical simulations. First, to investigate St. Venant's effects under ideal conditions, we utilized a thermally loaded homogeneous isotropic composite system with spherical symmetry. Second, to understand the nature of elastic Heyn strains and the strain partitioning in single and multiphase polycrystalline materials, we modeled a virtual thin film sample under thermal loading where the boundaries were constrained. In both cases, thermal loading was chosen instead of mechanical loading since, in cubic materials, the coefficient of thermal expansion is isotropic. Both of these simulations were performed in ABAQUS CAE. Finally, to simulate in-situ diffraction tensile tests on single and multiphase materials loaded into the plastic regime and unloaded, we used the FEpX code which has an advanced single-crystal plasticity module. In this chapter, we will present the particulars of setting up and executing the models for the above three cases.

3.2- St. Venant's Stresses in a Homogeneous Isotropic Sample

To investigate the development of St. Venant's stresses in homogeneous isotropic material systems, we developed a simple model to investigate the stresses caused by the thermal expansion of a spherical inclusion inside a spherical shell. A schematic of the system is shown in Fig. 3.1.

The thermal expansion was input by pre-defined field modules [110]. The whole sample system was heated to 100°C. Plastic deformation is not allowed in the system. For all contact surfaces, tie-constraint was defined to prevent sliding of the inclusion with respect to the shell. The composite model does not have prescribed displacement or rotation boundary conditions, but rather equation constraints that instead define a relation between two points to impose symmetry

conditions. Equation constraints allow the inclusion and the matrix to deform symmetrically and prevent global displacement of the composite system. The material properties specified using Handbook data are listed in Table 3.1.

During model execution the C3D8R (8-node linear brick with reduced integration), 3D mesh element, was tried at first, to save computation power. However, this approach created resolution problems at the interface. Then the mesh was converted to C3D20 (20-node linear brick) elements to discretize all of the components to obtain a satisfactory level of spatial resolution at the interface. Several mesh sizes were tested to minimize any effects of mesh-size dependency. For an inclusion having a 5 mm radius and a matrix shell with a 50 mm radius, a mesh size of 0.5 mm was employed within the interface between the inclusion and the matrix to capture the large stress gradients. (grey area in Fig. 3.1). The mesh size in the central part of inclusion is 0.3 mm (green region in Fig. 3.1) and a coarser mesh (red region in Fig. 3.1), 2mm, was used within the central region of the matrix for the same system since the effect of large stress gradients is not observed in this part of the matrix. The final model contains more than 50,000 elements. Calculations are converged approximately 12 hours on a workstation when the system is fully elastic.

Table 3.1: Mechanical and thermal properties of the components along the loading axis. The mechanical parameters of steel, aluminum alloy, copper, and tungsten were obtained from the Metals Handbook, *[112, 113]*.

	Young's Modulus E / GPa	Poisson's Ratio ν	Shear Modulus G / GPa	Yield Strength σ_y / MPa	Room-temperature CTE / 10^{-6}/ °C
1018 Carbon Steel (Fe)	200	0.29	78	~ 370 (tensile)	12.5
Aluminum Alloy 6061 (Al)	69	0.33	26	~ 270 (tensile)	23.6
Copper (Cu)	115	0.31	44	~ 235 (tensile)	17.3
Tungsten (W)	400	0.28	156	~ 750 (tensile)	4.4

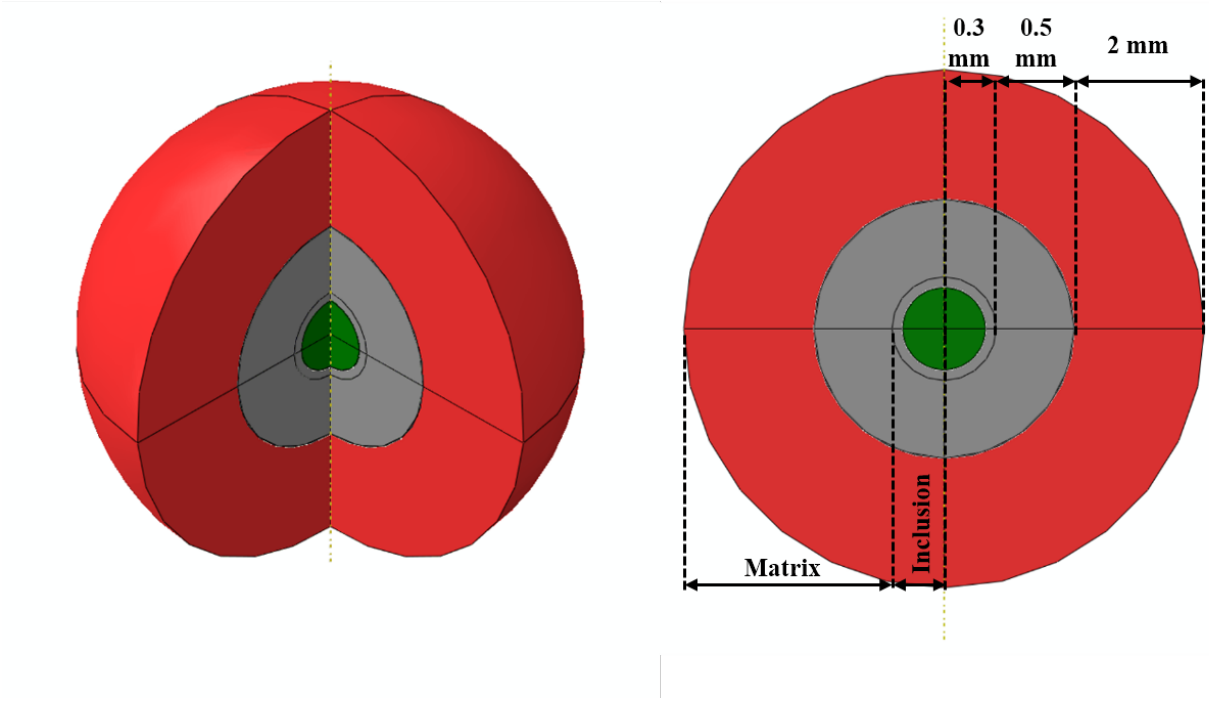

Figure 3.1: Schematic diagrams of the FEM model for r_{Inc} = 5 mm and R_{Mat} = 50 mm (The different mesh sizes are delineated by color).

3.3- Thermal Expansion of Single and Multiphase Materials under Constraint

In this study, we used numerical simulation is used to construct a self-consistent model of x-ray stress/strain analysis in order to investigate the origin of elastic Heyn stresses/strains in a homogeneously loaded region where St. Venant's stress fields were minimized.

3.3.1- Grain Definition and Mesh Geometry

In this model, we constructed a polycrystalline thin-film specimen, one single grain thick, wherein the orientation and the location of the individual anisotropic crystallites were exactly known. All grains were randomly distributed in a mesh generated using ABAQUS CAE. In the single-phase model, 400 hexagonal crystallites are arranged in a 20 x 20 x 1 matrix (Fig. 3.2). To increase the sampling statistics, in the multiphase model 676 hexagonal crystallites are arranged in a 26 x 26 x 1 matrix. We used hexagonal prism-shaped grains to increase elastic grain-to-grain interactions. These hexagonal grains were complemented by partial grains (shaded gray) at the edges to obtain a smooth boundary. These edge grains were defined to be elastically isotropic.

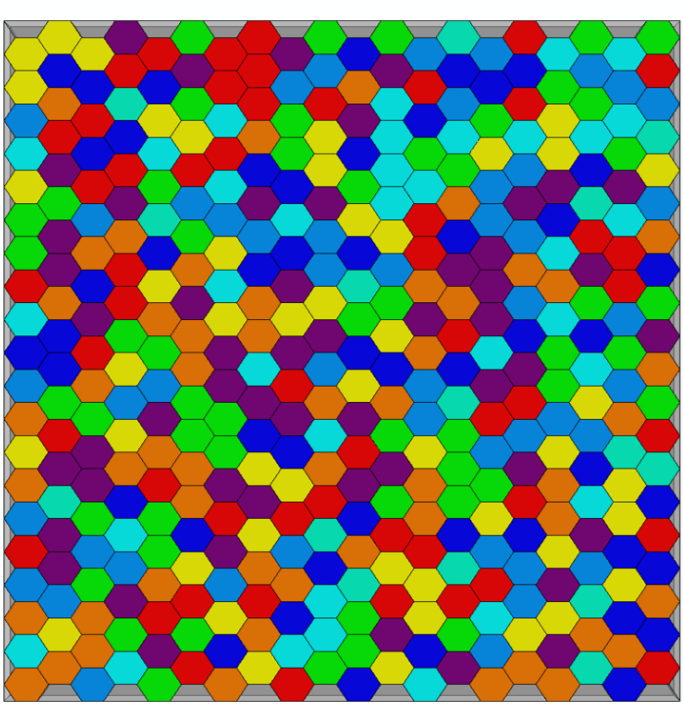

ψ	Color
0	Red
18.43	Orange
26.57	Dark Blue
33.21	Light Blue
39.23	Turquoise
45	Green
56.79	Purple
71.57	Yellow

Figure 3.2: Top view of ABAQUS mesh containing 400 anisotropic grains with isotropic edge (and corner) grains.

All of the interior crystallites were defined to be fully anisotropic. C3D20 (20-node linear brick) elements with a mesh size of 0.5 mm were used to discretize these crystallites. All grain surfaces were connected with tie-constraints. In addition, equation constraints were defined to prevent the global displacement of the model. To induce thermal expansion step-wise homogeneous thermal loading and unloading steps were applied over the entire mesh as predefined temperature fields (Fig. 3.3). Since the coefficient of thermal expansion is isotropic in cubic materials, symmetrically distributed constraints were introduced at the boundaries to create both far-field stresses in the film and resultant interaction (Heyn) stresses between crystals. These boundary conditions were defined such that the mesh could only expand out of the film plane. In

other words, the mesh was placed under (compressive) far-field plane-stress conditions. This served two purposes: (1) It maximized the interaction stresses between crystals and (2) For an isotropic material the problem could be solved analytically as well.

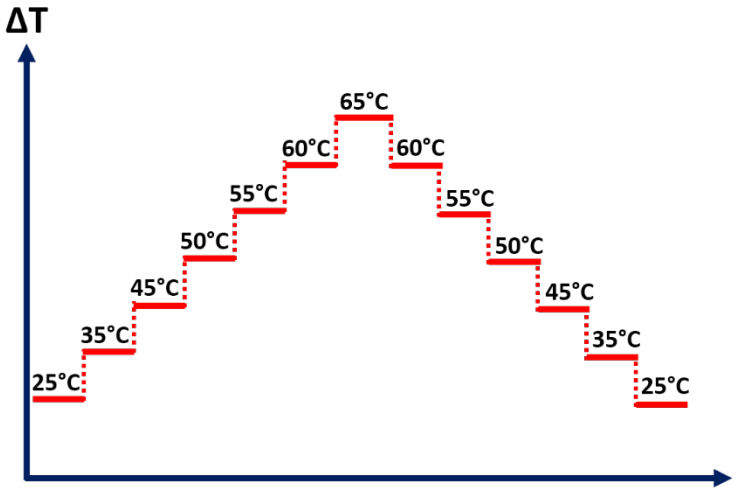

Figure 3.3: Step-wise thermal loading and unloading of the numerical model.

3.3.2- Definition of Grain Orientations

We used the approach and programs developed by Song [107] to calculate the crystallographic directions coincident with the axes of the sample coordinate system for crystallites that would diffract with a particular reflection (hkl) for various ψ angles between 0 and 90 degrees. This procedure is as follows:

A general unit cell was shown in Fig. 3.4 where $\boldsymbol{a, b\ and\ c}$ are the lattice vectors and $\boldsymbol{\alpha}$, $\boldsymbol{\beta\ and\ \gamma}$ are the angles between lattice vectors. When $\boldsymbol{a, b\ and\ c}$ vectors are equal to each other and the angles $\boldsymbol{\alpha}$, $\boldsymbol{\beta\ and\ \gamma}$ are equal to 90° the resultant unit cell is called a cubic cell.

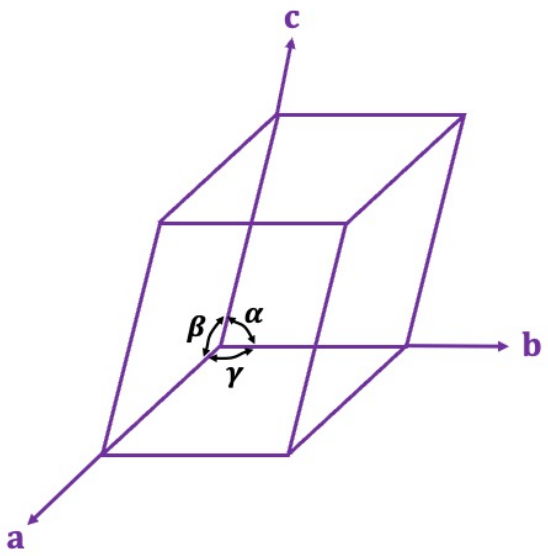

Figure 3.4: Illustration of a general unit cell with three basis vectors, a, b and c.

In cubic structures, the cartesian crystal frame, shown in Fig. 3.5, is parallel to the cubic unit cell. However, this is not the case for non-cubic structures. In this thesis, we will not go into the conversion of non-cubic structure basis vectors to cartesian crystal frame. These calculations can be found in the literature [114].

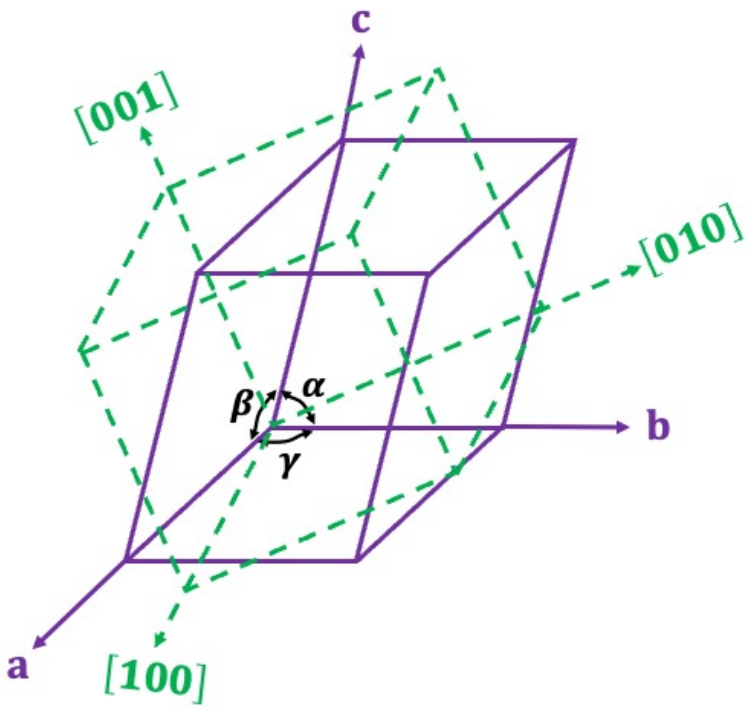

Figure 3.5: The relationship between basis vectors and cartesian crystal coordinates.

In a diffraction experiment, four different coordinate systems are necessary to fully define the orientation relationships between the sample, diffracting grains, and the diffractometer. With the relationships between all of the axes, the diffracting set of planes can be predicted for a given specimen orientation. **Sample axes** denoted as $\vec{S}_i$ where $i \in (1,3)$ or z,y,x defines the sample orientation with respect to the diffraction process and the loading direction if any. In our case, the loading direction is assumed as $\vec{S}_1 \equiv z$. **Grain axes** define the crystal axes which are coincident with the ***sample axes*** for a given grain. Suppose that a hypothetical material consists of "M" grains. The $\vec{G}_i^j,\ i \epsilon(1,3), j \epsilon(1, M)$ coordinates are specific to the grain defined by the index j. $\vec{G}_i^j$ which

is parallel to the $\vec{S}_i$ are the crystal directions. $\vec{G}_i^j = \left[\vec{a}_i^j, \vec{b}_i^j, c_i^j\right]$ where $\vec{a}_i^j, \vec{b}_i^j, c_i^j$ are the indices of the crystal directions in the j[th] grain along $\vec{S}_i$ (Fig. 3.6).

The grain axes, $\vec{G}_i^j$, are related to the crystal axes $\langle h00 \rangle$ through crystal symmetry. The angles, shown in Fig. 3.7, $\boldsymbol{p}$, $\boldsymbol{q}$, $\boldsymbol{r}$ between $\vec{G}_i^j$ and unit cell axes, $\langle h00 \rangle$ are defined by vector algebra:

$$[00h].\vec{G}_3^j = p \qquad \text{Eq. (3-1-a)}$$

$$[0h0].\vec{G}_2^j = q \qquad \text{Eq. (3-1-b)}$$

$$[h00].\vec{G}_1^j = r \qquad \text{Eq. (3-1-c)}$$

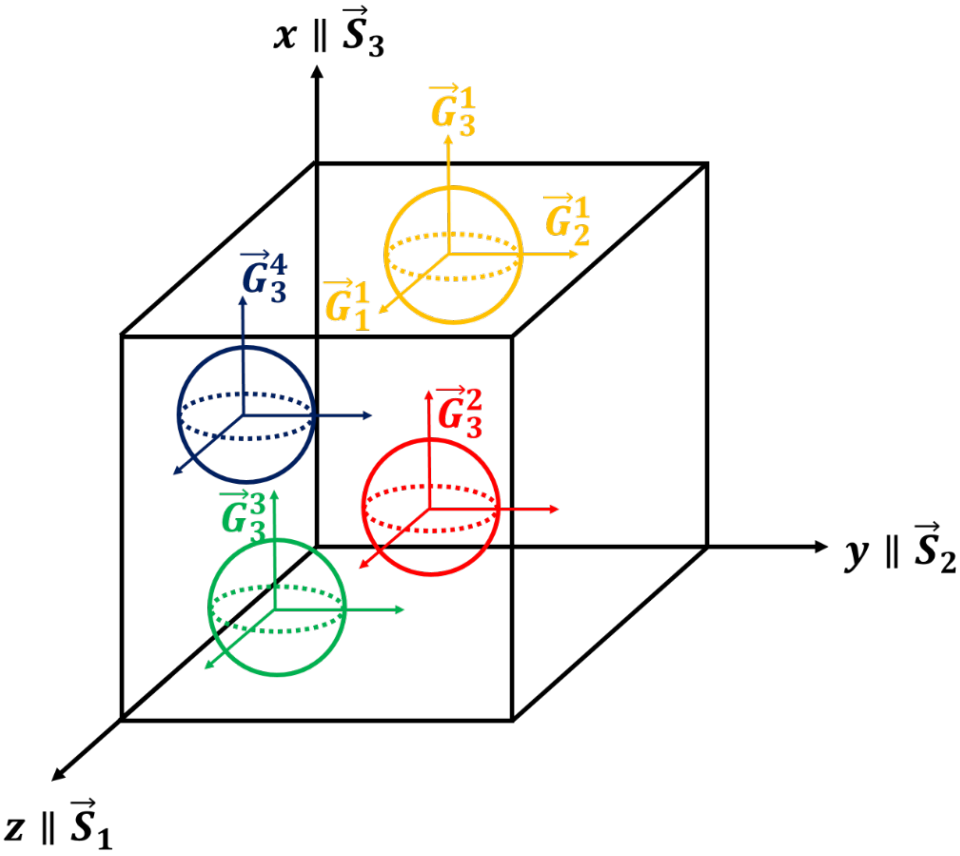

Figure 3.6: Hypothetical material consisting of grains whose crystal axes are parallel to the sample coordinates.

These are needed to compute the elastic modulus for the $\vec{G}_i^j$ coordinate system through the fourth-rank tensor transformation rule. In addition, the Schmid factors of each grain which are necessary for plastic deformation can be calculated.

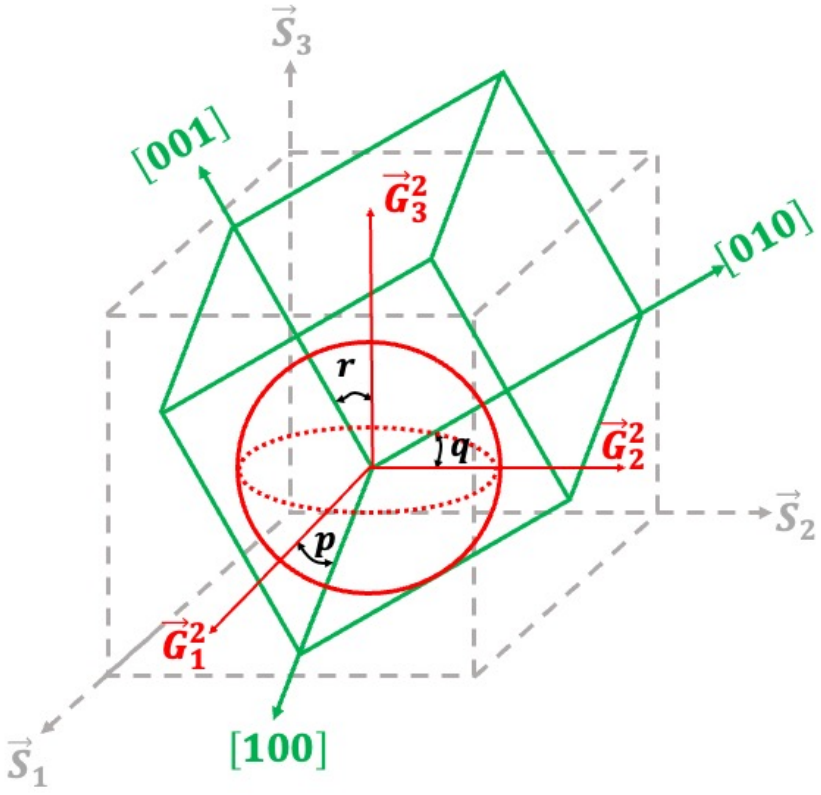

Figure 3.7: The relationship between grain, sample and, crystal coordinate systems.

At this point, **laboratory axes (diffractometer axes)** in which diffraction takes place should be introduced. These are defined with respect to sample axes. Here incident and transmitted beam vectors, $\vec{k}_0, \vec{k}_t$ are defined in the sample coordinate system, $\vec{S}_i$. The orientation of the sample with respect to $\vec{k}_0$ is adjusted to obtain diffraction from a particular reflection (hkl) of a particular (j^{th}) grain. In the diffraction condition, the angle between the crystal direction [hkl] and $\vec{k}_0$ is called the complementary Bragg angle, $\frac{\pi}{2} - \theta_B$. Then a diffracted beam, $\vec{k}_d$, forms. From the Laue conditions, $\vec{k}_0$, $\vec{k}_d$, $\vec{k}_t$ and $[hkl]$ has to be co-planar and the angle between $\vec{k}_d$ and $\vec{k}_t$ is $2\theta_B$ (Fig. 3.8-a). The orientation of $\vec{S}_i$ with respect to $[hkl]$ is defined by the Euler angles, ϕ, ψ (Fig. 3.8-b).

Since the crystallographic orientation of the (j[th]) grain in $\vec{S}_i$ is fixed by the crystal directions $\vec{G}_i^j = \left[\vec{a}_i^j, \vec{b}_i^j, c_i^j\right]$, ϕ, ψ can be computed from vector algebra, assume that $\phi = 0$:

$$\cos(90 - \psi_j) = \frac{ha_1^j + kb_1^j + lc_1^j}{\sqrt{h^2+k^2+l^2}\sqrt{a_1^{j\,2} + b_1^{j\,2} + c_1^{j\,2}}} \quad \text{Eq. (3-2-a)}$$

$$G_2 = [hkl]\ x\ G_1 \quad \text{Eq. (3-2-b)}$$

$$G_3 = G_2\ x\ G_1 \quad \text{Eq. (3-2-c)}$$

Consequently, for each (j[th]) grain in the diffraction condition for a particular (hkl) reflection, there is a specific set of orientation angles, ϕ_j, ψ_j.

For a polycrystalline sample, multiple grains, $M^D_{\phi,\psi}$, can be in the diffraction condition for a given set of Euler angles, ϕ_j, ψ_j. We define the laboratory axes $\vec{L}_i(\phi, \psi)$ i$\epsilon(1,3)$ as the global diffraction coordinate system for all $M^D_{\phi,\psi}$. For all of these grains, the normal of the family of diffracted (j[th]) grain, $\langle hkl \rangle_j$, is parallel to the $\vec{L}_3$. Therefore, these grains form a set with virtual fiber texture, with texture axis (hkl). However, for each such grain, the crystal directions along $\vec{G}_i^j = \left[\vec{a}_i^j, \vec{b}_i^j, c_i^j\right]$ are different.

In the present study, these calculations were carried out for (200), (222), and (420) reflections for eight ψ angles between 0 and 90 degrees. In general, four to eighteen grains at each ψ tilt were defined. Then, all of these grains were placed randomly through random number generator in the mesh. First of all, all chosen grains for the simulation were listed starting from 200-ψ-0 to 420-ψ-71.57 and then each grain was assigned to a random number between 1 and 400. Secondly, a second random number generator in the form of a 20 x 20 box was utilized to

determine the position of the grains in the mesh by assigning numbers between 1 to 400. Finally, the designated "jth" grain was placed into the "jth" position in the mesh.

To check the randomness of the mesh, stereographic projection of the grains that belong to (200) reflection was shown in Fig. 3.9. The r axis represents the ψ angle and the theta axis shows the grains having different orientations around 200 reflections. Grains at all ψ-ensembles are distributed homogeneously around the theta axis.

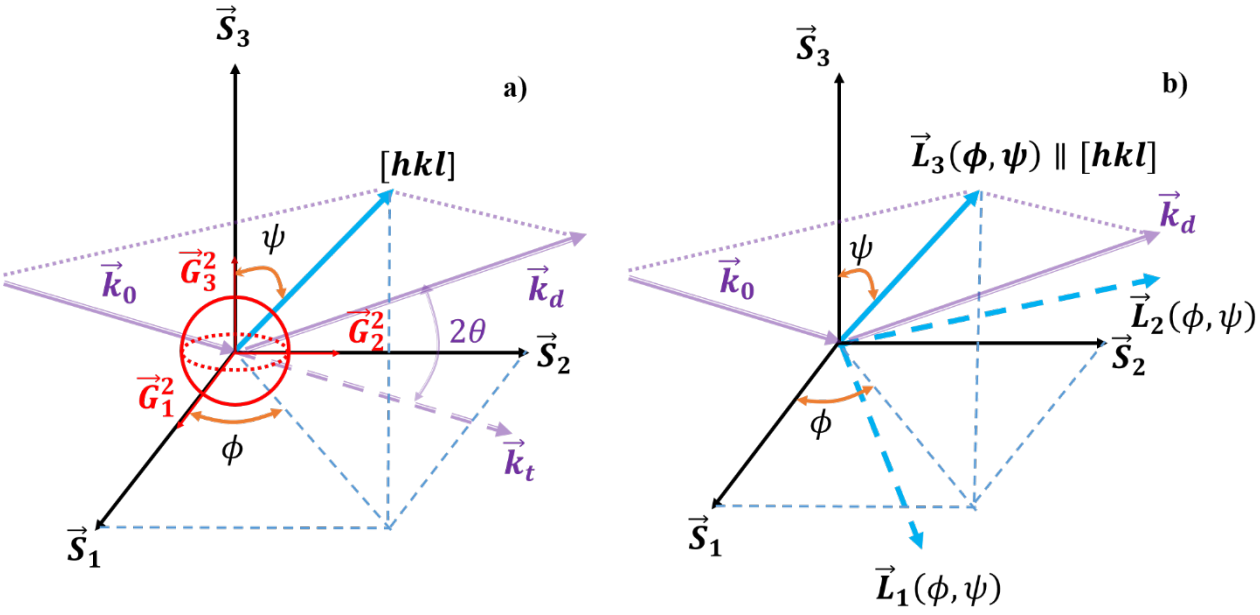

Figure 3.8: a) Schematic of diffraction geometry with a) the sample axes b) laboratory axes.

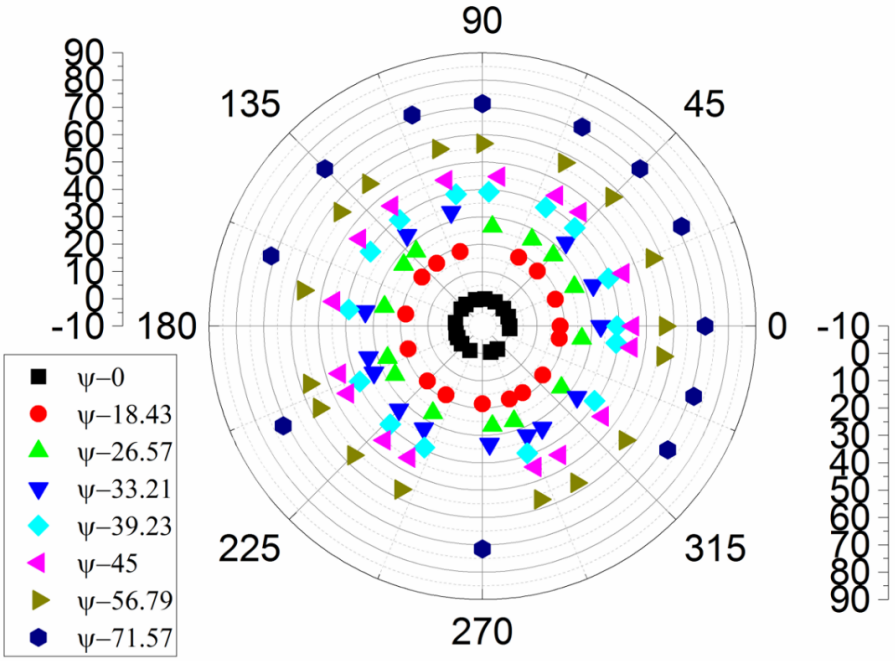

Figure 3.9: Stereographic projection of the 200 grains placed in the mesh of finite element modeling.

3.3.3- Material Constants Calculations

Precise calculation of stress values from the strains measured via diffraction requires the knowledge of Young's Modulus, E, and Poisson's ratio, ν, for specific orientations within the crystallographic plane defining the surface of the thin films. Therefore, in order to obtain stress values, elastic constants must be defined with respect to sample axes, $\vec{S}_i$. The modulus of elasticity for an arbitrary crystallographic direction hkl, is given by:

$$E_{hkl} = \frac{1}{S^S_{1111}} \qquad \text{Eq. (3-3)}$$

Where the compliance is defined in the sample coordinate system, $\vec{S_i}$ and can be calculated from the tensor transformation as shown:

$$S_{11}^s = S_{1111}^s = a_{im}a_{jn}a_{ko}a_{lp}S_{mnop}\ (i,j,k,l = 1; and\ m,n,o,p = 1,2,3) \quad \text{Eq. (3-4)}$$

After changing the tensor notation suffixes into the matrix notation ones [50] and getting rid of the zero components due to thermodynamics and symmetry, the equation becomes:

$$\frac{1}{E_{hkl}} = S_{11}^s = S_{11} - 2\left[(S_{11} - S_{12}) - \frac{S_{44}}{2}\right](a_{11}^2a_{12}^2 + a_{12}^2a_{13}^2 + a_{13}^2a_{11}^2) \quad \text{Eq. (3-5)}$$

Where one needs three independent variables in compliance matrices and direction cosines in order to define Young's Modulus of an individual crystal. Compliance matrix $(S_{11}^s, S_{22}^s, S_{33}^s, S_{12}^s, S_{13}^s, S_{23}^s)$ can be calculated by using the similar formula:

$$S_{12}^s = S_{12} - \left[(S_{11} - S_{12}) - \frac{S_{44}}{2}\right](a_{11}^2a_{21}^2 + a_{12}^2a_{22}^2 + a_{13}^2a_{23}^2) \quad \text{Eq. (3-6)}$$

$$S_{13}^s = S_{13} - \left[(S_{11} - S_{12}) - \frac{S_{44}}{2}\right](a_{11}^2a_{31}^2 + a_{12}^2a_{32}^2 + a_{13}^2a_{33}^2) \quad \text{Eq. (3-7)}$$

The Poisson's ratio (ν) for an anisotropic crystal varies with orientation as follows:

$$\nu_{12} = -\frac{S_{12}^s}{S_{11}^s} \quad \text{Eq. (3-8-a)}$$

$$\nu_{13} = -\frac{S_{13}^s}{S_{11}^s} \quad \text{Eq. (3-8-b)}$$

Where ν_{12} and ν_{13} are the Poisson's ratios along orthogonal axes perpendicular to the longitudinal stress direction.

Since the crystallographic orientation of the (j[th]) grain in $\vec{S}_i$, $\vec{G}_i^j = \left[\vec{a}_i^j, \vec{b}_i^j, c_i^j\right]$ is known the effective elastic constants of individual crystals can be calculated by converting the (Eq. 3-5):

$$\frac{1}{E_{\vec{S}_1}} = S'_{11} = S_{11} - 2\left[(S_{11} - S_{12}) - \frac{S_{44}}{2}\right]\frac{(a_1^2 b_1^2 + b_1^2 c_1^2 + c_1^2 a_1^2)}{(a_1^2 + b_1^2 + c_1^2)^2} \quad \text{Eq. (3-9)}$$

Here S_{11}, S_{12}, S_{44} are the three independent elastic compliances of the crystal if we assume the crystal is cubic [50] and S'_{11} is defined in the specimen coordinate system for a particular grain. The rest of the elastic constants of the grain in the sample axes can be evaluated in the same way. With $\vec{G}_i^j = \left[\vec{a}_i^j, \vec{b}_i^j, c_i^j\right]$, the Schmid factor of each crystal can be calculated as well.

Two different ways exist to define orientation and materials constants for each crystal in ABAQUS CAE. The first way is by altering the $\vec{G}_i^j = \left[\vec{a}_i^j, \vec{b}_i^j, c_i^j\right]$ to Euler angles (any convention). This enables the user to define same materials constants (S_{11}, S_{12}, S_{44}) for each crystal. A subroutine can be employed to introduce Euler angles. The second approach is much easier: since we have the elastic constants of each grain in the sample axes, these can be introduced to the simulation directly as anisotropic crystal properties in the sample (model) coordinates. We used this (second) the second approach in our ABAQUS CAE calculations.

3.4- Elastoplastic Loading of Single and Multiphase Polycrystalline Materials

For this model, we used the Finite Element Polycrystals (FEpX) modeling framework of Dawson and Boyce for simulating the mechanical loading of single/multiphase polycrystalline materials due to its ease of use and proven applicability [111]. With this framework, the

mechanical behavior of polycrystalline solids can be simulated. Complete descriptions of FEpX can be found in references [115, 116, 111].

In these models, virtual polycrystalline samples containing approximately 600,000, 10-node tetrahedral elements for single-phase materials and 1000,000, 10-node tetrahedral elements for multiphase materials were constructed using Romain Quey's Neper code [117] which builds a Voronoi construction of the domain to define grains and then discretizes the grains into the finite elements. The single-phase Cu and W models had 1500 grains. The two-phase Cu – W system had 2500 grains, equally distributed between Cu and W. The initial model dimensions (Fig. 3.10) were 1 mm x 1 mm x 3 mm[9].

We determined the average grain size and nearest number of grains in the model by taking XY and YZ cross-sections and performing a basic stereological analysis. The grain size for the two-phase model was approximately .08±.01 mm, with each grain having 8±1 nearest neighbors. In addition, the grain size for the single-phase model was around .12±.02 mm, with each grain having 7±1 nearest neighbors. More details about these calculations will be presented in the results section.

[9] While we use metric units as a convenience, these values are really defined as FEpX model units.

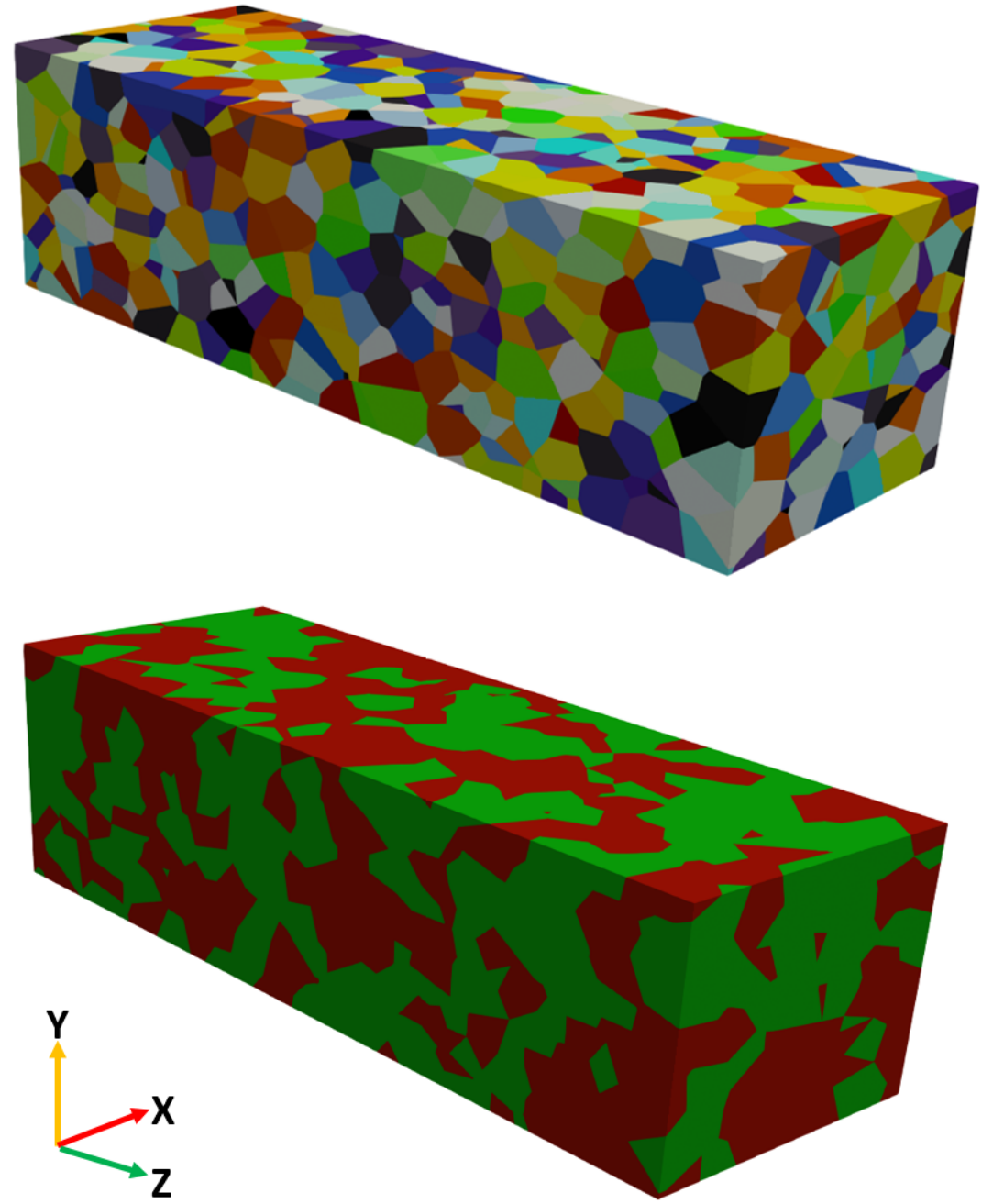

Figure 3.10: Phase and grain distributions for the copper-tungsten virtual composite. For the phase distribution, red indicates copper; blue indicates tungsten.

The evolution of the slip system strengths was modeled with a modified Voce type hardening law:

$$\dot{g}^{\alpha} = h_0 \left(\frac{g_s(\dot{\gamma}) - g^{\alpha}}{g_s(\dot{\gamma}) - g_0}\right)^{n'} \dot{\gamma} \qquad \text{Eq. (3-10-a)}$$

$$g_s(\dot{\gamma}) = g_1 \left(\frac{\dot{\gamma}}{\dot{\gamma}_s}\right)^{m'} and\ \dot{\gamma} = \sum_{\alpha} |\dot{\gamma}^{\alpha}| \qquad \text{Eq. (3-10-b)}$$

Where $g_0, g_1, \dot{\gamma}, \dot{\gamma}_s, h_0, m'$ and n' are initial slip system strength, reference value of saturation strength, fixed-state strain rate scaling coefficient, saturation strength strain rate scaling coefficient, strength hardening rate coefficient, saturation strength rate scaling exponent, and power on modified Voce hardening term. The single crystal compliance constants (S_{11}, S_{12}, S_{44}) are converted into the stiffness constants (C_{11}, C_{12}, C_{44}).

The grain orientations calculated for individual crystals can be implemented FEpX in the form of Euler angles. Thus, Euler angles are obtained from grain orientations with three steps for each grain:

a) The rotation matrix is calculated for each crystal from the dot product of sample basis axes $(\vec{C}_i^k)$ and grain orientations $(\vec{G}_i^k)$ in the normalized form as shown:

$$\vec{R}_{ij} = \vec{C}_i^k . \vec{G}_i^k = \begin{bmatrix} 1 & 0 & 0 \\ 0 & 1 & 0 \\ 0 & 0 & 1 \end{bmatrix} \begin{bmatrix} \frac{a_1}{\sqrt{a_1^2+b_1^2+c_1^2}} & \frac{b_1}{\sqrt{a_1^2+b_1^2+c_1^2}} & \frac{c_1}{\sqrt{a_1^2+b_1^2+c_1^2}} \\ \frac{a_2}{\sqrt{a_2^2+b_2^2+c_2^2}} & \frac{b_2}{\sqrt{a_2^2+b_2^2+c_2^2}} & \frac{c_2}{\sqrt{a_2^2+b_2^2+c_2^2}} \\ \frac{a_3}{\sqrt{a_3^2+b_3^2+c_3^2}} & \frac{b_3}{\sqrt{a_3^2+b_3^2+c_3^2}} & \frac{c_3}{\sqrt{a_3^2+b_3^2+c_3^2}} \end{bmatrix} \qquad \text{Eq. (3-11)}$$

b) The generalized rotation matrix can be written in the form of three Euler angles representing the rotation around three axes (ϕ, θ, ψ):

$$\vec{R}_{ij} = \begin{bmatrix} R_{11} & R_{12} & R_{13} \\ R_{21} & R_{22} & R_{23} \\ R_{31} & R_{32} & R_{33} \end{bmatrix} \quad \text{Eq. (3-12-a)}$$

$$\vec{R}_{ij} = \begin{bmatrix} \cos\theta\cos\phi & \sin\theta\sin\psi\cos\phi - \cos\psi\sin\phi & \sin\theta\cos\psi\cos\phi + \sin\psi\sin\phi \\ \cos\theta\sin\phi & \sin\theta\sin\psi\sin\phi + \cos\psi\cos\phi & \sin\theta\cos\psi\sin\phi - \sin\psi\cos\phi \\ -\sin\theta & \cos\theta\sin\psi & \cos\theta\cos\psi \end{bmatrix} \quad \text{Eq.(3-12-b)}$$

c) The Euler angles can be evaluated by solving the rotation matrix with a software package; in this research, MATLAB was used. We note that in FEpX, Kocks' convention of Euler angles (rather than the more common Bunge convention) must be used [118].

The loading mode was designed to replicate a tensile test in which the grips of the tensile tester hold the sample. Consequently, the stress fields in the material close to both grips should contain St. Venant stresses, while the free-body diagram of the mid-section of the material should have uniform tensile stresses distributed at its lateral boundaries. The simulation was performed in displacement control where the sample was loaded at a constant macroscopic strain rate $(\dot{\varepsilon})$. The strain rate can be calculated from the velocity which is the input in FEpX as follows:

$$\dot{\varepsilon} = \frac{d\varepsilon}{dt} = \frac{1}{L_0}\frac{dL(t)}{dt} = \frac{v(t)}{L_0} \quad \text{Eq. (3-13)}$$

3.5- Summary

In this chapter we described the finite element programs we used to study the distribution of stress/strain in (1) homogeneous solids with St. Venant stress fields, (2) Polycrystalline

materials under elastic load with only elastic interaction stresses, and (3) single-phase and two-phase polycrystalline materials which were loaded into the plastic regime and then relaxed. These last sets of models were used to study the formation of both elastic interaction strains as well as residual stresses due to the distribution of heterogeneous flow. In the following chapters, these results will be described, [119].

4- ST. VENANT AND FAR-FIELD STRESS FIELDS IN AN IDEAL SYSTEM

Based on our discussions presented in chapters 2 and 3 we decided to test if it is possible to identify residual stress fields in a model sample using our expanded definitions and see if we could define useful representative volume elements for virtual measurements in such a sample. While there have been efforts to compute the sizes of V_{RVE}, employing both analytical and numerical approaches [120, 121], extension of these approaches to measurement volumes, V_M , for diffraction experiments are not available. Further, due to the complexity of most models, a simpler approach might enjoy better usage for the specification of V_M for diffraction experiments. In what follows, we investigate the applicability of St. Venant's principle in specifying V_M for the stress fields arising in a quasi-homogeneous sample using analytical and numerical approaches. Our ideal model consists of a spherical inclusion embedded in a spherical shell of a different material (Fig. 4.1 & Fig. 3.4) where the inclusion and the shell have different coefficients of thermal expansion. For this system, both analytical and numerical solutions can be used to evaluate stress fields.

4.1- Material Definition

We considered Fe (Steel), Al alloy, Cu, and W (Table 4.1) as the materials for inclusion/shell models. For simplicity, we assumed that (1) both the inclusion and the shell are isotropic, with elastic moduli and coefficients of thermal expansion, E_i, ν_i, α_i, with i=m for the shell, and i=p for the inclusion, respectively, and (2) separate diffraction peaks can be measured

from both components. To maximize the tangential stress at the interface and to increase the hydrostatic stress exerted on the inclusion by the shell, the difference between the coefficient of thermal expansion and Young's Modulus between the inclusion and the shell must be large. Consequently, we chose Al – Fe, Cu –W, and Al – W as the ideal pairs for our study, with the second (higher CTE) material as the shell. Thus, the inclusion expands more than the shell during heating.

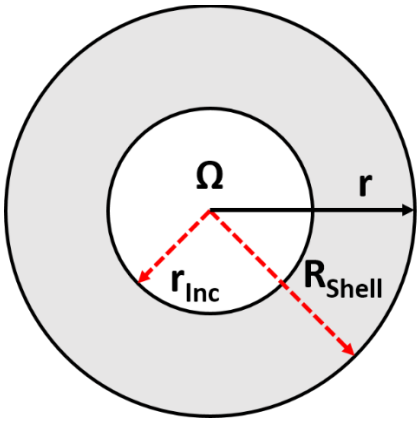

Figure 4.1: Spherical Eshelby inclusion in a finite spherical shell.

Table 4.1: Mechanical and thermal properties of the components along the loading axis. The mechanical parameters of steel, aluminum alloy, copper and tungsten were obtained from the Metals Handbook, *[112, 113]***.**

	Young's Modulus E / GPa	Poisson's Ratio ν	Shear Modulus G / GPa	Yield Strength σ_y / MPa	Room-temperature CTE / 10^{-6}/°C
1018 Carbon Steel (Fe)	200	0.29	78	~ 370 (tensile)	12.5
Aluminum Alloy 6061 (Al)	69	0.33	26	~ 270 (tensile)	23.6
Copper (Cu)	115	0.31	44	~ 235 (tensile)	17.3
Tungsten (W)	400	0.28	156	~ 750 (tensile)	4.4

4.2- General Analytical Solution of Spherical Eshelby Inclusion in a Finite Spherical Shell

In this part, the equations of average and position-dependent stress fields for a spherical Eshelby inclusion are presented[10]. To calculate stress fields within metal shell we make the following assumptions:

a) The shape of the inclusion is unchanged during heating. Consequently, the strain and stress in the enclosed inclusion will be uniform per the Eshelby formulation.

b) There is no yielding in either component.

All internal stresses existing in a free body at equilibrium, with no body forces or surface tractions applied at the surfaces, must obey the following differential equations:

$$\sigma_{ij,j} = 0 \qquad \text{Eq. (4-1-a)}$$

$$\sigma_{ij} \,.\, n_j = 0 \qquad \text{Eq. (4-1-b)}$$

From Eq. (4-1-a & b), it can be shown that the average of any stress over the whole body (V) is zero [2]:

$$\int_V \ \sigma_{ij} dV = 0 \qquad \text{Eq. (4-2)}$$

It should be pointed out that Eq. (4-2) is valid if and only if Eqs. (4-1-a & b) are satisfied. It can be shown by applying integration by parts to Eq. (4-2) and with x the distance coordinate in the j direction.

[10] These equations will also apply to composite materials where all neighboring inclusions are non-interacting with non-overlapping stress fields.

$$\int_V \sigma_{ij} dV = \int_S \sigma_{ik} n_k x_j dS - \int_V \sigma_{ik,k} x_j dV \qquad \text{Eq. (4-3)}$$

Where S is the surface of the body. The first integral on the right side is over the S at which $\sigma_{ik} \cdot n_k = 0$, Eq. (4-1-b), and the second integral is zero over the V where $\sigma_{ik,k} = 0$, Eq. (4-1-a).

For a two-phase material, in our case a spherical Eshelby inclusion with a finite spherical matrix (Fig. 4-1), Eq. (4-2) can be written as:

$$\int_V \sigma_{ij} dV = \int_{V-\Omega} \sigma_{ij} dV + \int_\Omega \sigma_{ij} dV = 0 \qquad \text{Eq. (4-4)}$$

Where Ω is the volume of the inclusion. Eq. (4-4) can be written by obtaining the fractions:

$$(V - \Omega)\langle\sigma_{ij}\rangle_{Shell} + (\Omega)\langle\sigma_{ij}\rangle_{Inc} = 0 \qquad \text{Eq. (4-5)}$$

If both sides are divided by V:

$$(1 - f)\langle\sigma_{ij}\rangle_{Shell} + f\langle\sigma_{ij}\rangle_{Inc} = 0 \qquad \text{Eq. (4-6)}$$

Here f is the volume fraction of the inclusion and $\langle\sigma_{ij}\rangle_{Inc}$, $\langle\sigma_{ij}\rangle_{Shell}$ are the average stresses in the inclusion and matrix, respectively. Eqs. (4-3 & 6) and the above statements are valid for all arbitrary systems which have multiple phases.

In our analysis, the whole composite system is heated so that the difference between the coefficient of thermal expansions of both constituents will cause misfit stresses between inclusion and the shell. As mentioned before, since the shape of the inclusion remains spherical the inclusion will be placed under hydrostatic pressure (p) by the shell. For the solution of the average stress field, all equations are solved for "p" starting from the displacements. Here using spherical coordinates makes the derivation simpler (Fig. 4.2).

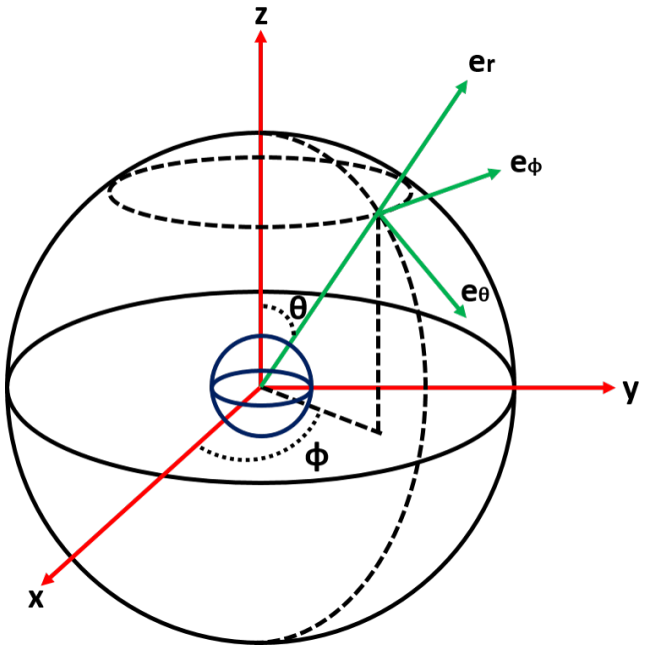

Figure 4.2: Representation of spherical coordinates in the composite system.

$$u_{r_{Inc}}(r,\theta,\phi) = u_{r_{Inc}}(r) = C_1 r + \frac{C_4}{r^2} \qquad \text{Eq. (4-7-a)}$$

$$u_{R_{Shell}}(r,\theta,\phi) = u_{R_{Shell}}(r) = C_2 r + \frac{C_3}{r^2} \qquad \text{Eq. (4-7-b)}$$

Here $u_{r_{Inc}}(r,\theta,\phi)$ and $u_{R_{Shell}}(r,\theta,\phi)$ are the radial displacement fields in the spherical inclusion and matrix, respectively. From Eq. (4-7-a), C_4 becomes zero because at r = 0 the displacement should also be zero. In addition, boundary conditions at the interface dictate that the displacement and force should be continuous. Therefore, displacements should be equal to each other at the boundary:

$$C_1 = C_2 + \frac{C_3}{r_{Inc}^3} \qquad \text{Eq. (4-8)}$$

The constitutive equations for three-dimensional problems in spherical coordinates for thermal loading can be expressed as:

$$\varepsilon_{rr}^{Inc} - \Delta\alpha\Delta T = \frac{1}{E_{Inc}}\left[\sigma_{rr}^{Inc} - 2v_{Inc}\sigma_{\theta\theta}^{Inc}\right] \quad \text{Eq. (4-9-a)}$$

$$\varepsilon_{\theta\theta}^{Inc} - \Delta\alpha\Delta T = \frac{1}{E_{Inc}}\left[\sigma_{\theta\theta}^{Inc} - v_{Inc}\left(\sigma_{rr}^{Inc} + \sigma_{\theta\theta}^{Inc}\right)\right] \quad \text{Eq. (4-9-b)}$$

$$\varepsilon_{rr}^{Shell} = \frac{1}{E_{Shell}}\left[\sigma_{rr}^{Shell} - 2v_{Shell}\sigma_{\theta\theta}^{Shell}\right] \quad \text{Eq. (4-9-c)}$$

$$\varepsilon_{\theta\theta}^{Shell} = \frac{1}{E_{Shell}}\left[\sigma_{\theta\theta}^{Shell} - v_{Shell}\left(\sigma_{rr}^{Shell} + \sigma_{\theta\theta}^{Shell}\right)\right] \quad \text{Eq. (4-9-d)}$$

where ε_{rr}^{Inc}, $\varepsilon_{\theta\theta}^{Inc}$, ε_{rr}^{Shell} and $\varepsilon_{\theta\theta}^{Shell}$ are radial and tangential strains in the inclusion and shell, and σ_{rr}^{Inc}, $\sigma_{\theta\theta}^{Inc}$, σ_{rr}^{Shell} and $\sigma_{\theta\theta}^{Shell}$ are radial and tangential stresses in the inclusion and shell. The elastic constants are denoted by E_{Inc}, E_{Shell}, v_{Inc} and v_{Shell}. "$\Delta\alpha$" represents the difference in thermal expansion between inclusion and shell and ΔT is the temperature deviation from equilibrium. To simplify the analysis, we assumed that only inclusion is heated, in this case, there will be no αΔT term in shell strain. Then strain components can be evaluated from displacements as follows:

$$\varepsilon_{rr} = \frac{du}{dr} \quad \text{Eq. (4-10-a)}$$

$$\varepsilon_{\theta\theta} = \frac{u}{r} \quad \text{Eq. (4-10-b)}$$

From Eqs. (4-10-a & b), Eqs. (4-9-a, b, c & d), Eq. (4-8) and Eqs. (4-7-a & b), the expressions for radial and tangential stresses were derived as:

$$\sigma_{rr}^{Inc} = \sigma_{\theta\theta}^{Inc} = \frac{E_{Inc}\left(C_2 + \frac{C_3}{r_{Inc}^3} - \Delta\alpha\Delta T\right)}{1-2v_{Inc}} \quad \text{Eq. (4-11-a)}$$

$$\sigma_{rr}^{Shell} = \frac{E_{Shell}C_2}{1-2v_{Shell}} - \frac{2E_{Shell}}{1+v_{Shell}}\frac{C_3}{r^3} \quad \text{Eq. (4-11-b)}$$

$$\sigma_{\theta\theta}^{Shell} = \frac{E_{Shell}C_2}{1-2v_{Shell}} + \frac{E_{Shell}}{1+v_{Shell}}\frac{C_3}{r^3} \quad \text{Eq. (4-11-c)}$$

To solve for C_1, C_2, and C_3, two different boundary conditions must be prescribed: The radial stress at the interface should be equal to each other and the radial stress at the outer surface should be zero. After boundary conditions applied, C_1, C_2 and C_3 are found as:

$$C_1 = \frac{E_{Inc}\Delta\alpha\Delta T\left[(1+v_{Shell})R_{Shell}^3+2(1-2v_{Shell})r_{Inc}^3\right]}{\left[2E_{Shell}(1-2v_{Inc})+E_{Inc}(1+v_{Shell})\right]R_{Shell}^3+\left[2E_{Inc}(1-2v_{Shell})-2E_{Shell}(1-2v_{Inc})\right]r_{Inc}^3} \quad \text{Eq. (4-12-a)}$$

$$C_2 = \frac{2E_{Inc}\Delta\alpha\Delta T(1-2v_{Shell})r_{Inc}^3}{\left[2E_{Shell}(1-2v_{Inc})+E_{Inc}(1+v_{Shell})\right]R_{Shell}^3+\left[2E_{Inc}(1-2v_{Shell})-2E_{Shell}(1-2v_{Inc})\right]r_{Inc}^3} \quad \text{Eq. (4-12-b)}$$

$$C_3 = \frac{E_{Inc}\Delta\alpha\Delta T(1+v_{Shell})R_{Shell}^3 r_{Inc}^3}{\left[2E_{Shell}(1-2v_{Inc})+E_{Inc}(1+v_{Shell})\right]R_{Shell}^3+\left[2E_{Inc}(1-2v_{Shell})-2E_{Shell}(1-2v_{Inc})\right]r_{Inc}^3} \quad \text{Eq. (4-12-c)}$$

The position-dependent stress field of spherical Eshelby inclusion in finite spherical shell can be written by plugging C_1, C_2, and C_3 into Eqs. (4-11-a, b & c):

$$\sigma_{rr}^{Inc} = \sigma_{\theta\theta}^{Inc} = p = \frac{2E_{Inc}E_{Shell}\Delta\alpha\Delta T\left(r_{Inc}^3-R_{Shell}^3\right)}{\left[2E_{Shell}(1-2v_{Inc})\left(R_{Shell}^3-r_{Inc}^3\right)+E_{Inc}(1+v_{Shell})R_{Shell}^3+2E_{Inc}(1-2v_{Shell})r_{Inc}^3\right]} \quad \text{Eq. (4-13-a)}$$

$$\sigma_{rr}^{Shell} = p * \frac{\left(r_{Inc}^3 r^3-R_{Shell}^3 r_{Inc}^3\right)}{r^3\left(r_{Inc}^3-R_{Shell}^3\right)} \quad \text{Eq. (4-13-b)}$$

$$\sigma_{\theta\theta}^{Shell} = p * \frac{\left(2r_{Inc}^3 r^3+R_{Shell}^3 r_{Inc}^3\right)}{2r^3\left(r_{Inc}^3-R_{Shell}^3\right)} \quad \text{Eq. (4-13-c)}$$

Since the equations for stress fields are known, strain fields can be calculated by using Eqs. (4-9-a, b, c & d). Using both stress and strain fields, strain energy density which is very important for decay rate calculation in St. Venant's principle, can be evaluated:

$$u_{Shell} = \frac{1}{2}(\sigma_{rr}\varepsilon_{rr} + 2\sigma_{\theta\theta}\varepsilon_{\theta\theta}) \quad \text{Eq. (4-14-a)}$$

$$u_{Shell} = \frac{3p^2 r_{Inc}^6}{2E_{Shell}(R_{Shell}^3 - r_{Inc}^3)^2}[(1 - 2v_{Shell} + \frac{R_{Shell}^6}{2r^6}(1 + v_{Shell})] \quad \text{Eq. (4-14-b)}$$

4.2.1- Force Balance at Overall Volume

Since the force balance at overall volume must be maintained over the composite system. We would like to check this. Eq. (4-2) can be written explicitly:

$$\int_V \sigma_{ij} dV = 3\int_{V_{Inc}} \sigma_{rr}^{Inc} * dV_{Inc} + \int_{V_{Shell}} \sigma_{rr}^{Shell} * dV_{Shell} + 2\int_{V_{Shell}} \sigma_{\theta\theta}^{Shell} * dV_{Shell} = 0 \quad \text{Eq. (4-15)}$$

Since the inclusion is under hydrostatic stress "*p*", the first term of the Eq. (4-15) is:

$$\int_{V_{Inc}} p * dV_{Inc} = \int_0^{2\pi} d\theta \int_0^{\pi} sin\phi d\phi \int_0^{r_{inc}} pr^2 dr = \frac{4}{3}\pi p {r_{inc}}^3 \quad \text{Eq. (4-16)}$$

The second and third terms of the Eq. (4-15) is evaluated by using Eq. (4-13-b & c)

$$\int_{V_{Shell}} \sigma_{rr}^{Shell} * dV_{Shell} = -\frac{4}{3}\pi p {r_{inc}}^3 + 4\pi p \frac{{r_{inc}}^3 {R_{Shell}}^3}{({R_{Shell}}^3 - {r_{inc}}^3)} \ln\left(\frac{R_{Shell}}{r_{inc}}\right) \quad \text{Eq. (4-17-a)}$$

$$\int_{V_{Shell}} \sigma_{\theta\theta}^{Shell} * dV_{Shell} = -\frac{4}{3}\pi p {r_{inc}}^3 - 2\pi p \frac{{r_{inc}}^3 {R_{Shell}}^3}{({R_{Shell}}^3 - {r_{inc}}^3)} \ln\left(\frac{R_{Shell}}{r_{inc}}\right) \quad \text{Eq. (4-17-b)}$$

The addition of Eq. (4-16), Eqs. (4-17-a & b) is equal to Eq. (4-15) and gives us zero, indicating that the forces- and, hence, the residual stresses- are balanced over the entire volume of the shell-inclusion system; the hydrostatic compressive stress in the inclusion is balanced by a multi-axial stress state in the shell.

Since the explicit form of "p" is known, the average stress of the shell can be calculated as follows:

$$\langle\sigma_{ij}\rangle_{Shell} = \frac{\int_{V_{Shell}} \sigma_{rr}^{Shell} * dV_{Shell} + 2\int_{V_{Shell}} \sigma_{\theta\theta}^{Shell} * dV_{Shell}}{3\int_{V_{Shell}} \sigma_{rr}^{Shell} * dV_{Shell}} \quad \text{Eq. (4-18-a)}$$

$$\langle\sigma_{ij}\rangle_{Shell} = \frac{2E_{Inc}E_{Shell}\Delta\alpha\Delta T r_{Inc}^3}{[2E_{Shell}(1-2\nu_{Inc})(R_{Shell}^3 - r_{Inc}^3) + E_{Inc}(1+\nu_{Shell})R_{Shell}^3 + 2E_{Inc}(1-2\nu_{Shell})r_{Inc}^3]} \quad \text{Eq. (4-18-b)}$$

4.2.2- Effect of Geometry and Material on the Critical Length (r^*)

An important parameter arising from St. Venant's principle is the critical length, r^*, beyond which the effects of an applied point force or geometric constraint are negligible [24]. Since the definition of "negligible" is somewhat subjective, the r^* values reported in the literature do not always agree with each other. Rather than using absolute (numerical) values, we defined a new variable, the stress threshold, Γ, to identify r^* in our shell-inclusion system. In this approach, we express r* in terms of radial and tangential stress values at the internal boundary between the inclusion and the shell. As specified by one of the boundary conditions at the interface, the radial stress component in the shell at the interface must be equal to "p". The maximum tangential stress will also occur in the shell section at the interface, and can be expressed as [122]:

$$\sigma_{\theta\theta}^{Shell} = p * \frac{f}{f-1} * \left(1 + \frac{R_{Shell}^3}{2r^3}\right) \quad \text{Eq. (4-19)}$$

We now define the threshold ratio, Γ, as the ratio of tangential stress at critical length, r^*, to maximum tangential stress.

$$\Gamma = \frac{\sigma_{\theta\theta}^{Shell}(r^*)}{\sigma_{\theta\theta}^{Shell}(Max)}$$ Eq. (4-20)

This expression can be expressed in terms of the hydrostatic stress, p, and configurational parameters:

$$\Gamma = \frac{p*\frac{f}{f-1}*\left(1+\frac{R_{Shell}^3}{2r^{*3}}\right)}{p*\frac{f}{f-1}*\left(1+\frac{R_{Shell}^3}{2r_{Inc}^3}\right)} = \frac{\left(1+\frac{R_{Shell}^3}{2r^{*3}}\right)}{\left(1+\frac{R_{Shell}^3}{2r_{Inc}^3}\right)}$$ Eq. (4-21-a)

Since the fraction of the inclusion, f, is equal to $\frac{r_{Inc}^3}{R_{Shell}^3}$, Eq. (4-21-a) can be simplified:

$$\Gamma = \frac{2f\left(1+\frac{R_{Shell}^3}{2r^{*3}}\right)}{2f+1}$$ Eq. (4-21-b)

For a given shell/inclusion system, whether the stresses in the shell, caused by the thermal expansion of the inclusion, decay below a given threshold value at its outer surface depend on the thickness of the shell and the radius of the inclusion[11]. The relationship between Γ, r^*, and f is given by:

$$\frac{r_{Inc}^3}{r^{*3}} = 2f(\Gamma - 1) + \Gamma$$ Eq. (4-22)

Since the ratio of the radii cannot be negative:

$$f > \frac{\Gamma}{2(1-\Gamma)}$$ Eq. (4-23)

[11] These values also define the volume fraction, *f,* of the inclusion.

Consequently, whether a given threshold value can be achieved or not in a particular system depends only on the volume fraction of the inclusion.

4.3- FEM Analysis vs. Analytical Computations

We used the ABAQUS program to check the analytical solutions. To see the effect of material properties and geometry, we investigated shell/inclusion systems with different diameters. For the Al – Fe system 15 different models, with a constant inclusion radius but varying shell radii ($R_{Mat} = 7.5, 25, 27.5, 30, 32.5, 35, 40, 45, 50, 55, 60, 65, 70, 75, 80\ mm$) were analyzed. For all cases the temperature increase was 100°C. In Fig. 4.3, the hydrostatic stress in the spherical Al inclusion as a function of (Fe) shell radius is plotted. We observe that: (1) The stress values calculated using our equations match those obtained by FEM, and (2) In the ranges studied, and in the absence of yielding, the thickness of the (Fe) shell matrix has little effect on the hydrostatic stress in the inclusion. We also observe acceptable agreement between radial and tangential stresses in the shells for all three systems (Al – Fe, Cu – W, and Al – W) as shown in Figs. 4.4 & 5. In these models, the shell radius was set to 50 mm, 10x of the inclusion radius, for all metallurgies. For these dimensions both the radial stress and the tangential stress components in the shell tend tangentially to zero at the shell surface; the limit of the tangential stress at infinity will be zero. $\lim_{r\to\infty} \sigma_{\theta\theta}^{Shell} = \lim_{r\to\infty} p * \frac{(2r_{Inc}^3 r^3 + R_{Shell}^3 r_{Inc}^3)}{2r^3(r_{Inc}^3 - R_{Shell}^3)} = 0$ Eq. (4-24)

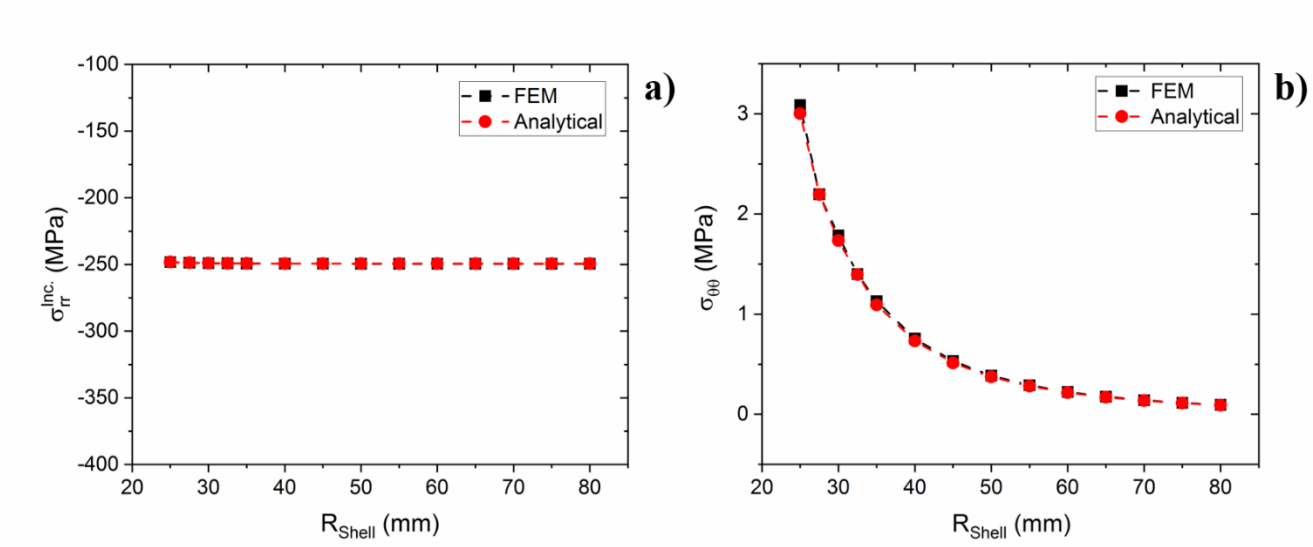

Figure 4.3: a) Hydrostatic stress state of the 5 mm inclusion with different shell radius and b) the surface tangential stress at the different shell radius in Al – Fe system ($\Delta\alpha_{Al-Fe}$ = 11.1E-06).

The radial stress of the shell at the interface is equal to the hydrostatic pressure, *p*, in the inclusion. The highest value of the tangential stress is also observed at the interface of the composite system. In order to evaluate the critical length (r*), we chose a threshold ratio (Γ) of 3%. In Fig. 4.6, r* values evaluated from Eq. (4-19), for 15 different diameter ratios for the Al – Fe system, and the r* values obtained from the FEM models are plotted. Again, we observe the reasonable agreement.

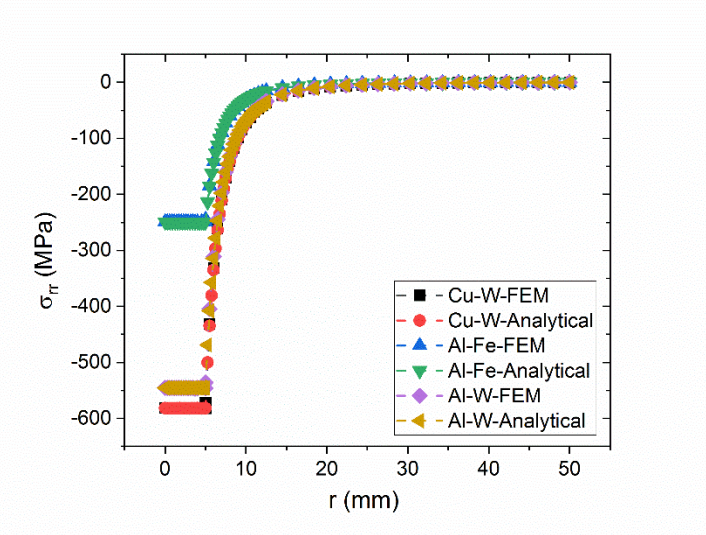

Figure 4.4: Radial stress distribution of three different systems in 5 mm inclusion with 50 mm matrix (For all three systems, the differences between FEM and closed-form solutions are less than 0.1%, $\Delta\alpha_{Cu-W}$=12.9E-06, $\Delta\alpha_{Al-Fe}$=11.1E-06 and $\Delta\alpha_{Al-W}$=19.2E-06).

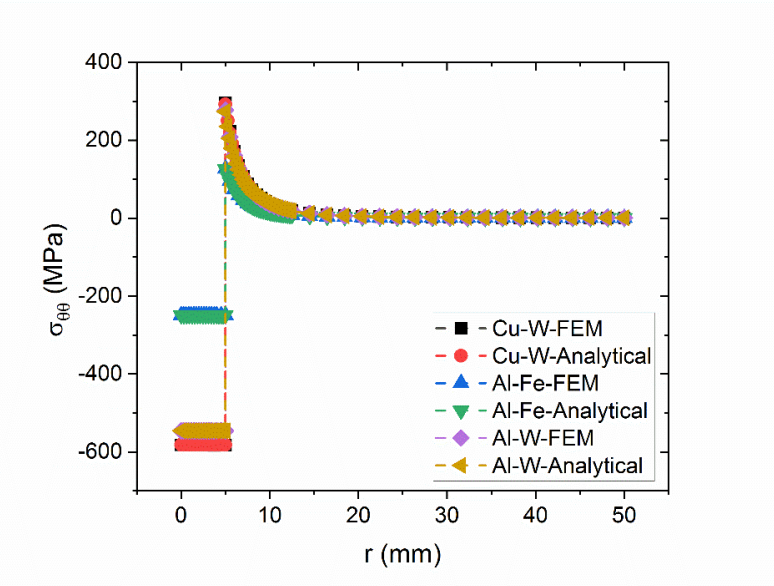

Figure 4.5: Tangential stress distribution of three different systems in 5 mm inclusion with 50 mm shell (For all three systems, FEM and quantification of the difference between them is less than 0.1%).

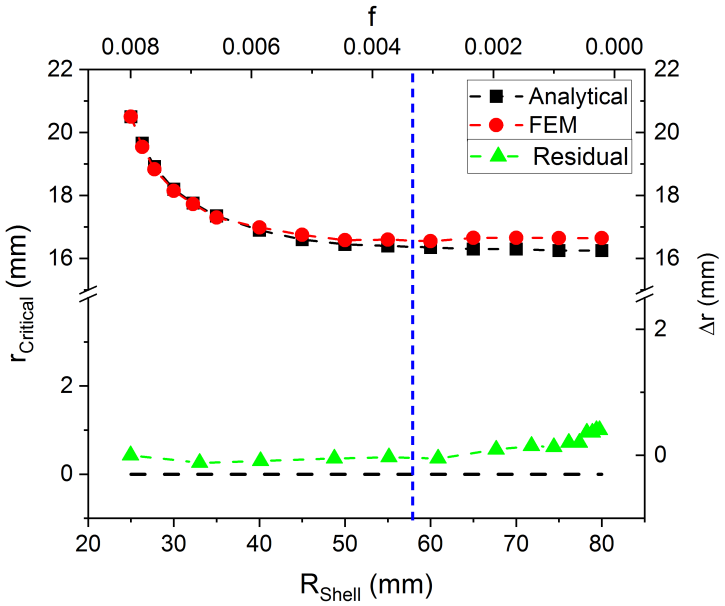

Figure 4.6: Critical lengths, r^*, for 15 different Fe shells encapsulating a 5 mm Al inclusion ($\Delta\alpha_{Al-Fe}$=11.1E-06). The top abscissa and right ordinate show the volume fraction, f, corresponding to a given shell radius, and $\Delta r = r^*_{FEM} - r^*_{Analytical}$, respectively.

The small differences between the r^* values computed from FEM and analytical equations for larger shell radii are due to errors caused by the coarse discretization of the outer regions in FEM for large shells: For large R_M stress magnitudes close to the outer surface of the shell are very small and fluctuate slightly due to the larger mesh elements used.

For a fixed inclusion radius, r_{Inc}, as the radius of the shell, R_M, decreases the volume fraction, f, of the inclusion increases. Consequently, the shell material over which the St. Venant stress fields can decay decreases. This results in steeper radial stress gradients (Fig. 4-7-a) within the shell volume and non-negligible tangential stresses at the shell surface (Fig. 4-7-b).

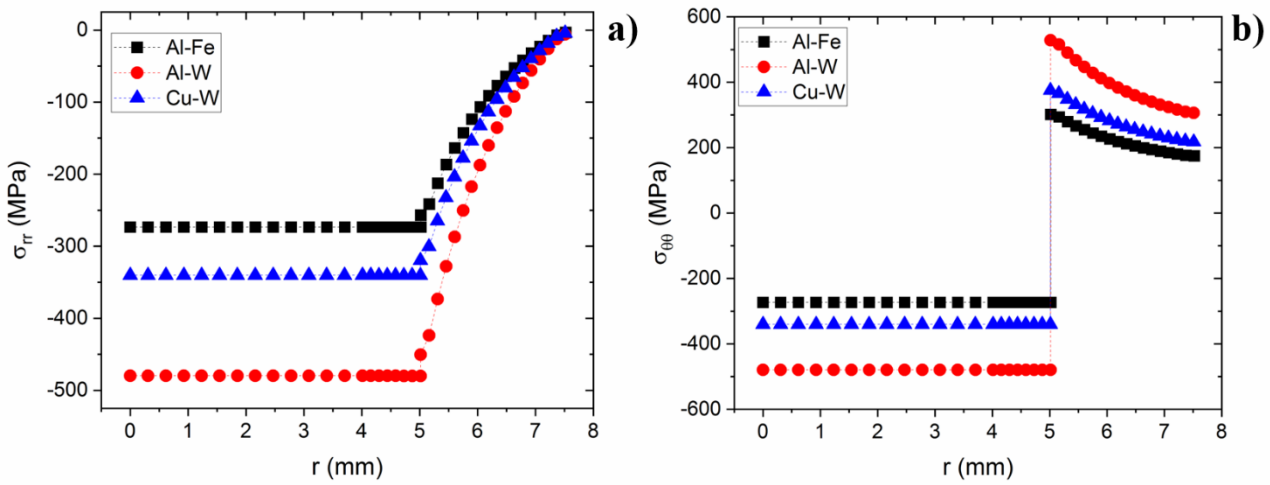

Figure 4.7: Variation of radial (a) and tangential (b) stresses with the position in three inclusion-shell systems with $\frac{r_{Inc}}{R_{Mat}} = 0.67$. In this case, f=0.3 while the maximum inclusion volume fraction required to achieve Γ=0.03, computed from Eq. (4-23) is 0.016.

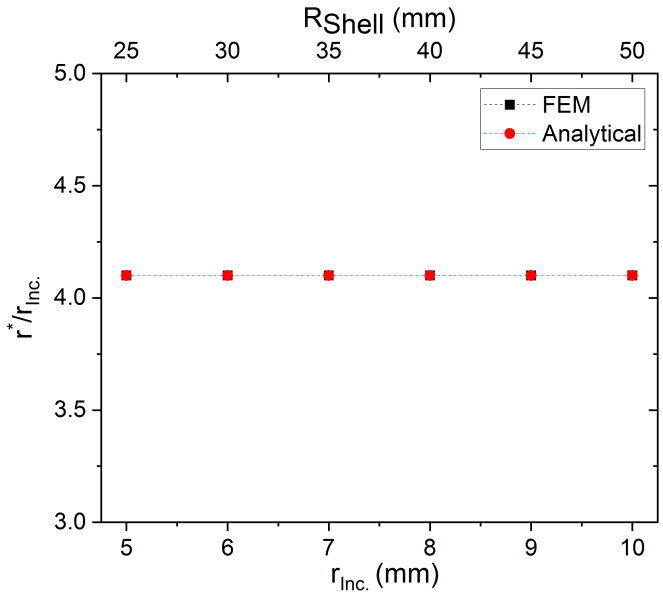

Figure 4.8: The calculated ratio of critical length to the radius of inclusion vs. radius of inclusion in the Al – Fe system. The volume fraction of the inclusion to the shell is kept constant.

To test the validity of Eq. (4-23) which predicts the maximum inclusion volume fraction allowable to achieve a given threshold value we modeled six inclusion-shell systems having the same volume fraction for three unique material pairs. The results are summarized in Fig. 4.8. As expected, for equal volume fractions (for constant f) the critical length is constant for a given threshold value for all sizes. This is also shown in Table 4.2 where we tabulate the critical lengths, r*, obtained from FEM and Eq. (4-23) for 3 different metallurgies, where all systems had the same geometry in which a 5 mm radius inclusion was surrounded by a 50 mm radius spherical shell. The results show that, as expected, the critical length depends only on the configurational parameters/geometry and not the material chemistry.

Table 4.2: The critical lengths, r^*, for 3 different metallurgies, with all systems consisting of a 5 mm radius inclusion surrounded by a 50 mm radius spherical shell.

f=.03	Al – W	Al – Fe	Cu – W
$R_{Mat} = 50\ mm$ $r_{Inc} = 5\ mm$	$\frac{r^*}{r_{Inc}}$		
Analytical	3.4	3.4	3.4
FEM	3.4	3.4	3.4

4.3.1- Strain Energy Approach for Critical Radius Determination

The decay of strain energy with distance from the point of application of a point load is another approach used to quantify the critical radius, r^*. In particular, Toupin [24] formulated an approach which yielded an exponential energy density decay profile for an elastic cylinder of

arbitrary length and regular cross-section, loaded only on one end C_0 with an arbitrary system of self-equilibrated forces:

$$U(s) \leq U(0)e^{-\frac{(s-l)}{s_c(l)}} \qquad \text{Eq. (4-25)}$$

Here $U(s)$ is the elastic energy stored in the sub-cylinder located beyond the distance *s* from the loaded end, $U(0)$ is the total energy, $s_c(l)$ is the characteristic decay length ($\equiv r^*$), l is the parameter $(l > 0)$ chosen to provide a small value of $s_c(l)$, being the length of the section between the cross-sections C_s and C_{s+l} of the cylinder.

Toupin's formulation is independent of the material. Subsequently, many studies used Toupin's decay formula for characteristic (critical) length calculations [123, 124, 125, 126]. However, Zhao provided a mathematical analysis showing that Toupin-type decay is different than Saint Venant's principle [127]. Consequently, the critical radii computed by both approaches should be different. In what follows we evaluate the critical radius, *r**, using both approaches.

Using the Eshelby analysis presented earlier, we find that the elastic strain energy in the entire inclusion-shell volume possesses the following form:

$$U = \frac{2\pi p^2 r_{Inc}^6 (1-2\nu_{Shell})(r^3 - r_{Inc}^3)}{E_{Shell}\left(r_{Inc}^3 - R_{Shell}^3\right)^2} - \frac{\pi p^2 r_{Inc}^6 R_{Shell}^6 (1+\nu_{Shell})}{E_{Shell}\left(r_{Inc}^3 - R_{Shell}^3\right)^2}\left(\frac{1}{r^3} - \frac{1}{r_{Inc}^3}\right) \qquad \text{Eq. (4-26)}$$

Eq. (4-26) describes a power-law decay profile. Consequently, an exponential strain energy decay function should not be applied to non-cylindrical bodies despite previous claims that this is a viable approach [123, 28]. However, even though Toupin's decay equation is not a rigorous universal solution when we plotted the strain energy density values obtained from Eqs. (4-25 & 26) and the FEM model, we observed that it provides a reasonable approximation for evaluating the critical

length. This is shown in Fig. 4.9, where the elastic strain energies obtained with these approaches are plotted for a spherical Al inclusion encapsulated in a Fe shell. We observe that the Toupin-type decay is rigorously correct and is equivalent to the St. Venant principle- in the regions close to the interface. The agreement is worse away from the inclusion-shell interface as shown in the inset figure. Still, we conclude that Toupin-type decay is an acceptable approximation because the differences between Toupin and power-law decay are very small in this range, and all three approaches would yield a critical radius close to the 20 mm value for I=.03.

Fig.4.9 also shows that Eq. (4-26), based on the Eshelby formulation, coincides with FEM results over the entire Al Inclusion-Fe shell system. To see if there was any material dependency of the internal energy decay, we modeled two additional systems, Al-inclusion, W-shell and Cu-inclusion, W-shell with identical dimensions, and compared results from FEM and Eq. (4-26).

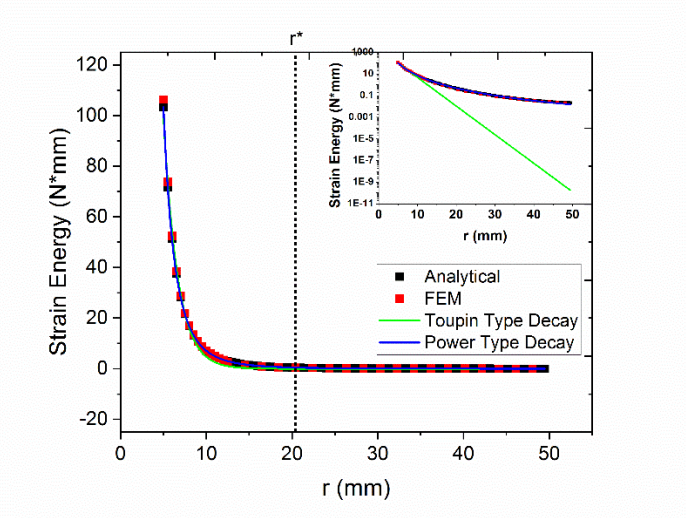

Figure 4.9: Strain energy for 5 mm inclusion and 50 mm shell in Al – Fe system. The log-scale inset shows the difference between the two types of decay.

Table 4.3: Fitted strain energy for 3 different couplings having 5 mm radius of inclusion and 50 mm radius shell.

$r_{Inc} = 5\ mm$	Al – Fe		Al – W		Cu – W	
$R_{Shell} = 50\ mm$	Analytical	FEM	Analytical	FEM	Analytical	FEM
A	19684±48	21774±129	45183±133	49450±305	51370±153	49519±295
n	-3.9 ± 0.1	-3.9 ± 0.1	-3.9 ± 0.1	-3.9 ± 0.1	-3.9 ± 0.1	-3.9 ± 0.1

For ease of comparison we regression-fitted all results to a power-law of the form:

$$y = Ax^n \qquad \text{Eq. (4-27)}$$

The results are tabulated in Table 4.3. While the constants, A, are different for each system, we observe the same decay exponent, n, for all cases.

4.3.2- Effect of Shell Geometry

To investigate the effects of shell geometry we modeled the stress distributions caused by the thermal expansion of a spherical inclusion contained within a cubical shell (SICS unit). For this case, there is no analytical solution. Our model showed that the hydrostatic stress in a spherical 5mm Al inclusion surrounded by a 100 mm x 100 mm x 100 mm ($4R_{Matrix}$) Fe cube differs only 1 MPa from that for the spherical inclusion within a 50 mm radius spherical shell. In addition, the variation of stresses with position within the cube and the sphere are comparable. (Figs. 4.10-a & b). We conclude that for shells with dimensions much larger than the critical radius, the shape of the shell is not a critical parameter in defining the stress distribution within the system[12].

[12] This conclusion follows directly from St. Venant's principle.

To construct a system more suitable for discussing residual definitions presented in Chapter 3, we constructed a model metal matrix composite (MMC) by stacking eight SICS units in a 2*x*2*x*2 arrangement (Fig. 4.11).

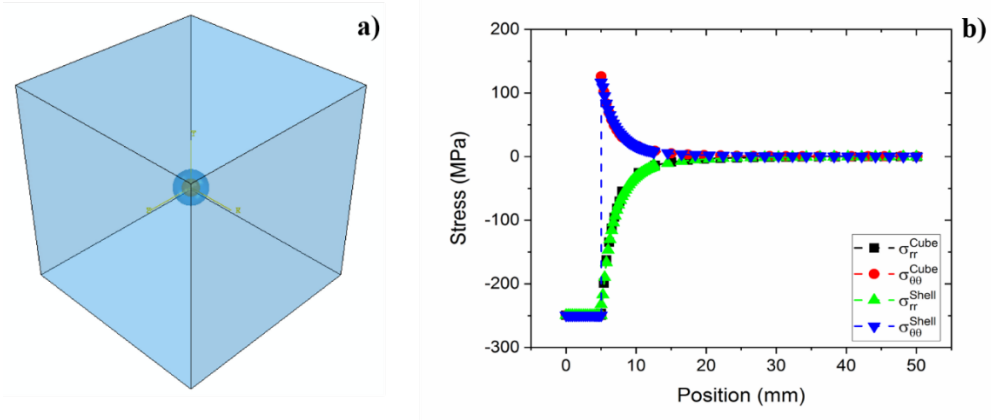

Figure 4.10: a) Spherical inclusion-in-cubic shell b) Variation of tangential and radial stresses with the position in shell and cube models.

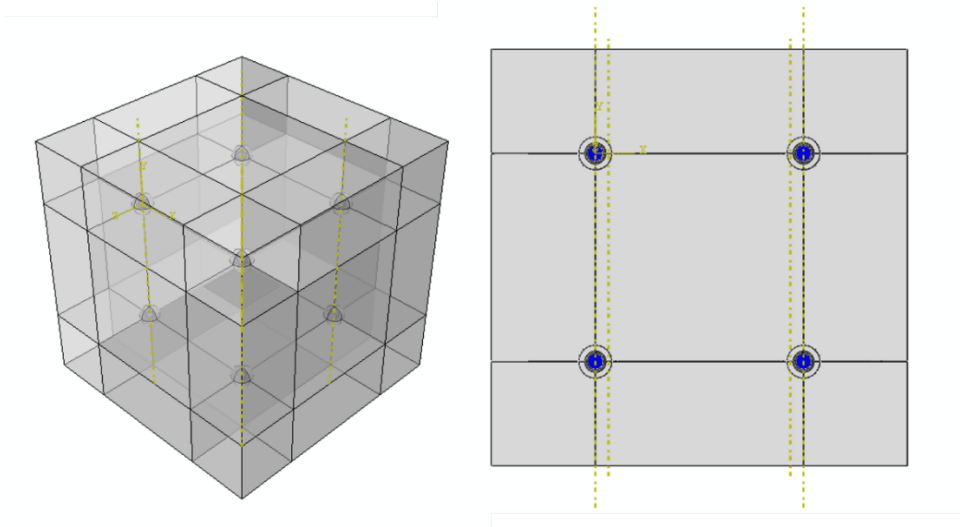

Figure 4.11: Eight spherical inclusion-in-cubic shell (SICS) units stacked in a 2x2x2 arrangement to form a metal-matrix composite (MMC) system.

We investigated the variations in the stress field distributions within the MMC system shown in Fig. 4.11 by changing the dimensions of the cubic shells which make up the matrix. In Fig. 4.12 the variation of radial and tangential stresses within two neighboring SICS of the MMC are plotted as a function of position for four different cubic-shell dimensions.

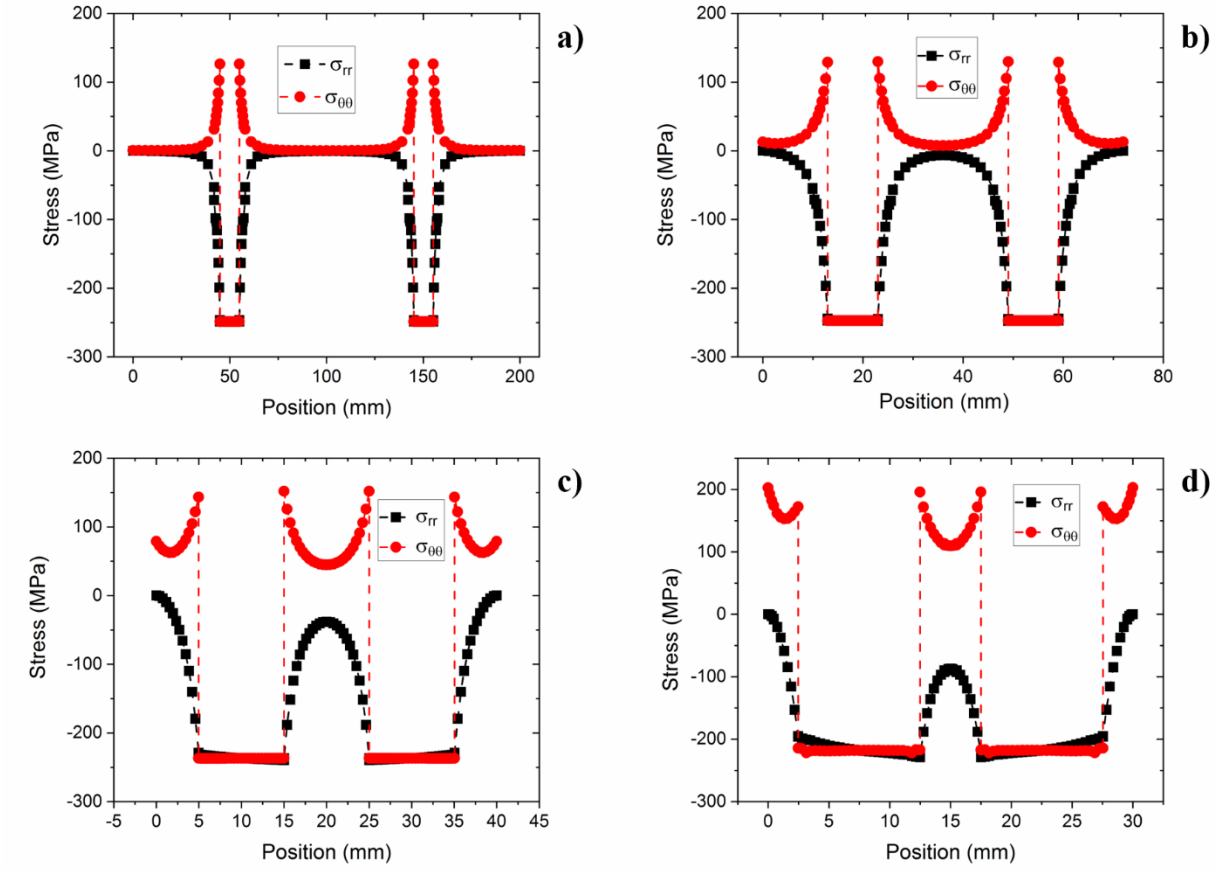

Figure 4.12: Variation of radial and tangential stresses within two neighboring SICS of the MMC as a function of position for four different cubic-shell dimensions. For all cases, the inclusion radius is 5 mm. The cube edge lengths are a) 200 mm, b) 72 mm, c) 40 mm, and d) 30 mm, respectively.

For the thicker cube shells (Figs. 4.12-a & b) both tangential and radial stresses decay to zero at the midpoint between the SICS; the tangential stresses decay to negligible values at the external surfaces[13]. If these SICS were sectioned out of the MMC, their stress states would not change. On the other hand, the stress fields of the thinner cube shells (Figs. 4.12 c & d) overlap in the MMC volume. For these cases, both the tangential and radial stresses are finite at the midpoint of the MMC and the tangential stresses are non-negligible at the free surfaces. In addition, the hydrostatic stress state within the inclusion is perturbed slightly, with such perturbation being more pronounced for the smallest system.

4.4- Implications of the MMC Stress Distribution for Diffraction Strain/Stress Measurements

4.4.1- Local vs. Average Stress Values

We used the residual stress distributions generated in the MMC model to check the validity of the definitions used in classifying residual stress fields. To make the discussion simpler we converted the radial and tangential stresses to Cartesian coordinates and plotted all six terms of the stress tensor over the central cross-section of the MMC corresponding to models shown in Figs. 4.12-a & d. These plots are shown in Figs. 4.13-a & b, respectively. For both cases, the local stress tensors associated with the matrix and inclusions are given by:

[13] The radial stresses must decay to zero at the free surfaces.

$$\left(\sigma_{ij}^{M}\right)_{x,y,z} = \begin{pmatrix} \sigma_{11}^{M} & \sigma_{12}^{M} & 0 \\ \sigma_{12}^{M} & \sigma_{22}^{M} & 0 \\ 0 & 0 & \sigma_{33}^{M} \end{pmatrix} \qquad \text{Eq. (4-28-a)}$$

$$\sigma_{ij}^{I} = \begin{pmatrix} \sigma_{11}^{I} & 0 & 0 \\ 0 & \sigma_{22}^{I} & 0 \\ 0 & 0 & \sigma_{33}^{I} \end{pmatrix} \qquad \text{Eq. (4-28-b)}$$

The stress components, $\left(\sigma_{ij}^{M}\right)_{x,y,z}$, depend on position. In the inclusion, the stress state is hydrostatic[14]. Consequently, the volume-averaged stress within the inclusion is equal to the local stress values, "p".

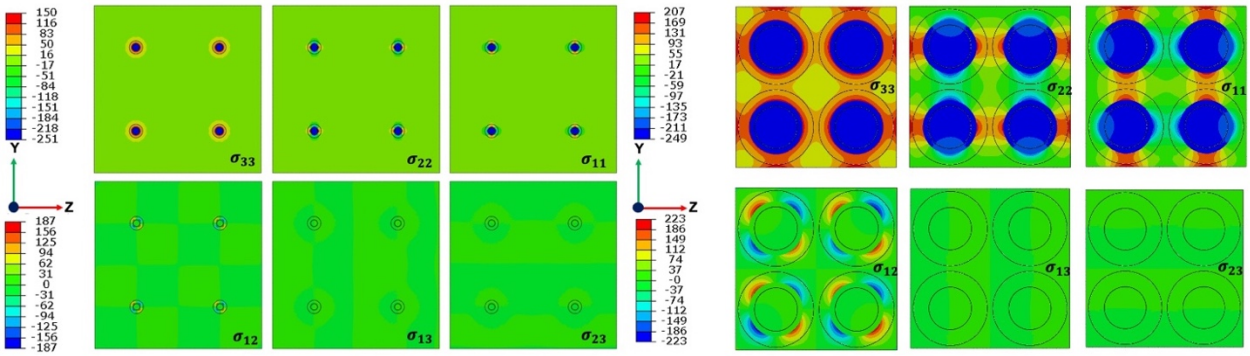

Figure 4.13: Variation of stress components over the central cross-section of a 2x2x2 MMC. For (a) the MMC is constructed of eight Fe Shell-Al inclusion SICS, with 200 mm edges. For (b) The SICS have edge lengths of 30 mm. In all cases, the inclusions have 5 mm radii.

[14] For simplicity, we neglect the small σ_{ij}^{I} perturbations in Fig. 4.13-d caused by the interactions of the stress fields.

4.4.2- Representative Volume Element Definition

To simplify the definition of the RVE for diffraction measurements we used the volume over which the force-balance is achieved. In the case of the MMC constructed from eight 200 mm edge-length SICS units (Fig. 4.11), each SICS achieves force equilibrium independently. In this case, proper removal[15] or the addition of one SICS unit would not change the stress distribution of the remaining SICS units or the stress state of the overall composite. The addition or removal of partial SICS units (same size inclusion but partial matrix) might change the stress distribution within the MMC if the inclusion was too close to the free surface. For MMCs consisting of a large number of SICS units, such change would be negligible. For such an MMC specimen the average residual stresses measured from the matrix and the inclusions would be independent of the size of the MMC.

In the case of the MMC constructed from eight 30 mm edge-length SICS units, the stress fields in the SICS unit overlap. Consequently, one cannot add or remove a SICS unit w/out modifying the overall stress distribution. Consequently, modeling would be needed to define the RVE in this case.

4.4.3- Effect of Beam Size and Position on $d_{\phi\psi}$ $vs.$ $sin^2\psi$

Consider a virtual diffraction experiment, where the representative volume of the MMC having 200 mm edge (it is the quadrant of the MMC) is illuminated with a monochromatic, plane-wave X-ray beam such that the incident and diffracted beam vectors are in the x-z plane.

[15] We assume a hypothetical separator which segments the system without inducing material waster or deformation.

In this geometry, diffraction strain measurements performed on inclusion reflections for stress fields depicted in Fig. 4.14, would yield identical flat (zero-slope), $\frac{d_{\psi}^{i}-d_{0}^{i}}{d_{0}^{i}} = (\varepsilon_{11}')_i \; vs. \sin^2\psi$ plots regardless of the beam size and the position of the beam. From the intercepts of which the stress, $\langle\sigma_{33}^{i}\rangle$, could be obtained using Eq. (1-11).

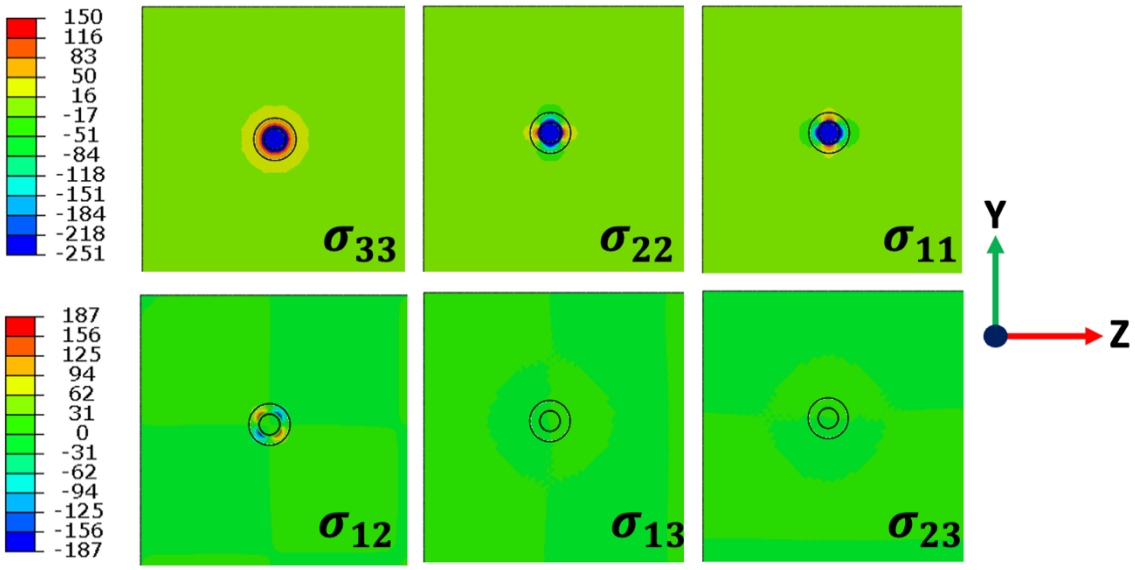

Figure 4.14: Variation of stress components over the representative volume of the central cross-section of a 2x2x2 MMC having a 200 mm edge.

The stress variation over the central cross-section of this volume is shown in Fig. 4.14. We observed that σ_{12} component shows different responses close to the matrix inclusion interface. We chose three directions where σ_{12} shows positive, negative, and zero stress as shown in Fig. 4.15. Thus, we decided to perform virtual diffraction experiments along with these directions, 1, 2, and 3 by using different beam sizes and positions of the beam.

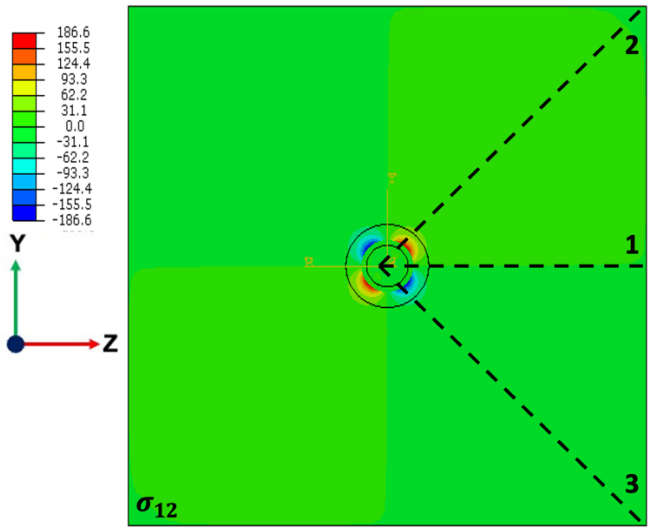

Figure 4.15: Variation of σ_{12} over the representative volume of the central cross-section of a 2x2x2 MMC having 200 mm edge. Three directions, 1, 2, and 3 are shown with dashed lines.

We calculated the average stresses for the matrix along with three directions in the sample coordinate system by using different beam sizes. These are shown in Fig. 4.16. For all directions, the larger the beam size is, the stress components are closer to zero. For better resolution, the experimenter needs to choose smaller beam sizes.

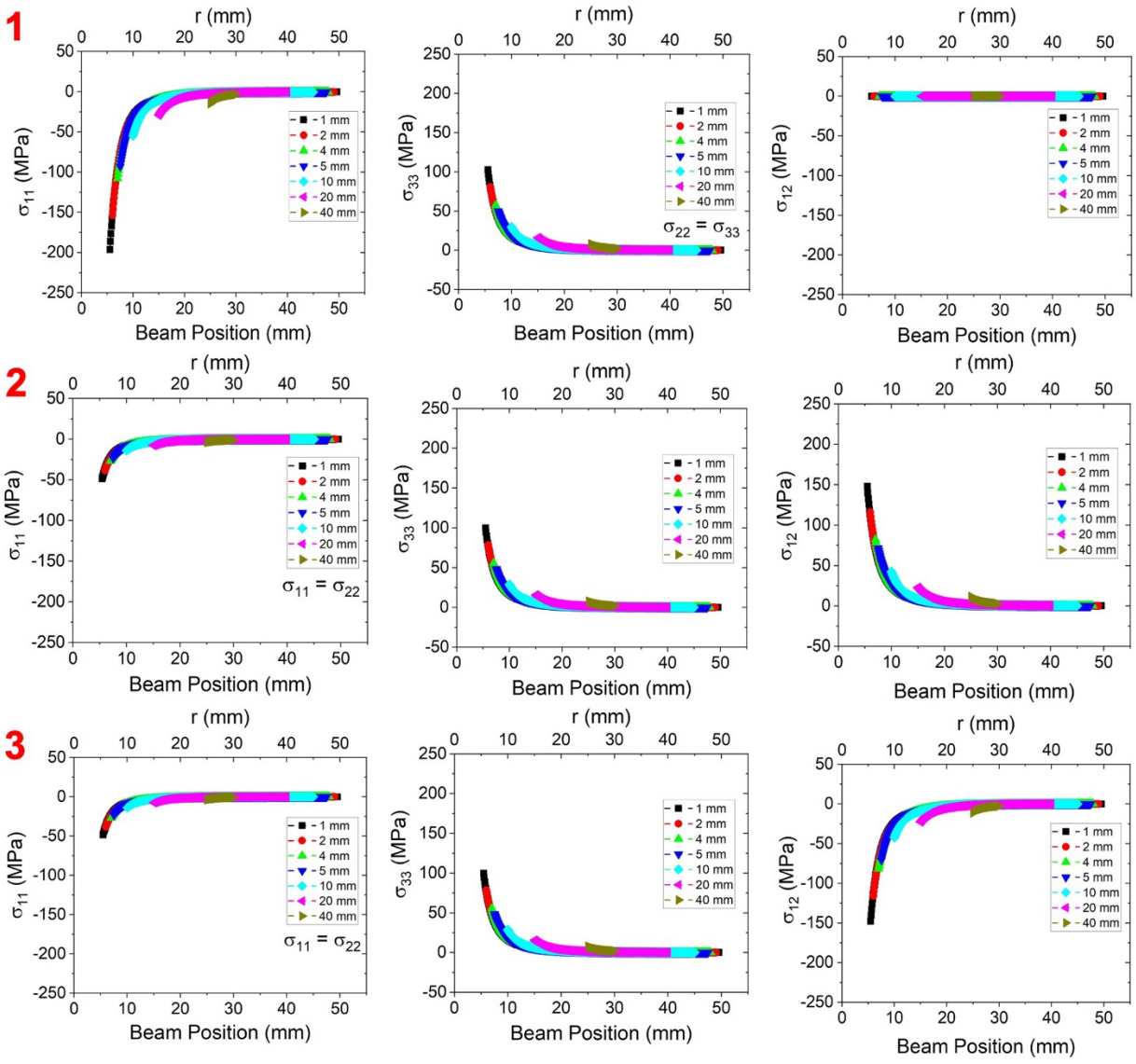

Figure 4.16: Average stresses calculated along 1,2 and 3 directions in sample coordinate system for different beam sizes.

Neglecting absorption effects, and assuming an infinitesimal grain size, such that all ψ-tilts sample infinitely many grains across the representative volume, the $\frac{d_\psi^M - d_0^M}{d_0^M}$ $vs.\sin^2\psi$ plots for matrix reflections will be linear and have finite slopes[16] depending on the position of the beam.

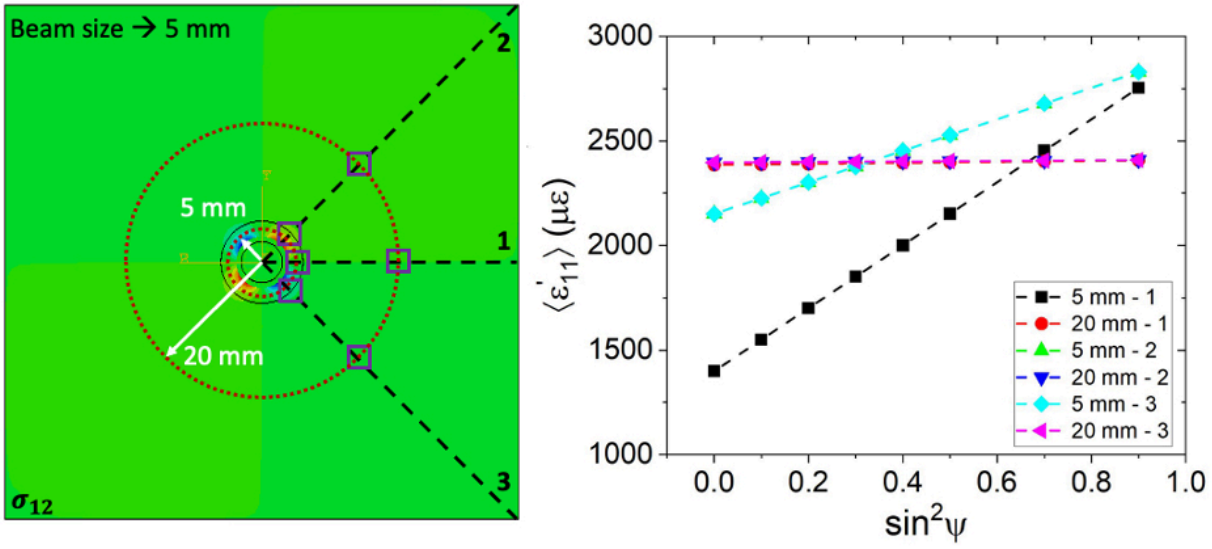

Figure 4.17: a) Position (shown in purple square box) of the 5 mm beam on the matrix along three directions on the representative volume, b) the (ε'_{11}) $vs.$ $\sin^2\psi$ plots belong to experiment performed in different beam positions.

In the case of Fig. 4.13-a, corresponding to the stress state shown in Fig. 4.12-a, almost 70% of the matrix volume is stress-free. Consequently, the volume-weighted strains obtained over the entire matrix by diffraction, $\langle\bar{\varepsilon}'_{11}\rangle_M$, will be very close to zero, yielding small average stress, $\langle\bar{\sigma}_{33}\rangle_M$, acting normal to the cross-section of Fig. 4.13-a. However, as it is shown in Fig. 4.16, the

[16] The stress state within the matrix is not hydrostatic.

results would be different if a 5 mm beam size is used at various positions. We performed the virtual experiments 5 mm and 20 mm away from the boundary along with different directions. The results can be seen from Fig. 4.17-b. Using the same beam sizes at different positions in the matrix yields different average stresses. This shows that the average stress can be used in computing the force-balance required for static equilibrium of the cross-section however, it is inadequate to represent the state of the matrix.

In the case of Fig. 4.13-b, the average stress components, $\langle \bar{\sigma}_{33} \rangle_M$, in the matrix will be much higher due to the interacting stress fields around the inclusions. However, these average stress values would still be inadequate in representing the stress state within the matrix. Reporting such $\langle \bar{\sigma}_{33} \rangle_M$ without the underlying distribution, $\left(\sigma_{ij}^{M}\right)_{x,y,z}$, could be misleading.

4.4.4- Classification of Local and Average Stress Distributions

In the cubic composite system, the FEM showed that all inclusions are under hydrostatic compressive stress and the average stress, $\langle \sigma_{33}^{Inc} \rangle$, in each inclusion is the same and approximately -250 MPa. On the other hand, the average radial stress, $\langle \sigma_{rr}^{Mat} \rangle$, and tangential stress, $\langle \sigma_{\theta\theta}^{Mat} \rangle$, are approximately 0 MPa for the MMCs formed with larger SICS units and finite for the smaller ones. We now examine each constituent one by one:

a) The hydrostatic stress state in the inclusion can be called pseudo-macro stress because (1) it is constant at all points within a given inclusion; (2) It is constant in all inclusions; (3) If a mechanical technique was used to section the specimen across any cross-section of an

MMC larger than the relevant RVE, the remaining material would not exhibit dimensional changes since residual stresses are balanced locally.

b) In the case of the matrix, the measured average residual stress depends on the sampling volume (beam size) (Fig 4.18). In such a case stress mapping over the entire SICS or MMC volume should be conducted since, due to the complex stress gradients close to the inclusion, average stresses would be of limited utility. In real piecewise isotropic MMCs containing high volume fractions of precipitates, the average stresses would be termed pseudo-macro stresses as well.

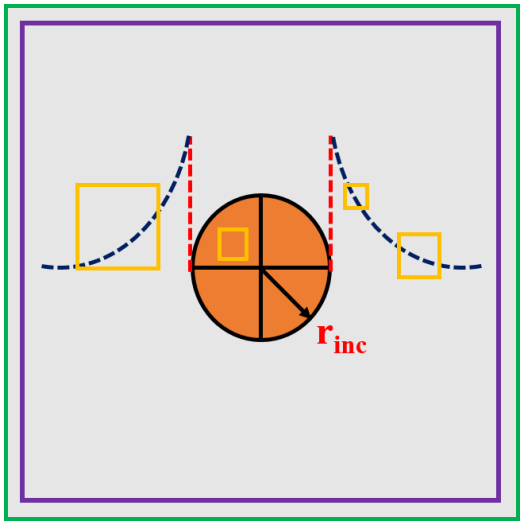

Figure 4.18: Metal matrix composite system with different sampling volumes.

4.5- Distribution of Applied Stresses in a SICS Systems

SICS system contained only residual stresses balanced between the shell and the inclusion. These stresses were generated to maintain compatibility/continuity of the material at the SICS

interface when the system was uniformly heated, and the inclusion tried to expand more than the surrounding shell; the surfaces of the SICS were free of applied stresses and tractions before, during and after heating. Numerical modeling of the stress field showed that the uniform hydrostatic stresses in the inclusion volume were balanced by position-dependent tangential and radial stresses in the shell. Modeling a metal-matrix composite system consisting of multiple, non-interacting, SICS units yielded similar results[17]. We observed that in this case: (1) the average (hydrostatic) residual stress tensor over all inclusions was equal to the residual stress tensor within any one inclusion and (2) if one only considered the stress state of the inclusions intersected by a given cross-section across the MMC- and thus ignoring the matrix stress fields contained in the same cross-section-, one would obtain a net force violating a condition of static equilibrium. Consequently, the residual stresses within the inclusions fit the definition of "pseudo-macro stresses" presented in Chapter 2. On the other hand, the residual stresses within the matrix exhibited highly localized distributions with strong gradients. These terms cannot be adequately represented by their average values unless: (1) the form of the gradients are known a priori and, (2) the volumes over which the averages are taken are accurately known. In the absence of such data, reporting average stress values from the matrix might not be useful for total life prediction, or fracture mechanics application [128].

In this section, we simulate the stress states generated in spherical inclusion contained within a cubical shell (SICS) system induced by forces applied at the cubic shell boundary and compare them to the residual stress distributions generated by mutual constraint of the shell and

[17] Similar considerations apply to MMCs with high inclusion volume fractions. However, in this case the inclusion stress tensors may have deviatoric components depending on the boundary conditions imposed by overlapping interaction stress fields.

the inclusion during uniform heating. We use two modes of loading: (1) uniaxial loading and (2) biaxial loading. For both cases, the cubic shell is Fe and the inclusion (volume fraction, f=0.001) is Al. The relevant geometry and dimensions are shown in Fig. 4.10-a. This model was loaded in uniaxial compression by applying distributed compression surface stress fields, σ_{33}^{0}, along the z-direction on the x-y faces. Bi-axial loading was modeled by adding distributed tensile surface stress fields along the x-direction, σ_{11}^{0}, on the y-z faces. The magnitude of the distributed applied stresses was -460 MPa and -425 MPa for uniaxial and biaxial loadings, respectively. No plastic flow was permitted.

4.5.1- Uniaxially Loaded SICS Model

The variation of the stress tensor components over the central x-y plane of the model is shown in Fig. 4.19. In regions far away from the inclusion, the stress field is uniaxial, and the stress component σ_{33} is equal to the stresses applied at the free boundary, σ_{33}^{0}. The stress field becomes triaxial in the shell regions near the inclusion due to St. Venant effects and is hydrostatic within the inclusion, this is expected from previous theoretical studies [129, 130].

Using the discussion presented in Section 2.12, the components of the stress tensor at any point, $\left(\sigma_{ij}\right)_{x,y,z}$, can be expressed as the sum of the far-field and St. Venant stresses. Consequently, we can obtain the St. Venant stresses at any point from:

$$\begin{pmatrix} \sigma_{11}^{SV} & \sigma_{12}^{SV} & \sigma_{13}^{SV} \\ \sigma_{21}^{SV} & \sigma_{22}^{SV} & \sigma_{23}^{SV} \\ \sigma_{31}^{SV} & \sigma_{32}^{SV} & \sigma_{33}^{SV} \end{pmatrix}_{x,y,z} = \begin{pmatrix} \sigma_{11} & \sigma_{12} & \sigma_{13} \\ \sigma_{12} & \sigma_{22} & \sigma_{23} \\ \sigma_{13} & \sigma_{23} & \sigma_{33} \end{pmatrix}_{x,y,z} - \begin{pmatrix} 0 & 0 & 0 \\ 0 & 0 & 0 \\ 0 & 0 & \sigma_{33}^{0} \end{pmatrix} \quad \text{Eq. (4-29)}$$

Variation of $\left(\sigma_{ij}^{SV}\right)_{x,y,z}$ across the SICS along the x-axis for $y = z = 0$ is shown in Fig. 4.20. Using these figures, we define three unique regions within the SICS model:

a) *Regions with uniform stresses in the cubic shell*: These regions have homogeneous stress states and can be represented by free-body diagrams with uniform far-field stresses acting on their boundaries. For the case analyzed here, the stress states of these regions can be considered as uniaxial compression.

b) *St. Venant regions in the shell material close to the inclusion*: The stress tensor components in this region have steep gradients and the stress state is tri-axial. The stress distributions on the face of free-body diagrams containing the inclusion interface are not uniform.

c) *The inclusion volume:* The stress state within the inclusion is homogeneous. The uniform internal stress within the inclusion is not equal to the far-field stress.

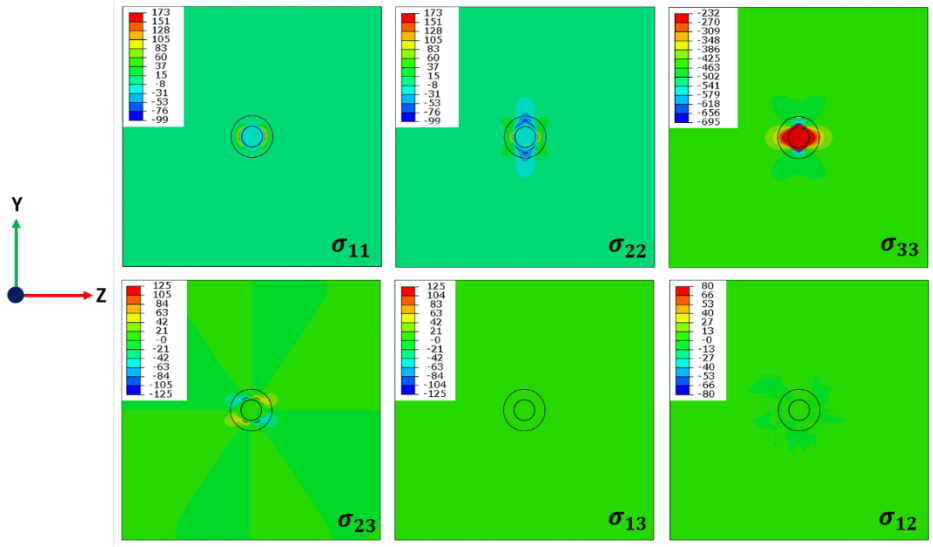

Figure 4.19: Variation of stress components over the central cross-section of a uniaxially loaded SICS. The SICS is constructed of Fe Shell-Al inclusion with 100 mm edges.

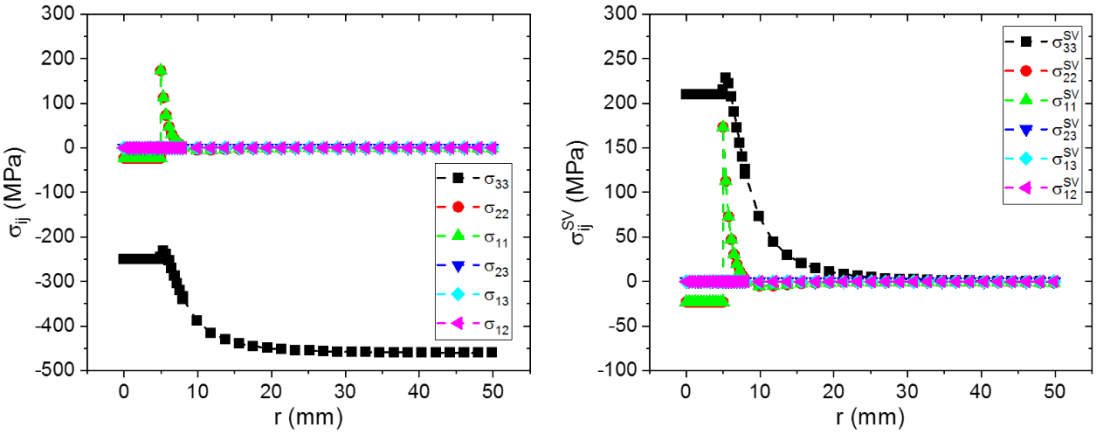

Figure 4.20: Variation of $\left(\sigma_{ij}^{SV}\right)_{x,y,z}$ across the uniaxially loaded SICS along the x-axis.

4.5.2- Biaxially Loaded SICS Model

The variation of the stress tensor components over the central x-y plane of the model is shown in Fig. 4.21. In regions far away from the inclusion, the stress field is biaxial, and the stress components σ_{33} and σ_{22} are equal to the stresses applied at the free boundary, σ_{22}^{0} and σ_{33}^{0}. The stress field becomes triaxial in the shell regions near the inclusion due to St. Venant effects and is hydrostatic within the inclusion, this is expected from previous theoretical studies [129, 130].

Using the discussion presented in Section 2.12, the components of the stress tensor at any point, $\left(\sigma_{ij}\right)_{x,y,z}$, can be expressed as the sum of the far-field and St. Venant stresses. Consequently, we can obtain the St. Venant stresses at any point from:

$$\begin{pmatrix} \sigma_{11}^{SV} & \sigma_{12}^{SV} & \sigma_{13}^{SV} \\ \sigma_{21}^{SV} & \sigma_{22}^{SV} & \sigma_{23}^{SV} \\ \sigma_{31}^{SV} & \sigma_{32}^{SV} & \sigma_{33}^{SV} \end{pmatrix}_{x,y,z} = \begin{pmatrix} \sigma_{11} & \sigma_{12} & \sigma_{13} \\ \sigma_{12} & \sigma_{22} & \sigma_{23} \\ \sigma_{13} & \sigma_{23} & \sigma_{33} \end{pmatrix}_{x,y,z} - \begin{pmatrix} 0 & 0 & 0 \\ 0 & \sigma_{22}^{0} & 0 \\ 0 & 0 & \sigma_{33}^{0} \end{pmatrix} \qquad \text{Eq. (4-29)}$$

Variation of $\left(\sigma_{ij}^{SV}\right)_{x,y,z}$ across the SICS along the x-axis for $y = z = 0$ is shown in Fig. 4.22. Using these figures, we define three unique regions within the SICS model:

a) *Regions with uniform stresses in the cubic shell*: These regions have homogeneous stress states and can be represented by free-body diagrams with uniform far-field stresses acting on their boundaries. For the case analyzed here, the stress states of these regions can be considered as biaxial compression.

b) *St. Venant regions in the shell material close to the inclusion*: The stress tensor components in this region have steep gradients and the stress state is tri-axial. The stress distributions on the face of free-body diagrams containing the inclusion interface are not uniform.

c) *The inclusion volume:* The stress state within the inclusion is homogeneous. The uniform internal stress within the inclusion is not equal to the far-field stress.

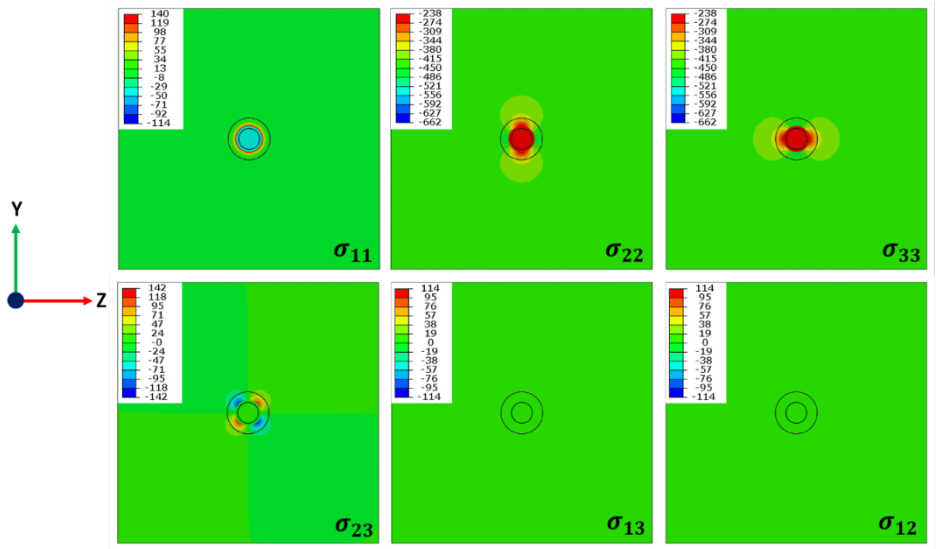

Figure 4.21: Variation of stress components over the central cross-section of a biaxially loaded SICS. The SICS is constructed of Fe Shell-Al inclusion with 100 mm edges.

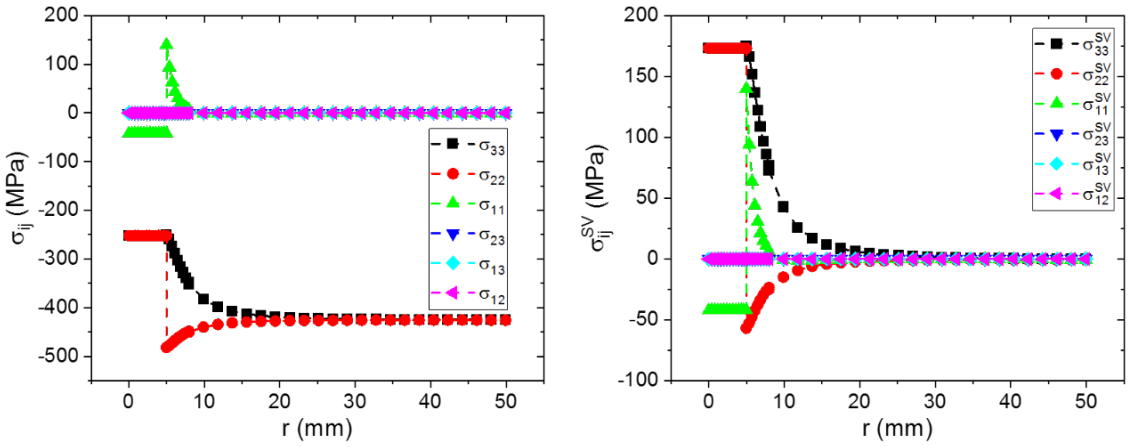

Figure 4.22: Variation of $\left(\sigma_{ij}^{SV}\right)_{x,y,z}$ across the biaxially loaded SICS along the x-axis.

4.6- Summary

In the case of thermally loaded SICS and MMC systems, there is no macrostress field and the observed residual stress field in the inclusion is called pseudo-macro stress. On the other hand, the residual stresses within the matrix exhibited highly localized distributions with strong gradients due to St. Venant stresses. However, in the case of uniaxially and biaxially loaded SICS models, there is far-field stress which corresponds to the macrostress field in the matrix away from the inclusion-shell interface. From this point, we can argue that any definition provided in the literature (e.g. Macherauch) that depends on the scale fails to describe the stress state of the heated composite system. The stress field in the inclusion fits Macherauch's type I stress definition. However, the scale is not enough to describe a stress field in the inclusion. In addition, If a mechanical relaxation method was used to section the specimen across any cross-section of an MMC larger than the

relevant RVE, the remaining material would not exhibit dimensional changes since residual stresses are balanced locally.

The ideal composite system shows us that a simpler isotropic inclusion-shell system might have a relatively complex stress field and it must not be underestimated. One needs to be careful during the measurements, it requires significant preparation and material characterization.

In the next chapter, we described virtual diffraction stress experiments in ideal, polycrystalline, thin-films at which local stress variations are observed due to the change of elastic moduli and/or the coefficient of thermal expansion from grain to grain.

5- STRESSES UNDER THERMAL EFFECTS IN IDEAL POLYCRYSTALLINE THIN FILMS

In this chapter, we describe virtual diffraction stress experiments in ideal, polycrystalline, thin films[18] simulated using ABAQUS CAE. Single and two-phase films, in which the crystal orientations of all grains were specified, were subjected to free and constrained thermal expansion and loaded into elastic and elastoplastic deformation regions. These models were constructed such that in the regions of interest there were no St. Venant stresses. Local perturbations of the far-field stress (Heyn stresses) arose only in models where elastic moduli and/or the coefficient of thermal expansion changed from grain to grain along a direction within the sample volume.

For all models, we used finite element modeling to obtain local stress and strain distributions in all grains in the sample coordinates. In addition, we also computed the expected $\varepsilon'_{hkl}\ vs.\sin^2\psi$ plots based on local strains in grains diffracting into several reflections, hkl, and analyzed these plots using the standard formalisms described in Chapter 1. Thus we were able to compare the real space and diffraction-averaged stresses and strains in our ideal samples. These studies are described below.

[18] In contrast, the models constructed in Chapter 4 were based on isotropic homogeneous continuum, and contained no grains or grain boundaries. Local stress variations in these models (St. Venant stresses) were caused solely by sample geometry and boundary conditions in response to thermal and/or mechanical loads.

5.1- Materials Selection

We constructed single-phase Cu and W models as well as a two-phase Cu – W model. Selected properties of Cu and W are shown in Table 5.1. These elements were chosen to simplify/optimize both modeling and any future experiments. The following were considered:

a) Cu and W single crystals have cubic symmetry, FCC and BCC respectively, and consequently have isotropic coefficients of thermal expansion (CTE). Thus, in the unconstrained state polycrystalline, single-phase Cu and W specimens should expand isotropically, without the formation of thermal Heyn stresses between grains of various orientations in either case.

b) At room temperature, the CTE of Cu is almost 3.6*x* the CTE of W. Thus, Cu and W grains should mutually constrain each other from achieving their equilibrium dimensions during unconstrained heating of the two-phase sample, causing the formation of inter-phase Heyn stresses. Due to the large difference in the CTEs of the individual phases, these stresses are expected to be quite large.

c) The Zener index, $\eta_Z = {}^{2C_{44}}/_{(C_{11}-C_{12})}$, of W is 1.0. Thus, W grains are elastically isotropic. When a polycrystalline W sample is externally loaded there should be no elastic strain incompatibility between grains of different crystal orientations along any sample direction; inter-grain Heyn stresses due to elastic incompatibility will be zero for all grains.

d) For Cu, literature values for η_Z are between 2.8 to 3.2. Thus, in Cu single crystals the <111> directions will be almost *3x* stiffer than the <100> directions. Other <hkl> directions will have stiffness values between these extrema. Consequently, when a polycrystalline Cu sample is externally loaded, elastic strain incompatibility between grains of different

crystal orientations along any sample direction should cause significant inter-grain Heyn stresses to keep displacements in adjoining grains equal across the relevant grain boundary.

e) Cu and W have quite different stiffness coefficients; W crystals are much stiffer than Cu along any direction. Consequently, inter-phase Heyn stresses are expected in both Cu and W grains in a two-phase system subjected to external loads. The interphase stresses in isotropic W grains should occur due to the mutual constraint between neighboring Cu and W grains. The interphase stresses in anisotropic Cu grains should contain contributions from constraints by surrounding W grains as well as a constraint from surrounding Cu grains with different orientations.

f) Cu and W have quite different plastic flow properties. W has a very high yield point and is quite brittle. Cu is ductile. In a Cu – W sample loaded beyond the yield point of the two-phase sample, plastic strains in Cu grains would be larger. Consequently, if such a sample is unloaded after plastic deformation, Heyn stresses due to plastic incompatibility should be observed in both Cu and W grains due to mutual constraint.

g) Cu and W can be considered mutually insoluble in each other for all compositions between RT and 2700°C (Fig. 5.1-a). Consequently, any Cu – W sample is a mechanical mixture of pure Cu and W crystallites bonded to each other with rigid boundaries. This simplifies the specification of elastic constants in each grain and justifies using rigidly bonded (tie-constrained) boundaries between grains.

h) Finally, for most practical x-ray wavelengths, non-overlapping diffraction peaks are accessible for diffraction measurements for both Cu and W phases (Fig. 5.1-b).

Table 5.1: The Zener index, stiffness, and compliance constants for selected crystals and coefficients of thermal expansion of Cu and W *[131]*.

			10^{10} Pa			10^{-11} Pa^{-1}			GPa		1/°C
	Structure	Zener Index	C_{11}	C_{12}	C_{44}	S_{11}	S_{12}	S_{44}	E	v	Room-temperature CTE / 10^{-6}
Cu	FCC	3.20	16.84	12.14	7.54	1.50	-0.63	1.33	112	0.34	16.7
W	BCC	1.00	50.1	19.8	15.14	0.26	-0.07	0.66	385	0.27	4.6

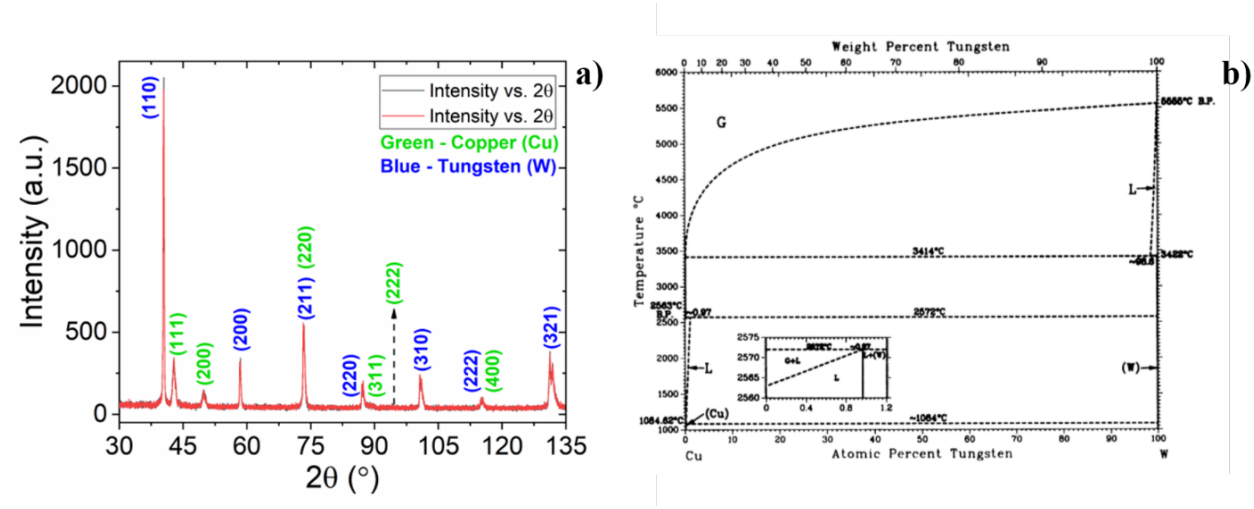

Figure 5.1: a) X-ray diffraction pattern of Cu – W sample containing 50% Cu – 50% W, and b) binary phase diagram of Cu and W *[132]*.

5.2- Modelling Approach

Fig. 5-2 depicts the mesh used in single-phase W or Cu finite-element models. All 400 hexagonal-prism shaped anisotropic grains in this model, arranged as a 20 *x* 20 *x* 1 array, are oriented in the sample coordinate system, $\vec{S}_i$, such that they will diffract into one of the chosen

reflections, 200, 222 or 420 (Figs. 5.2-a, b & c, respectively) at the ψ-tilts specified[19] in Table 5.2. Here the population number for each ψ–ensemble[20], N_{ψ}^{hkl} , and its volume fraction, f_{ψ}^{hkl}, are also tabulated.

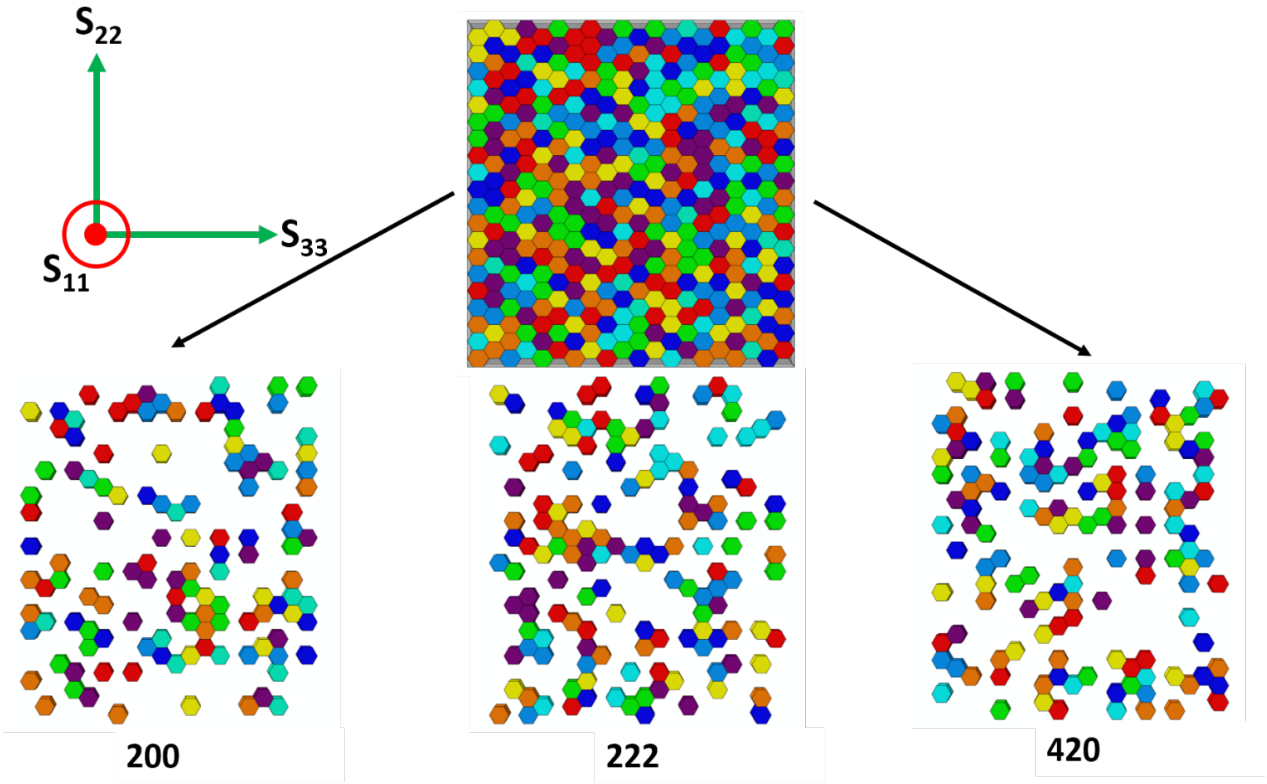

Figure 5.2: Distribution of (200), (222) & (420) reflections for the single-phase W finite element mesh.

[19] Extended details of the computation of the grain orientations and the placement of the particular grains in the mesh were presented in Section 3.3.

[20] We define a "ψ–ensemble" as the population of grains diffracting into a given reflection at a given ψ–tilt.

Table 5.2: The color coding of each ψ angle for each reflection in the finite element mesh.

ψ(°)	0	18.43	26.57	33.21	39.23	45	56.79	71.57
Color	Red	Orange	Dark Blue	Light Blue	Turquoise	Green	Purple	Yellow
$N_{\psi}^{200}, f_{\psi}^{200}$	16, 0.040	16, 0.040	14, 0.035	14, 0.035	15, 0.038	17, 0.043	17, 0.043	12, 0.030
$N_{\psi}^{222}, f_{\psi}^{222}$	18, 0.045	18, 0.045	18, 0.045	17, 0.043	16, 0.040	18, 0.045	18, 0.045	17, 0.043
$N_{\psi}^{420}, f_{\psi}^{420}$	18, 0.045	18, 0.045	17, 0.043	16, 0.040	18, 0.045	18, 0.045	17, 0.043	17, 0.043

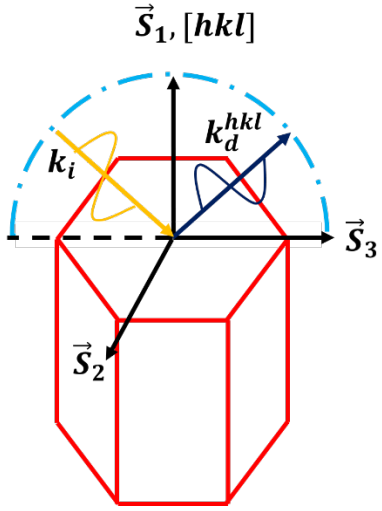

Figure 5.3: Scattering geometry for a single grain of the FEM mesh, oriented for diffraction at ψ=0 into the hkl reflection. In this figure, the [hkl] direction is coincident with the $\vec{S}_3$ sample axis, and $\vec{S}_3$ is in coplanar with the incident and diffracted beam vectors k_i, k_d^{hkl}, respectively.

The diffraction geometry for a single crystal of the FEM mesh, oriented properly to contribute to the *hkl* reflection at $\psi = 0$ is shown in Fig. 5.3. In this figure, the incident and diffracted beam vectors, $\vec{k}_i, \vec{k}_d^{hkl}$ are in the plane defined by the sample axes, $\vec{S}_1, \vec{S}_3$. Hence the in-

plane angle (Fig. 1.7), $\phi = 0$. This geometry applies to all grains belonging to the ψ–volume for $\psi = 0$. For grains diffracting at other ψ–tilts, the relevant [*hkl*] direction will make the appropriate angle, ψ , with sample axis $\vec{S}_3$.

It is important to note that all grains belonging to a given ψ–ensemble for a particular reflection contribute to the diffraction peak for that ψ–tilt. Since each grain may have a different average lattice strain due to the local Heyn stresses, we can write the fundamental equation of diffraction stress/strain analysis, Eqs. (1-11 & 16), for the i^{th} grain within a given ψ–volume as[21]:

$$\left(\frac{\langle d^{hkl}_{\phi=0,\psi}\rangle - d^{hkl}_0}{d^{hkl}_0}\right)_{i,\psi} = \langle \varepsilon^{hkl}_{\phi\psi}\rangle_{i,\psi} = \langle \varepsilon'_{11,\psi}\rangle_{i,\psi} = \left[\left(\langle \varepsilon_{11}\rangle_{i,\psi} - \langle \varepsilon_{33}\rangle_{i,\psi}\right) * \sin^2\psi + \langle \varepsilon_{33}\rangle_{i,\psi}\right] \qquad \text{Eq. (5-1-a)}$$

$$\langle \varepsilon'_{11,\psi}\rangle_{i,\psi} = \langle \tfrac{1+\nu}{E}\rangle_{hkl} \langle \sigma_{33}\rangle_{i,\psi} \sin^2\psi - \langle \tfrac{\nu}{E}\rangle_{hkl} \left(\langle \sigma_{11}\rangle_{i,\psi} + \langle \sigma_{22}\rangle_{i,\psi} + \langle \sigma_{33}\rangle_{i,\psi}\right) \qquad \text{Eq. (5-1-b)}$$

In these equations, carats, $\langle\ \ \rangle_{i,\psi}$, indicate averages of the relevant strain terms over the i^{th} grain of a particular ψ–ensemble.

To simulate the $\langle \varepsilon'_{11,\psi}\rangle_i \ vs. \sin^2\psi$ plot which would be obtained by diffraction for a given reflection we used two approaches; first utilizing the strain output of the FEM model with Eq. (5-1-a) and second, utilizing the stress output of the FEM model with Eq. (5-1-b). We describe below the first approach:

a) For each grain belonging to a given ψ–ensemble of a specific reflection, we first obtained the average strains in sample coordinates, $\langle \varepsilon_{11}\rangle_{i,\psi}, \langle \varepsilon_{33}\rangle_{i,\psi}$, by computing the numerical

[21] Eqs. (1-11 & 16) and Eqs. (5-1-a &b) are similar. For practical reasons, we changed the coordinate system.

averages of the corresponding strain components reported by the FEM program at all nodes within the grain volume[22].

b) Then, we computed the average strain, $\langle \varepsilon'_{11,\psi} \rangle_{i,\psi}$, for this grain by substituting the average strain terms, $\langle \varepsilon_{11} \rangle_{i,\psi}, \langle \varepsilon_{33} \rangle_{i,\psi}$, and the ψ angle in Eq. (5-1-a).

c) We repeated steps 1 and 2 for all grains belonging to the particular ψ–ensemble.

d) We repeated steps 1, 2, and 3 for all eight ψ–ensembles used in the model for each particular reflection.

We then plotted the computed $\langle \varepsilon'_{11,\psi} \rangle_{i,\psi}$ vs. $\sin^2 \psi$ for the particular reflection. This yielded a scatter plot with N_{ψ}^{hkl} strain values at each ψ–tilt, with each strain value corresponding to a particular diffracting grain. Using this formalism we obtained $\langle \varepsilon'_{33,\psi} \rangle_{i,\psi}$ vs. $\sin^2 \psi$ scatter plots for the 200, 222, and 420 reflections of the relevant phases for all Cu, W, and Cu – W models.

The second approach, utilizing the stress output of the FEM model, is similar[23]. In this formalism, we substituted the average stress tensor of each grain into the Eq. (5-1-b), along with the diffraction elastic constants, $\langle \frac{1+\nu}{E} \rangle_{hkl}, \langle \frac{\nu}{E} \rangle_{hkl}$, for the particular reflection, calculated at the Kröner and/or Neerfeld-Hill limits, to compute the $\langle \varepsilon'_{11,\psi} \rangle_{i,\psi}$ vs. $\sin^2 \psi$ scatter plots for all reflections.

The $\langle \varepsilon'_{11,\psi} \rangle_{i,\psi}$ vs. $\sin^2 \psi$ scatter plots were then analyzed for diffraction-averaged stress/strain values for the entire model using the approaches described in Chapter 1. This approach

[22] This approach is justified since all grains have identical volumes and the same number of elements and nodes.

[23] This approach was only employed when the stress tensor of the film contained at least one non-zero term, $\sigma_{ij} \neq 0$.

is analogous to grain-by-grain measurement of the average lattice strain within single grains of a polycrystalline ensemble, where these strains are grouped according to their orientation (ψ–tilt) and analyzed using the classical approaches to obtain stress/strain values for the entire diffracting volume.

5.3- Results and Discussion

5.3.1- Free Thermal Expansion of Single-phase W & Cu Films

In this section, we simulated unconstrained expansion of the single-phase W and Cu models by modeling a 75 °C temperature excursion. These models served as a rigorous test of our model since their output could be rigorously predicted from theory: Since (1) the films were free to expand along the sample axes, $\vec{S}_i, i = 1,3$, at all points, and (2) the CTE of both W and Cu are isotropic, thermal strains, ε_{ij}^{Th} must be isotropic and no residual stresses, at any scale, are expected. Further, since the thermal stresses are independent of direction, $\varepsilon_{ij}^{Th} \neq f(\psi)$, we expect linear, zero-slope, $\langle \varepsilon'_{11,\psi} \rangle_{i,\psi}$ vs. $sin^2\psi$ plots for all reflections, independent of the form of the material's C_{ijkl} tensor.

For both the W and Cu models, we observed the expected grain average strain and stress tensors at all points:

$$\langle \varepsilon_{ij} \rangle_{i,\psi} = \begin{bmatrix} \varepsilon^{Th} & 0 & 0 \\ 0 & \varepsilon^{Th} & 0 \\ 0 & 0 & \varepsilon^{Th} \end{bmatrix} \qquad \text{Eq. (5-2-a)}$$

$$\langle \sigma_{ij} \rangle_{i,\psi} = \begin{bmatrix} 0 & 0 & 0 \\ 0 & 0 & 0 \\ 0 & 0 & 0 \end{bmatrix} \qquad \text{Eq. (5-2-b)}$$

where $\varepsilon^{Th} = \alpha_j . \Delta T, j = \text{Cu, W}$. Given Eq. (5-1-a), the average strain, $\langle \varepsilon'_{11,\psi} \rangle_{i,\psi}$, for each grain in both models was constant, $\langle \varepsilon'_{11,\psi} \rangle_{i,\psi} = \langle \varepsilon_{11} \rangle_i = \varepsilon^{Th}$, and independent of ψ, for all reflections. This yielded the expected linear, zero-slope plots of $\langle \varepsilon'_{11,\psi} \rangle_{i,\psi}$ vs. $sin^2\psi$ for all reflections of both W and Cu, (Figs. 5.4-a & b). We note that all terms of the strain tensor, Eq. (5-2-a), are eigenstrains and thus, are not linked to stresses by Hooke's law [2].

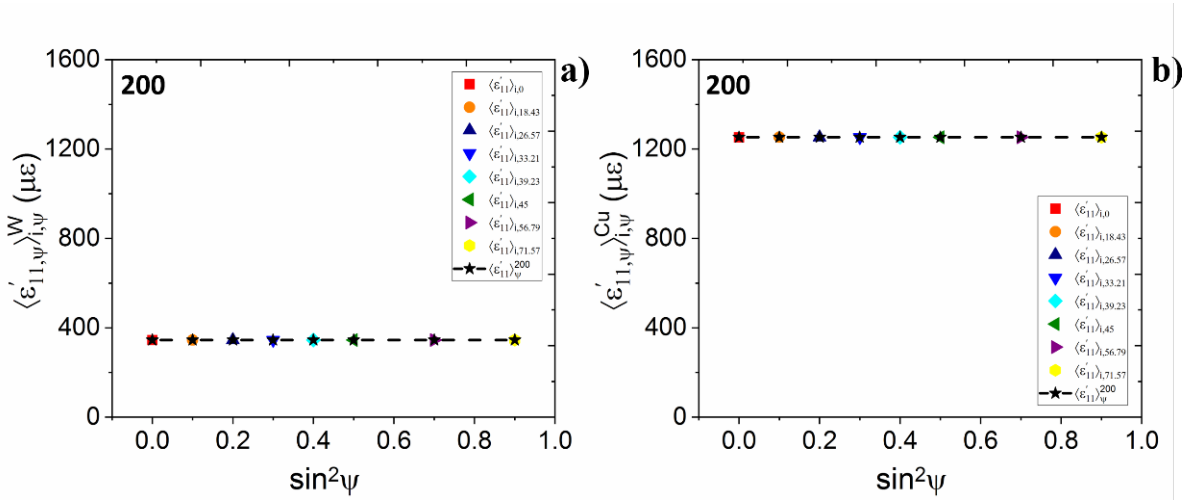

Figure 5.4: Computed $\langle \varepsilon'_{11,\psi} \rangle_{i,\psi}$ vs. $sin^2\psi$ plots for all reflections of W (a) and Cu (b) models heated 100 °C without boundary constraint. Lattice strains, $\langle \varepsilon'_{11,\psi} \rangle_{i,\psi}$, are identical for all grains diffracting into all reflections.

5.3.2- Heating Single-phase W & Cu Films under Bi-axial Boundary Constraint

To induce thermally residual stresses in our ideal, single-phase thin film samples, we specified (essential) homogeneous displacement constraints at the model boundaries in the film

plane. Consequently, upon heating, the grains could only expand freely normal to the film surface (in the $\vec{S}_1$ direction); the in-plane displacements *v, w*, were kept at zero by reaction forces distributed uniformly over the model boundaries. As we discussed in Chapters 1, 2, and the introduction of this chapter, the stress state within a polycrystalline solid subjected to this mode of loading will depend on its Zener index. Consequently, we expect different stress distributions in the W and Cu models. These results are presented next.

5.3.2.1- Heating Single-phase W Films under Bi-axial Boundary Constraint

Since all W grains are isotropic in elastic and thermal loading, the local strain tensor at any point $P(x, y, z)$ within the W-model is expected to be homogeneous, of the form:

$$\left(\varepsilon_{ij}\right)_{x,y,z} = \begin{bmatrix} \varepsilon_{11} & 0 & 0 \\ 0 & 0 & 0 \\ 0 & 0 & 0 \end{bmatrix} \qquad \text{Eq. (5-3)}$$

$\varepsilon_{11}(x, y, z)$ is the total lattice strain along with the sample normal, $\vec{S}_1$. It is the sum of two components: an elastic strain caused by the boundary constraint, $(\varepsilon_{11}^{B.C.})_{x,y,z}$, plus the thermal strain, ε^{Th}, due to the temperature increase. From basic elasticity analysis we obtain;

$$(\varepsilon_{11}^{B.C.})_{x,y,z} \equiv \varepsilon_{11}^{B.C.} = \frac{2\nu}{(1-\nu)}\varepsilon^{Th} \qquad \text{Eq. (5-4-a)}$$

$$(\varepsilon_{11})_{x,y,z} \equiv \varepsilon_{11} = \varepsilon^{Th}\frac{(1+\nu)}{(1-\nu)} \qquad \text{Eq. (5-4-b)}$$

The corresponding local stress tensor at point $P(x, y, z)$ should have the form of an isotropic plane stress tensor:

$$\left(\sigma_{ij}\right)_{x,y,z} = \begin{bmatrix} 0 & 0 & 0 \\ 0 & \sigma_{22} & 0 \\ 0 & 0 & \sigma_{33} \end{bmatrix}; \quad \sigma_{22} = \sigma_{33} = \frac{-E}{(1-\nu)}\varepsilon_{th} \qquad \text{Eq. (5-5)}$$

for all points, $P(x, y, z)$.

Table 5.3: Stress and strain tensor for the edge-constrained W thin film model heated to 75°C, computed using various approaches. The XRD values are the reflection averages of the stress and strain terms.

Parameter	Eqs. (5-4 & 5)	ABAQUS-CAE	XRD Analysis
Thermal strain , ε_{ij}^{Th}	$\begin{bmatrix} 345 & 0 & 0 \\ 0 & 345 & 0 \\ 0 & 0 & 345 \end{bmatrix}$	$\begin{bmatrix} 345 & 0 & 0 \\ 0 & 345 & 0 \\ 0 & 0 & 345 \end{bmatrix}$[24]	-
Boundary constraint strain, $\varepsilon_{ij}^{B.C.}$	$\begin{bmatrix} 255 & 0 & 0 \\ 0 & -345 & 0 \\ 0 & 0 & -345 \end{bmatrix}$	-	-
Total Strain $(\varepsilon_{ij}^{Th} + \varepsilon_{ij}^{B.C.})$; $\bar{\varepsilon}_{ij}$	$\begin{bmatrix} 600 & 0 & 0 \\ 0 & 0 & 0 \\ 0 & 0 & 0 \end{bmatrix}$	$\begin{bmatrix} 600 & 0 & 0 \\ 0 & 0 & 0 \\ 0 & 0 & 0 \end{bmatrix}$	$\begin{bmatrix} 600 & 0 & 0 \\ 0 & 0 & 0 \\ 0 & 0 & 0 \end{bmatrix}$
Stress σ_{ij}; $\bar{\sigma}_{ij}$ (MPa)	$\begin{bmatrix} 0 & 0 & 0 \\ 0 & -182 & 0 \\ 0 & 0 & -182 \end{bmatrix}$	$\begin{bmatrix} 0 & 0 & 0 \\ 0 & -182 & 0 \\ 0 & 0 & -182 \end{bmatrix}$	$\begin{bmatrix} 0 & 0 & 0 \\ 0 & -182 & 0 \\ 0 & 0 & -182 \end{bmatrix}$

The stress and strain values in the sample coordinate system, computed using these equations for our W model, are listed in Table 5.3 for a temperature increase of 75°C. The corresponding results from the FEM analysis are also included. We observe excellent agreement between the values obtained from the FEM simulation and the analytical computations. As expected, the FEM simulations yielded isotropic stress and strain distributions within the model

[24] This tensor is obtained from Section 5.3.1, from the model where we computed the free thermal expansion of a single-phase W film.

volume (Figs. 5.5-a & b). Consequently, average stress and strains are identical to their local values and are independent of the type of averaging and the size and location of the averaging volume.

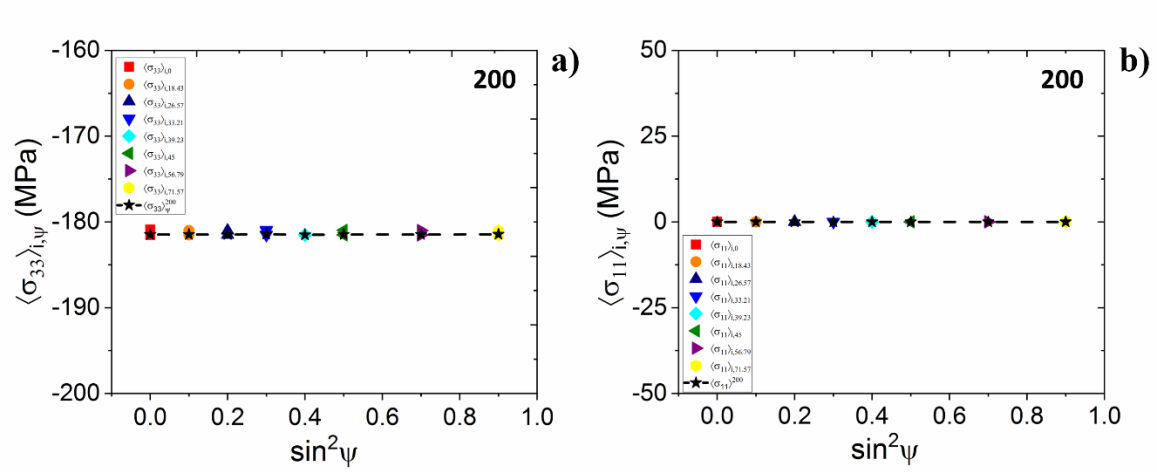

Figure 5.5: Grain averaged stress values in sample coordinates, $\langle\boldsymbol{\sigma_{22}}\rangle_{i,\psi} = \langle\boldsymbol{\sigma_{33}}\rangle_{i,\psi}$ (a) and $\langle\boldsymbol{\sigma_{11}}\rangle_{i,\psi}$ (b) for the $\boldsymbol{\psi}$ -ensembles diffracting into the 200 reflection. At each ψ there are $\boldsymbol{N_{\psi}^{200}}$ identical stress values. Plots for the 222 and 420 reflections were identical.

The stresses in the sample coordinate system were also calculated by simulating and analyzing $\langle\varepsilon'_{11,\psi}\rangle_{i,\psi}^{W}$ $vs.\sin^2\psi$ graphs for all reflections using Eqs. (5-1-a & b) respectively[25]. In Fig. 5.6, the $\langle\varepsilon'_{11,\psi}\rangle_{i,\psi}^{W}$ vs. $\sin^2\psi$ graph for the 200 reflection is shown. As expected, 222 and 420 reflections also yielded identical plots. Consequently, the reflection average stress tensors,

[25] We used the grain averages of the strain values from the FEM output to simulate the $\varepsilon_{\phi\psi}$ vs. $\sin^2\psi$ graphs using Eq. (5-1-a), and used Eq. (5-1-b) to obtain the reflection average stress value.

$\langle \sigma_{ij}^{D} \rangle^{hkl}$, were identical for all reflections. The diffraction elastic constants used in calculations, $\frac{1+\nu}{E}, \frac{\nu}{E}$, are shown in Table 5.4.

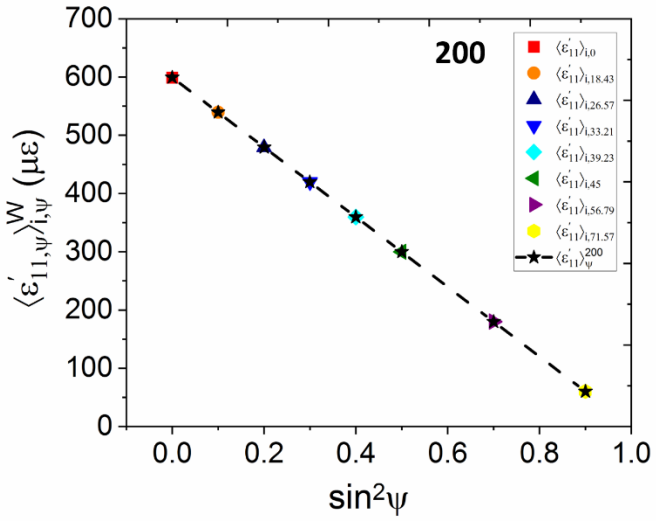

Figure 5.6: $\langle \varepsilon'_{11,\psi} \rangle^{W}_{i,\psi}$ *vs.* $sin^2\,\psi$ plot computed from the strain output of the W model subjected to a 75 °C temperature increase with its in-plane edges constrained. At each ψ there are N^{200}_{ψ} identical strain values.

Table 5.4: Diffraction elastic constants of W calculated from the W stiffness tensor using various approaches *[2, 56]*. These values are independent of reflection since W is isotropic.

(TPa)$^{-1}$	Reuss	Voigt	Kröner	Neerfeld-Hill
$\frac{-\nu}{E}(S_1)$	-0.70	-0.70	-0.70	-0.70
$\frac{1+\nu}{E}\left(\frac{S_2}{2}\right)$	3.30	3.30	3.30	3.30

Table 5.3 and Figs. 5.5 & 6 show that the x-ray values for the reaction stresses induced in the heated polycrystalline W film by the edge constraints are macrostresses since:

a) $\langle \sigma_{ij}^{D} \rangle^{hkl}$ are independent of the reflection chosen for the measurement.

b) $\langle \sigma_{ij}^{D} \rangle^{hkl}$ will be the same for any measurement volume within the model.

c) All reflections yield regular (linear) $\langle \varepsilon'_{11,\psi} \rangle_{i,\psi}$ $vs. sin^2 \psi$.

As expected, the elastic constraint imposed by the edges did not cause any Heyn stresses within the W film.

5.3.2.2- Heating of Cu Thin Films under Biaxial Constraint

Our first set of models showed that W and Cu thin films subjected to free thermal expansion contained homogeneous, isotropic thermal eigenstrains. For both cases, all components of the local stress tensors were zero at all points. Constrained heating of a W film also resulted in a homogeneous strain distribution. In this case, the fixed boundaries caused reaction stresses to counteract the thermal expansion and the local strains were the sum of elastic and thermal components. The stress/strain distributions obtained from numerical modeling agreed with all analytical calculations performed assuming an ideal isotropic continuum. In the next set of models, we extend our modeling to elastically heterogeneous materials. These models were based on a thin film slab consisting of anisotropic Cu grains. The population number for each ψ–ensemble, N_{ψ}^{hkl} , and its volume fraction, f_{ψ}^{hkl}, diffracting into reflections, 200, 222 or 420 at the specified ψ-tilts, are identical to the W-model (Table 5.2). However, the distribution of elastic moduli in the film is highly heterogeneous.

In Fig. 5.7, we plot the effective Young's moduli and Poisson's ratio, $\langle E\rangle_{\psi}^{\vec{S}_2}$, $\langle E\rangle_{\psi}^{\vec{S}_3}$, along with the in-plane axes, $\vec{S}_2$, $\vec{S}_3$, and the average Poisson's ratio, $\langle\frac{\nu_{21}+\nu_{31}}{2}\rangle_{\psi}$, along the film normal, $\vec{S}_1$, of the crystallites in the diffraction position for the 200, 222 and 420 Cu reflections. These terms link the lattice strain along the diffraction direction, $\vec{L}'_{\psi}$, with the in-plane stresses imposed by the boundary constraints. In these figures, the average modulus of all grains belonging to a particular reflection, $\langle E\rangle^{hkl}$, and the bulk average, $\bar{E}_{Cu}$, are shown by the dashed and dotted lines respectively. We observe the following:

a) The effective Young's moduli, $(E_i)_{\psi}^{hkl}$, and Poisson's ratios, $(\nu_i)_{\psi}^{hkl}$, in sample coordinates, of the grains[26] diffracting at various ψ tilts can be significantly different from each other, and average elastic moduli computed from single-crystal compliances, S_{ijkl}, of Cu at various limits (Table 5.1).

b) The ψ-ensemble averages of the elastic moduli, $\langle E\rangle_{\psi}^{hkl}$, $\langle\nu\rangle_{\psi}^{hkl}$, for a given reflection can be significantly different from each other and the isotropic bulk average. For example, the effective Young's modulus of the grains in position for diffraction at ψ = 33.21° ($\sin^2\psi = 0.4$) into the 200 reflection, $\langle E\rangle_{33.21}^{200}$, is ~80% of $\bar{E}_{Cu}$.

c) Reflection averages, $\langle E\rangle^{hkl}$, $\langle\nu\rangle^{hkl}$, taken over all grains, diffracting into a particular reflection for all ψ-tilts, approach the macroscopic average for all reflections studied here.

[26] $(E_i)_{\psi}^{hkl}$ denotes the Young's modulus, along an axis to be specified, of the i^{th} grain diffracting into the *hkl* reflection at angle ψ.

Contrary to predictions in the literature, all $\langle E \rangle_{\psi}^{hkl}$ values were approximately constant for the 420 reflection, within 5% of the bulk average, $\bar{E}_{Cu}$, while $\langle E \rangle_{\psi}^{hkl}$ for both 200 and 222 reflections[27] showed significant deviations from the reflection and bulk averages, $\langle E \rangle^{hkl}$, $\bar{E}_{Cu}$, respectively [82, 49]. Thus, as far as elastic moduli are concerned, the diffraction volumes for the 002 and 222 reflections do not constitute representative volume elements with $\langle E \rangle^{hkl} \neq \bar{E}_{Cu}$. For the 420 reflection, even the individual ψ-volumes yield elastic moduli close to the values computed for bulk, untextured, polycrystalline Cu.

We note, however, that the discussion above does not take into account interaction between grains. The grains of all reflections are intermingled (Fig. 5.2), and it does not follow, a-priori, that the strains within the ψ-volumes of the 420 reflection will yield the correct far-field stress in diffraction analysis. We used the FEM results to investigate this issue.

[27] These belong to the *hhh* and *h00* families, previously suggested for use in diffraction stress analysis (Chapter 1.3.5.3).

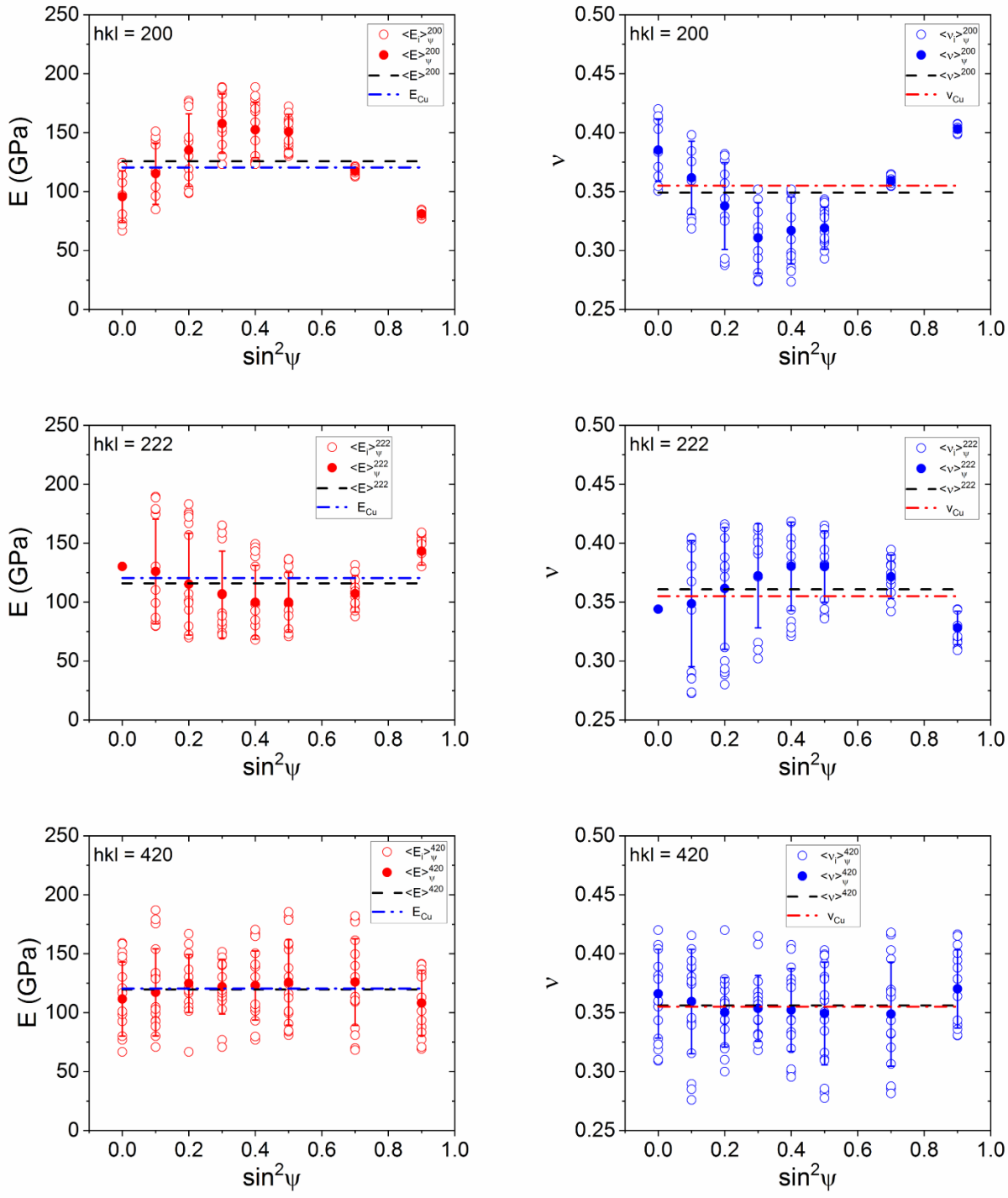

Figure 5.7: Young's modulus and Poisson's ratio distribution for Cu with reflections hkl = 200, 222, 420 at different ψ angles

We used ABAQUS-CAE to model the thermo-mechanical response of the Cu thin-film heated under fixed boundary conditions in the film plane. The stress/strain distributions were computed and analyzed under (1) mostly elastic loading, and (2) elastoplastic loading.

5.3.2.2.1- Edge-constrained Cu Film at Incipient Plastic Flow

In this simulation, the mesh was subjected to a 25°C temperature increase from room temperature. The expected strain and stress tensors for all points, $P(x, y, z)$ in an equivalent isotropic Cu thin film for fully elastic loading Eqs. (5-4 & 5) are presented in Table 5.5. Here we also tabulate numerical averages of the stress and strain tensors, $\bar{\sigma}_{ij}, \bar{\varepsilon}_{ij}$, and the standard deviations[28] for the model parameters. There is reasonable agreement between the analytical calculations and the finite element model results, even though some grains deformed plastically in the model.

In Fig. 5.8, we plot the average plastic strains in the plane of the film, $\langle \varepsilon_{33}^{pl} \rangle_{\psi}^{hkl}$ and out of the plane of the film $\langle \varepsilon_{11}^{pl} \rangle_{\psi}^{hkl}$ as a function of $sin^2\psi$ for all reflections. We observe that, even though the average plastic strains are negligible for most ψ-ensembles, the grain populations oriented to diffract into the 200 reflection for ψ= 33.21°, 39.23° and 45°, and into the 222 reflection for ψ= 33.21°, exhibit small but finite averages. In Table 5.6, the position and grain average plastic and elastic strain tensors for the highly deformed grains in these ψ-ensembles are listed. For comparison, the values for one grain that exhibited no plastic flow are also included (last row).

[28] The grain average stress and strain values in the model were not normally distributed. Thus, the standard deviations listed do not adequately describe the dispersion associated with the numerical averages shown in Table 5.5.

We observe that: (1) the highly-deformed grains are randomly distributed in the mesh, (2) all such grains exhibit some degree of compressive flow in the plane of the film, and (3) the maximum plastic strain values are reasonably small. We also observe that most grains which underwent plastic flow exhibit much lower elastic strains than the mesh averages (Table 5.5), indicating some degree of load shedding to stiffer grains.

Table 5.5: Stress and strain tensors for the edge-constrained Cu thin film model heated from 25°C obtained from Eqs. (5-4 & 5) and the finite element model. The terms in parentheses denote standard deviations.

Parameter	Eqs. (5-4 & 5)	ABAQUS-CAE
Thermal strain , ε_{ij}^{Th}	$\begin{bmatrix} 418 & 0 & 0 \\ 0 & 418 & 0 \\ 0 & 0 & 418 \end{bmatrix}$	$\begin{bmatrix} 418 & 0 & 0 \\ 0 & 418 & 0 \\ 0 & 0 & 418 \end{bmatrix}$
Boundary constraint strain, $\varepsilon_{ij}^{B.C.}$	$\begin{bmatrix} 430 & 0 & 0 \\ 0 & -418 & 0 \\ 0 & 0 & -418 \end{bmatrix}$	-
Total Strain $(\varepsilon_{ij}^{Th} + \varepsilon_{ij}^{B.C.})$; $\bar{\varepsilon}_{ij}$	$\begin{bmatrix} 848 & 0 & 0 \\ 0 & 0 & 0 \\ 0 & 0 & 0 \end{bmatrix}$	$\begin{bmatrix} 892(110) & 0(0) & 0(0) \\ 0(0) & -1(90) & -3(36) \\ 0(0) & -3(36) & 0(86) \end{bmatrix}$
Stress σ_{ij}; $\bar{\sigma}_{ij}$ (MPa)	$\begin{bmatrix} 0 & 0 & 0 \\ 0 & -74 & 0 \\ 0 & 0 & -74 \end{bmatrix}$	$\begin{bmatrix} 0(5) & 0(0) & 0(5) \\ 0(0) & -76(10) & 0 \\ 0(5) & 0 & -74(10) \end{bmatrix}$

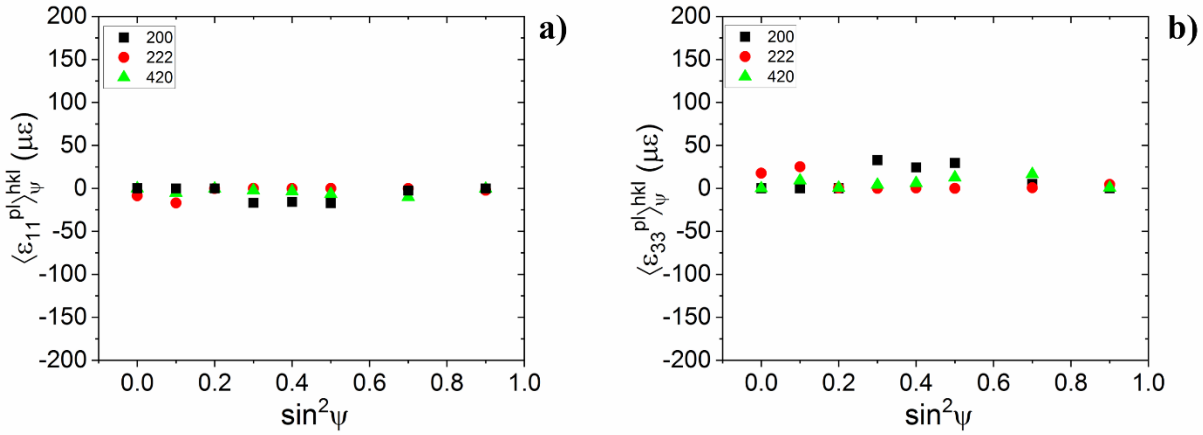

Figure 5.8: ψ-volume averages of plastic strain values in sample coordinates, $\langle \varepsilon_{11}^{pl} \rangle_{\psi}^{hkl}$ (a) and $\langle \varepsilon_{33}^{pl} \rangle_{\psi}^{hkl}$ (b) for the ψ -ensembles diffracting into the 200, 222 & 420 reflections.

Table 5.6: Plastic and elastic strain tensors for the highest deformed grains in the edge-constrained Cu thin film model. The grain in the last row is fully elastic and is included for comparison.

Grain Position #	Reflection, ψ (°)	$\langle \varepsilon_{ij}^{pl} \rangle$ (με)	$\langle \varepsilon_{ij}^{el} \rangle$ (με)
4	200, 33.21	$\begin{bmatrix} 202 & 0 & 0 \\ 0 & -106 & -56 \\ 0 & -56 & -95 \end{bmatrix}$	$\begin{bmatrix} 821 & 0 & 0 \\ 0 & -54 & -49 \\ 0 & -49 & 134 \end{bmatrix}$
63	200, 33.21	$\begin{bmatrix} 182 & 0 & 0 \\ 0 & -90 & 41 \\ 0 & 41 & -92 \end{bmatrix}$	$\begin{bmatrix} 828 & 0 & 0 \\ 0 & -58 & 42 \\ 0 & 42 & 108 \end{bmatrix}$
226	200, 39.23	$\begin{bmatrix} 134 & 0 & 0 \\ 0 & -53 & -39 \\ 0 & -39 & -81 \end{bmatrix}$	$\begin{bmatrix} 731 & 0 & 0 \\ 0 & 59 & -54 \\ 0 & -54 & 132 \end{bmatrix}$
251	200, 39.23	$\begin{bmatrix} 152 & 0 & 0 \\ 0 & -44 & -23 \\ 0 & -23 & -108 \end{bmatrix}$	$\begin{bmatrix} 772 & 0 & 0 \\ 0 & 9 & -22 \\ 0 & -22 & 71 \end{bmatrix}$
75	200, 45	$\begin{bmatrix} 85 & 0 & 0 \\ 0 & -21 & -16 \\ 0 & -16 & -63 \end{bmatrix}$	$\begin{bmatrix} 701 & 0 & 0 \\ 0 & 111 & -32 \\ 0 & -32 & 40 \end{bmatrix}$
125	200, 45	$\begin{bmatrix} 116 & 0 & 0 \\ 0 & -66 & -43 \\ 0 & -43 & -50 \end{bmatrix}$	$\begin{bmatrix} 721 & 0 & 0 \\ 0 & -32 & -63 \\ 0 & -63 & 184 \end{bmatrix}$
305	200, 45	$\begin{bmatrix} 165 & 0 & 0 \\ 0 & -77 & 19 \\ 0 & 19 & -88 \end{bmatrix}$	$\begin{bmatrix} 722 & 0 & 0 \\ 0 & 0 & 11 \\ 0 & 11 & 149 \end{bmatrix}$
153	222, 18.43	$\begin{bmatrix} 204 & 0 & 0 \\ 0 & -40 & 34 \\ 0 & 34 & -164 \end{bmatrix}$	$\begin{bmatrix} 930 & 0 & 0 \\ 0 & 69 & 67 \\ 0 & 67 & -111 \end{bmatrix}$
222	420, 26.57	$\begin{bmatrix} 0 & 0 & 0 \\ 0 & 0 & 0 \\ 0 & 0 & 0 \end{bmatrix}$	$\begin{bmatrix} 1147 & 0 & 0 \\ 0 & -64 & 11 \\ 0 & 11 & -168 \end{bmatrix}$

5.3.2.2.2- Stress Distribution in Sample Coordinates

Finite element analysis of our model yielded the local stress/strain components for each node in the sample coordinate system. In order to simplify the analysis and match it to the

diffraction measurements we computed four types of average stress tensor terms from these local values [74]:

a) **Grain average stress tensor, $\langle \boldsymbol{\sigma_{ij}} \rangle_i$:** the average stress tensor within a particular, i^{th}, grain obtained by averaging stresses at each node within that grain.
b) **ψ-volume average stress tensor, $\langle \boldsymbol{\sigma_{ij}} \rangle_{\psi}^{\boldsymbol{hkl}}$:** the average stress tensor within a particular ψ-volume for a given reflection obtained by averaging the stress tensor of all grains in the diffraction condition at the designated ψ for the given reflection.
c) **Reflection average stress tensor, $\langle \boldsymbol{\sigma_{ij}} \rangle^{\boldsymbol{hkl}}$**: the average stress tensor where the average was taken over all grains diffracting at all ψ-tilts for a particular reflection, *hkl*.
d) **Global average stress tensor, $\bar{\boldsymbol{\sigma}}_{\boldsymbol{ij}}$:** the average stress tensor for the entire sample volume, where the average was taken over all grains in the model. $\bar{\sigma}_{ij}$ of the current model is listed in Table 5.5.

In Fig. 5.9, we plot the grain average stress tensors along in-plane[29] and normal sample axes,$\vec{S}_3, \vec{S}_1$; $\langle \sigma_{33} \rangle_{i,\psi}, \langle \sigma_{11} \rangle_{i,\psi}$, respectively, for all reflections as a function of $\sin^2\psi$. In these plots, the corresponding ψ-volume averages $\langle \sigma_{ij} \rangle_{\psi}^{hkl}$ and their standard deviations are also shown. These average stresses contain contributions from Heyn stresses caused by elastic and (minimal) plastic incompatibility. These terms can be obtained from:

$$\langle \sigma_{ij} \rangle_i^* = \langle \sigma_{ij} \rangle_i - \bar{\sigma}_{ij} \quad \text{Eq. (5-6-a)}$$

$$\langle \sigma_{ij} \rangle_{\psi}^{*,hkl} = \langle \sigma_{ij} \rangle_{\psi}^{hkl} - \bar{\sigma}_{ij} \quad \text{Eq. (5-6-b)}$$

[29] The stress values and distributions for $\langle \sigma_{22} \rangle_i$ were similar to $\langle \sigma_{33} \rangle_i$.

For the out-of-plane direction, $\vec{S}_1$, the global average normal stress must be zero, $\bar{\sigma}_{11} \equiv 0$. Consequently, all stress terms in this direction are Heyn stresses: $\langle\sigma_{11}\rangle_i = \langle\sigma_{11}\rangle_i^*$, $\langle\sigma_{ij}\rangle_\psi^{hkl} = \langle\sigma_{ij}\rangle_\psi^{*,hkl}$. The stress values plotted in Fig. 5.9 show that, for the in-plane directions, $\vec{S}_2, \vec{S}_3$, the grain averaged Heyn stresses can be up to 40% of the global average constraint stress. The ψ-volume averages of the stress components, $\langle\sigma_{ij}\rangle_\psi^{hkl}$, are closer to the global average stresses, $\bar{\sigma}_{ij}$. However, $\langle\sigma_{ij}\rangle_\psi^{hkl}$ can be up to 15% different from $\bar{\sigma}_{ij}$, especially for the 200 and 222 reflections. Consequently, such volumes cannot be considered representative volume elements (RVE). For the 420 reflection, on the other hand, $\langle\sigma_{ij}\rangle_\psi^{420}$ were within a few percent of $\bar{\sigma}_{ij}$ for all ψ.

In Table 5.7 the reflection average stress tensors, $\langle\sigma_{ij}\rangle^{hkl}$, are listed for the 200, 222, and 420 reflections. We observe that $\langle\sigma_{ij}\rangle^{hkl}$ for all three reflections are quite close to the global average stress tensor, $\bar{\sigma}_{ij}$ shown in Table 5.5. Thus, to precision within the error of typical diffraction measurements, the Heyn stresses were averaged out from all three (mutually exclusive) reflection volumes, V_{hkl}. From this perspective V_{hkl} can be considered RVEs. We next investigate if the diffraction stress analysis formalism, which forces a linear least-squares average on the strains along the diffraction vectors of various ψ–volumes, yields correct stress values when applied to a sample that contains such heterogeneous stress states.

Table 5.7: Reflection average stress tensors, $\langle \sigma_{ij} \rangle^{hkl}$, for the 200, 222, and 420 reflections. The terms in parentheses denote standard deviations.

$\langle \sigma_{ij} \rangle^{200}$ (MPa)	$\langle \sigma_{ij} \rangle^{222}$ (MPa)	$\langle \sigma_{ij} \rangle^{420}$ (MPa)
$\begin{bmatrix} 1(5) & 0(0) & 0(5) \\ 0 & -70(8) & 0 \\ 0(5) & 0 & -78(10) \end{bmatrix}$	$\begin{bmatrix} 1(5) & 0(0) & -1(5) \\ 0 & -78(10) & 0 \\ -1(5)(0) & 0 & -75(9) \end{bmatrix}$	$\begin{bmatrix} 0(5) & 0(0) & -1(5) \\ 0 & -74(9) & 0 \\ -1(5)(0) & 0 & -76(10) \end{bmatrix}$

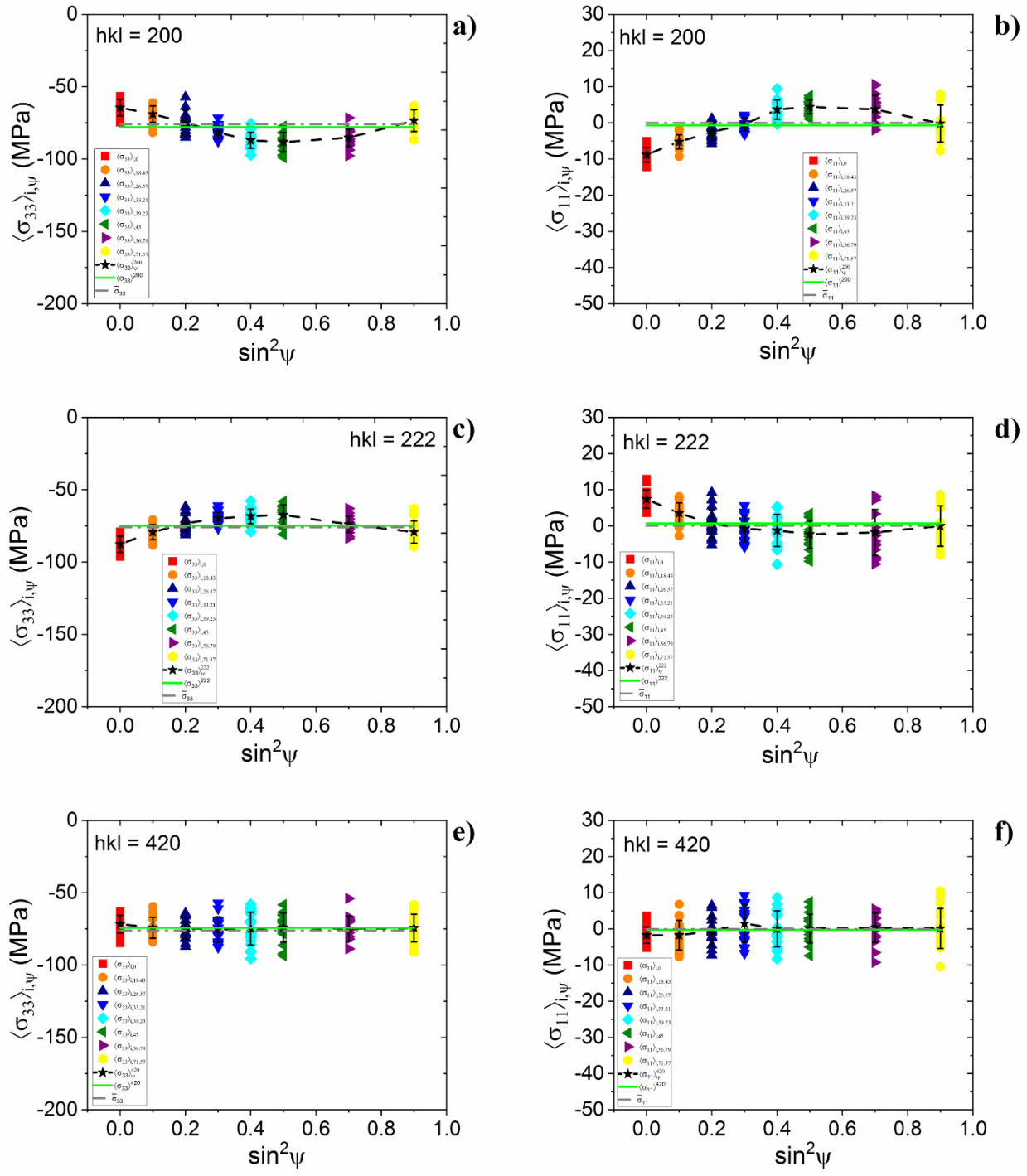

Figure 5.9: The grain stress averaged values along in-plane (a, c, e) and normal (b, d, f) sample axes; $\langle \sigma_{33} \rangle_{i,\psi}$, $\langle \sigma_{11} \rangle_{i,\psi}$, respectively, for all reflections as a function of $\sin^2\psi$.

5.3.2.2.3-Diffraction Strain/Stress Analysis

To simulate the diffraction stress analysis for our virtual sample we computed the average strain for each grain in the model, $\langle \varepsilon'_{11,\psi} \rangle_{i,\psi}$, by substituting its average strain tensor obtained from the finite element model into Eq. (1-11). This yielded the $\langle \varepsilon'_{11,\psi} \rangle_{i,\psi}^{Cu}$ $vs. \sin^2 \psi$ plots shown in Figs. 5.6-a, c & e. We also computed the Heyn interaction strains, $\langle \varepsilon'_{11,\psi} \rangle_{i,\psi}^{*-Cu}$, for each grain from:

$$\langle \varepsilon'_{11,\psi} \rangle_{i,\psi}^{*-Cu} = \langle \varepsilon'_{11,\psi} \rangle_{i,\psi}^{Cu} - \langle \varepsilon'_{11,\psi} \rangle_{i,\psi}^{0-Cu} \qquad \text{Eq. (5-7)}$$

Here ε_{ψ}^{0} is the strain at the particular ψ-angle for the equivalent isotropic Cu slab subjected to edge constraint during heating[30]. $\langle \varepsilon'_{11,\psi} \rangle_{i,\psi}^{*-Cu}$ $vs. \sin^2 \psi$ plots are shown in Figs. 5.6-b, d & f.

To obtain the reflection average stress, $\langle \sigma_{33}^{D} \rangle^{hkl}$, we used Eq. (5-1-b), the slopes of least squares lines fitted to the $\langle \varepsilon'_{11,\psi} \rangle_{i,\psi}^{Cu}$ $vs. \sin^2 \psi$ data for each reflection, and diffraction elastic constants at Voigt, Reuss, Kröner, and Neerfeld-Hill limits shown in Table 5.8. These results are shown in Table 5.9.

[30] This is computed by substituting the strain tensor for the equivalent isotropic Cu slab (Table 5.5) into Eq. (1-11).

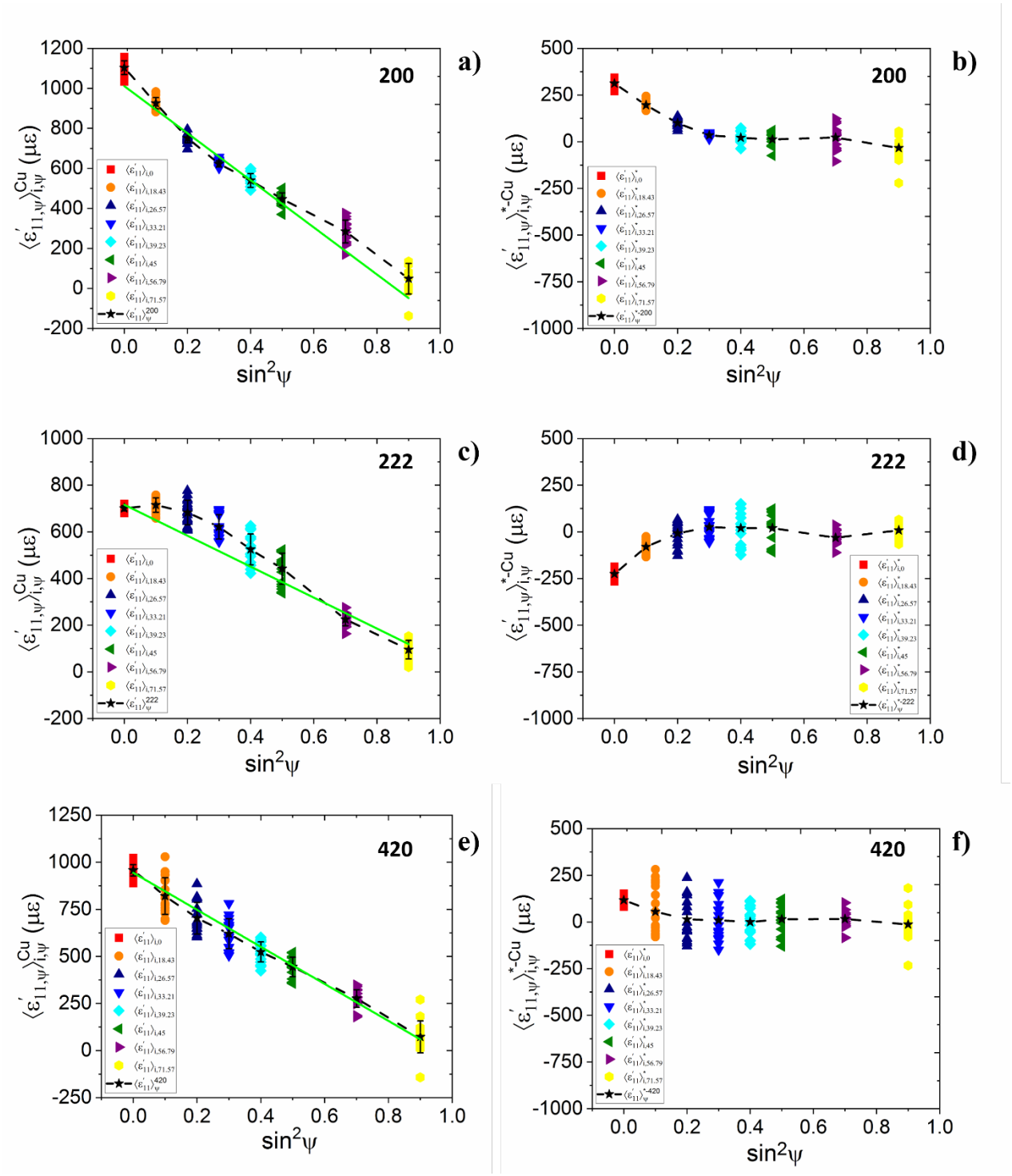

Figure 5.10: $\langle \varepsilon'_{11,\psi} \rangle_{i,\psi}^{Cu}$ *vs.* $sin^2\psi$ (a, c, e) and $\langle \varepsilon'_{11,\psi} \rangle_{i,\psi}^{*-Cu}$ *vs.* $sin^2\psi$ (b, d, f) plots for studied reflections of the edge constrained Cu film at incipient plastic flow.

Table 5.8: Diffraction Elastic Constants of non-textured polycrystalline Cu at various limits.

$(TPa)^{-1}$	hkl	Voigt	Reuss	Neer.-Hill	Kröner
$\frac{-\boldsymbol{v}}{\boldsymbol{E}}(\boldsymbol{S_1})$	200	2.24	6.28	4.26	3.73
$\frac{-\boldsymbol{v}}{\boldsymbol{E}}(\boldsymbol{S_1})$	222	2.24	1.40	1.82	1.93
$\frac{-\boldsymbol{v}}{\boldsymbol{E}}(\boldsymbol{S_1})$	420	2.24	3.94	3.09	2.87
$\frac{\boldsymbol{1+v}}{\boldsymbol{E}}\left(\frac{\boldsymbol{S_2}}{\boldsymbol{2}}\right)$	200	9.17	21.28	15.23	13.63
$\frac{\boldsymbol{1+v}}{\boldsymbol{E}}\left(\frac{\boldsymbol{S_2}}{\boldsymbol{2}}\right)$	222	9.17	6.65	7.86	8.24
$\frac{\boldsymbol{1+v}}{\boldsymbol{E}}\left(\frac{\boldsymbol{S_2}}{\boldsymbol{2}}\right)$	420	9.17	14.26	11.73	11.04

Table 5.9: The average stresses obtained from simulated diffraction analysis of the plots shown in Fig. 5.10.

$\langle\sigma_{33}^{D}\rangle^{hkl}$ (MPa)	Voigt	Reuss	Neer.-Hill	Kröner
200	-119 ± 6	-51 ± 3	-71 ± 4	-80 ± 5
222	-72 ± 7	-100 ± 8	-84 ± 8	-81 ± 7
420	-107 ± 4	-69 ± 2	-84 ± 3	-89 ± 3

Comparing Tables 5.7 & 9, we observe that, while the stress values obtained from diffraction analysis, $\langle \sigma_{33}^{D} \rangle^{hkl}$, using the Kröner and Neerfeld-Hill limits[31] for all three reflections are close to the expected average stress values in the sample coordinates: they are, in general, slightly higher.

To further investigate this issue we analyzed the plots in Figs. 5.10-a, c & e in terms of strain in the sample coordinates using Eq. (5-1-a). Table 5.10 lists the reflection average strain values, $\langle \varepsilon_{33}^{D} \rangle^{hkl}$, $\langle \varepsilon_{11}^{D} \rangle^{hkl}$, obtained directly from the slopes and intercepts of these plots. We also list the arithmetic averages of these terms, $\langle \varepsilon_{11} \rangle^{hkl}$, $\langle \varepsilon_{33} \rangle^{hkl}$, computed from the average strains in the sample coordinates for grains belonging to particular reflections. The averages obtained from diffraction analysis are different from the arithmetic averages in real space. In particular, while the real space average strains in the direction of the film normal, $\langle \varepsilon_{11} \rangle^{hkl}$, are almost identical for all three reflections and the model average, $\bar{\varepsilon}_{11}$, the magnitudes of diffraction averages of this strain term reflect the anisotropic compliances associated with these reflections: the stiffest direction, [222], shows the smallest strain, while the most compliant, [200], has the highest elastic deformation. The differences in the in-plane strain terms, $\langle \varepsilon_{33}^{D} \rangle^{hkl}$ and $\langle \varepsilon_{33} \rangle^{hkl}$ for all reflections probably arise due to the forced linear fit on non-linear $\langle \varepsilon'_{11,\psi} \rangle_{i,\psi}^{Cu}$ $vs.\sin^2\psi$ data, where the non-linearities are caused primarily by Heyn stresses arising in response to elastic incompatibility.

[31] Voigt and Reuss limits are limiting cases and are not physical. Thus we will not discuss these results. They are included for completeness.

We note that the uncertainty values for the diffraction values are not directly comparable to those associated with real space values. The former are "fit" errors, reflecting the inadequacy of the linear model; the latter describe real population dispersions.

Table 5.10: The average strains in sample coordinates obtained from simulated diffraction analysis of the plots shown in Fig. 5.10. The averages for the reflection-ensembles in real space are also included, along with the model averages.

Reflection / Strain term	Isotropic (Eq. 5-4)	Model average	200	222	420
$\langle \varepsilon_{33}^{D} \rangle^{hkl} (\mu\varepsilon)$	-	-	-81±21	44±21	-27±23
$\langle \varepsilon_{11}^{D} \rangle^{hkl} (\mu\varepsilon)$	-	-	1009±9	790±9	-919±10
$\langle \varepsilon_{33} \rangle^{hkl} (\mu\varepsilon)$	0	0±82	44±95	-30±72	5±85
$\langle \varepsilon_{11} \rangle^{hkl} (\mu\varepsilon)$	848	892±110	889±120	872±120	890±106

5.3.2.3- Pervasive Plastic Deformation

In this simulation, the mesh was heated from room temperature to 100°C. The expected strain and stress tensors for all points, $P(x, y, z)$, in an equivalent isotropic Cu thin film for elastoplastic loading (Eqs. (5-4 & 5)) are presented in Table 5.11. In this table, numerical averages of the stress and strain tensors, $\bar{\sigma}_{ij}, \bar{\varepsilon}_{ij}$ and the standard deviations for the model parameters are also tabulated. The analytical calculations were carried out assuming that the material is fully elastically loaded. Since all of the grains deformed plastically in this model, there is no agreement between the analytical calculations and finite element results.

Table 5.11: Stress and strain tensors for the edge-constrained Cu thin film model heated from 25°C obtained from Eqs. (5-4 & 5) and the finite element model. The terms in parentheses denote standard deviations.

Parameter	Eqs. (5-4 & 5)	ABAQUS-CAE
Thermal strain , ε_{ij}^{Th}	$\begin{bmatrix} 1253 & 0 & 0 \\ 0 & 1253 & 0 \\ 0 & 0 & 1253 \end{bmatrix}$	$\begin{bmatrix} 1253 & 0 & 0 \\ 0 & 1253 & 0 \\ 0 & 0 & 1253 \end{bmatrix}$
Boundary constraint strain, $\varepsilon_{ij}^{B.C.}$	$\begin{bmatrix} 1290 & 0 & 0 \\ 0 & -1253 & 0 \\ 0 & 0 & -1253 \end{bmatrix}$	-
Total elastic strain $(\varepsilon_{ij}^{Th} + \varepsilon_{ij}^{B.C.})$; $\bar{\varepsilon}_{ij}$	$\begin{bmatrix} 2543 & 0 & 0 \\ 0 & 0 & 0 \\ 0 & 0 & 0 \end{bmatrix}$	$\begin{bmatrix} 1959(312) & 0(0) & 0(0) \\ 0(0) & 640(226) & 0(34) \\ 0(0) & 0(34) & 653(249) \end{bmatrix}$
Stress σ_{ij}; $\bar{\sigma}_{ij}$ (MPa)	$\begin{bmatrix} 0 & 0 & 0 \\ 0 & -222 & 0 \\ 0 & 0 & -222 \end{bmatrix}$	$\begin{bmatrix} -1(4) & 0(0) & 0(5) \\ 0(0) & -105(10) & 0 \\ 0(5) & 0 & -105(10) \end{bmatrix}$
Plastic strain (ε_{ij}^{Pl})	-	$\begin{bmatrix} 1333(656) & 0(2) & 0(0) \\ 0(2) & -659(350) & 6(231) \\ 0(0) & 6(231) & -674(344) \end{bmatrix}$

In Fig. 5.11, we plot the average plastic strains in the plane of the film, $\langle \varepsilon_{33}^{pl} \rangle_{\psi}^{hkl}$ and out of the plane of the film $\langle \varepsilon_{11}^{pl} \rangle_{\psi}^{hkl}$ as a function of $sin^2\psi$ for all reflections. We observe that: (1) average plastic strains for all ψ-ensembles are finite. (2) the grain populations oriented to diffract into the 200 reflection for ψ= 0° exhibit a small amount of plastic strains. (3) all grains exhibit some degree of compressive flow in the plane of the film. (4) average plastic strain for grains oriented to diffract into the 420 reflection is approximately equal to the global average plastic strain. In other words, uniform plastic deformation is observed for the grains that belong to the ψ-ensembles of 420 reflection.

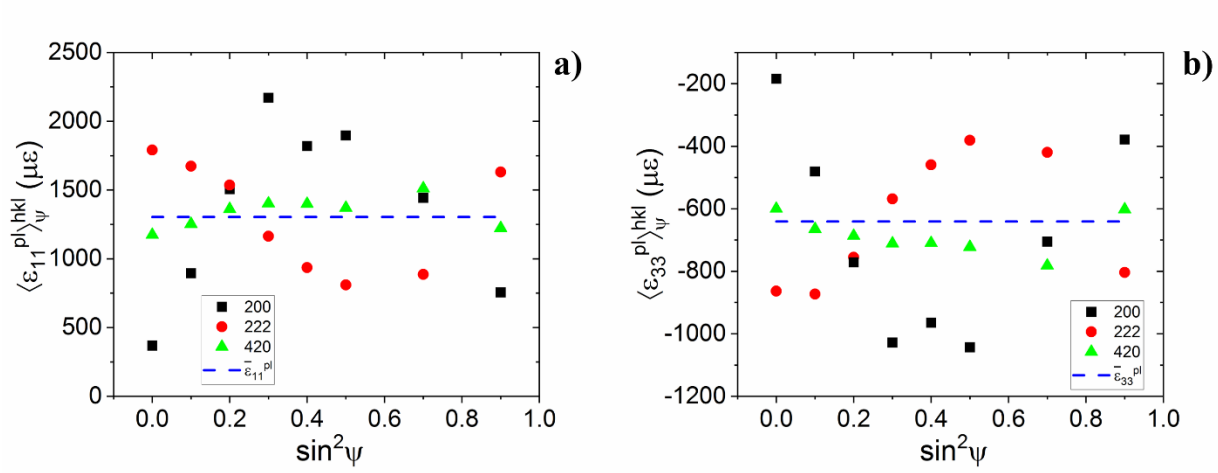

Figure 5.11: ψ-volume averages of plastic strain values in sample coordinates, $\langle\varepsilon_{11}^{pl}\rangle_{\psi}^{hkl}$ (a) and $\langle\varepsilon_{33}^{pl}\rangle_{\psi}^{hkl}$ (b) for the ψ -ensembles diffracting into the 200, 222 & 420 reflections.

5.3.2.3.1- Stress Distribution in Sample Coordinates

Finite element analysis of our model yielded the local strain/stress components for each node in the sample coordinate system. We computed four types of average stress tensor terms from these local values as it was summarized in Section 5.3.2.2.1.

In Fig. 5.12, we plot the grain average stress tensors along in-plane and normal sample axes, $\vec{S}_3, \vec{S}_1$; $\langle\sigma_{33}\rangle_{i,\psi}, \langle\sigma_{11}\rangle_{i,\psi}$, respectively, for all reflections as a function of $\sin^2\psi$. The corresponding ψ-volume averages $\langle\sigma_{ij}\rangle_{\psi}^{hkl}$ and their standard deviations are also plotted in these figures. These average stresses contain contributions from Heyn stresses caused by elastic and plastic incompatibility and they can be obtained from Eqs. (5-6-a & b). For the out-of-plane direction, $\vec{S}_1$, the global average normal stress must be zero. Consequently, all stress terms in this direction are Heyn stresses. The stress values plotted in Fig. 5.12 shows that, the grain average Heyn stresses can be up to 20% of the global average constrain stress for the in-plane directions,

$\vec{S}_2, \vec{S}_3$. The ψ-volume averages of the stress components, $\langle\sigma_{ij}\rangle_{\psi}^{hkl}$, are closer to the global average stresses, $\bar{\sigma}_{ij}$. However, $\langle\sigma_{ij}\rangle_{\psi}^{hkl}$ can be up to 10% different from $\bar{\sigma}_{ij}$, especially for 200 reflections. Consequently, such volumes cannot be considered as a representative volume element (RVE). For 222 and 420 reflection, on the other hand, $\langle\sigma_{ij}\rangle_{\psi}^{222}$ and $\langle\sigma_{ij}\rangle_{\psi}^{420}$ were within a few percent of $\bar{\sigma}_{ij}$ for all ψ.

In Table 5.12, the reflection average stress tensors, $\langle\sigma_{ij}\rangle^{hkl}$, are listed for 200, 222 and 420 reflections. We observe that $\langle\sigma_{ij}\rangle^{hkl}$ are similar to the global average stress tensor, $\bar{\sigma}_{ij}$ shown in Table 5.11. Thus, Heyn stresses were averaged out from all three mutually exclusive reflection volumes, V_{hkl}, within the error of typical diffraction measurements. From this perspective, V_{hkl} can be considered RVEs.

We next investigate if the diffraction stress analysis formalism yields the correct stress values when applied to a sample containing heterogeneous stress states.

Table 5.12: Reflection average stress tensors, $\langle\boldsymbol{\sigma_{ij}}\rangle^{\boldsymbol{hkl}}$, for the 200, 222, and 420 reflections. The terms in parentheses denote standard deviations.

$\langle\boldsymbol{\sigma_{ij}}\rangle^{\mathbf{200}}$ **(MPa)**	$\langle\boldsymbol{\sigma_{ij}}\rangle^{\mathbf{222}}$ **(MPa)**	$\langle\boldsymbol{\sigma_{ij}}\rangle^{\mathbf{420}}$ **(MPa)**
$\begin{bmatrix} -1(4) & 0(0) & 0(0) \\ 0 & -105(9) & 0(5) \\ 0(0) & 0(5) & -105(10) \end{bmatrix}$	$\begin{bmatrix} 1(4) & 0(0) & 0(0) \\ 0 & -106(9) & 0(5) \\ 0(0) & 0(5) & -105(9) \end{bmatrix}$	$\begin{bmatrix} -1(4) & 0(0) & 0(0) \\ 0 & -104(9) & 0(5) \\ 0(0) & 0(5) & -106(9) \end{bmatrix}$

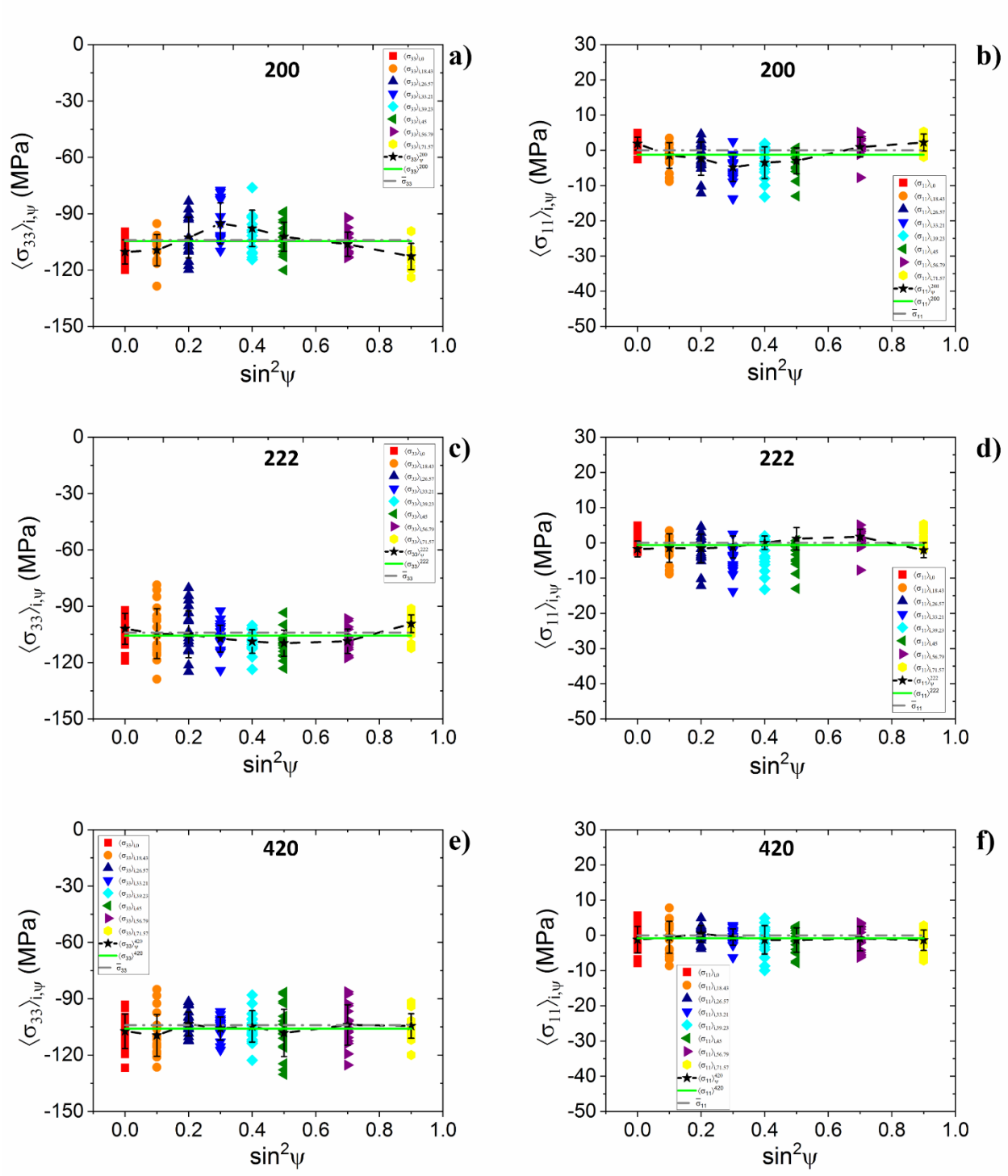

Figure 5.12: The grain stress averaged values along in-plane (a, c, e) and normal (b, d, f) sample axes; $\langle\sigma_{33}\rangle_{i,\psi}$, $\langle\sigma_{11}\rangle_{i,\psi}$, respectively, for all reflections as a function of $\sin^2\psi$.

5.3.2.3.2- Diffraction Strain/Stress Analysis

The average strain for each grain in the model, $\langle \varepsilon'_{11,\psi} \rangle_{i,\psi}$, were computed by substituting its average strain tensor obtained from the finite element model into Eq. (1-11). This yielded the $\langle \varepsilon'_{11,\psi} \rangle_{i,\psi}^{Cu}$ $vs. \sin^2 \psi$ plots shown in Figs. 5.13.a, c & e. For each grain, we also computed the Heyn interaction strains, $\langle \varepsilon'_{11,\psi} \rangle_{i,\psi}^{*-Cu}$, from Eq. (5-7). $\langle \varepsilon'_{11,\psi} \rangle_{i,\psi}^{*-Cu}$ $vs. \sin^2 \psi$ plots are shown in Figs. 5.13-b, d & f.

To obtain the reflection average stress, $\langle \sigma_{33}^{D} \rangle^{hkl}$, we used Eq. (5-1-b), the slopes of least squares lines fitted to the $\langle \varepsilon'_{11,\psi} \rangle_{i,\psi}^{Cu}$ $vs. \sin^2 \psi$ data for each reflection, and diffraction elastic constants at Voigt, Reuss, Kröner, and Neerfeld-Hill limits shown in Table 5.8. These results are shown in Table 5.13.

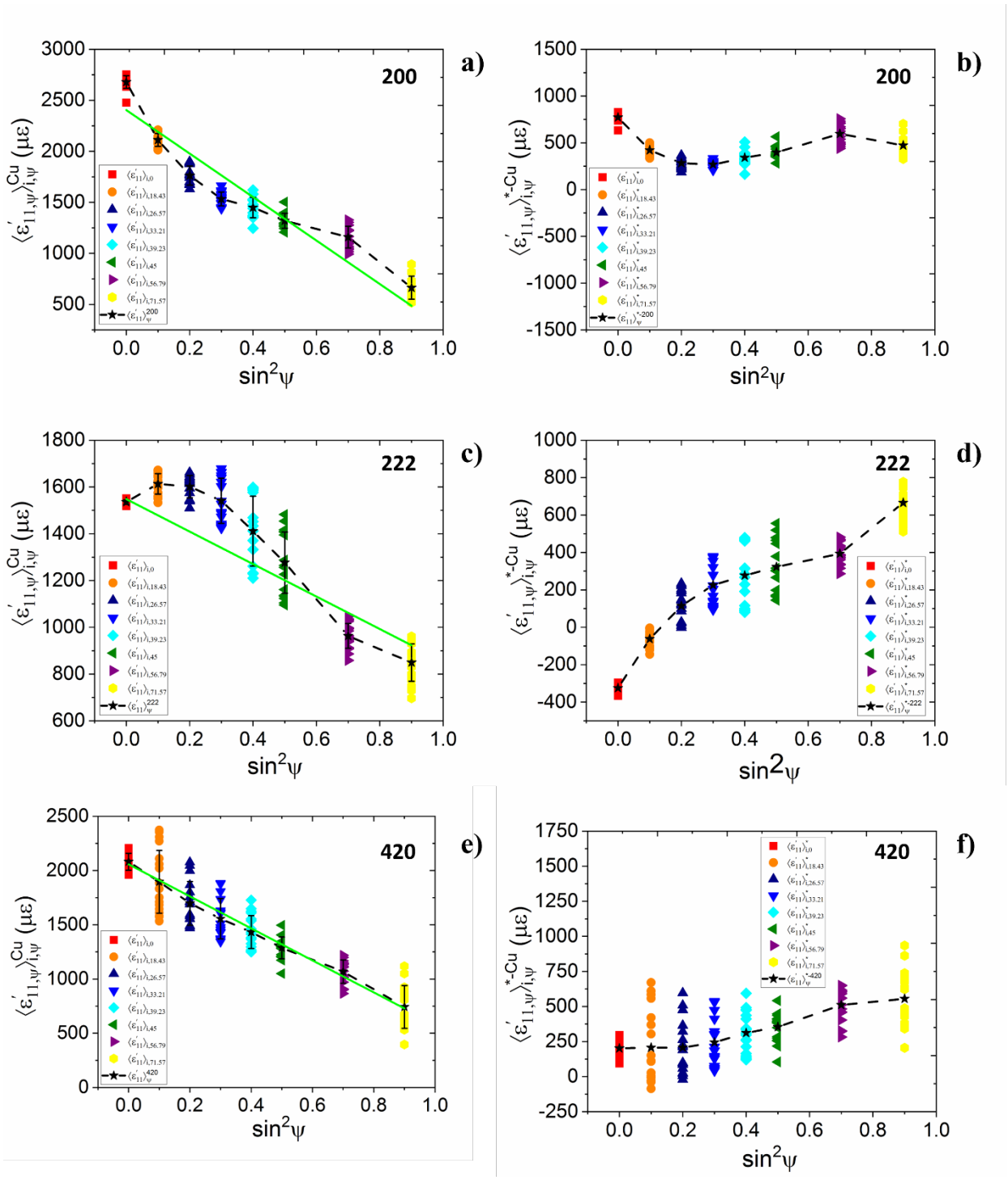

Figure 5.13: $\langle \varepsilon'_{11,\psi} \rangle_{i,\psi}^{Cu}$ *vs.* $sin^2\,\psi$ (a, c, e) and $\langle \varepsilon'_{11,\psi} \rangle_{i,\psi}^{*-Cu}$ *vs.* $sin^2\,\psi$ (b, d, f) plots for studied reflections of the Cu mesh under plastic loading.

Table 5.13: The average stresses obtained from simulated diffraction analysis of the plots shown in Fig. 5.14.

$\langle \sigma_{33}^{D} \rangle^{hkl}$ (MPa)	Voigt	Reuss	Neer.-Hill	Kröner
200	-233 ± 35	-100 ± 15	-140 ± 20	-156 ± 22
222	-76 ± 16	-104 ± 21	-88 ± 17	-84 ± 17
420	-161 ± 8	-104 ± 4	-126 ± 4	-134 ± 5

Comparing Tables 5.12 & 13, we observe that the stress values obtained from diffraction analysis, $\langle \sigma_{33}^{D} \rangle^{hkl}$, obtained using the Kröner and Neerfeld-Hill limits for all three reflections, are different from the expected average stress values in the sample coordinates. The stiffest direction, [222] has the lowest $\langle \sigma_{33}^{D} \rangle^{222}$, whereas the most compliant direction, [200], has the highest $\langle \sigma_{33}^{D} \rangle^{200}$ values.

To further investigate this issue, Figs. 5.13-a, c & e were analyzed in terms of strains in the sample coordinates using Eq. (5-1-a). Table 5.14 lists the reflection average strain values, $\langle \varepsilon_{11}^{D} \rangle^{hkl}$, $\langle \varepsilon_{33}^{D} \rangle^{hkl}$, obtained directly from the slopes and intercepts of these plots. We also list the arithmetic averages of these terms, $\langle \varepsilon_{11} \rangle^{hkl}$, $\langle \varepsilon_{33} \rangle^{hkl}$, computed from the average strains in the sample coordinates for grains belonging to particular reflections. The averages obtained from diffraction analysis are different from the arithmetic averages in real space. The real space average strains in the direction of the film normal, $\langle \varepsilon_{11} \rangle^{hkl}$, are almost identical for all three reflections, and the model average, $\bar{\varepsilon}_{11}$. However, the magnitudes of diffraction averages of this strain term reflect the anisotropic compliances associated with these reflections: the stiffest direction, [222] shows the smallest strain, while the most compliant, [200] has the highest elastic deformation. The

differences in the in-plane strain terms, $\langle \varepsilon_{33}^{D} \rangle^{hkl}$ and $\langle \varepsilon_{33} \rangle^{hkl}$ for all reflections probably arise due to the forced linear fit on non-linear $\langle \varepsilon'_{11,\psi} \rangle_{i,\psi}^{Cu}$ $vs.\sin^2\psi$ data, where the non-linearities are caused primarily by Heyn stresses arising in response to elastic and plastic incompatibility.

Table 5.14: The average strains in sample coordinates obtained from simulated diffraction analysis of the plots shown in Fig. 5.14. The averages for the reflection-ensembles in real space are also included, along with the model averages.

Reflection / Strain term	Isotropic (Eq. 5-4)	Model average	200	222	420
$\langle \varepsilon_{33}^{D} \rangle^{hkl}$ $(\mu\varepsilon)$	-	-	273±303	854±138	581±50
$\langle \varepsilon_{11}^{D} \rangle^{hkl}$ $(\mu\varepsilon)$	-	-	2404±118	1548±23	2057±22
$\langle \varepsilon_{33} \rangle^{hkl}$ $(\mu\varepsilon)$	0	653±249	712±300	569±305	654±328
$\langle \varepsilon_{11} \rangle^{hkl}$ $(\mu\varepsilon)$	2543	1959±312	1895±548	1925±592	1960±106

5.3.2.3.2.1- Determination of Oscillations in $\langle \varepsilon'_{11,\psi} \rangle_{i,\psi}$ vs. $\sin^2\psi$

To check the significance of oscillations in $\langle \varepsilon'_{11,\psi} \rangle_{i,\psi}$ vs. $\sin^2\psi$; (1) We removed the first two ψ-ensemble points from $\langle \varepsilon'_{11,\psi} \rangle_{i,\psi}$ vs. $\sin^2\psi$ plots (2) We analyzed the plots for diffraction-averaged stress values. (3) the computed averaged stresses from these plots were compared with the ones calculated from $\langle \varepsilon'_{11,\psi} \rangle_{i,\psi}$ vs. $\sin^2\psi$ plots containing all ψ-ensembles. (4) If the change of the computed stress is within the error limit of the diffraction measurement, plots are called linear; if not, standard diffraction formalism cannot be used to analyze $\langle \varepsilon'_{11,\psi} \rangle_{i,\psi}$ vs. $\sin^2\psi$ plots. This analysis must be performed in all measurements because the agreement with the computed

average stresses is insufficient to prove the validity of a stress computation. Thus, we performed this analysis to our plastically deformed hypothetical Cu sample.

Comparing Tables 5.13 & 15, we observe that the stress values obtained from diffraction analysis after removal of first two ψ-ensembles, $\langle \sigma_{33}^{D} \rangle^{hkl}$, obtained using the Kröner and Neerfeld-Hill limits for all three reflections are different from the ones obtained from without removing the first two ψ-ensembles. The change of $\langle \sigma_{33}^{D} \rangle^{hkl}$ values for [222] and [200] directions can be up to 60% different whereas, for [420] direction, the change is around 15%. We conclude that $\langle \varepsilon'_{11,\psi} \rangle_{i,\psi}$ vs. $\sin^2 \psi$ for all three reflections show oscillatory behavior.

Table 5.15: The average stresses obtained from simulated diffraction analysis of the plots shown in Fig. 5.14 after removal of the first two ψ-ensemble points.

$\langle \sigma_{33}^{D} \rangle^{hkl}$ (MPa)	Voigt	Reuss	Neer.-Hill	Kröner
200	-150 ± 16	-65 ± 7	-90 ± 9	-101 ± 11
222	-129 ± 9	-177 ± 15	-150 ± 10	-143 ± 6
420	-141 ± 6	-91 ± 4	-111 ± 5	-118 ± 4

5.3.3- Free Expansion of Cu – W Virtual Sample

The final model utilizing the virtual single-layer polycrystalline thin film sample simulated the free thermal expansion of a two-phase Cu – W sample heated from RT to 90°C. These elements are mutually insoluble in each other. Consequently, the sample is essentially a mechanical mixture of the two sets of grains where the grains are connected across rigid boundaries normal to the film surfaces. When such a film is heated uniformly, the film boundaries are free to expand. However,

since the CTEs of Cu and W are very different, 16.7 vs. 4.6 ppm, respectively, grains belonging to the two-phases are expected to mutually constrain each other. In particular, in the direction of the film normal, $\vec{S}_1$, the W grains will constrain the Cu grains from expanding to their equilibrium heights, placing them in compression. Such constraints can result in plastic flow within the softer Cu grains. Concurrently, the Cu grains will pull the W grains past their equilibrium heights, placing them in tension. Since the yield point of W is much higher than Cu, there should be no plastic flow in the W grains. There will also be an in-plane constraint, resulting in Heyn stresses due to thermal and elastic incompatibility. Overall, we expect triaxial stress states in the grains of both phases, even though there will be no external forces or tractions on any of the film's boundaries. Consequently, the overall global averages of all stress components, $\bar{\sigma}_{ij}$, should be zero.

5.3.3.1- State of Stress in Sample Coordinates

Tables 5.16 & 17 show the global average stress and lattice strain[32] tensors and their distribution parameters. These averages were computed over all grains, both Cu and W, in the model. The minimum (MIN), maximum (MAX) values reflect the extrema in the relevant grain average stresses/strains. We observe that, as expected, all $\bar{\sigma}_{ij} = 0$. However, four stress terms, $\bar{\sigma}_{ii}$ and $\bar{\sigma}_{12}$ exhibit wide distributions. The full width (FW) of these in-plane stresses are quite large, indicating that some grains possess significant interaction stresses. Both the extrema and the dispersion of the out-of-plane normal stress, $\bar{\sigma}_{11}$, is much smaller, approximately half of the in-

[32] This average is the sum of thermal and elastic strains.

plane stresses. The out-of-plane shear stresses, $\bar{\sigma}_{j1}$, are zero with approximately zero dispersion. This is due to the isotropic CTEs of the (cubic) Cu and W grains.

Table 5.16: Global average stress tensor of the entire Cu – W film heated to 90°C and its dispersion parameters. The model contains 676 grains, 352 Cu, and 324 W. All values are in MPa.

(MPa)	$\bar{\sigma}_{11}$	$\bar{\sigma}_{22}$	$\bar{\sigma}_{33}$	$\bar{\sigma}_{23}$	$\bar{\sigma}_{13}$	$\bar{\sigma}_{12}$
Average	0	0	0	0	0	0
STD	28	55	55	28	0	0
FW	112	259	273	203	0	1
MAX	51	156	178	100	0	1
MIN	-61	-103	-95	-103	0	0

Table 5.17: Average lattice strain tensor of the entire Cu – W film heated to 90°C and its dispersion parameters. All values are in microstrain (με).

$(\mu\varepsilon)$	$\bar{\varepsilon}_{11}$	$\bar{\varepsilon}_{22}$	$\bar{\varepsilon}_{33}$	$\bar{\varepsilon}_{23}$	$\bar{\varepsilon}_{13}$	$\bar{\varepsilon}_{12}$
Average	300	374	370	0	0	-2
STD	38	105	107	0	0	57
FW	187	486	560	1	1	296
MAX	406	690	646	0	0	141
MIN	219	205	85	-1	0	-155

In contrast to the stress values, all lattice strain values are finite, as expected from thermal expansion. However, the two-phase film, consisting of cubic grains, exhibits anisotropic average thermal expansion; the out-of-plane normal strain, $\bar{\varepsilon}_{11}$, is larger than the in-plane strains. All average shear strains, $\bar{\varepsilon}_{ij,i\neq j} = 0$. Consequently, we can attribute the (average) anisotropic thermal expansion to the film geometry; the in-plane boundary conditions are equal to each other; $\bar{\varepsilon}_{33} = \bar{\varepsilon}_{22}$; $\bar{\varepsilon}_{23} = 0$, but the film can expand more out of the plane; $\bar{\varepsilon}_{11} = 1.14\ x\ \bar{\varepsilon}_{33}$.

Tables 5.18, 19 & 20 list the average stress, lattice strain, and plastic strain tensors in the Cu phase and their dispersion parameters. All normal stresses, $\bar{\sigma}_{ii}^{Cu}$, are finite and compressive while the shear stresses $\bar{\sigma}_{ij,i\neq j}^{Cu}$, are zero. The dispersion parameters for these shear stress components are much smaller than the corresponding values of the global stress tensor, $\bar{\sigma}_{ij}$.

The average normal lattice strains of the Cu phase, $\bar{\varepsilon}_{ii}^{Cu}$, are much larger, *2.5 to 4 x*, than the global average strains of the entire model, $\bar{\varepsilon}_{ii}$. The strain dispersions are also much larger in the Cu phase. In addition, while the average plastic strain for the Cu phase can be considered zero (Table 5.20), the dispersion parameters of the plastic strains show that some have significant plastic flow. We note that the average in-plane plastic shear strain and its dispersion is the largest component in this case.

Table 5.18: Average stress tensor for the Cu phase of the Cu – W film heated to 90°C and its dispersion parameters. This phase contains 352 grains. All values are in MPa.

(MPa)	$\bar{\sigma}_{11}^{Cu}$	$\bar{\sigma}_{22}^{Cu}$	$\bar{\sigma}_{33}^{Cu}$	$\bar{\sigma}_{12}^{Cu}$	$\bar{\sigma}_{13}^{Cu}$	$\bar{\sigma}_{23}^{Cu}$
Average	-24	-44	-44	0	0	-1
STD	13	24	24	0	0	23
FW	67	131	137	1	0	101
MAX	6	28	42	1	0	54
MIN	-61	-103	-95	0	0	-47

Table 5.19: Average lattice strain tensor for the Cu phase of the Cu – W film heated to 90°C and its dispersion parameters. All values are in microstrain (με).

	$\bar{\varepsilon}_{11}^{Cu}$	$\bar{\varepsilon}_{22}^{Cu}$	$\bar{\varepsilon}_{33}^{Cu}$	$\bar{\varepsilon}_{12}^{Cu}$	$\bar{\varepsilon}_{13}^{Cu}$	$\bar{\varepsilon}_{23}^{Cu}$
Average	1158	911	920	1	0	-9
STD	86	206	211	1	0	142
FW	612	1123	1329	4	2	868
MAX	1452	1539	1642	4	1	397
MIN	840	416	313	-1	0	-470

Table 5.20*:* Average plastic strain tensor for the Cu phase of the Cu – W film heated to 90°C and its dispersion parameters. All values are in microstrain (με).

	$\bar{\varepsilon}_{11}^{pl,Cu}$	$\bar{\varepsilon}_{22}^{pl,Cu}$	$\bar{\varepsilon}_{33}^{pl,Cu}$	$\bar{\varepsilon}_{12}^{pl,Cu}$	$\bar{\varepsilon}_{13}^{pl,Cu}$	$\bar{\varepsilon}_{23}^{pl,Cu}$
Average	-5	2	4	3	1	-14
STD	13	54	55	3	1	167
FW	142	581	587	17	5	1466
MAX	84	187	365	15	4	798
MIN	-58	-394	-222	-1	-1	-668

Tables 5.21 & 22 list the average stress and lattice strain tensors in the W phase and their dispersion parameters. The phase and grain average plastic strains in this phase were negligible. All normal stresses, $\bar{\sigma}_{ii}^{W}$, are finite and tensile; opposite in sign to the corresponding Cu phase-average stress terms. All shear stresses, $\bar{\sigma}_{ij,i\neq j}^{W}$, are zero. Comparing Tables 5.16, 18 & 21, we observe that the average normal phase stresses obey the average stress equilibrium condition [57]:

$$f_{Cu}\bar{\sigma}_{ii}^{Cu} + f_{W}\bar{\sigma}_{ii}^{W} = 0 \qquad \text{Eq. (5-8)}$$

The dispersion parameters for the phase-average W stress components are smaller than the corresponding values for the global stress tensor, $\bar{\sigma}_{ij}$.

Table 5.21: Average stress tensor for the W phase of the Cu – W film heated to 90°C and its dispersion parameters. This phase contains 324 grains. All values are in MPa.

(MPa)	$\bar{\sigma}_{11}^{W}$	$\bar{\sigma}_{22}^{W}$	$\bar{\sigma}_{33}^{W}$	$\bar{\sigma}_{12}^{W}$	$\bar{\sigma}_{13}^{W}$	$\bar{\sigma}_{23}^{W}$
Average	27	49	47	0	0	1
STD	10	35	38	0	0	34
FW	55	174	210	1	0	203
MAX	51	156	178	0	0	100
MIN	-4	-18	-32	0	0	-103

Table 5.22: Average lattice strain tensor for the W phase of the Cu – W film heated to 90°C and its dispersion parameters. All values are in microstrain (με).

	$\bar{\varepsilon}_{11}^{W}$	$\bar{\varepsilon}_{22}^{W}$	$\bar{\varepsilon}_{33}^{W}$	$\bar{\varepsilon}_{12}^{W}$	$\bar{\varepsilon}_{13}^{W}$	$\bar{\varepsilon}_{23}^{W}$
Average	301	373	370	0	0	1
STD	40	103	110	0	0	56
FW	210	523	648	1	1	335
MAX	425	690	734	0	0	165
MIN	215	168	85	-1	0	-170

Comparing Tables 5.17 & 22, we observe that the overall lattice strain tensor of the model is almost equal to the average lattice strain tensor of the W phase. This is expected since W is much stiffer than Cu. Since the average lattice strain tensors of the W and Cu grains are so

different, we expect the Cu grains to expand more toward their center, away from any neighboring W grains. Thus, the surface of such a sample should exhibit some roughness.

5.3.3.1.1- Phase-average Stress Components in Sample Coordinates Selected by Diffraction

Tables 5.18 & 21 listed phase-average stress tensors. Due to the phase-specific nature of diffraction, the intensity obtained from a given reflection measured at a given ϕ, ψ angle contains contributions only from the grain population of the ψ-ensemble of the particular phase. Thus, we need to add phase (Ph) superscripts to the grain average stress tensor, $\langle\sigma_{ij}\rangle_{i,\psi}^{Ph}$, the ψ-volume average stress tensor, $\langle\sigma_{ij}\rangle_{\psi}^{Ph-hkl}$, and reflection average stress tensor , $\langle\sigma_{ij}\rangle^{Ph-hkl}$, to specify the phase-dependency of these terms. Similar terms are defined for the corresponding strain averages. In Figs. 5.14 & 15, we plot the grain averages of the stress terms, $\langle\sigma_{11}\rangle_{i,\psi}^{Ph}$, $\langle\sigma_{33}\rangle_{i,\psi}^{Ph}$, of all grains for all ψ-tilts of all three reflections of the Cu and W phases ($Ph = Cu, W$). The solid symbols in these plots are the corresponding ψ-volume average stress values, $\langle\sigma_{11}\rangle_{\psi}^{Ph-hkl}$, $\langle\sigma_{33}\rangle_{\psi}^{Ph,-hkl}$. Their standard deviations are also marked. We see that, for each reflection, the ψ-volume average stress values are close to each other for all ψ. The reflection average stresses, Table 5.22, are close to the phase-average stress tensors. Thus, the reflection volumes can be considered representative volume elements for specific phases, but they **CANNOT BE REPRESENTATIVE** of the sample as a whole. This shows that these phase-specific average stresses are not macro-stresses or far-field stresses. They are pseudo-macro stresses.

Table 5.23: Reflection average stress tensors for the Cu and W phases of the Cu – W film heated to 90°C. The phase-average stress tensor is also included for ease of comparison. All values are in MPa.

Reflection	Cu-phase	W-phase
200	$\langle\sigma_{ij}\rangle^{Cu-200} = \begin{bmatrix} -23 & 0 & 0 \\ 0 & -43 & 0 \\ 0 & 0 & -42 \end{bmatrix}$	$\langle\sigma_{ij}\rangle^{W-200} = \begin{bmatrix} 27 & 0 & 0 \\ 0 & 49 & 0 \\ 0 & 0 & 48 \end{bmatrix}$
222	$\langle\sigma_{ij}\rangle^{Cu-222} = \begin{bmatrix} -24 & 0 & 0 \\ 0 & -45 & 0 \\ 0 & 0 & -45 \end{bmatrix}$	$\langle\sigma_{ij}\rangle^{W-222} = \begin{bmatrix} 26 & 0 & 0 \\ 0 & 50 & 0 \\ 0 & 0 & 43 \end{bmatrix}$
420	$\langle\sigma_{ij}\rangle^{Cu-420} = \begin{bmatrix} -24 & 0 & 0 \\ 0 & -44 & 0 \\ 0 & 0 & -44 \end{bmatrix}$	$\langle\sigma_{ij}\rangle^{W-420} = \begin{bmatrix} 27 & 0 & 0 \\ 0 & 49 & 0 \\ 0 & 0 & 48 \end{bmatrix}$
	$\bar{\sigma}_{ij}^{Cu} = \begin{bmatrix} -24 & 0 & 0 \\ 0 & -44 & 0 \\ 0 & 0 & -44 \end{bmatrix}$	$\bar{\sigma}_{ij}^{W} = \begin{bmatrix} 27 & 0 & 0 \\ 0 & 49 & 0 \\ 0 & 0 & 47 \end{bmatrix}$

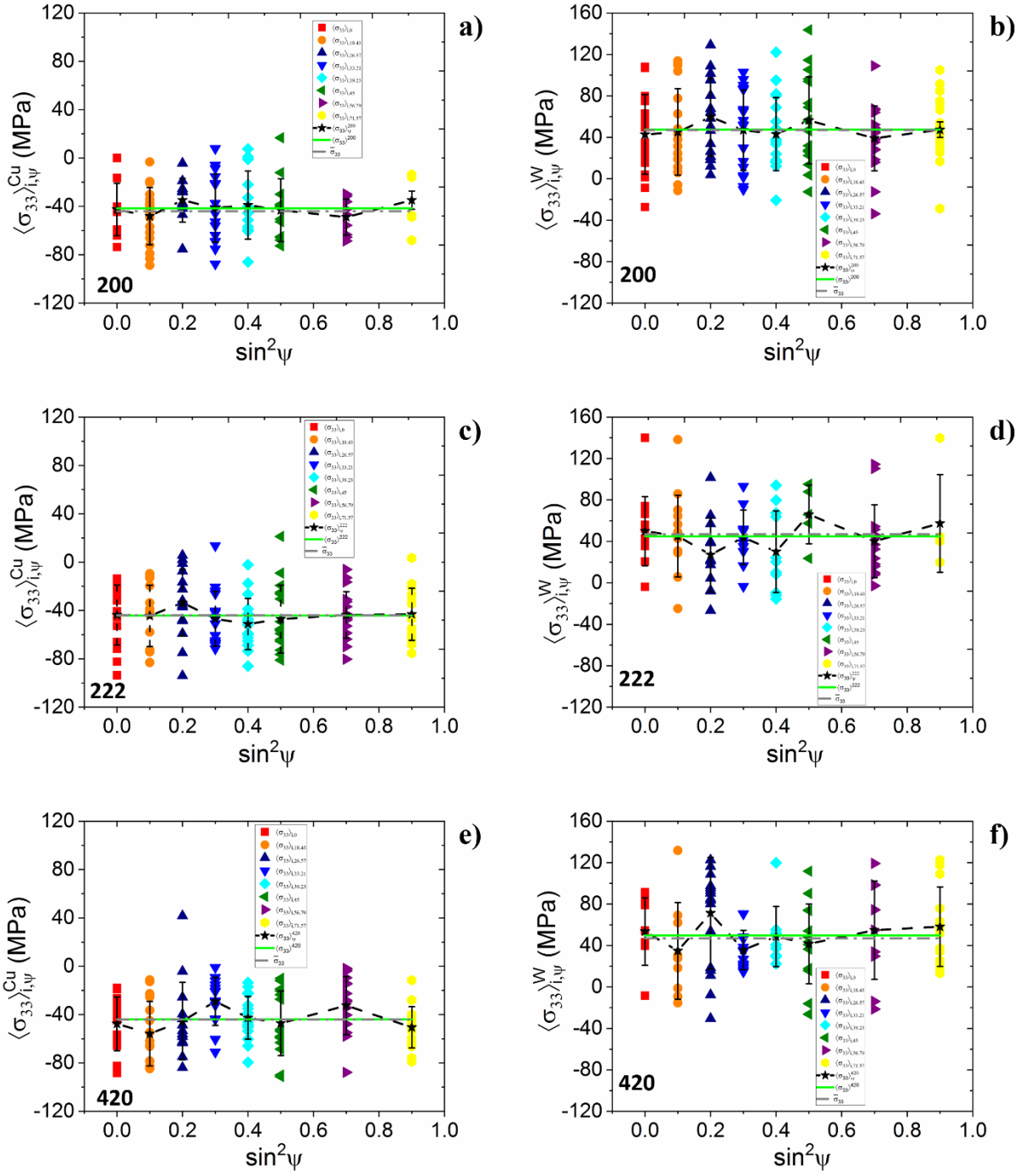

Figure 5.14: The phase-average, Cu (a, c, e) and W (b, d, f), grain stress values along in-plane sample axis; $\langle\sigma_{33}\rangle_{i,\psi}$, , respectively, for all reflections as a function of $\sin^2\psi$.

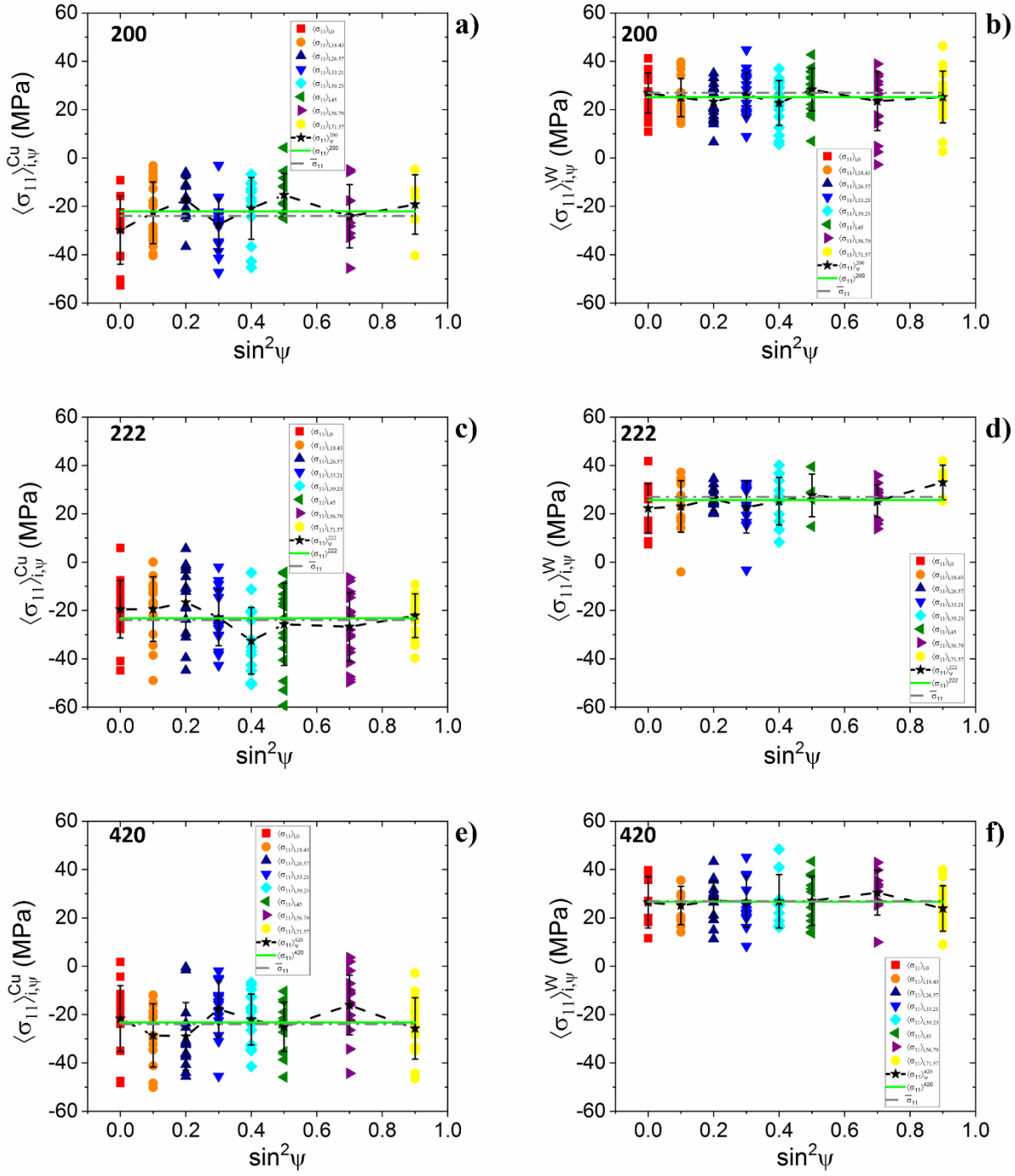

Figure 5.15: The phase-average, Cu (a, c, e) and W (b, d, f), grain stress values along out-of-plane sample axis; $\langle\sigma_{11}\rangle_{i,\psi}$, , respectively, for all reflections as a function of $\sin^2\psi$.

5.3.3.2- Diffraction Stress Analysis

In Fig. 5.18, we plot the $\langle \varepsilon'_{11} \rangle^{Ph}_{i,\psi}$ $vs. \sin^2 \psi$ data for all three reflections of the two-phases computed from the output of the FEA model. While the strain data is quite scattered, the average values are close to linear for both phases. Linear regression fits to both sets yielded opposite slopes as expected.

Analysis of the slopes and intercepts of the fitter linear regression models were first used to compute the phase-averages of strains in the sample coordinate system. In this case, the relevant equation is:

$$\langle \varepsilon^{hkl}_{\phi=0,\psi} \rangle^{Ph}_{i,\psi} = \langle \varepsilon'_{11,\psi} \rangle^{Ph}_{i,\psi} = \left[\left(\langle \varepsilon_{33,\psi} \rangle^{Ph}_{i,\psi} - \langle \varepsilon_{11,\psi} \rangle^{Ph}_{i,\psi} \right) * \sin^2 \psi + \langle \varepsilon_{11,\psi} \rangle^{Ph}_{i,\psi} \right] \quad \text{Eq. (5-9)}$$

Where the index "*i*" refers to a particular grain of phase, *Ph*, diffracting at angle ψ.

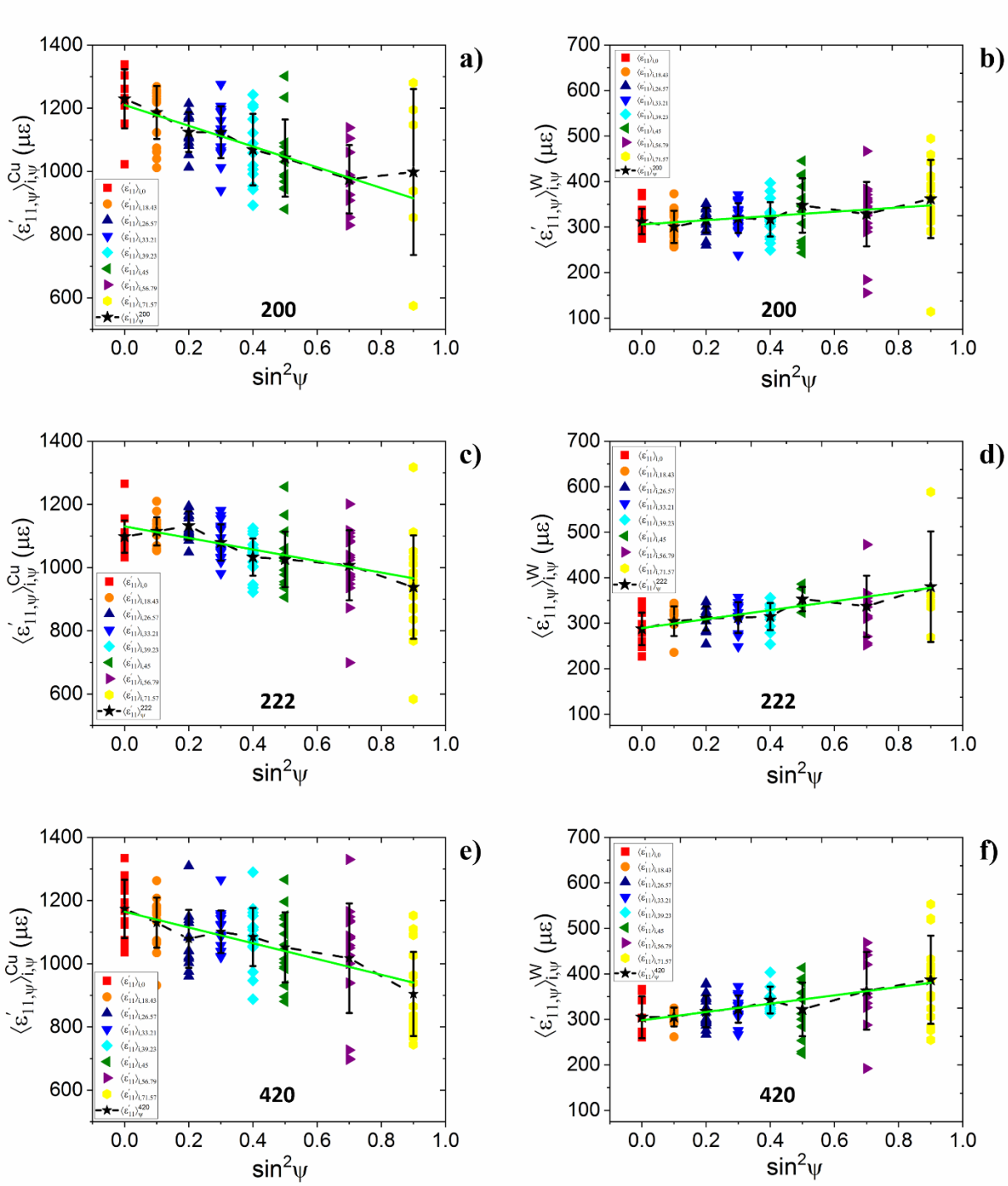

Figure 5.16: $\langle \varepsilon'_{11,\psi} \rangle_{i,\psi}^{Ph}$ *vs.* $sin^2\,\psi$ plots for studied reflections of each phase in Cu – W mesh under the thermal loading.

From the slopes and intercepts of lines fitted to the data shown in Fig. 5.12, we obtain the phase-specific reflection average strains, $\langle \varepsilon_{ij}^{D} \rangle^{Ph-hkl}$, in sample coordinates. These results and their regression-fit errors are presented in Tables 5.24 & 25 for Cu and W phases, respectively[33]. Also included are the reflection average strain tensors in the sample coordinates, computed from real space strain values, $\langle \varepsilon_{ij} \rangle^{Ph-hkl}$, obtained from the finite element analysis for each phase, as well as the overall phase average. The values in parentheses show the "regression-fit-errors" and standard deviations for the regression analysis values and real space averages, respectively. We observe that the strain tensors obtained from linear regression from all reflections agree quite well with the real space averages for both phases. On the other hand, the slopes of the $\langle \varepsilon'_{11,\psi} \rangle_{i,\psi}^{Ph}$ $vs. \sin^2 \psi$ plots are quite different. Consequently, any computation which utilized only slopes would have yielded significantly different answers for each reflection.

Table 5.26 shows the reflection average stress tensors for each phase computed from the average strain tensors listed in Tables 5.24 & 25 and isotropic Hooke's law. In this computation the isotropic elastic constants of bulk Cu and W were used, not reflection-specific diffraction elastic constants. We observe reasonable agreement with the real space values shown in Table 5.23.

Finally, in Table 5.27, we list the reflection-specific stress terms, $\langle \sigma_{33}^{D} - \sigma_{11}^{D} \rangle^{Ph-hkl}$, obtained only from the slopes of the $\langle \varepsilon'_{11,\psi} \rangle_{i,\psi}^{Ph}$ $vs. \sin^2 \psi$ for each phase. Since the magnitudes of $\langle \sigma_{11} \rangle^{Ph-hkl}$, $\langle \sigma_{33} \rangle^{Ph-hkl}$ are comparable, this parameter is not useful in absolute terms.

[33] In these tables, we used symmetry of the model in the film plane to set $\langle \varepsilon_{11} \rangle^{Ph-hkl} = \langle \varepsilon_{22} \rangle^{Ph-hkl}$ for the diffraction analysis. The actual strain values from each grain along the relevant sample axes were used to compute real space averages.

Table 5.24: Slopes and intercepts of lines fitted to $\langle \varepsilon'_{11,\psi} \rangle^{Ph}_{i,\psi}$ $vs.\ sin^2\psi$ data and the corresponding reflection average strain tensors for the Cu phase. The corresponding real space averages are also included. All values are in microstrain (με).

Reflection	Slope	Intercept	$\langle \varepsilon^D_{ij} \rangle^{Ph-hkl}$	$\langle \varepsilon_{ij} \rangle^{Ph-hkl}$
200	-290 (46)	1200(19)	$\begin{bmatrix} 1200(19) & 0 & 0 \\ 0 & 910(50) & 0 \\ 0 & 0 & 910(50) \end{bmatrix}$	$\begin{bmatrix} 1164(84) & 0 & 0 \\ 0 & 893(221) & 0 \\ 0 & 0 & 939(197) \end{bmatrix}$
222	-192(27)	1125(13)	$\begin{bmatrix} 1125(13) & 0 & 0 \\ 0 & 934(30) & 0 \\ 0 & 0 & 934(30) \end{bmatrix}$	$\begin{bmatrix} 1152(85) & 0 & 0 \\ 0 & 925(205) & 0 \\ 0 & 0 & 906(217) \end{bmatrix}$
420	-247(35)	1161(17)	$\begin{bmatrix} 1161(17) & 0 & 0 \\ 0 & 914(39) & 0 \\ 0 & 0 & 914(39) \end{bmatrix}$	$\begin{bmatrix} 1158(87) & 0 & 0 \\ 0 & 909(195) & 0 \\ 0 & 0 & 920(215) \end{bmatrix}$
Phase average				$\begin{bmatrix} 1158(86) & 0 & 0 \\ 0 & 911(206) & 0 \\ 0 & 0 & 920(211) \end{bmatrix}$

Table 5.25: Slopes and intercepts of lines fitted to $\langle \varepsilon'_{11,\psi} \rangle^{Ph}_{i,\psi}$ $vs.\ sin^2\psi$ data and the corresponding reflection average strain tensors for the W phase. The corresponding real space averages are also included. All values are in microstrain (με).

Reflection	Slope	Intercept	$\langle \varepsilon^D_{ij} \rangle^{Ph-hkl}$	$\langle \varepsilon_{ij} \rangle^{Ph-hkl}$
200	53(15)	307(7)	$\begin{bmatrix} 307(7) & 0 & 0 \\ 0 & 359(17) & 0 \\ 0 & 0 & 359(17) \end{bmatrix}$	$\begin{bmatrix} 300(38) & 0 & 0 \\ 0 & 374(105) & 0 \\ 0 & 0 & 370(107) \end{bmatrix}$
222	78(19)	294(8)	$\begin{bmatrix} 294(8) & 0 & 0 \\ 0 & 371(21) & 0 \\ 0 & 0 & 371(21) \end{bmatrix}$	$\begin{bmatrix} 302(38) & 0 & 0 \\ 0 & 380(94) & 0 \\ 0 & 0 & 357(101) \end{bmatrix}$
420	89(21)	300(11)	$\begin{bmatrix} 300(11) & 0 & 0 \\ 0 & 389(23) & 0 \\ 0 & 0 & 389(23) \end{bmatrix}$	$\begin{bmatrix} 302(45) & 0 & 0 \\ 0 & 369(109) & 0 \\ 0 & 0 & 379(122) \end{bmatrix}$
Phase average				$\begin{bmatrix} 302(40) & 0 & 0 \\ 0 & 373(103) & 0 \\ 0 & 0 & 370(110) \end{bmatrix}$

Table 5.26: The computed reflection average stresses from the average strain tensors listed in Tables 5.24 & 25, and isotropic Hooke's law.

Reflection	Cu-phase	W-phase
200	$\begin{bmatrix} -12(13) & 0 & 0 \\ 0 & -37(15) & 0 \\ 0 & 0 & -37(15) \end{bmatrix}$	$\begin{bmatrix} 25(9) & 0 & 0 \\ 0 & 41(12) & 0 \\ 0 & 0 & 41(12) \end{bmatrix}$
222	$\begin{bmatrix} -21(8) & 0 & 0 \\ 0 & -38(9) & 0 \\ 0 & 0 & -38(9) \end{bmatrix}$	$\begin{bmatrix} 23(11) & 0 & 0 \\ 0 & 47(15) & 0 \\ 0 & 0 & 47(15) \end{bmatrix}$
420	$\begin{bmatrix} -18(10) & 0 & 0 \\ 0 & -40(12) & 0 \\ 0 & 0 & -40(12) \end{bmatrix}$	$\begin{bmatrix} 33(14) & 0 & 0 \\ 0 & 60(17) & 0 \\ 0 & 0 & 60(17) \end{bmatrix}$
Phase average	$\begin{bmatrix} -17(10) & 0 & 0 \\ 0 & -38(12) & 0 \\ 0 & 0 & -38(12) \end{bmatrix}$	$\begin{bmatrix} 27(11) & 0 & 0 \\ 0 & 49(15) & 0 \\ 0 & 0 & 49(15) \end{bmatrix}$

Table 5.27: The reflection-specific stress terms, $\langle \sigma_{33}^{D} - \sigma_{11}^{D} \rangle^{Ph-hkl}$ obtained from the slopes of the $\langle \varepsilon'_{11} \rangle_{i,\psi}^{Ph}$ $vs.$ $sin^2\,\psi$.

Reflection	200	222	420
(MPa)	$\langle \sigma_{33}^{D} - \sigma_{11}^{D} \rangle^{Ph-hkl}$	$\langle \sigma_{33}^{D} - \sigma_{11}^{D} \rangle^{Ph-hkl}$	$\langle \sigma_{33}^{D} - \sigma_{11}^{D} \rangle^{Ph-hkl}$
Cu	-42 ± 44	-44 ± 44	-44 ± 44
W	48 ± 37	45 ± 37	50 ± 41

5.4- Summary

In this chapter, we used finite element modeling to obtain local stress and strain distributions of virtual materials under thermal loading. In addition, the expected ε'_{hkl} $vs.\sin^2\psi$

plots were computed for several reflections, and these plots were analyzed using the standard formalisms. We compared these results with the real space stresses/strains in our ideal samples.

We found that macrostresses were observed in the constrained W and Cu samples. Due to having heterogeneous elastic constants, Heyn stresses are seen in Cu. In addition, variations in local stresses/strains were observed in ψ-ensembles for 200 and 222 reflections in this sample. Therefore, we can say that these volumes are not representative volume elements. Consequently, non-linearities in $\varepsilon'_{hkl}\ vs.\ \sin^2\psi$ plots were observed. We found out that these non-linearities are oscillations by following a procedure defined in section 5.3.2.3.2.1.

In the case of the Cu – W sample, only Heyn stresses (average of microstresses) were observed due to differential deformation and different amounts of expansion of phases. In addition, phase-specific average stresses are pseudo-macro stresses. $\varepsilon'_{hkl}\ vs.\ \sin^2\psi$ plots were computed. And it was found that even though calculated average strains from linear least square fitting are in agreement with the real space values, any computation of stresses utilizing only slopes would have yielded significantly different answers for each reflection.

In the next chapter, we will go one step further and increase the complexity of our virtual diffraction stress experiments in ideal, 3-D polycrystalline samples at which local stress variations are caused due to the change of elastic moduli from grain to grain and/or St. Venant fields.

6- FAR-FIELD MECHANICAL STRESSES IN IDEAL POLYCRYSTALLINE SYSTEMS

The sample geometries modeled in Chapter 5 were based on an ideal thin film that contained hexagonal-prism-shaped grains arranged in either a 20x20x1 array (400 grains) or a 26x26x1 array (676 grains). Simulation of the diffraction stress/strain formalism with this simple model was useful in clarifying the effects of heterogeneous distributions of elastic and plastic strains on the computed results. However, since these were not realistic samples, the applicability of our conclusions to actual tensile deformation of polycrystalline single-phase W and Cu, and two-phase Cu – W samples. These models are three-dimensional, contain many more grains, and utilize more realistic grain shapes and grain size distributions. In addition, we incorporated in these models more realistic plastic deformation responses which included experiment-based strain hardening as needed.

In this chapter, we first present the extended details of our model and define the gage and grip sections of our virtual three-dimensional specimen through preliminary finite element analysis. We then present our work in five steps. In the first step, we examine the partitioning of stresses and strains within the grains of single-phase W and Cu samples loaded in the elastic regime under displacement control and determine the diffraction elastic constants of these (virtual) samples in simulated experiments. In the second step, we extend the single-phase Cu sample past its yield point, and discuss the partitioning of elastic strains within the sample at maximum extension and after unloading. In the third step, we present the partitioning of internal stresses in a Cu – W sample loaded in the elastic regime under displacement control, and determine the

diffraction elastic constants of the individual phases in this regime. In the fourth step, we extend the Cu – W past its yield point, and discuss the partitioning of elastic strains within the sample at maximum extension and after unloading. Finally, we discuss the types of deformation distributions in these samples and show that plastic flow smooths out stress distributions in both single-phase and two-phase samples.

6.1- Materials Selection

Selected elastic properties of Cu and W are shown in Chapter 5. The refined Voce hardening parameters were estimated from fitting an experimental stress-strain data for single-phase Cu and are listed in Table 6.1. In the case of a single-phase W sample, these parameters were not estimated, we used higher hardening parameters to prevent the plastic deformation of the W phase. The stress-strain curves for single-phase Cu and W are shown in Fig. 6.1.

Table 6.1: Refined Voce hardening parameters of Cu and W.

	10^9 Pa	10^9 Pa					
	σ_Y	h_0	g_0	g_1	$\dot{\gamma}_0$	m	$\dot{\gamma}_s$
Cu	222	350	106	130	0.001	0.025	5
W	1200	32	1200	2000	0.001	0.025	5

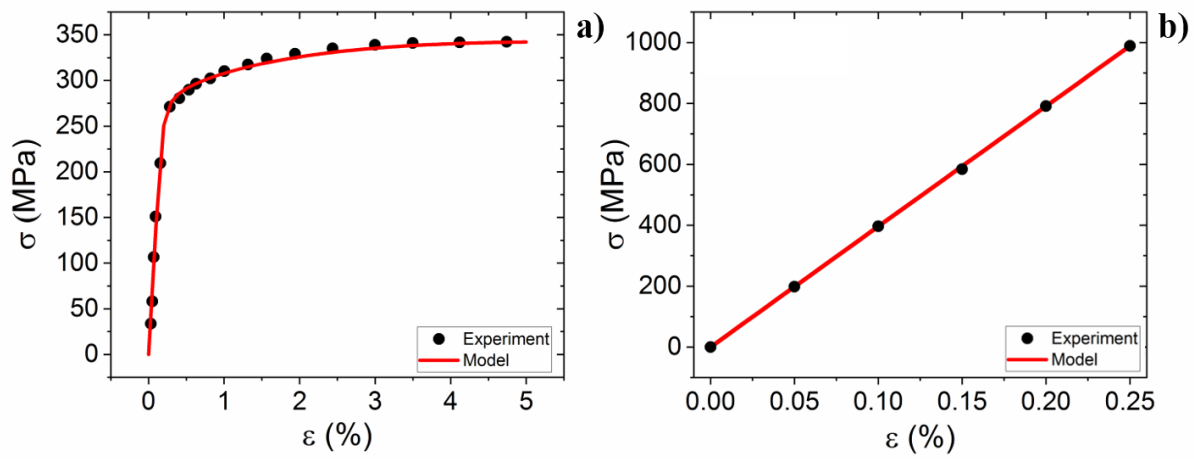

Figure 6.1: Refined and Experimental Stress-Strain Curve of a) Cu, b) W. The experimental data is collected from the Atlas of Stress-Strain Curves *[133]*.

6.2- Model Definition and Meshing

We specified a virtual sample in the shape of a square prism with dimensions 1x1x3 mm, and used Voronoi tessellation to create a three-dimensional grain structure within it. The Neper program was, then, used to mesh our virtual polycrystalline sample [119]. Fig. 6.2 depicts the mesh used in single-phase W and Cu finite element models. All 1500 grains have realistic three-dimensional grain shapes. The distribution of the grain volumes is log-normal (Fig. 6.3). Each grain is oriented in the sample coordinate system, $\vec{S}_i$, such that it will diffract into one of the chosen reflections, 111, 200, 220, 311, 420 for Cu and 110, 200, 211, 220, 310 for W, at the ψ-tilts specified in Tables 6.2 & 3, respectively. In these tables, the population for each ψ-ensemble, N_{ψ}^{hkl}, and its volume fraction, f_{ψ}^{hkl}, are also listed.

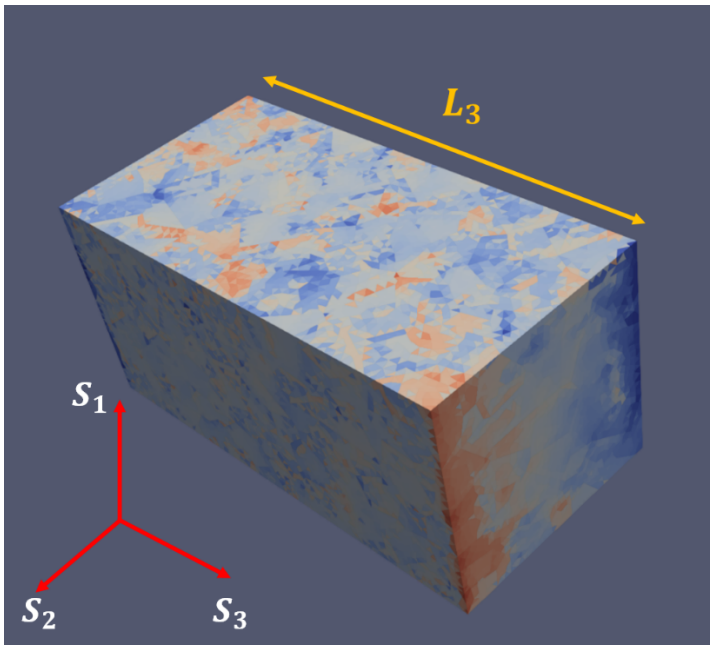

Figure 6.2: Schematic of the virtual sample used in FEpX. ParaView software was used for visualization.

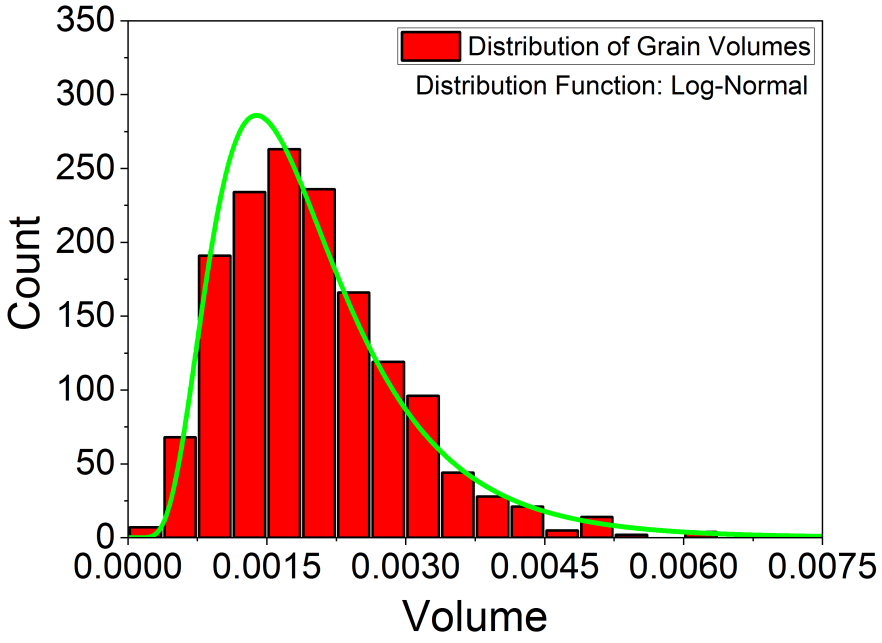

Figure 6.3: Distribution of Grain Volumes in W and Cu mesh.

Table 6.2: The population number for each ψ-ensemble N_{ψ}^{hkl} , and its volume fraction, f_{ψ}^{hkl} in finite element mesh of Cu sample.

ψ(°)	0	18.43	26.57	33.21	39.23	45	56.79	71.57
$N_{\psi}^{111}, f_{\psi}^{111}$	96, 0.069	21, 0.014	31, 0.020	11, 0.007	57, 0.040	110, 0.072	119, 0.081	23, 0.016
$N_{\psi}^{200}, f_{\psi}^{200}$	39, 0.025	46, 0.032	59, 0.035	73, 0.048	74, 0.048	14, 0.010	45, 0.033	12, 0.008
$N_{\psi}^{220}, f_{\psi}^{220}$	41, 0.029	17, 0.011	24, 0.017	7, 0.005	23, 0.013	12, 0.008	35, 0.022	13, 0.007
$N_{\psi}^{311}, f_{\psi}^{311}$	14, 0.008	44, 0.030	8, 0.005	14, 0.008	12, 0.007	10, 0.008	17, 0.009	49, 0.033
$N_{\psi}^{420}, f_{\psi}^{420}$	66, 0.046	32, 0.023	87, 0.061	15, 0.009	20, 0.014	75, 0.048	18, 0.010	17, 0.011

Table 6.3: The population number for each ψ-ensemble N_{ψ}^{hkl} , and its volume fraction, f_{ψ}^{hkl} in finite element mesh of W sample.

ψ(°)	0	18.43	26.57	33.21	39.23	45	56.79	71.57
$N_{\psi}^{110}, f_{\psi}^{110}$	29, 0.019	35, 0.020	23, 0.017	32, 0.023	11, 0.007	12, 0.008	38, 0.026	15, 0.009
$N_{\psi}^{200}, f_{\psi}^{200}$	34, 0.024	36, 0.024	54, 0.033	60, 0.042	61, 0.041	69, 0.054	35, 0.023	28, 0.018
$N_{\psi}^{211}, f_{\psi}^{211}$	66, 0.044	29, 0.018	35, 0.023	36, 0.022	41, 0.026	36, 0.024	37, 0.024	55, 0.036
$N_{\psi}^{220}, f_{\psi}^{220}$	44, 0.028	12, 0.007	41, 0.027	29, 0.022	27, 0.017	44, 0.031	37, 0.021	34, 0.023
$N_{\psi}^{310}, f_{\psi}^{310}$	42, 0.028	51, 0.038	41, 0.026	39, 0.028	41, 0.026	46, 0.032	38, 0.023	28, 0.019

6.3- Loading Geometry

We used displacement control to simulate tensile tests of our virtual specimens, with tractions applied at the square faces of the cubic prisms. Since FEpX also applies local stresses to ensure static equilibrium, we first computed the stress/strain distributions in an isotropic

polycrystalline virtual sample[34] to identify regions where St. Venant stresses caused by these additional tractions might be finite. In Fig. 6.4-a, we plot the grain average stress values in sample coordinates, $\langle\sigma_{33}\rangle_{I,\psi}$, with position, z, along the S_3 axis[35] for the isotropic cubic prism loaded in tension to 790 MPa. The stress profile is symmetric with three unique sections: In sections A, there are significant St, Venant effects, with $\langle\sigma_{33}\rangle_{I,\psi} \in (700,950)$ MPa. "B sections" are transition regions, with $\langle\sigma_{33}\rangle_{I,\psi} \in (725, 825)$ MPa. In section C, the grain average stresses are within 3% of the far-field stresses. Consequently, for stress analysis we define two regions:

a) Grip regions: these are sections A and B close to the sample ends in which St. Venant effects are finite even for an isotropic material. These sections in our sample are defined between $0 < z < 0.75$ and $2.25 < z < 3$.

b) Gage region: In this region, the far-field stress (σ_{33}^{o}) is within 5% of the applied stress ($\sigma_{33}^{App.}$) with $z \in (0.75, 2.25)$ (Fig. 6.4-b).

[34] For this sample, the Zener anisotropy index was specified as exactly 1.00. The plastic flow was not permitted.

[35] For a given position, z, along $\vec{S}_3$, the average stresses at any position (x,y) in the $\vec{S}_1 - \vec{S}_2$ plane are plotted.

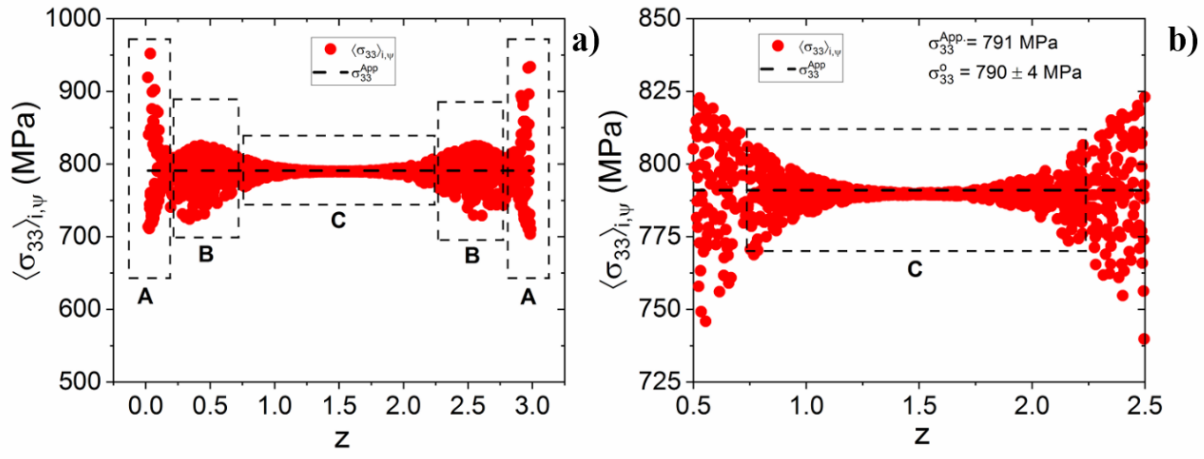

Figure 6.4: Grain average stress values in sample coordinates, $\langle\sigma_{33}\rangle_{i,\psi}$ along z a) between 0 to 3 b) between 0.5 and 2.25.

We also investigated the dependency of the axial stress distributions on the applied load. In Fig. 6.5, the variation with axial position, z, of all grain average stress components, $\langle\sigma_{ij}\rangle_{I,\psi}$, are shown for five different applied loads[36]. We observe that $\langle\sigma_{ij}\rangle_{I,\psi}(z) \neq f(\sigma_{33}^{App.})$.

[36] In these plots, stress tensor components were normalized with the $\sigma_{33}^{App.}$: $\langle\sigma_{ij}^{N}\rangle_{i,\psi} = \frac{\langle\sigma_{ij}\rangle_{i,\psi}}{\sigma_{ij}^{App.}}$.

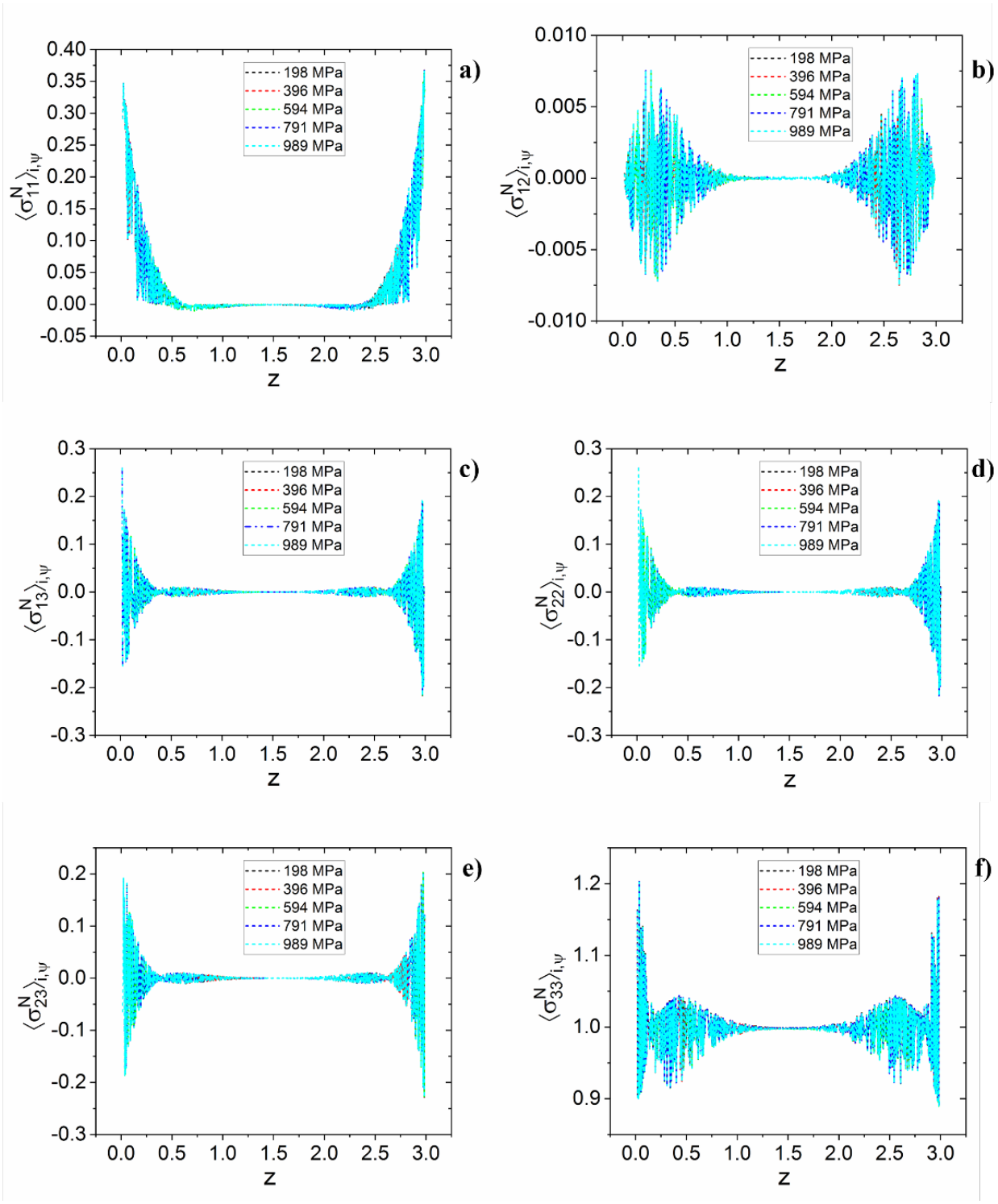

Figure 6.5: Variation of $\langle\sigma^N_{ij}\rangle_{i,\psi}$ with position for five different tensile loads in the isotropic bar.

6.4- Results

6.4.1- Uniaxial Tension of Single-phase W Bar

We simulated uniaxial tension of single-phase W specimens by elastically extending the bar by 0.25%. This corresponds to the applied tensile stress of 989 MPa in the tensile test curve (Fig. 6.1). Table 6.4 shows the global average stress tensors and their distribution parameters. These values were computed over all grains, both in grip and gage sections, in the model. The minimum and maximum values reflect the extrema in the relevant grain average stresses/strains. We observe that, while the average axial stress is quite close to the far-field stress, $\bar{\sigma}_{33} = 987$ MPa, the average transverse normal stresses are finite: $\bar{\sigma}_{11} = \bar{\sigma}_{22} = 32$ MPa. Five stress terms, $\bar{\sigma}_{ii}$, $\bar{\sigma}_{13}$ *and* $\bar{\sigma}_{23}$ exhibit wide distributions; the full width of these in-plane stresses are quite large, indicating that some grains are under triaxial stress states. This is due to grip boundary conditions. Only the mean out-of-plane shear stress, $\bar{\sigma}_{12}$, is zero with approximately zero dispersion. This is due to the isotropic elastic properties of W.

Table 6.4: Global average stress tensor of the entire W bar loaded to 989 MPa and its dispersion parameters. The model contains 1500 grains. All values are in MPa.

(MPa)	$\bar{\sigma}_{11}$	$\bar{\sigma}_{12}$	$\bar{\sigma}_{13}$	$\bar{\sigma}_{22}$	$\bar{\sigma}_{23}$	$\bar{\sigma}_{33}$
Average	**32**	**0**	**0**	**32**	**0**	**987**
Std. Dev	75	2	31	75	31	28
Maximum	363	7	257	389	201	1189
Minimum	-10	-7	-215	-10	-226	879
Full Width	**374**	**15**	**471**	**399**	**427**	**310**

Table 6.5: Average lattice strain tensor of the entire W bar loaded to 989 MPa and its dispersion parameters. The model contains 1500 grains. All values are in microstrain (με).

(με)	$\bar{\varepsilon}_{11}$	$\bar{\varepsilon}_{12}$	$\bar{\varepsilon}_{13}$	$\bar{\varepsilon}_{22}$	$\bar{\varepsilon}_{23}$	$\bar{\varepsilon}_{33}$
Average	**-660**	**0**	**1**	**-660**	**-1**	**2490**
Std. Dev	146	6	103	146	102	134
Maximum	-29	25	846	-45	662	2760
Minimum	-776	-24	-706	-795	-744	1790
Full Width	**747**	**49**	**1552**	**750**	**1406**	**970**

Similar to the stress values, all lattice normal strain values are finite and we observe compressive out-of-plane normal strains, $\bar{\varepsilon}_{11}$ and $\bar{\varepsilon}_{22}$. All average shear strains $\bar{\varepsilon}_{ij,i\neq j} = 0$. These results show that we need to investigate the W bar under two sections; gage and grip sections (Fig. 6.6).

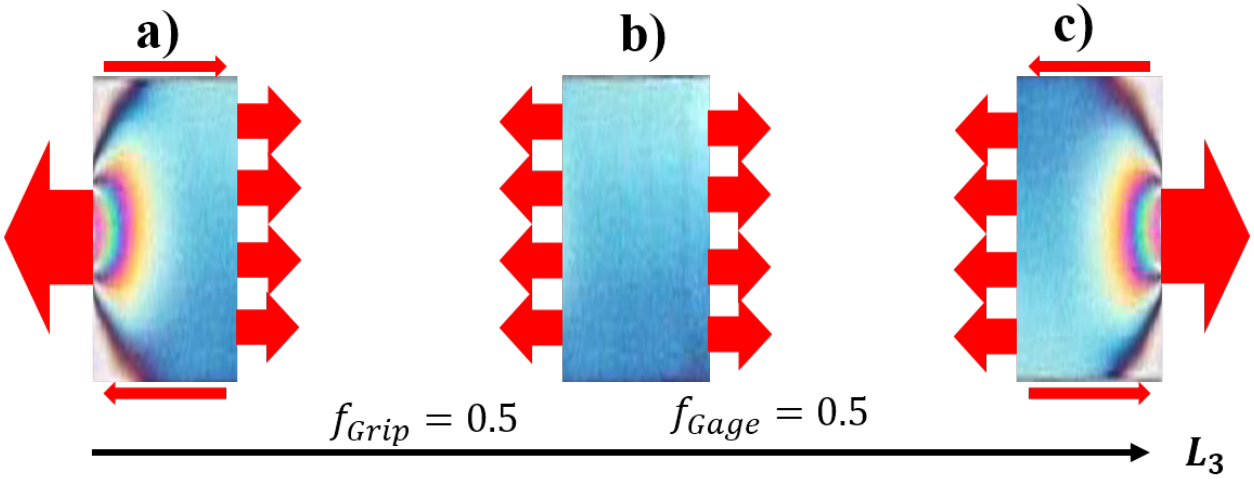

Figure 6.6: Schematic free-body diagram of W bar extended along L_3 direction. The gage and grip sections are defined and they have equal volume fractions.

6.4.1.1- Analysis of Gage Section of W Bar

The gage section of this model served as a rigorous test since the stress/strain distributions could be rigorously predicted from theory. Since the elastic properties of W are isotropic, the local elastic strain tensor at any point $P(x, y, z)$ within the gage section of the W model is expected to be homogeneous, of the form:

$$\left(\varepsilon_{ij}\right)_{x,y,z} = \begin{bmatrix} -\nu\varepsilon_{33} & 0 & 0 \\ 0 & -\nu\varepsilon_{33} & 0 \\ 0 & 0 & \varepsilon_{33} \end{bmatrix} \quad \text{Eq. (6-1)}$$

Here $\varepsilon_{ij}(x, y, z)$ is the total lattice strain along the loading direction, $\vec{S}_3$ caused by the applied load. From the linear elasticity theory:

$$\left(\sigma_{ij}\right)_{x,y,z} = \begin{bmatrix} 0 & 0 & 0 \\ 0 & 0 & 0 \\ 0 & 0 & \sigma_{33} \end{bmatrix}; \quad \varepsilon_{ij} = S_{ijkl}\sigma_{kl} \quad \text{Eq. (6-2)}$$

for all point $P(x, y, z)$.

The stress and strain values in the sample coordinate system, computed using these equations for the gage section of our W model, are listed in Table 6.6. The corresponding results from the FEM analysis are also included. We observe excellent agreement between the values obtained from the FEM simulation and the analytical calculations. As expected, the FEM simulations yield isotropic stress, strain distributions within the model (Fig. 6.7-a & b). Consequently, average stress and strains are identical to their local values and are independent of the type of averaging and the size and location of the averaging volume.

Table 6.6: Stress and strain tensor for the gage section of the extended W model, computed using various approaches. The XRD values are the reflection averages of the stress and strain terms.

Parameter	Eqs. (6-1 & 2)	FEpX	XRD Analysis
Elastic strain , ε_{ij}	$\begin{bmatrix} -716 & 0 & 0 \\ 0 & -716 & 0 \\ 0 & 0 & 2555 \end{bmatrix}$	$\begin{bmatrix} -724(7) & 0 & 0 \\ 0 & -723(7) & 0 \\ 0 & 0 & 2540(14) \end{bmatrix}$	$\begin{bmatrix} -724(1) & 0 & 0 \\ 0 & -724(1) & 0 \\ 0 & 0 & 2546(2) \end{bmatrix}$
Stress σ_{ij}; $\bar{\sigma}_{ij}$ (MPa)	$\begin{bmatrix} 0 & 0 & 0 \\ 0 & 0 & 0 \\ 0 & 0 & 987 \end{bmatrix}$	$\begin{bmatrix} -2(2) & 0 & 0(2) \\ 0(2) & -2(2) & 0(2) \\ 0(2) & 0(2) & 987(5) \end{bmatrix}$	$\begin{bmatrix} 0 & 0 & 0 \\ 0 & 0 & 0 \\ 0 & 0 & 988(1) \end{bmatrix}$

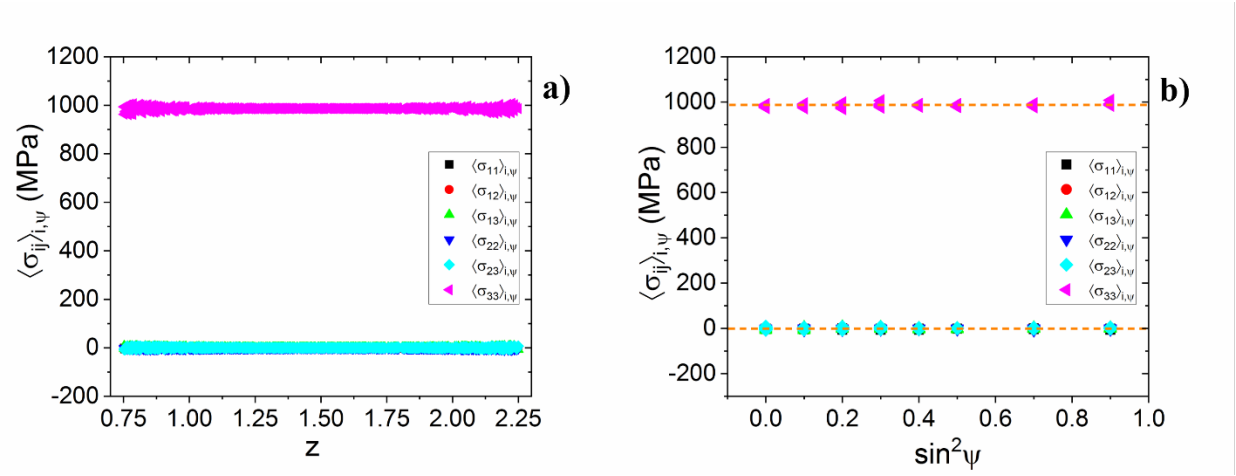

Figure 6.7: Grain average stress values in sample coordinates, $\langle\boldsymbol{\sigma_{ij}}\rangle_{i,\psi}$ a) sorted with respect to z b) for $\boldsymbol{\psi}$ -ensembles diffracting into all reflections. At each ψ there are $\boldsymbol{N_{\psi}^{hkl}}$ identical stress values. Plots for the individual reflections were identical.

The stresses in the sample coordinate system were also computed by simulating and analyzing $\langle\varepsilon'_{11,\psi}\rangle_{i,\psi}^{W}$ $vs.\sin^2\psi$ graphs for all reflections using Eqs. (5-1-a & b) respectively. In Fig. 6.8, the $\langle\varepsilon'_{11,\psi}\rangle_{i,\psi}^{W}$ $vs.\sin^2\psi$ graph for 110 reflection is shown. All other reflections also yielded

identical plots. Consequently, the reflection average stress tensors $\langle \sigma_{ij}^{D} \rangle^{hkl}$, were identical for all reflections. The diffraction elastic constants used in calculations, $\frac{1+v}{E}, \frac{v}{E}$, are shown in Table 5.4.

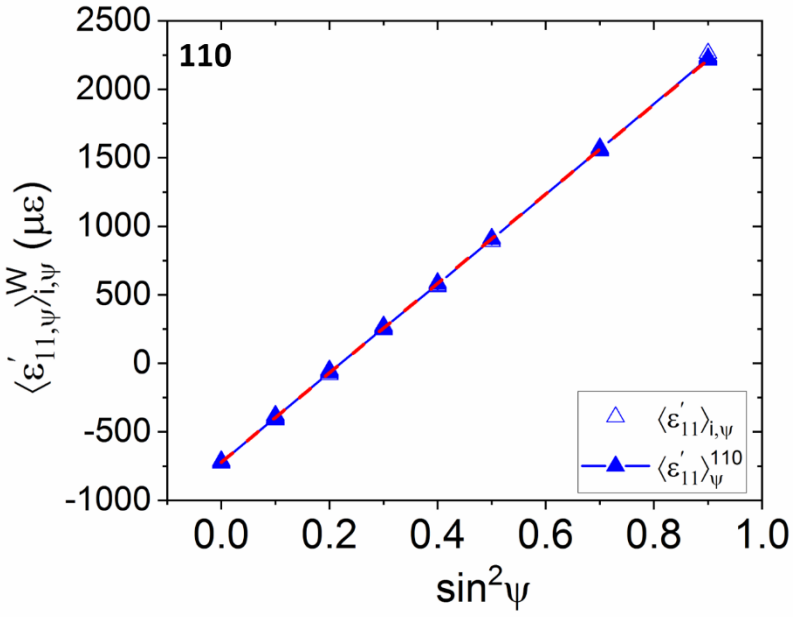

Figure 6.8: $\langle \varepsilon'_{11,\psi} \rangle_{i,\psi}^{W}$ $vs.$ sin^2 ψ plot computed from the strain output of the W model extended along the z-direction. At each ψ, there are N_{ψ}^{110} identical strain values.

Table 6.6 and Figs. 6.7 & 8 show that St. Venant effects are negligible in the gage section. Consequently, the stress components obtained from diffraction analysis are macrostresses since:

a) $\langle \sigma_{ij}^{D} \rangle^{hkl}$ are independent of the reflection chosen for the measurement.

b) $\langle \sigma_{ij}^{D} \rangle^{hkl}$ will be the same for any measurement volume within the gage section of the model.

c) All reflections yield regular (linear) $\langle \varepsilon'_{11,\psi} \rangle_{i,\psi}$ $vs. sin^2 \psi$.

6.4.1.2- Analysis of Grip Sections of W Bar

The gage section of our W model showed that the W bar subjected to applied stress contained homogeneous, isotropic stress and strain distributions. Local stress and strain tensors were equal to global ones. The stress/strain distributions obtained from numerical modeling agreed with all analytical calculations performed assuming an ideal isotropic continuum. In the case of grip sections of the W bar, we expect some grains to have triaxial stress states due to the grip boundary conditions (Table 6.4). We tabulated numerical averages of the stress and strain tensors $\bar{\sigma}_{ij}, \bar{\varepsilon}_{ij}$, and the standard deviations for the model parameters. The expected strain and stress tensors for all points $P(x, y, z)$ in a homogeneous, isotropic W bar for fully elastic loading Eqs. (6-2 & 3) are also presented in Table 6.7. We observe non-negligible differences between the analytical and the finite element model results for most stress and strain components. These differences are due to St. Venant effects only and change the dimensionality of the stress tensor.

Table 6.7: Stress and strain tensor for the grip section of the extended W model, computed using various approaches. The XRD values are the reflection averages of the stress and strain terms (terms in parentheses are STD values, not errors).

Parameter	Eqs. (6-1 & 2)	FEpX
Elastic strain , ε_{ij}; $\bar{\varepsilon}_{ij}$	$\begin{bmatrix} -716 & 0 & 0 \\ 0 & -716 & 0 \\ 0 & 0 & 2555 \end{bmatrix}$	$\begin{bmatrix} -600(186) & 0(8) & 2(145) \\ 0(8) & -600(186) & -3(143) \\ 2(145) & -3 & 2450(175) \end{bmatrix}$
Stress σ_{ij}; $\bar{\sigma}_{ij}$ (MPa)	$\begin{bmatrix} 0 & 0 & 0 \\ 0 & 0 & 0 \\ 0 & 0 & 987 \end{bmatrix}$	$\begin{bmatrix} 66(94) & 0(3) & 1(44) \\ 0(3) & 66(94) & -1(44) \\ 1(44) & -1(44) & 987(39) \end{bmatrix}$

6.4.1.2.1- Stress Distributions in Sample Coordinates

In Fig. 6.9, we plot the grain average stress components for all grains in the grip section as a function of $\sin^2\psi$. These average stresses contain contributions from St. Venant effects caused by boundary conditions. We observe that individual grains can have very different (average) stress tensors from each other and the global averages of the gage region.

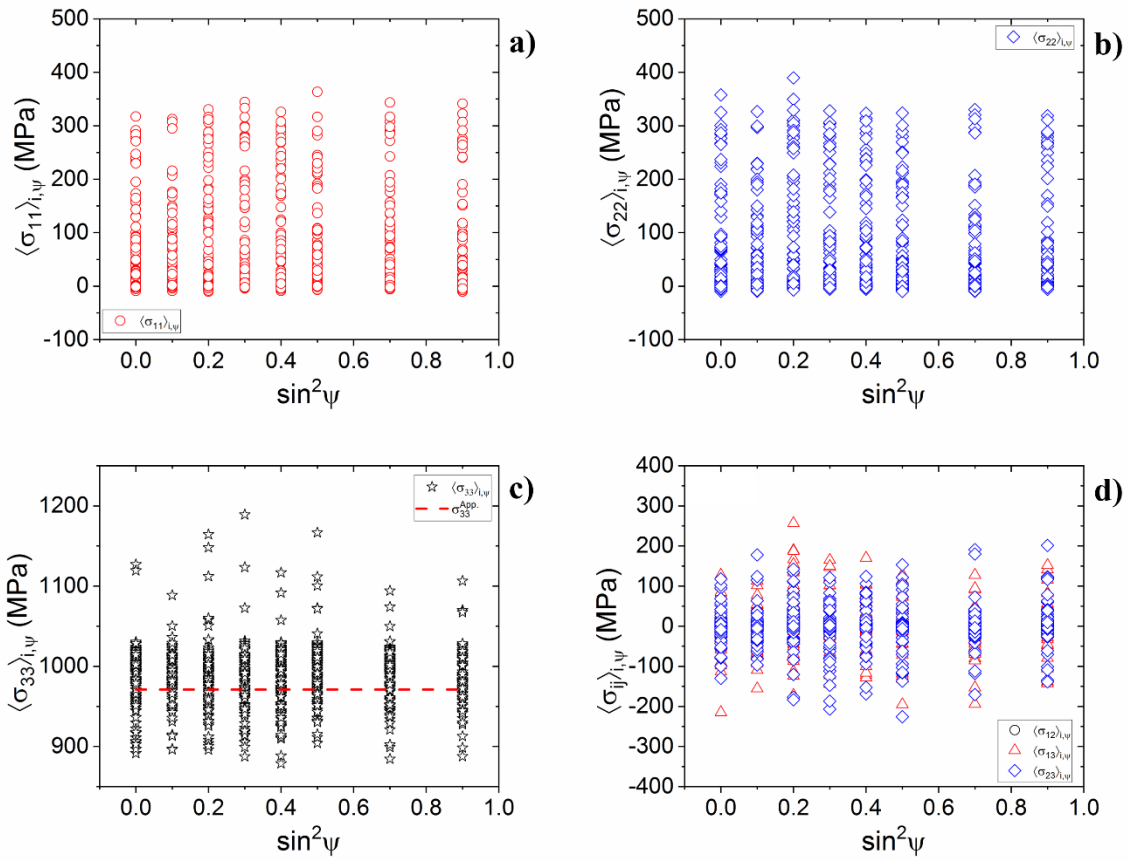

Figure 6.9: The grain stress average values a) $\langle\sigma_{11}\rangle_{i,\psi}$, b) $\langle\sigma_{22}\rangle_{i,\psi}$, c) $\langle\sigma_{33}\rangle_{i,\psi}$ d) shear stresses, for all grains as a function of $\sin^2\psi$.

The ψ-volume averages of the stress components, $\langle\sigma_{ij}\rangle_{\psi}^{hkl}$, are listed in Table 6.8. $\langle\sigma_{33}\rangle_{\psi}^{hkl}$ averages are closer to the global average stresses, $\bar{\sigma}_{33}$. For the out-of-plane direction, $\vec{S}_1$ and $\vec{S}_2$, ψ-volume averages, $\langle\sigma_{11}\rangle_{\psi}^{hkl}, \langle\sigma_{22}\rangle_{\psi}^{hkl}$ can be up to 40% different than $\bar{\sigma}_{11}, \bar{\sigma}_{22}$. Consequently, these volumes cannot be considered to be representative volume elements.

Table 6.8: ψ-ensemble average stress tensors, $\langle \sigma_{ij} \rangle_{\psi}^{hkl}$, for the 110, 200, 211, 220, and 310 reflections.

	0	**18.43**	**26.57**	**33.21**	**39.23**	**45**	**56.79**	**71.57**
110	$\begin{pmatrix} 40 & 0 & -6 \\ 0 & 39 & -8 \\ -6 & -8 & 1000 \end{pmatrix}$	$\begin{pmatrix} 54 & 1 & 6 \\ 1 & 71 & 0 \\ 6 & 0 & 999 \end{pmatrix}$	$\begin{pmatrix} 95 & 1 & -23 \\ 1 & 96 & 6 \\ -23 & 6 & 984 \end{pmatrix}$	$\begin{pmatrix} 48 & 0 & 1 \\ 0 & 26 & 9 \\ 1 & 9 & 974 \end{pmatrix}$	$\begin{pmatrix} 87 & 2 & -23 \\ 2 & 48 & -33 \\ -23 & -33 & 990 \end{pmatrix}$	$\begin{pmatrix} 26 & 0 & -2 \\ 0 & 13 & 1 \\ -2 & 1 & 991 \end{pmatrix}$	$\begin{pmatrix} 52 & 0 & -2 \\ 0 & 37 & -11 \\ -2 & -11 & 995 \end{pmatrix}$	$\begin{pmatrix} 38 & 0 & 18 \\ 0 & 60 & 33 \\ 18 & 33 & 1001 \end{pmatrix}$
200	$\begin{pmatrix} 97 & 0 & 11 \\ 0 & 74 & -13 \\ 11 & -13 & 991 \end{pmatrix}$	$\begin{pmatrix} 70 & 0 & -18 \\ 0 & 64 & 6 \\ -18 & 6 & 979 \end{pmatrix}$	$\begin{pmatrix} 59 & 0 & 12 \\ 0 & 69 & 0 \\ 12 & 0 & 985 \end{pmatrix}$	$\begin{pmatrix} 87 & 0 & 16 \\ 0 & 93 & -17 \\ 16 & -17 & 981 \end{pmatrix}$	$\begin{pmatrix} 77 & 0 & 4 \\ 0 & 77 & -3 \\ 4 & -3 & 975 \end{pmatrix}$	$\begin{pmatrix} 59 & 0 & 2 \\ 0 & 38 & -2 \\ 2 & -2 & 981 \end{pmatrix}$	$\begin{pmatrix} 48 & 0 & -12 \\ 0 & 47 & -1 \\ -12 & -1 & 992 \end{pmatrix}$	$\begin{pmatrix} 98 & 0 & -7 \\ 0 & 112 & -7 \\ -7 & -7 & 984 \end{pmatrix}$
211	$\begin{pmatrix} 54 & -1 & -8 \\ -1 & 53 & -1 \\ -8 & -1 & 982 \end{pmatrix}$	$\begin{pmatrix} 61 & -1 & -4 \\ -1 & 64 & -2 \\ -4 & -2 & 1009 \end{pmatrix}$	$\begin{pmatrix} 105 & 1 & 22 \\ 1 & 120 & 11 \\ 22 & 11 & 989 \end{pmatrix}$	$\begin{pmatrix} 76 & 0 & 15 \\ 0 & 82 & -11 \\ 15 & -11 & 989 \end{pmatrix}$	$\begin{pmatrix} 60 & 0 & 10 \\ 0 & 73 & 2 \\ 10 & 2 & 980 \end{pmatrix}$	$\begin{pmatrix} 19 & 1 & 0 \\ 1 & 35 & -11 \\ 0 & -11 & 1005 \end{pmatrix}$	$\begin{pmatrix} 87 & -1 & 6 \\ -1 & 81 & -9 \\ 6 & -9 & 974 \end{pmatrix}$	$\begin{pmatrix} 71 & 0 & 0 \\ 0 & 69 & 6 \\ 0 & 6 & 988 \end{pmatrix}$
220	$\begin{pmatrix} 63 & 0 & -10 \\ 0 & 69 & 1 \\ -10 & 1 & 993 \end{pmatrix}$	$\begin{pmatrix} 77 & 0 & 1 \\ 0 & 69 & -6 \\ 1 & -6 & 986 \end{pmatrix}$	$\begin{pmatrix} 59 & 0 & 24 \\ 0 & 70 & 1 \\ 24 & 1 & 982 \end{pmatrix}$	$\begin{pmatrix} 59 & 0 & -8 \\ 0 & 58 & -5 \\ -8 & -5 & 993 \end{pmatrix}$	$\begin{pmatrix} 46 & 2 & -15 \\ 2 & 37 & -12 \\ -15 & -12 & 1011 \end{pmatrix}$	$\begin{pmatrix} 69 & 0 & 0 \\ 0 & 75 & 15 \\ 0 & 15 & 990 \end{pmatrix}$	$\begin{pmatrix} 54 & -1 & -9 \\ -1 & 45 & 11 \\ -9 & 11 & 999 \end{pmatrix}$	$\begin{pmatrix} 71 & 1 & 14 \\ 1 & 78 & 0 \\ 14 & 0 & 985 \end{pmatrix}$
310	$\begin{pmatrix} 83 & 1 & 3 \\ 1 & 84 & 1 \\ 3 & 1 & 975 \end{pmatrix}$	$\begin{pmatrix} 53 & 0 & -4 \\ 0 & 67 & 5 \\ -4 & 5 & 994 \end{pmatrix}$	$\begin{pmatrix} 75 & 0 & 16 \\ 0 & 70 & 2 \\ 16 & 2 & 978 \end{pmatrix}$	$\begin{pmatrix} 52 & 0 & -11 \\ 0 & 66 & 2 \\ -11 & 2 & 969 \end{pmatrix}$	$\begin{pmatrix} 85 & 0 & 3 \\ 0 & 72 & 12 \\ 3 & 12 & 988 \end{pmatrix}$	$\begin{pmatrix} 66 & 0 & -12 \\ 0 & 72 & -12 \\ -12 & -12 & 1005 \end{pmatrix}$	$\begin{pmatrix} 73 & -1 & -8 \\ -1 & 59 & 14 \\ -8 & 14 & 978 \end{pmatrix}$	$\begin{pmatrix} 39 & 0 & -6 \\ 0 & 42 & 10 \\ -6 & 10 & 986 \end{pmatrix}$

Table 6.9: Reflection average stress tensors, $\langle\sigma_{ij}\rangle^{hkl}$, for the 110, 200, 211, 220, and 310 reflections. The components of these tensors were obtained by averaging the particular average stress components, $\langle\sigma_{ij}\rangle_{i,\psi}$, (in the sample coordinates) of all grains for all ψ–tilts for each reflection.

$\langle\sigma_{ij}\rangle^{110}$ (MPa)	$\langle\sigma_{ij}\rangle^{200}$ (MPa)	$\langle\sigma_{ij}\rangle^{211}$ (MPa)	$\langle\sigma_{ij}\rangle^{220}$ (MPa)	$\langle\sigma_{ij}\rangle^{310}$ (MPa)
$\begin{bmatrix} 54 & 0 & -3 \\ 0 & 48 & -1 \\ -3 & -1 & 991 \end{bmatrix}$	$\begin{bmatrix} 72 & 0 & 2 \\ 0 & 70 & -6 \\ 2 & -6 & 982 \end{bmatrix}$	$\begin{bmatrix} 67 & 0 & 4 \\ 0 & 71 & 0 \\ 4 & 0 & 987 \end{bmatrix}$	$\begin{bmatrix} 67 & 0 & -2 \\ 0 & 67 & 3 \\ -2 & 3 & 986 \end{bmatrix}$	$\begin{bmatrix} 66 & 0 & 1 \\ 0 & 66 & -2 \\ 1 & -2 & 987 \end{bmatrix}$

In Table 6.9, the reflection average stress tensors, $\langle\sigma_{ij}\rangle^{hkl}$, are listed for the 110, 200, 211, 220, and 310 reflections. We observe that $\langle\sigma_{ij}\rangle^{hkl}$ for all five reflections are close to the global average stress tensor of the grip region, $\bar{\sigma}_{ij}$ shown in Table 6.7. From this perspective V_{hkl} can be considered representative volume elements.

We next investigate if the diffraction stress analysis formalism, which forces a linear least-squares average along the diffraction vectors of various ψ–volumes, yields correct stress values when applied to a sample that contains St. Venant stresses.

6.4.1.2.2- Diffraction Strain/Stress Analysis of the Grip Regions

To simulate the diffraction stress analysis for the grip regions of our sample, we computed the average strain for each grain in this region, $\langle\varepsilon'_{11,\psi}\rangle_{i,\psi}$, by substituting its average strain tensor obtained from the finite element model into Eq. (1-11). This yielded the $\langle\varepsilon'_{11,\psi}\rangle^{W}_{i,\psi}$ $vs.\sin^2\psi$ plots shown in Fig. 6.10. Compared to the corresponding plots for the gage section (Fig. 6.9), these plots show significant scatter in the grain strains, and exhibit some non-linearities.

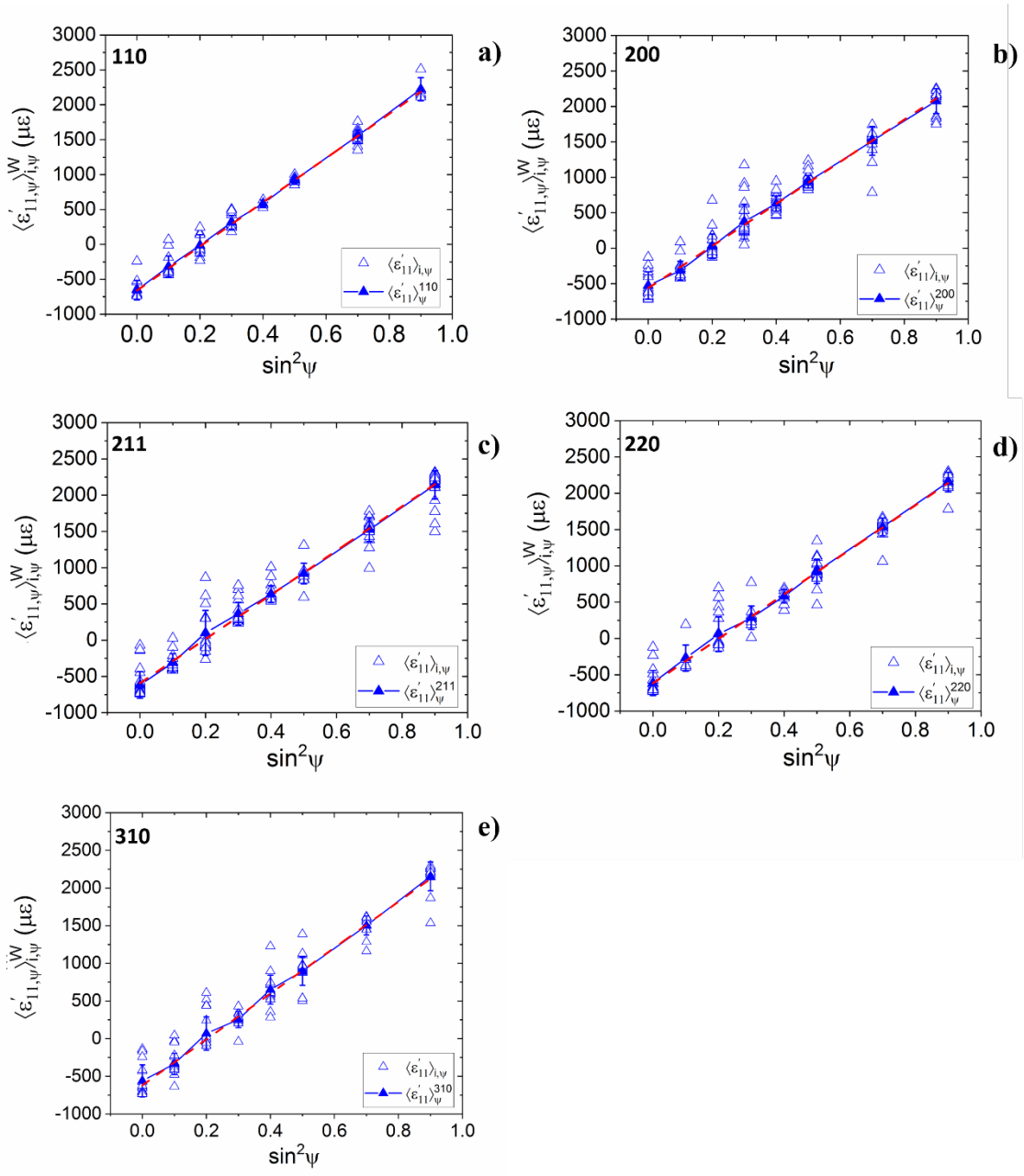

Figure 6.10: $\langle\varepsilon'_{11,\psi}\rangle^{W}_{i,\psi}$ *vs.* $sin^2\psi$ plots for studied reflections of the grip section of uniaxially loaded W bar.

To obtain the reflection average stress, $\langle\sigma_{33}^{D}\rangle^{hkl}$, we used Eq. (5-1-b), the slopes of least squares lines fitted to the $\langle\varepsilon'_{11,\psi}\rangle_{i,\psi}^{W}\ vs.\sin^2\psi$ data for each reflection, and the diffraction elastic constants at Voigt, Reuss, Kröner, and Neerfeld-Hill limits (Table 5.8). The computed stresses are shown in Table 6.10. Since the elastic moduli of W are identical for these four limits, the same stress value is obtained for each limit for a given reflection. The differences between the reflections, on the other hand, are due to St. Venant effects.

Table 6.10: The average stresses, $\langle\sigma_{33}^{D}\rangle^{Cu-hkl}$, obtained from simulated diffraction analysis of the plots shown in Fig. 6.10.

$\langle\sigma_{33}^{D}\rangle^{hkl}$ (MPa)	Voigt	Reuss	Neer.-Hill	Kröner
110	959±11	959±11	959 ±11	959±11
200	901±14	901±14	901±14	901±14
211	922±13	922±13	922±13	922±13
220	929±12	929±12	929±12	929±12
310	923±18	923±18	923±18	923±18

Table 6.11: The average strains in sample coordinates obtained from simulated diffraction analysis of the plots shown in Fig. 6.10. The averages for the reflection-ensembles in real space are also included, along with the model averages.

Reflection / Strain term	Isotropic (Eq. 6-3)	Model average	110	200	211	220	310
$\langle \varepsilon_{11}^{D} \rangle^{hkl} (\mu\varepsilon)$	-	-	-660±17	-562±21	-590±19	-593±19	-618±28
$\langle \varepsilon_{33}^{D} \rangle^{hkl} (\mu\varepsilon)$	-	-	2503±36	2408±45	2450±42	2455±42	2422±59
$\langle \varepsilon_{11} \rangle^{hkl} (\mu\varepsilon)$	-716	-660±146	-618±158	-581±198	-600±197	-611±167	-597±188
$\langle \varepsilon_{33} \rangle^{hkl} (\mu\varepsilon)$	2555	2490±134	2480±127	2430±181	2430±197	2460±161	2440±177

To further investigate this issue we analyzed the plots in Fig. 6.11 in terms of strain in the sample coordinates using Eq. (5-1-a). Table 5.10 lists the reflection average strain values, $\langle \varepsilon_{11}^{D} \rangle^{hkl}$, $\langle \varepsilon_{33}^{D} \rangle^{hkl}$, obtained directly from the slopes and intercepts of these plots. We also list the arithmetic averages of these terms, $\langle \varepsilon_{11} \rangle^{hkl}$, $\langle \varepsilon_{33} \rangle^{hkl}$, computed from the average strains in the sample coordinates for grains belonging to particular reflections. The averages obtained from diffraction analysis are different from the arithmetic averages in real space. The real space average strains in the transverse direction, $\langle \varepsilon_{11} \rangle^{hkl}$, are almost identical for all five reflections, and the model average, $\bar{\varepsilon}_{11}$. The same argument is also valid for the average strains along the loading direction. The differences in the in-plane strain terms, $\langle \varepsilon_{33}^{D} \rangle^{hkl}$ and $\langle \varepsilon_{33} \rangle^{hkl}$ for all reflections probably arise due to the forced linear fit on non-linear $\langle \varepsilon'_{11,\psi} \rangle_{i,\psi}^{W}$ $vs. \sin^2 \psi$ data, where the non-linearities are caused primarily by St. Venant stresses arising in response to boundary conditions.

In conclusion, the grip sections contain complicated stress/strain profiles due to FEpX boundary conditions. Such distributions introduce non-linearity in $\langle \varepsilon'_{11,\psi} \rangle^{W}_{i,\psi}$ $vs. \sin^2 \psi$ plots. The gage section, on the other hand, is under homogeneous uniaxial stress and yields the expected response for isotropic and W specimens. The introduction of crystal anisotropy and plastic flow will add interaction stresses into the model. Decomposition of these contributions from the St. Venant effects will be non-trivial for the stress distributions in the grip sections Consequently, in the following models, we will only consider the stress/strain distributions in the gage sections.

6.4.2- Uniaxial Tension of Single-phase Cu Bar

In this model, the single-phase Cu bar was extended to 5% strain corresponding to 334 MPa applied load (Fig. 6.1). In Fig. 6.11-a, we plot the global average stress components for the gage section vs. applied load during this extension. The average stress, $\bar{\sigma}_{33}$, increases linearly with applied load, σ^{app}. All other average stress components, $\bar{\sigma}_{ij,i\neq j=3}$, have zero values for all $\sigma_{33}^{App.}$. The dispersions of all $\bar{\sigma}_{ij}$, on the other hand, increase significantly with the plastic flow. In Fig. 6.11-b, we plot the global average strain components for the gage section vs. macroscopic extension strain, $\varepsilon_{33}^{App.}$. The dispersions of all $\bar{\varepsilon}_{ij}$ also increase significantly with the plastic flow.

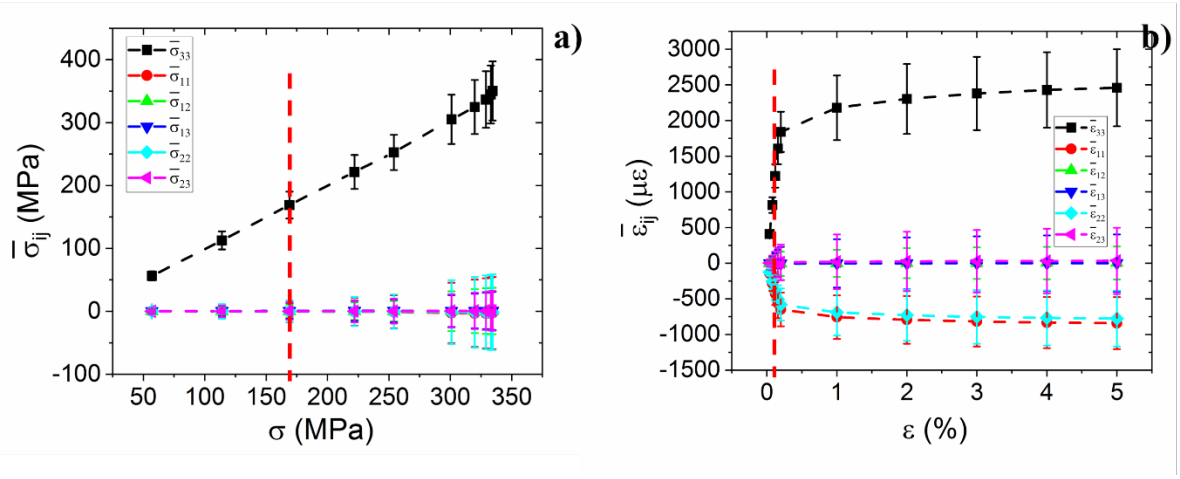

Figure 6.11: a) global average stress vs. applied stress b) global average lattice strain vs. applied strain.

By analyzing the data shown in Figs. 6.11-a & b we determined the proportional limit of the model material to be 220 MPa, corresponding to ~0.16% strain. These values are indicated by dashed lines in Fig. 6.11.

6.4.2.1- Uniaxial Tension of Single-phase Cu Bar at Elastic Regime

To analyze the distribution of Heyn stresses due to elastic incompatibility, we extended our virtual Cu sample to 1198 με, corresponding to 169.5 MPa applied load, along the $\vec{S}_3$ direction. As it can be seen from Fig. 6.11, this loading step is still within the macroscopic elastic limit. The expected strain and stress tensors for all points, $P(x, y, z)$, in an equivalent isotropic Cu bar for elastic loading (Eqs. (6-1 & 2)) are presented in Table 6.12. In this table, global average stress and lattice-strain tensors, $\bar{\sigma}_{ij}, \bar{\varepsilon}_{ij}$ and their standard deviations computed from the finite element model are also tabulated. We observe reasonable agreement between the analytical and the FEpX results

for both stresses and strains. However, the model averages show significant dispersions. These dispersions are due to the Heyn stresses arising to counteract elastic incompatibility between neighboring anisotropic Cu grains in the mesh.

Table 6.12: Stress and strain tensor for the gage section of the extended Cu model, computed using various approaches. The XRD values are the reflection averages of the stress and strain terms.

Parameter	Eqs. (6-1 & 2)	FEpX
Elastic strain ε_{ij}; $\bar{\varepsilon}_{ij}$	$\begin{bmatrix} -383 & 0 & 0 \\ 0 & -383 & 0 \\ 0 & 0 & 1198 \end{bmatrix}$	$\begin{bmatrix} -429(159) & -5(121) & -4(145) \\ -5(121) & -385(150) & -6(155) \\ -4(145) & -6(155) & 1220(165) \end{bmatrix}$
Stress σ_{ij}; $\bar{\sigma}_{ij}$ (MPa)	$\begin{bmatrix} 0 & 0 & 0 \\ 0 & 0 & 0 \\ 0 & 0 & 169.5 \end{bmatrix}$	$\begin{bmatrix} 5(17) & 0(11) & 0(12) \\ 0(11) & 7(18) & 0(14) \\ 0(12) & 0(14) & 169(21) \end{bmatrix}$

6.4.2.1.1- Stress Distributions in Sample Coordinates

In Table 6.13, we list the # of grains for each psi tilt and the volume fraction of the psi-volume for the gage section of the Cu specimen. Due to the random placement of grains, some psi-volumes have very small populations, notably those at ψ=33.21°, 45° for the 200 reflection.

Table 6.13: The population number for each ψ-ensemble N_{ψ}^{hkl} in the gage section of the Cu sample.

ψ(°)	0	18.43	26.57	33.21	39.23	45	56.79	71.57
N_{ψ}^{111}	47	14	18	4	35	59	59	11
N_{ψ}^{200}	19	23	37	38	26	8	23	6
N_{ψ}^{220}	20	9	11	1	9	2	22	8
N_{ψ}^{311}	6	19	6	7	9	5	7	23
N_{ψ}^{420}	32	14	41	6	11	30	8	9

In Fig. 6.12, we plot the grain average stress tensors for the 420 reflection[37] as a function of $\sin^2\psi$. The corresponding ψ-volume averages, $\langle\sigma_{ij}\rangle_{\psi}^{hkl}$, are also plotted in these figures. For the transverse directions, $\vec{S}_1, \vec{S}_2$, the global average normal stresses must be zero. Consequently, all stress terms in these directions are Heyn stresses. From the stress values plotted in Fig. 6.12, we observe that the grain average Heyn stresses due to elastic incompatibility, $\langle\sigma_{ij}\rangle_{i,\psi}$ can be up to 25% of the global average stress, $\bar{\sigma}_{33}$. The ψ-volume averages of the stress components, $\langle\sigma_{ij}\rangle_{\psi}^{hkl}$, are generally closer to the global average stresses, $\bar{\sigma}_{ij}$. However, there are ψ-volumes where $\langle\sigma_{ij}\rangle_{\psi}^{hkl}$ can be up to 10% different than $\bar{\sigma}_{ij}$. Consequently, these volumes cannot be considered as RVEs.

[3737] Other reflections exhibited similar responses and will not be shown for brevity.

In Table 6.14, the reflection average stress tensors, $\langle\sigma_{ij}\rangle^{hkl}$, are listed for the 111, 200, 220, 311, and 420 reflections. We observe that all reflection averages, $\langle\sigma_{ij}\rangle^{hkl}$, are quite close to the global average stress tensor, $\bar{\sigma}_{ij}$, shown in Table 6.12. Thus, to precision within the error of typical diffraction measurements, the Heyn stresses were averaged out from all (mutually exclusive) reflection volumes, V_{hkl}. From this perspective V_{hkl} can be considered RVEs.

We next investigate if the diffraction stress analysis formalism, which forces a linear least-squares average on the strains along the diffraction vectors of various ψ–volumes, yields correct stress values when applied to a sample that contains such heterogeneous stress states.

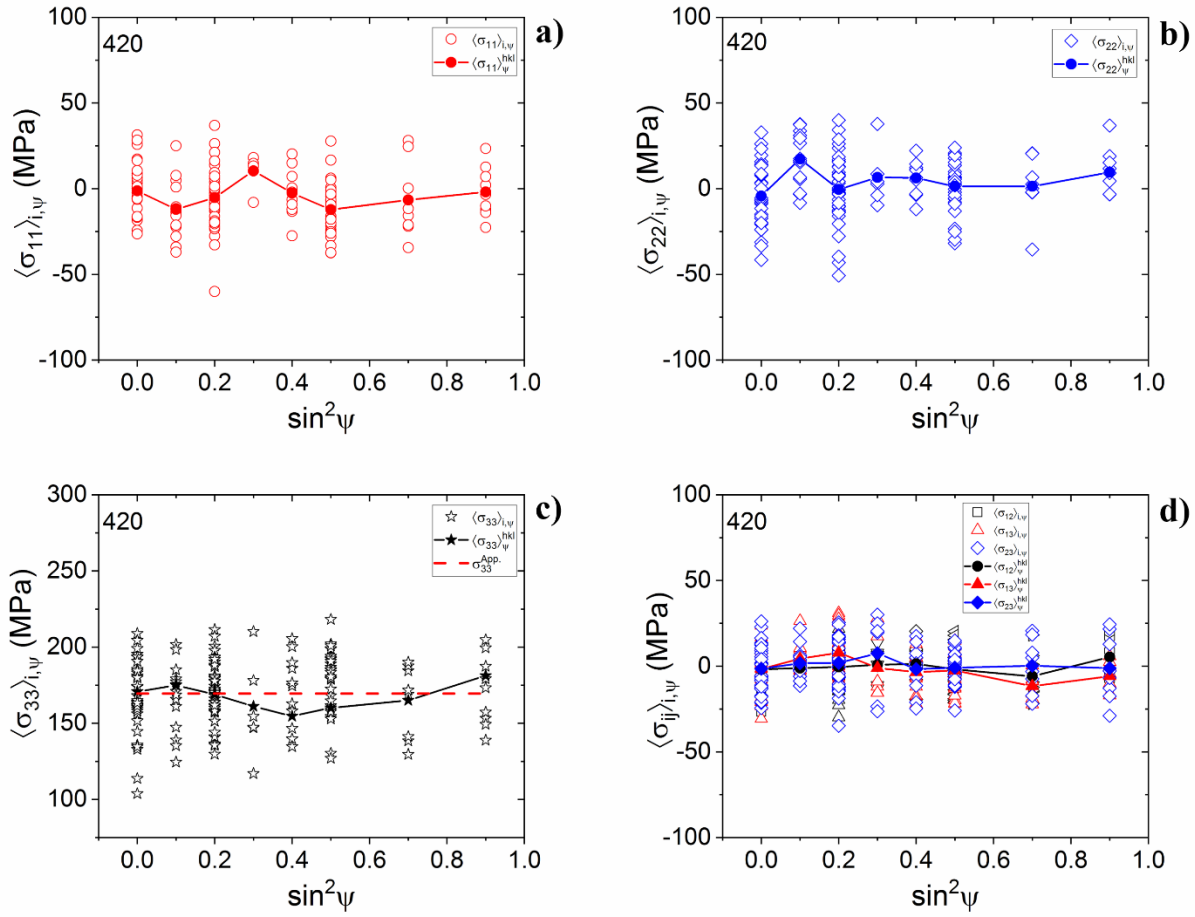

Figure 6.12: The grain stress average values a) $\langle\sigma_{11}\rangle_{i,\psi}$, b) $\langle\sigma_{22}\rangle_{i,\psi}$, c) $\langle\sigma_{33}\rangle_{i,\psi}$ d) shear stresses, for all grains diffracting into 420 reflection as a function of $\sin^2\psi$.

Table 6.14: Reflection average stress tensors, $\langle\sigma_{ij}\rangle^{hkl}$, for the 111, 200, 220, 311 and 420 reflections. The components of these tensors were obtained by averaging the particular average stress components, $\langle\sigma_{ij}\rangle_{i,\psi}$, (in the sample coordinates) of all grains for all ψ–tilts for each reflection.

$\langle\sigma_{ij}\rangle^{111}$ (MPa)	$\langle\sigma_{ij}\rangle^{200}$ (MPa)	$\langle\sigma_{ij}\rangle^{220}$ (MPa)	$\langle\sigma_{ij}\rangle^{311}$ (MPa)	$\langle\sigma_{ij}\rangle^{420}$ (MPa)
$\begin{bmatrix} 6 & 0 & 1 \\ 0 & -4 & -1 \\ 1 & -1 & 165 \end{bmatrix}$	$\begin{bmatrix} -5 & 1 & 1 \\ 1 & 1 & 2 \\ 1 & 2 & 173 \end{bmatrix}$	$\begin{bmatrix} -4 & 0 & -2 \\ 0 & 4 & 0 \\ -2 & 0 & 173 \end{bmatrix}$	$\begin{bmatrix} 2 & 3 & 1 \\ 3 & 1 & -1 \\ 1 & -1 & 167 \end{bmatrix}$	$\begin{bmatrix} -5 & -1 & 0 \\ -1 & 2 & 0 \\ 0 & 0 & 170 \end{bmatrix}$

6.4.2.1.2- Diffraction Strain/Stress Analysis

To simulate diffraction stress analysis for the gage section of our virtual Cu sample, we computed the average strain for each grain in the model, $\langle \varepsilon'_{11,\psi} \rangle_{i,\psi}$, by substituting its average strain tensor obtained from the finite element model into Eq. (1-11). This yielded the $\langle \varepsilon'_{11,\psi} \rangle_{i,\psi}^{Cu}$ $vs. \sin^2 \psi$ plots shown in Fig. 6.13. We also computed the Heyn interaction strains, $\langle \varepsilon'_{11,\psi} \rangle_{i,\psi}^{*Cu}$, for each grain from Eq. (5-7). These are shown in Fig. 6.14. To obtain the reflection average stress $\langle \sigma_{33}^{D} \rangle^{hkl}$, we used Eq. (5-1-b), the slopes of least squares lines fitted to the $\langle \varepsilon'_{11,\psi} \rangle_{i,\psi}^{Cu}$ $vs. \sin^2 \psi$ data for each reflection, and diffraction elastic constants at Voigt, Reuss, Kröner, and Neerfeld-Hill limits shown in Table 5.8. These results are shown in Table 6.15.

Comparing Tables 6.14 & 15, we observe that, for the 111, 200, 220, and 311 reflections, the axial stress values obtained from diffraction analysis, $\langle \sigma_{33}^{D} \rangle^{hkl}$, using the Kröner values for $S_2/2$ are not close to the expected average stress values in the sample coordinates. On the other hand, $\langle \sigma_{33}^{D} \rangle^{hkl}$ for 420 reflection is approximately the same as the global average stress, $\bar{\sigma}_{33} = 169$ MPa.

To further investigate this issue, we analyzed Fig 6.13 in terms of strain in the sample coordinates using Eq. (5-1-a). Table 6.16 lists the reflection average strain, $\langle \varepsilon_{11}^{D} \rangle^{hkl}$, $\langle \varepsilon_{33}^{D} \rangle^{hkl}$, obtained directly from the slopes and intercepts of these plots. We also list the arithmetic averages of these terms, $\langle \varepsilon_{11} \rangle^{hkl}$, $\langle \varepsilon_{33} \rangle^{hkl}$, computed from the average strains in the sample coordinates for grains belonging to particular reflections. The averages obtained from diffraction analysis for reflections except 220 are similar to the arithmetic averages in real space. For 220 reflection, the sampling statistics might be a problem since there is only 1 grain at ψ=33.21° and two grains at ψ=45°. The differences in the in-plane strain terms, $\langle \varepsilon_{33}^{D} \rangle^{hkl}$ and $\langle \varepsilon_{33} \rangle^{hkl}$ for all reflections

probably arise due to the forced linear fit on non-linear $\langle \varepsilon'_{11,\psi} \rangle_{i,\psi}^{Cu}$ $vs. \sin^2 \psi$ data, where the non-linearities are caused primarily by Heyn stresses arising in response to elastic incompatibility.

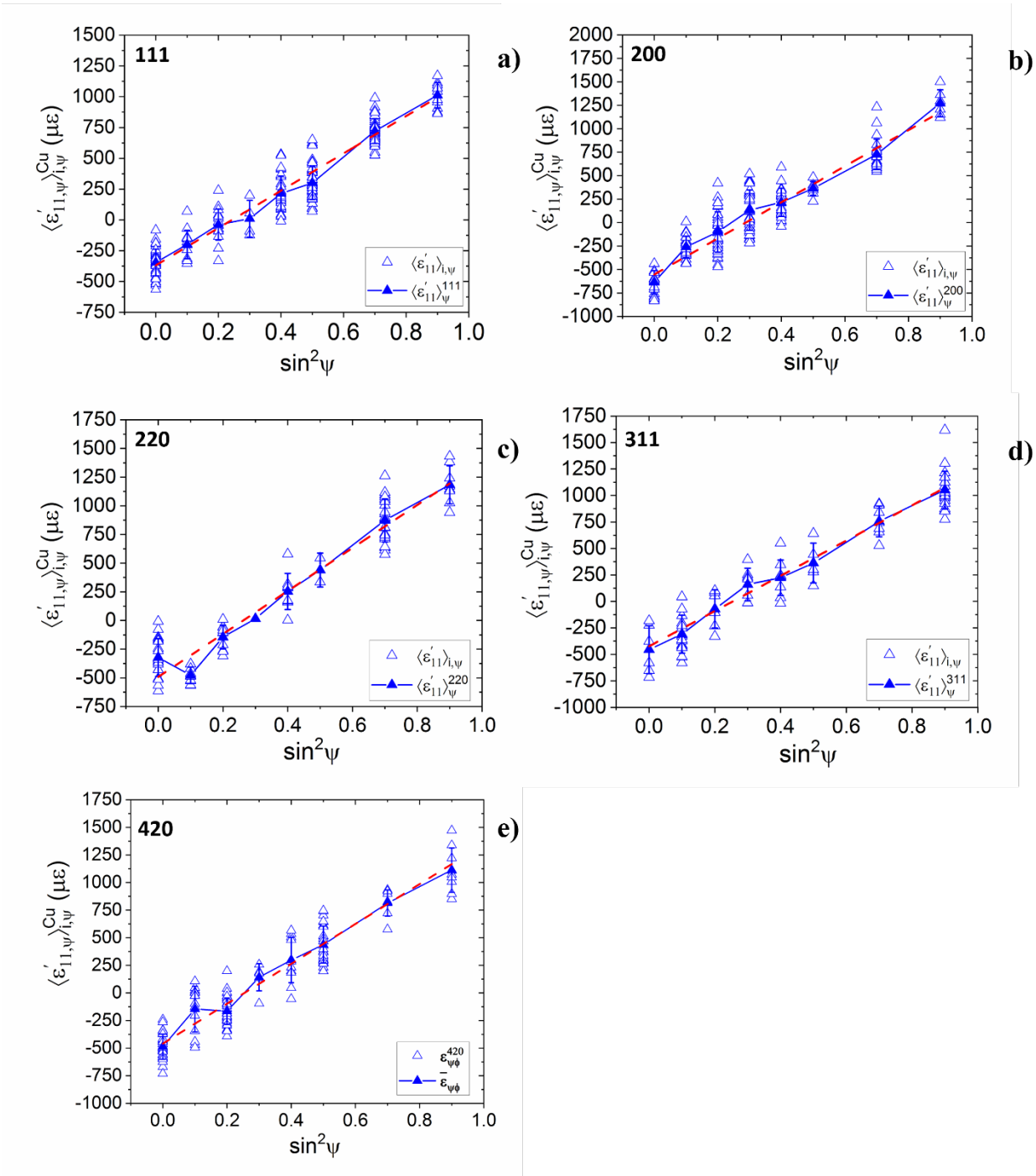

Figure 6.13: $\langle\varepsilon'_{11,\psi}\rangle^{Cu}_{i,\psi}$ *vs.* $sin^2\psi$ plots for all reflections of gage section of Cu bar uniaxially loaded to 169.5 MPa.

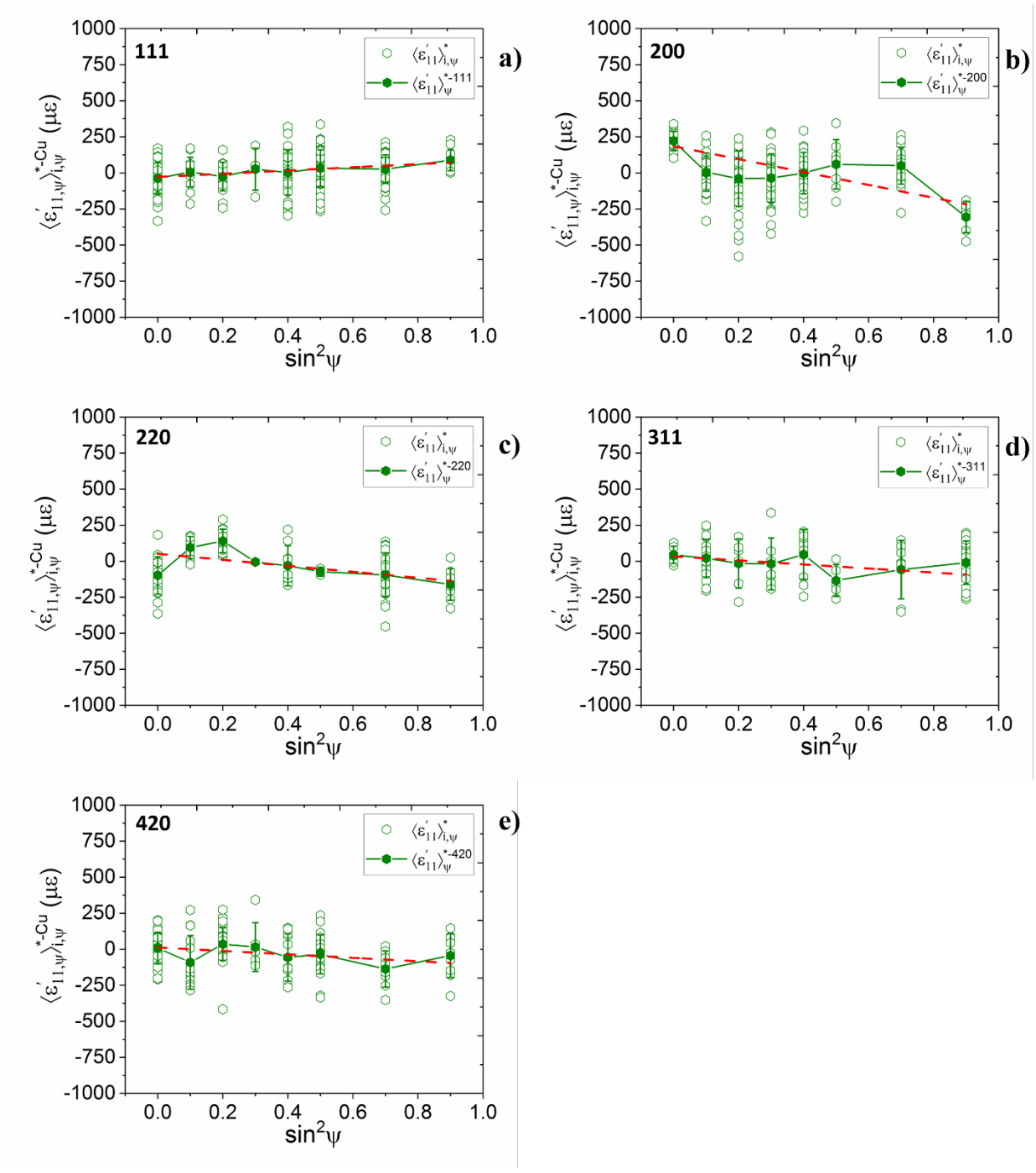

Figure 6.14: $\langle \varepsilon'_{11,\psi} \rangle^{*-Cu}_{i,\psi}$ *vs.* $sin^2\psi$ plots for all reflections of gage section of Cu bar uniaxially loaded to 169.5 MPa.

Table 6.15: The average stresses, $\langle \sigma_{33}^{D} \rangle^{Cu-hkl}$, obtained from simulated diffraction analysis of the plots shown in Fig. 6.14.

$\langle \sigma_{33}^{D} \rangle^{hkl}$ (MPa)	Voigt	Reuss	Neer.-Hill	Kröner
111	165±6	228±8	192±7	184±6
200	210±12	90±5	126±7	141±8
220	204±15	182±14	192±14	196±15
311	181±7	116±5	141±6	150±6
420	197±9	127±6	154±7	164±7

Table 6.16: The average strains in sample coordinates obtained from simulated diffraction analysis of the plots shown in Fig. 6.14. The averages for the reflection-ensembles in real space are also included, along with the model averages.

Reflection / Strain term	Isotropic (Eq. 6-3)	Model average	111	200	220	311	420
$\langle \varepsilon_{11}^{D} \rangle^{hkl} (\mu\varepsilon)$	-	-	-369±28	-553±53	-491±70	-423±33	-459±35
$\langle \varepsilon_{33}^{D} \rangle^{hkl}$ $(\mu\varepsilon)$	-	-	1245±53	1370±110	1383±140	1240±65	1347±79
$\langle \varepsilon_{11} \rangle^{hkl}$ $(\mu\varepsilon)$	-383	-429±156	-384±130	-572±118	-359±125	-402±154	-404±163
$\langle \varepsilon_{33} \rangle^{hkl}$ $(\mu\varepsilon)$	1198	1220±165	1200±151	1300±156	1170±141	1210±168	1280±320

.

6.4.2.2- Determination of Diffraction Elastic Constants for Single-phase W & Cu

In what follows we simulate the measurement of diffraction elastic constants (DECs). For this purpose, we employed the traditional procedure [19]. As before, these computations were performed only for the gage sections of our virtual W and Cu samples.

6.4.2.2.1-Diffraction Determination of DECs for Single-phase W

The loads to which the W model was loaded, and the slopes, m_{hkl}, and intercepts, I_{hkl} of the $\langle \varepsilon'_{11,\psi} \rangle^{W}_{i,\psi}$ $vs. sin^2\psi$ plots for these loads (and their fit errors), are listed in Table 6.17. As expected, we obtain identical m_{hkl}, I_{hkl} for all reflections.

Table 6.17: m_{hkl}, and I_{hkl} of the $\langle \varepsilon'_{11,\psi} \rangle^{W}_{i,\psi}$ $vs. sin^2\psi$ plots for the loads, 198, 396, 594, 792, 990 MPa.

	m_{hkl}	I_{hkl}	$\sigma_{33}^{App.}$ (MPa)
(110)	654± 0.4	-145±0.2	198
(200)	1310±1.0	-289±0.4	396
(211)	1960±1.6	-434±0.6	594
(220)	2610±2.1	-579±0.8	792
(310)	3260±2.7	-723±1.0	990

In Fig. 6.15, we plot the variation of these slopes and intercepts with applied load. Since $m_{hkl} = \frac{S_2}{2}\sigma_{33}^{App.}$ and $I_{hkl} = -S_1\sigma_{33}^{App.}$, these DEC values can be obtained from the slopes of Figs. 6.15-a & b. These values, S_1^{SP-Sim} and $\frac{S_2}{2}^{SP-Sim}$, are listed in Table 6.18. We observe that the

diffraction analysis yields exactly the elastic moduli computed from the single crystal compliances of W. We conclude that, as expected, the analysis formalism is valid for fully isotropic materials.

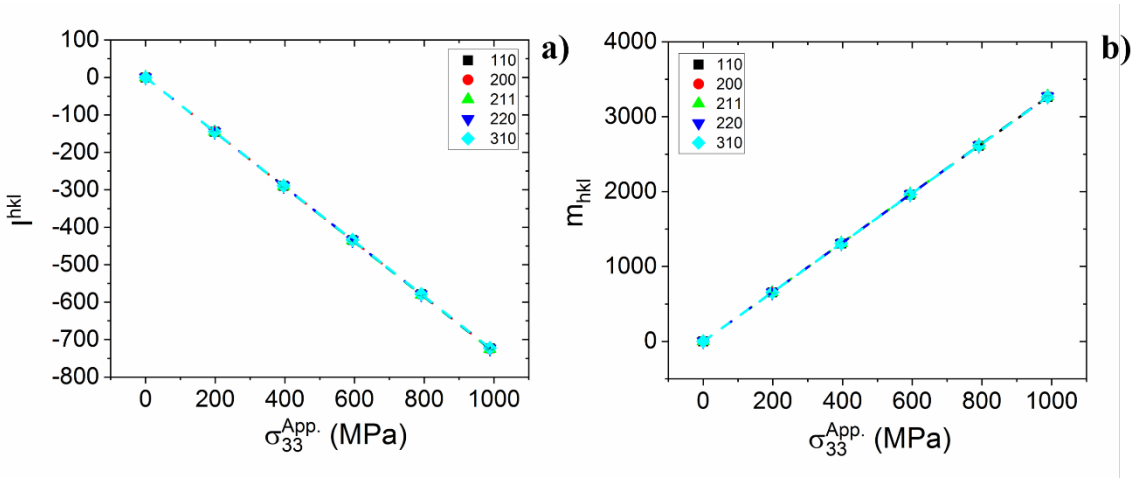

Figure 6.15: Variation of I_{hkl} and m_{hkl} with respect to $\sigma_{33}^{App.}$ for all reflections in the gage section of W.

Table 6.18: Diffraction elastic constants, S_1^{SP-Sim} and $\frac{S_2}{2}^{SP-Sim}$, obtained from the FEA analysis of the gage section of single-phase W. Values computed from single-elastic compliances at the Voigt. Reuss, Neerfeld-Hill and Kröner limits are also shown.

	Reuss/Voigt/Neer.-Hill/Kröner		Simulation	
$(TPa)^{-1}$	S_1	$S_2/2$	S_1^{SP-Sim}	$\frac{S_2}{2}^{SP-Sim}$
(110)	-0.73	3.30	-0.73	3.30
(200)	-0.73	3.30	-0.73	3.30
(211)	-0.73	3.30	-0.73	3.30
(220)	-0.73	3.30	-0.73	3.30
(310)	-0.73	3.30	-0.73	3.30

6.4.2.2.2-Diffraction Determination of DECs for Single-phase Cu

To test the effects of Heyn stresses arising due to elastic incompatibility at the grain boundaries of a polycrystalline sample with anisotropic crystallites, we modeled the DEC

measurement for our single-phase Cu sample. In this set of simulations, the (virtual) Cu sample was loaded to 56.5, 113, and 159.5 MPa along $\vec{S}_3$. All of these loads are in the elastic region for Cu (Fig. 6.11). Diffraction elastic constants S_1^{SP-Sim} and $\frac{S_2}{2}^{SP-Sim}$ for the gage section of single-phase Cu bar, computed from the variation of the slopes and intercepts of the $\langle \varepsilon'_{11,\psi} \rangle_{I,\psi}^{Cu}$ vs. $\sin^2\psi$ with applied load, are tabulated, respectively, in Tables 6.19 & 20. DEC values computed from single-elastic compliances at the Voigt. Reuss, Neerfeld-Hill and Kröner limits are also shown. For ease of comparison, we include the deviation of the simulation values from the Kröner limit.

In the case of 111, 311, and 420 reflections the S_1^{SP-Sim} and $\frac{S_2}{2}^{SP-Sim}$ values are within 11% or less of the Kröner limit, and can be considered acceptable. The values for 200 and 222 reflections, on the other hand, are problematic. For the 220 reflection, both S_1^{SP-Sim} and $\frac{S_2}{2}^{SP-Sim}$ values fall outside the ranges, 0.38 TPa^{-1}, 1.14 TPa^{-1}, respectively, spanned by the Voigt and Reuss limits. This might be a sampling issue: For the 220 reflection, the ψ-ensembles for the 33.21° and 45° ψ-tilts contain one and two grains, respectively. These ψ-ensembles cannot be considered representative volume elements.

For the 200 reflection, both S_1^{SP-Sim} and $\frac{S_2}{2}^{SP-Sim}$ are between the Voigt and Reuss limits. However, in both cases, these are about 20% different than the Kröner limit, which usually agrees much better with experimental values reported in the literature [107]**.** This might also be a sampling issue, however, the populations of the ψ-ensembles for the 200 reflection are comparable with those of the 111, 311, and 420 reflections, and this reflection has the second-highest reflection population. To investigate these issues further, we performed a larger simulation by modeling the

stress-strain responses of four additional (random) models, each with 1500 grains, and analyzing the results together with the original model. An example $\langle \varepsilon'_{11,\psi} \rangle^{Cu}_{I,\psi}$ vs. $\sin^2\psi$ plot is shown in Fig. 6.16.

Table 6.19: Diffraction elastic constant, S_1^{SP-Sim}, obtained from the FEA analysis of the gage section of single-phase Cu. Values are computed from single-elastic compliances at the Voigt, Reuss, Neerfeld-Hill and Kröner limits. % Deviation of simulated S_1^{SP-Sim} from Kröner was also shown.

S_1 (TPa)$^{-1}$	Reuss	Voigt	Neer.-Hill	Kröner	S_1^{SP-Sim}	% Dev. From Kröner
(111)	-1.40	-2.24	-1.83	-1.93	-2.17±0.01	11
(200)	-6.28	-2.24	-4.26	-3.73	-2.92±0.01	22
(220)	-2.62	-2.24	-2.43	-2.38	-2.76±0.01	9
(311)	-3.98	-2.24	-3.11	-2.88	-2.62±0.01	11
(420)	-3.94	-2.24	-3.09	-2.87	-2.75±0.01	4

Table 6.20: Diffraction elastic constant, $\frac{S_2^{SP-Sim}}{2}$, obtained from the FEA analysis of the gage section of single-phase Cu. Values are computed from single-elastic compliances at the Voigt, Reuss, Neerfeld-Hill and Kröner limits. % Deviation of simulated $\frac{S_2}{2}^{SP-Sim}$ from Kröner was also shown.

$S_2/2$ (TPa)$^{-1}$	Reuss	Voigt	Neer.-Hill	Kröner	$\frac{S_2}{2}^{SP-Sim}$	% Dev. From Kröner
(111)	6.65	9.17	7.91	8.24	8.78±0.01	6
(200)	21.28	9.17	15.23	13.63	10.90±0.01	20
(220)	10.31	9.17	9.74	9.58	10.82±0.01	11
(311)	14.39	9.17	11.78	11.09	9.87±0.01	11
(420)	14.26	9.17	11.72	11.04	10.14±0.01	8

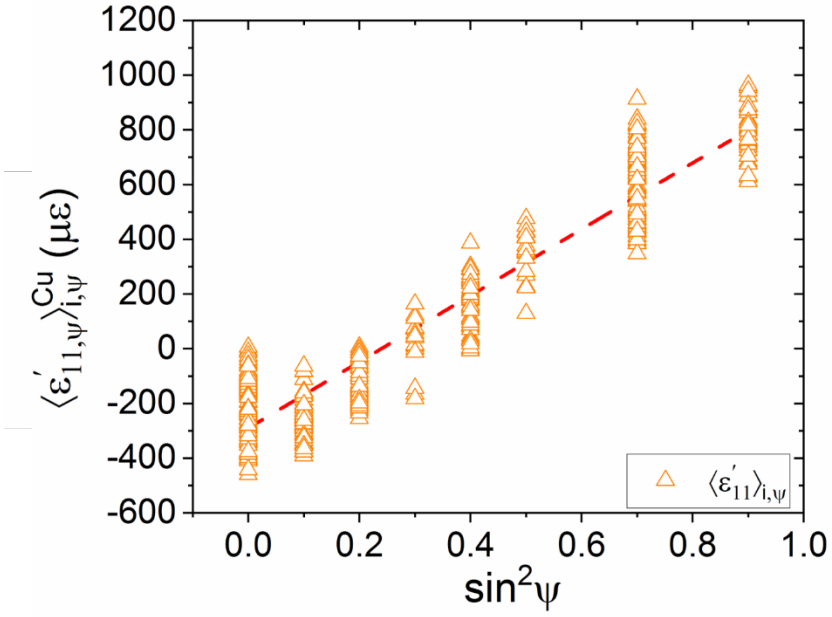

Figure 6.16: $\langle \varepsilon'_{11,\psi} \rangle_{i,\psi}^{Cu}$ $vs.$ $sin^2\psi$ plot for the Cu 220 reflection of the combined model at $\sigma_{33}^{App.} = 113\ MPa$. Strain values from all 417 grains of the 220 reflection in the gage section are plotted.

Table 6.21: Population distribution of grains in the gage section of the combined model.

ψ(°)	0	18.43	26.57	33.21	39.23	45	56.79	71.57	N_{hkl}^{Total}
N_{ψ}^{111}	212	62	76	30	150	245	292	55	1122
N_{ψ}^{200}	94	121	159	168	175	37	132	33	919
N_{ψ}^{220}	98	56	58	15	44	20	95	31	417
N_{ψ}^{311}	36	130	31	26	27	17	55	98	420
N_{ψ}^{420}	167	81	226	36	48	191	45	38	832
N_{ψ}^{Total}	607	450	550	275	444	510	619	255	3710

The population distribution of grains in the gage section of the combined model, with a total of 3710 grains, is shown in Table 6.21. All populations have increased approximately five-fold. The ψ-ensemble with the smallest population, 15 grains, still belongs to the 220 reflection at ψ=33.21°.

In Table 6.22, we summarize the results of the stress analysis of the combined model. The slopes, m_{hkl}, and intercepts, I_{hkl} obtained from regression fit the $\langle \varepsilon'_{11,\psi} \rangle_{i,\psi}^{Cu}$ $vs. sin^2\psi$ plots, and their fit errors are listed. In contrast to the W response (Table 6.17), the m_{hkl}, I_{hkl} values for all reflections are different, reflecting the anisotropy of the Cu.

Table 6.22: Slopes, m_{hkl}, and intercepts, I_{hkl} ,of regression fits of $\langle \varepsilon'_{11,\psi} \rangle_{i,\psi}^{Cu}$ $vs.$ $sin^2\psi$ plots for applied loads, 56.5, 113, 159.5 MPa for the gage section of the combined sample.

$\sigma_{33}^{App.}$ (MPa)	56.5 MPa		113 MPa		159.5 MPa	
	m_{hkl}	I_{hkl}	m_{hkl}	I_{hkl}	m_{hkl}	I_{hkl}
(111)	493±5	-121±2	985±10	-241±5	1480±14	-361±7
(200)	609±8	-158±3	1220±17	-315±7	1830±25	-473±10
(220)	605±10	-145±5	1210±20	-290±9	1820±30	-435±14
(311)	558±8	-141±4	1120±16	-282±9	1670±24	-422±13
(420)	580±8	-145±3	1160±15	-289±6	1740±23	-433±9

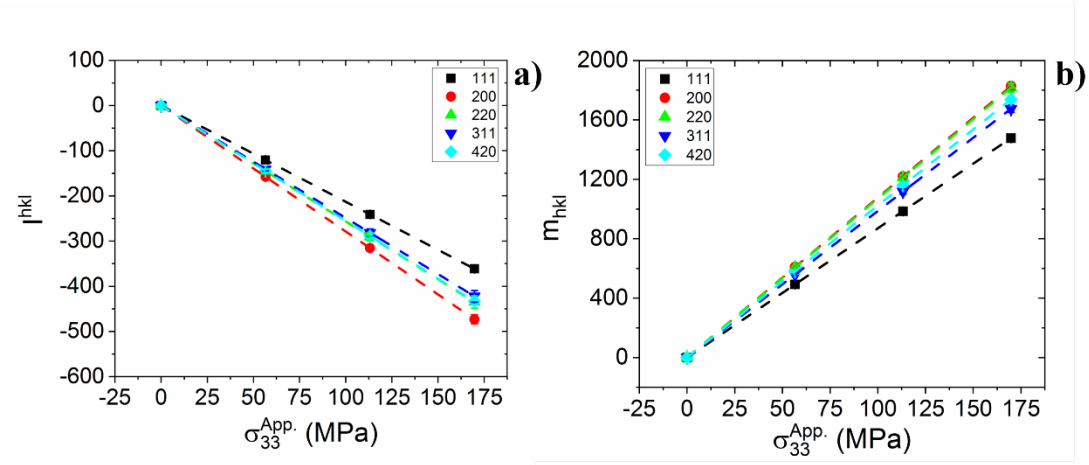

Figure 6.17: Variation of I_{hkl} and m_{hkl} with respect to $\sigma_{33}^{App.}$ for all reflections in the gage section of combined Cu sample

Table 6.23: Diffraction elastic constant, S_1^{SP-Sim}, obtained from the FEA analysis of the gage section of combined Cu sample. Values are computed from single-elastic compliances at the Voigt, Reuss, Neerfeld-Hill and Kröner limits. % Deviation of simulated S_1^{SP-Sim} from Kröner was also shown.

S_1 (TPa)$^{-1}$	Reuss	Voigt	Neer.-Hill	Kröner	S_1^{SP-Sim}	% Dev. From Kröner
(111)	-1.40	-2.24	-1.83	-1.93	-2.13±0.01	9
(200)	-6.28	-2.24	-4.26	-3.73	-2.79±0.01	25
(220)	-2.62	-2.24	-2.43	-2.38	-2.55±0.01	6
(311)	-3.98	-2.24	-3.11	-2.88	-2.49±0.01	14
(420)	-3.94	-2.24	-3.09	-2.87	-2.55±0.01	11

Table 6.24: Diffraction elastic constant, $\frac{S_2}{2}^{SP-Sim}$, obtained from the FEA analysis of the gage section of combined Cu sample. Values are computed from single-elastic compliances at the Voigt, Reuss, Neerfeld-Hill and Kröner limits. % Deviation of simulated $\frac{S_2}{2}^{SP-Sim}$ from Kröner was also shown. Young's Modulus, E^{hkl}, and Poisson's ratio, ν^{hkl}, are calculated from S_1^{SP-Sim} and $\frac{S_2}{2}^{SP-Sim}$ values.

$S_2/2$ (TPa)$^{-1}$	Reuss	Voigt	Neer.-Hill	Kröner	$\frac{S_2}{2}^{SP-Sim}$	% Dev. From Kröner	E^{hkl} (GPa)	ν^{hkl}
(111)	6.65	9.17	7.91	8.24	8.70±0.01	5	152	0.32
(200)	21.28	9.17	15.23	13.63	10.77±0.01	21	125	0.35
(220)	10.31	9.17	9.74	9.58	10.68±0.01	10	123	0.31
(311)	14.39	9.17	11.78	11.09	9.87±0.01	10	136	0.34
(420)	14.26	9.17	11.72	11.04	10.24±0.01	7	130	0.33

In Fig. 6.17, we plot the variation of these slopes and intercepts with applied load. The values for S_1^{SP-Sim} and $\frac{S_2}{2}^{SP-Sim}$ obtained from the slopes of regression fits in Figs. 6.17-a & b, respectively, are listed in Tables 6.23 & 24. Comparing these values with those for the original (small) model, Tables 6.18 & 19, respectively, we observe that a five-fold population increase has changed the $\frac{S_2}{2}^{SP-Sim}$ values for all reflections by 1% or less. The $\frac{S_2}{2}^{SP-Sim}$ value for the 220

reflection is still outside the Reuss – Voigt range, and the deviation of the $\frac{S_2}{2}^{SP-Sim}$ value for the 200 reflection is still around 20%. We observe larger changes in the S_1^{SP-Sim} values, between 2 to 8 %, obtained for the combined model. Notably, the S_1^{SP-Sim} value for the 220 reflection is, now, in the Reuss – Voigt range, having dropped by 8%. We note that the real space stress and strain averages for all of these reflections were equal to the macroscopic values, indicating that the reflection volumes could be considered RVEs. We decided to compare the DECs obtained from our models with the $\frac{-\nu}{E}$ and $\frac{1+\nu}{E}$ values obtained from the macroscopic values for Young's modulus, E=138 GPa, ν=0.33, calculated from the stress-strain curve of Cu shown in Fig. 6.1. This comparison is shown in Table 6.25[38]. We observe agreement within 10% for all reflections, including the 200. We conclude that, for our model, it is better to use macroscopic elastic moduli rather than DEC values.

As a final check of the results, we combined all $\langle \varepsilon'_{11,\psi} \rangle_{I,\psi}^{hkl}$ data from all reflections at each ψ and computed the elastic constants of the gage section using the full data-set, rather than relying on taking averages of averages. These values are shown in Table 6.26 and they agree with macroscopic elastic moduli values within 4%. $\langle E'_{11,\psi} \rangle_{I,\psi}^{Cu}$ vs. $\sin^2\psi$ sketched from all reflections at each ψ is shown in Fig. 6.18.

[38] Here we list S_1^{SP-Sim} and $\frac{S_2^{SP-Sim}}{2}$ values computed by assuming that the ψ-volume strains are linear or volume-weighted averages of the grain strains. The results are equivalent within the dispersion of the data.

Table 6.25: DEC values for each model used in the combined analysis, their averages, and $\frac{-\nu}{E}$ and $\frac{1+\nu}{E}$ values computed from macroscopic values. All values are in TPa^{-1}.

Macroscopic	$\frac{-\nu}{E}$	$\frac{1+\nu}{E}$		
$(TPa)^{-1}$	-2.38	9.63	-	-
	Arithmetic Averages		Volume-weighted Averages	
$(TPa)^{-1}$	S_1^{SP-Sim}	$\frac{S_2}{2}^{SP-Sim}$	S_1^{SP-Sim}	$\frac{S_2}{2}^{SP-Sim}$
Model 0	-2.76±0.01	10.81±0.02	-3.01±0.01	11.01±0.02
Model 1	-2.77±0.01	10.82±0.02	-2.69±0.01	10.55±0.02
Model 2	-2.92±0.01	11.14±0.02	-2.62±0.01	10.64±0.02
Model 3	-2.75±0.01	10.99±0.02	-2.84±0.01	10.96±0.02
Model 4	-2.63±0.01	10.79±0.02	-2.64±0.01	10.82±0.02
Average	-2.77±0.09	10.91±0.14	-2.76±0.09	10.80±0.14

Table 6.26: DEC values for the combined model computed using the full data set from all reflections at each ψ. Young's Modulus, E, and Poisson's ratio, ν, are calculated from DEC values.

$(TPa)^{-1}$	S_1^{SP-Sim}	$\frac{S_2}{2}^{SP-Sim}$	E	ν
All	-2.47±0.01	9.81±0.02	136	0.34

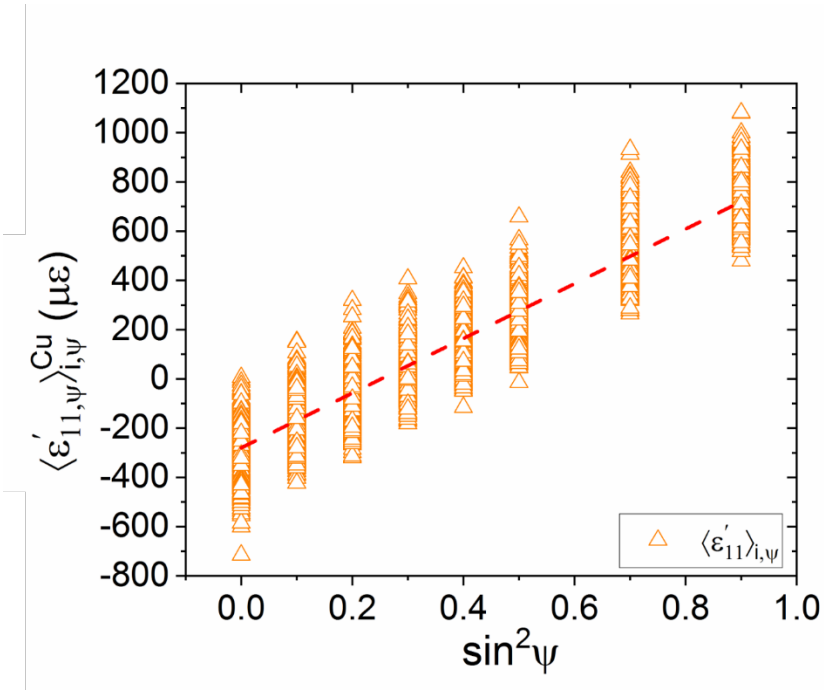

Figure 6.18: $\langle \varepsilon'_{11,\psi} \rangle^{Cu}_{i,\psi}$ *vs.* $sin^2\psi$ plot from all reflection at each ψ for the combined model at $\sigma^{App.}_{33} = 113\ MPa$. Strain values from all 3710 grains in the gage section are plotted.

6.4.2.3- Uniaxial Tension of Single-phase Cu Bar at Plastic Regime

To investigate the effect of plastic flow on Heyn stresses, we extended our virtual Cu sample[39] to 5000 με, corresponding to 334.5 MPa applied load, along the $\vec{S}_3$ direction. This load is within the macroscopic plastic region (Fig. 6.11). In Fig. 6.19, we plot the equivalent plastic strains, $\langle \varepsilon^{eqpl} \rangle^{hkl}_{\psi}$ as a function of $sin^2\psi$ for all reflections. We observe that: (1) average equivalent plastic strains are finite for all ψ-ensembles. (2) average equivalent plastic strain for grains oriented to diffract into all reflections is approximately equal to the global average equivalent plastic strain. As a result, uniform plastic deformation is observed for all reflections.

[39] We use the 7500 grain Cu sample for better statistics.

The expected strain and stress tensors for all points, $P(x, y, z)$, in an equivalent isotropic Cu bar for elastic loading (Eqs. (6-1 & 2)) are presented in Table 6.27. In this table, global average stress and lattice-strain tensors, $\bar{\sigma}_{ij}, \bar{\varepsilon}_{ij}$ and their standard deviations computed from the finite element model are also tabulated. We note that analytical calculations were carried out assuming a linear elastic model. Even though all grains underwent extensive plastic flow in this model, there is reasonable agreement between the analytical calculations and FEpX results. However, the strain and stress components reported by the model exhibit large dispersions due to the Heyn stresses arising to counteract elastic and plastic incompatibility between neighboring anisotropic Cu grains in the mesh.

Table 6.27: Stress and strain tensor for the gage section of the extended Cu model, computed using various approaches. The XRD values are the reflection averages of the stress and strain terms.

Parameter	Eqs. (6-1 & 2)	FEpX
Elastic strain ε_{ij}; $\bar{\varepsilon}_{ij}$	$\begin{bmatrix} -756 & 0 & 0 \\ 0 & -756 & 0 \\ 0 & 0 & 2364 \end{bmatrix}$	$\begin{bmatrix} -815(373) & -5(229) & -30(425) \\ -5(229) & -816(391) & -2(448) \\ -30(425) & -2(448) & 2470(539) \end{bmatrix}$
Stress σ_{ij}; $\bar{\sigma}_{ij}$ (MPa)	$\begin{bmatrix} 0 & 0 & 0 \\ 0 & 0 & 0 \\ 0 & 0 & 334.5 \end{bmatrix}$	$\begin{bmatrix} -3(59) & 0(37) & 0(30) \\ 0(37) & -3(59) & 0(32) \\ 0(30) & 0(14) & 351(48) \end{bmatrix}$

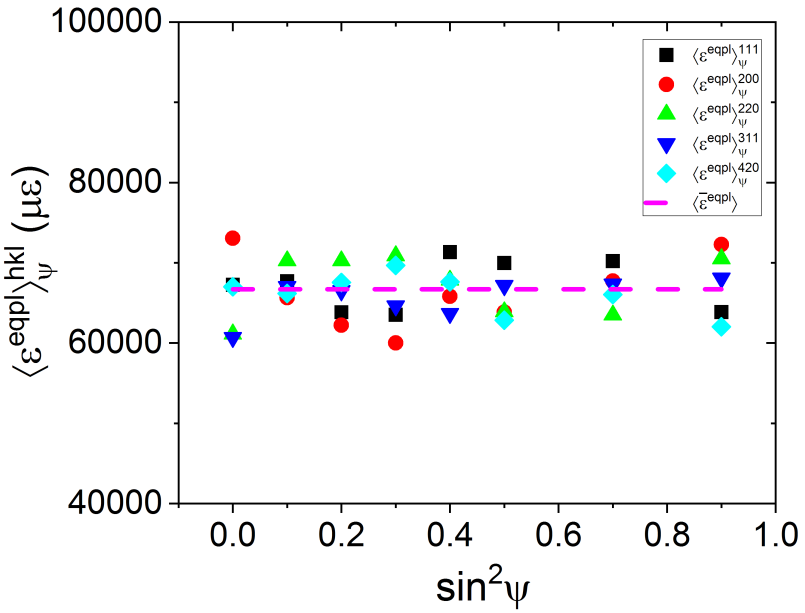

Figure 6.19: ψ-volume averages of equivalent plastic strain values in sample coordinates, $\langle \boldsymbol{\varepsilon}^{\boldsymbol{eqpl}} \rangle_{\boldsymbol{\psi}}^{\boldsymbol{hkl}}$ for the $\boldsymbol{\psi}$ -ensembles diffracting into the 111, 200, 220,311 & 420 reflections.

6.4.2.3.1- Stress Distributions in Sample Coordinates

In Fig. 6.20, we plot the grain average stress tensors for the 420 reflection as a function of $\sin^2\psi$. The corresponding ψ-volume averages $\langle \sigma_{ij} \rangle_{\psi}^{hkl}$ are also plotted in these figures. For the transverse directions, $\vec{S}_1, \vec{S}_2$, the global average normal stresses must be zero. Consequently, all stress terms in these directions are Heyn stresses. From the stress values plotted in Fig. 6.20, we observe that the grain average Heyn stresses due to elastic and plastic incompatibility, $\langle \sigma_{ij} \rangle_{i,\psi}$ can be up to 70% of the global average stress, $\bar{\sigma}_{33}$. The dispersion of stress in sample coordinates increases with the increasing plastic flow. The ψ-volume averages of the stress components, $\langle \sigma_{ij} \rangle_{\psi}^{hkl}$, are generally close to the global average stresses, $\bar{\sigma}_{ij}$; the maximum difference between

$\langle\sigma_{ij}\rangle_{\psi}^{hkl}$ and $\bar{\sigma}_{ij}$ is less than 10%. Consequently, within the precision of a routine measurement, most of these ψ-volumes can be considered representative volume elements.

In Table 6.28, the reflection average stress tensors, $\langle\sigma_{ij}\rangle^{hkl}$, are listed for the 111, 200, 220, 311, and 420 reflections. We observe that all reflection averages, $\langle\sigma_{ij}\rangle^{hkl}$, except 111 reflection, are quite close to the global average stress tensor, $\bar{\sigma}_{ij}$ shown in Table 6.27; for the 111 reflection, we observe finite transverse normal stresses. Since Heyn stresses were averaged out from the (mutually exclusive) reflection volumes, V_{hkl}, for the 200, 220, 311 and 420 reflections, these V_{hkl} can be considered RVEs.

Table 6.28: Reflection average stress tensors, $\langle\sigma_{ij}\rangle^{hkl}$, for the 111, 200, 220, 311, and 420 reflections. The components of these tensors were obtained by averaging the particular average stress components, $\langle\sigma_{ij}\rangle_{i,\psi}$, (in the sample coordinates) of all grains for all ψ–tilts for each reflection.

$\langle\sigma_{ij}\rangle^{111}$ (MPa)	$\langle\sigma_{ij}\rangle^{200}$ (MPa)	$\langle\sigma_{ij}\rangle^{220}$ (MPa)	$\langle\sigma_{ij}\rangle^{311}$ (MPa)	$\langle\sigma_{ij}\rangle^{420}$ (MPa)
$\begin{bmatrix} 22 & 0 & 0 \\ 0 & -21 & -1 \\ 0 & -1 & 343 \end{bmatrix}$	$\begin{bmatrix} -14 & 0 & 0 \\ 0 & 4 & 0 \\ 0 & 0 & 357 \end{bmatrix}$	$\begin{bmatrix} -12 & 2 & -3 \\ 2 & 8 & 1 \\ -3 & 1 & 354 \end{bmatrix}$	$\begin{bmatrix} -5 & 1 & -1 \\ 1 & 4 & 2 \\ -1 & 2 & 353 \end{bmatrix}$	$\begin{bmatrix} -17 & -1 & 4 \\ -1 & 2 & -1 \\ 4 & -1 & 353 \end{bmatrix}$

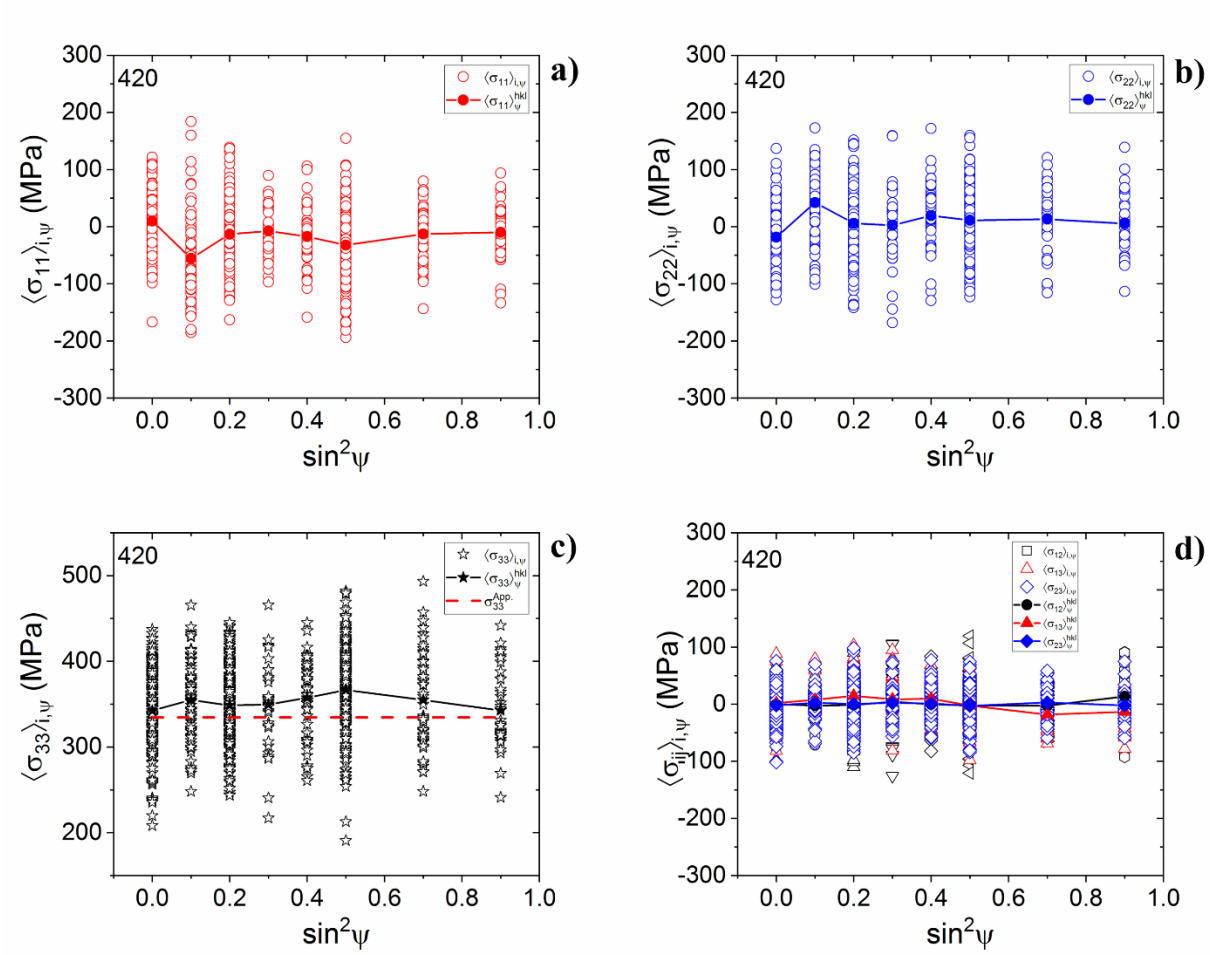

Figure 6.20: The grain stress average values a) $\langle\sigma_{11}\rangle_{i,\psi}$, b) $\langle\sigma_{22}\rangle_{i,\psi}$, c) $\langle\sigma_{33}\rangle_{i,\psi}$ d) shear stresses, for all grains diffracting into 420 reflection as a function of $\sin^2\psi$..

6.4.2.3.2- Diffraction Strain/Stress Analysis

To simulate diffraction stress analysis for the gage section of our virtual Cu sample, we computed the average strain for each grain in the model, $\langle\varepsilon'_{11,\psi}\rangle_{i,\psi}$, by substituting its average strain tensor obtained from the finite element model into Eq. (1-11). This yielded the $\langle\varepsilon'_{11,\psi}\rangle_{i,\psi}^{Cu}\ vs.\sin^2\psi$ plots shown in Fig. 6.21. We also computed the Heyn interaction strains, $\langle\varepsilon'_{11,\psi}\rangle_{i,\psi}^{*Cu}$, for each grain from Eq. (5-7). These are shown in Fig. 6.22.

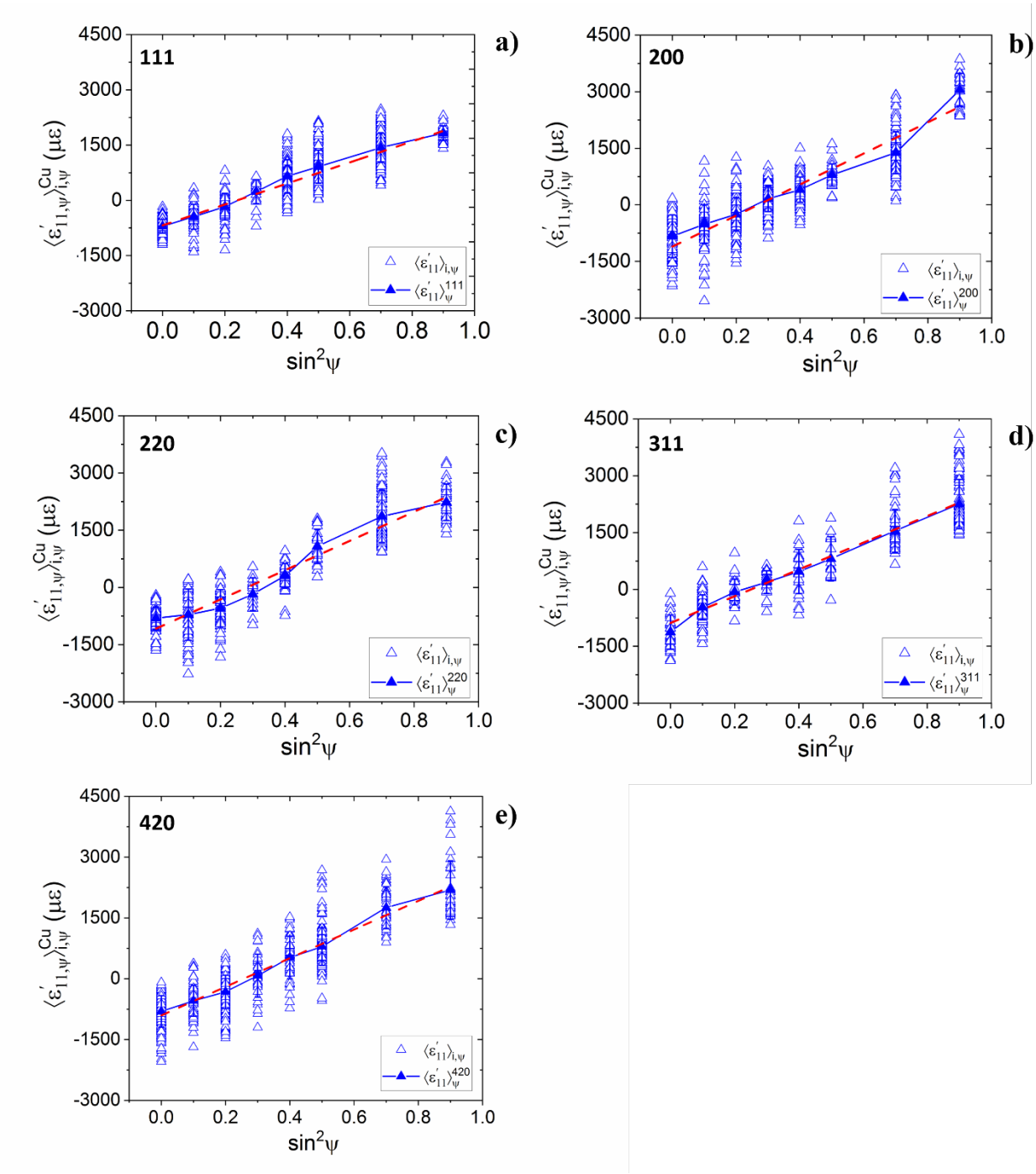

Figure 6.21: $\langle \varepsilon'_{11,\psi} \rangle^{Cu}_{i,\psi}$ *vs.* $sin^2\psi$ plots for all reflections of gage section of Cu bar uniaxially loaded to 334.5 MPa.

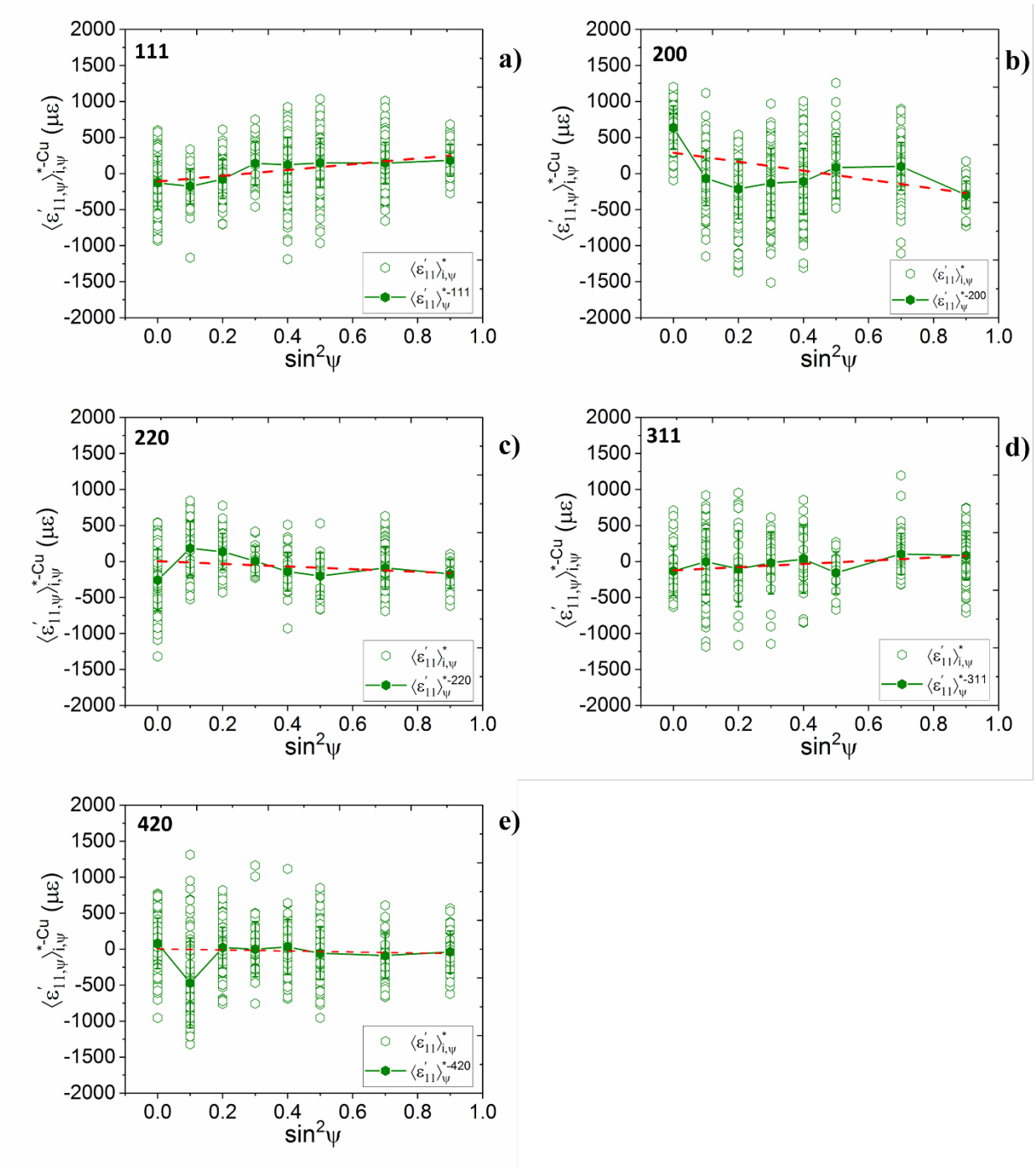

Figure 6.22: $\langle\varepsilon'_{11,\psi}\rangle^{*-Cu}_{i,\psi}$ *vs.* $sin^2\psi$ plots for all reflections of gage section of Cu bar uniaxially loaded to 334.5 MPa.

To obtain the reflection average stress $\langle\sigma_{33}^{D}\rangle^{hkl}$, we used Eq. (5-1-b), the slopes of least squares lines fitted to the $\langle\varepsilon'_{11,\psi}\rangle_{i,\psi}^{Cu}$ $vs.\sin^2\psi$ data for each reflection, and diffraction elastic constants at Voigt, Reuss, Kröner, Neerfeld-Hill shown in Table 5.8 and simulated ones ($DEC^{SP-Sim.}$) shown in Table 6.24. These results are shown in Table 6.29.

Table 6.29: The average stresses, $\langle\sigma_{33}^{D}\rangle^{Cu-hkl}$, obtained from simulated diffraction analysis of the plots shown in Fig. 6.19. For comparison, $\bar{\sigma}_{ij} = 351\ MPa$.

$\langle\sigma_{33}^{D}\rangle^{hkl}$ (MPa)	Voigt	Reuss	Neer.-Hill	Kröner	$DEC^{SP-Sim.}$
111	313±9	431±13	363±11	348±10	330±10
200	451±40	194±17	272±24	303±27	384±35
220	419±33	373±30	394±31	401±32	360±29
311	387±22	246±14	301±17	320±19	359±20
420	397±17	343±11	310±13	329±14	355±15

Comparing Tables 6.28 & 29, we observe that, for the 220, 311, and 420 reflections, the axial stress values obtained from diffraction analysis, $\langle\sigma_{33}^{D}\rangle^{hkl}$, using $\frac{S_2}{2}^{SP-Sim}$ are quite close to the global average stress, $\bar{\sigma}_{33} = 351$ MPa, in the sample coordinates. On the other hand, $\langle\sigma_{33}^{D}\rangle^{hkl}$ for 111 and 200 reflections deviate, respectively, -6% and +9% from this value. While not ideal, these values are acceptable for routine practice. We note, however, that the $\langle\varepsilon'_{11,\psi}\rangle_{i,\psi}$ vs. $\sin^2\psi$ plots in Fig. 6.21 are non-linear. To check the significance of these non-linearities, we utilized our

method introduced in Chapter 5, where we remove the first two values $\langle \varepsilon'_{11,\psi} \rangle_{i,\psi}$ and re-calculate the stresses. These results are shown in Table 6.30:

Table 6.30: The average stresses obtained from simulated diffraction analysis of the plots shown in Fig. 6.21 after removal of first two ψ-ensemble points.

$\langle \sigma_{33}^{D} \rangle^{hkl}$ (MPa)	Simulated	% Dev. from Table 6.29
111	315±18	5%
200	415±45	8%
220	398±37	10%
311	331±15	8%
420	383±19	7%

Comparing Tables 6.29 & 30, we observe that, the stress values obtained from diffraction analysis after removal of first two ψ-ensembles, $\langle \sigma_{33}^{D} \rangle^{hkl}$, obtained using the simulated limits for all reflections are different than the ones obtained from without removing the first two ψ-ensembles. The change of $\langle \sigma_{33}^{D} \rangle^{hkl}$ values for all directions can be up to 10 % different. We conclude that $\langle \varepsilon'_{11,\psi} \rangle_{i,\psi}$ vs. $\sin^2 \psi$ for all reflections show some oscillatory behavior.

Table 6.31: The average strains in sample coordinates obtained from simulated diffraction analysis of the plots shown in Fig. 6.21. The averages for the reflection-ensembles in real space are also included, along with the model averages.

Reflection / Strain term	Isotropic (Eq. 6-3)	Model average	111	200	220	311	420
$\langle \varepsilon_{11}^{D} \rangle^{hkl} (\mu\varepsilon)$	-	-	-694±45	-1120±176	-1090±146	-904±73	-937±62
$\langle \varepsilon_{33}^{D} \rangle^{hkl} (\mu\varepsilon)$	-	-	2176±85	3020±371	2750±304	2650±198	2744±155
$\langle \varepsilon_{11} \rangle^{hkl} (\mu\varepsilon)$	-756	-814±373	-778±370	-822±378	-886±396	-825±366	-815±360
$\langle \varepsilon_{33} \rangle^{hkl} (\mu\varepsilon)$	2364	2470±539	2520±538	2410±481	2540±610	2490±599	2430±520

To further investigate this issue, we analyzed Fig 6.21 in terms of strain in the sample coordinates using Eq. (5.1-a). Table 6.31 lists the reflection average strain, $\langle \varepsilon_{11}^{D} \rangle^{hkl}$, $\langle \varepsilon_{33}^{D} \rangle^{hkl}$, obtained directly from the slopes and intercepts of these plots. We also list the arithmetic averages of these terms, $\langle \varepsilon_{11} \rangle^{hkl}$, $\langle \varepsilon_{33} \rangle^{hkl}$, computed from the average strains in the sample coordinates for grains belonging to particular reflections. Table 6.32 summarizes these strain tensors. In Table 6.33, we list the stresses in the sample coordinates obtained from these strain tensors. For this computation, we used the isotropic Hooke's law with (1) the elastic moduli of individual reflections, E^{hkl}, ν^{hkl}, computed from Tables 6.24 & 25, (2) the elastic moduli of the combined model, E, ν, computed from Tables 6.27.

Thus, for the entire sample, we have the following strain tensors:

Table 6.32: Global strain tensors from the isotropic equation, model average, and for the reflections in the model.

$\boldsymbol{\varepsilon_{ij}}$ **(Eq. (6-1 &2))**	$\begin{pmatrix} -756 & & \\ & -756 & \\ & & 2364 \end{pmatrix}$
$\boldsymbol{\bar{\varepsilon}_{ij}}$	$\begin{pmatrix} -814 & & \\ & -814 & \\ & & 2470 \end{pmatrix}$
$\boldsymbol{\langle \varepsilon_{ij}^{D} \rangle^{111}}$	$\begin{pmatrix} -694 & & \\ & -694 & \\ & & 2176 \end{pmatrix}$
$\boldsymbol{\langle \varepsilon_{ij}^{D} \rangle^{200}}$	$\begin{pmatrix} -1120 & & \\ & -1120 & \\ & & 3020 \end{pmatrix}$
$\boldsymbol{\langle \varepsilon_{ij}^{D} \rangle^{220}}$	$\begin{pmatrix} -1090 & & \\ & -1090 & \\ & & 2750 \end{pmatrix}$
$\boldsymbol{\langle \varepsilon_{ij}^{D} \rangle^{311}}$	$\begin{pmatrix} -904 & & \\ & -904 & \\ & & 2650 \end{pmatrix}$
$\boldsymbol{\langle \varepsilon_{ij}^{D} \rangle^{420}}$	$\begin{pmatrix} -937 & & \\ & -937 & \\ & & 2744 \end{pmatrix}$

Table 6.33: The computed reflection average stresses from the average strain tensors listed in Table 6.32 and (1) E^{hkl}, ν^{hkl}, (2) E, ν.

(MPa)	E^{hkl}, ν^{hkl}	E, ν
111	$\begin{pmatrix} 4 & & \\ & 4 & \\ & & 333 \end{pmatrix}$	$\begin{pmatrix} 12 & & \\ & 12 & \\ & & 304 \end{pmatrix}$
200	$\begin{pmatrix} -20 & & \\ & -20 & \\ & & 364 \end{pmatrix}$	$\begin{pmatrix} -32 & & \\ & -32 & \\ & & 389 \end{pmatrix}$
220	$\begin{pmatrix} -57 & & \\ & -57 & \\ & & 302 \end{pmatrix}$	$\begin{pmatrix} -52 & & \\ & -52 & \\ & & 340 \end{pmatrix}$
311	$\begin{pmatrix} -3 & & \\ & -3 & \\ & & 357 \end{pmatrix}$	$\begin{pmatrix} -4 & & \\ & -4 & \\ & & 358 \end{pmatrix}$
420	$\begin{pmatrix} -7 & & \\ & -7 & \\ & & 352 \end{pmatrix}$	$\begin{pmatrix} -5 & & \\ & -5 & \\ & & 370 \end{pmatrix}$

In Table 6.33, we observe that computed reflection average stresses from E^{hkl}, ν^{hkl} are in reasonable agreement with the computed ones from E, ν. The difference in the axial stresses between the two is up to % 11. Comparing Tables 6.28 & 33, we observe that 311 and 420 reflections have close values whereas, other reflections have differences. Even though 200, 222, 311, and 420 reflections were considered as RVEs, the computed stress tensors for those reflections are not equal to real space reflection averages. We see that diffraction stress formalism does not work even if some reflections are considered as RVEs. We can conclude for diffraction stress formalism work, each ψ volume must be RVEs. We also understand that the calculated stress tensors from Table 6.32 are representative for 311, 420 reflections.

6.4.2.4- Single-phase Cu Bar at Zero External Load after Tensile Plastic Flow

In this simulation, the virtual single-phase Cu bar was unloaded completely after being extended to 5 % total strain. The far-field stress is zero. Consequently, any stress components which might exist within the sample volume must be self-equilibrating. Table 6.34 shows the global average stress tensors and their distribution parameters. These values were calculated over all grains in gage sections. The minimum and maximum values reflect the extrema in the relevant grain average stresses/strains. The average stress tensor components are zero. However, all stress terms exhibit wide distributions; These are caused in response to the heterogeneous distribution of plastic flow in the grains, and also contain contributions from the heterogeneous distribution of elastic moduli. Similar to the global stress averages, all average lattice strain values are also approximately zero, with wide distributions (Table 6.35).

Table 6.34: Global average stress tensor of the gage section of Cu bar at zero external load after plastic flow and its dispersion parameters. All values are in MPa.

(MPa)	$\bar{\sigma}_{11}$	$\bar{\sigma}_{12}$	$\bar{\sigma}_{13}$	$\bar{\sigma}_{22}$	$\bar{\sigma}_{23}$	$\bar{\sigma}_{33}$
Average	**-2**	**0**	**0**	**-2**	**0**	**0**
Std. Dev	33	22	18	34	19	32
Maximum	126	80	74	118	77	109
Minimum	-154	-79	-92	-142	-60	-139
Full Width	**280**	**159**	**176**	**260**	**137**	**248**

Table 6.35: Average lattice strain tensor of the gage section of Cu bar at zero external load after plastic flow and its dispersion parameters. All values are in microstrain (με).

(με)	$\bar{\varepsilon}_{11}$	$\bar{\varepsilon}_{12}$	$\bar{\varepsilon}_{13}$	$\bar{\varepsilon}_{22}$	$\bar{\varepsilon}_{23}$	$\bar{\varepsilon}_{33}$
Average	**16**	**5**	**-3**	**22**	**3**	**-47**
Std. Dev	410	326	239	422	252	320
Maximum	1540	1450	957	1510	865	1390
Minimum	-1490	-1120	-934	-1320	-859	-1270
Full Width	3020	2570	1891	2830	1720	2660

6.4.2.4.1- Stress Distributions in Sample Coordinates

In Fig. 6.23, we plot the grain average stress components for all grains in the grip section as a function of $\sin^2\psi$. These average stresses contain contributions because of elastic and plastic incompatibility. We observe that individual grains can have very different (average) stress tensors from each other and the global averages of the gage region.

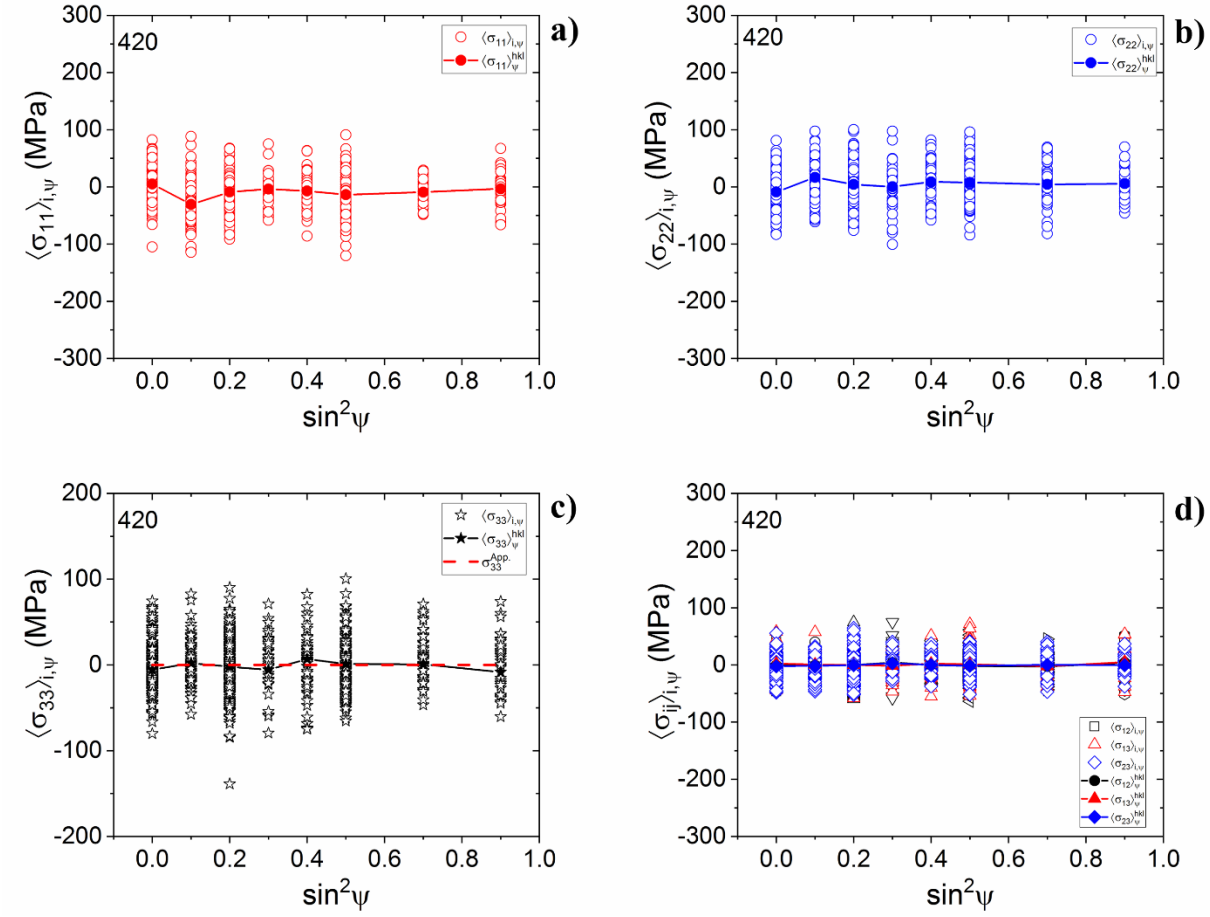

Figure 6.23: The grain stress average values a) $\langle\sigma_{11}\rangle_{i,\psi}$, b) $\langle\sigma_{22}\rangle_{i,\psi}$, c) $\langle\sigma_{33}\rangle_{i,\psi}$ d) shear stresses, for all grains as a function of $\sin^2\psi$.

The ψ-volume averages of the stress components, $\langle\sigma_{ij}\rangle_{\psi}^{hkl}$, are listed in Table 6.36. 13 out of 25, psi-volumes have stress tensors that have large determinants, these cannot be considered representative volumes, and will cause oscillations in $\langle\varepsilon'_{11,\psi}\rangle_{i,\psi}^{Cu}$ $vs.\sin^2\psi$. plots of the particular reflections. However, if we check the reflection averages of the stresses in sample coordinates, Table 6.37, we observe that these variations are averaged out to zero. Consequently, for our virtual

sample with its relatively low plastic strain distribution, reflection volumes are representative volume elements.

Table 6.36: ψ-ensemble average stress tensors, $\langle \sigma_{ij} \rangle_{\psi}^{hkl}$, for the 111, 200, 220, 311, and 420 reflections.

	0	18.43	26.57	33.21	39.23	45	56.79	71.57
111	$\begin{pmatrix} -2 & 0 & -2 \\ 0 & -3 & 1 \\ -2 & 1 & -6 \end{pmatrix}$	$\begin{pmatrix} -10 & -1 & 1 \\ -1 & 7 & 3 \\ 1 & 3 & 2 \end{pmatrix}$	$\begin{pmatrix} -10 & -1 & -2 \\ -1 & -5 & 1 \\ -2 & 1 & -2 \end{pmatrix}$	$\begin{pmatrix} -2 & -1 & 5 \\ -1 & -1 & -4 \\ 5 & -4 & -6 \end{pmatrix}$	$\begin{pmatrix} 6 & 1 & 4 \\ 1 & -9 & 1 \\ 4 & 1 & 7 \end{pmatrix}$	$\begin{pmatrix} 15 & 1 & -2 \\ 1 & -19 & 0 \\ -2 & 0 & 1 \end{pmatrix}$	$\begin{pmatrix} 24 & -1 & -1 \\ -1 & -27 & 1 \\ -1 & 1 & 1 \end{pmatrix}$	$\begin{pmatrix} 4 & -1 & -5 \\ -1 & -4 & -6 \\ -5 & -6 & -8 \end{pmatrix}$
200	$\begin{pmatrix} 28 & -1 & -2 \\ -1 & -22 & 2 \\ -2 & 2 & 16 \end{pmatrix}$	$\begin{pmatrix} 3 & 1 & -4 \\ 1 & 0 & -1 \\ -4 & -1 & 3 \end{pmatrix}$	$\begin{pmatrix} -12 & 1 & -3 \\ 1 & 5 & -2 \\ -3 & -2 & -2 \end{pmatrix}$	$\begin{pmatrix} -16 & -1 & 2 \\ -1 & 7 & 0 \\ 2 & 0 & -2 \end{pmatrix}$	$\begin{pmatrix} -16 & 0 & 1 \\ 0 & 12 & -1 \\ 1 & -1 & -8 \end{pmatrix}$	$\begin{pmatrix} -13 & -5 & 6 \\ -5 & 6 & -1 \\ 6 & -1 & -10 \end{pmatrix}$	$\begin{pmatrix} -6 & 0 & 2 \\ 0 & 6 & -3 \\ 2 & -3 & -4 \end{pmatrix}$	$\begin{pmatrix} -9 & 1 & 4 \\ 1 & 5 & 2 \\ 4 & 2 & 20 \end{pmatrix}$
220	$\begin{pmatrix} -12 & -1 & -1 \\ -1 & 1 & 2 \\ -1 & 2 & -5 \end{pmatrix}$	$\begin{pmatrix} 9 & 0 & -5 \\ 0 & 5 & -5 \\ -5 & -5 & -4 \end{pmatrix}$	$\begin{pmatrix} 0 & 3 & -12 \\ 3 & -5 & 0 \\ -12 & 0 & 7 \end{pmatrix}$	$\begin{pmatrix} -5 & 4 & -2 \\ 4 & -3 & 0 \\ -2 & 0 & 1 \end{pmatrix}$	$\begin{pmatrix} -17 & -2 & -3 \\ -2 & 7 & 3 \\ -3 & 3 & 8 \end{pmatrix}$	$\begin{pmatrix} -13 & 3 & 3 \\ 3 & -6 & -3 \\ 3 & -3 & 2 \end{pmatrix}$	$\begin{pmatrix} -15 & -2 & 4 \\ -2 & 7 & 1 \\ 4 & 1 & 7 \end{pmatrix}$	$\begin{pmatrix} -17 & 3 & -2 \\ 3 & 13 & -1 \\ -2 & -1 & -11 \end{pmatrix}$
311	$\begin{pmatrix} -12 & 5 & -3 \\ 5 & 7 & 0 \\ -3 & 0 & 6 \end{pmatrix}$	$\begin{pmatrix} 3 & -7 & -3 \\ -7 & -4 & 1 \\ -3 & 1 & 2 \end{pmatrix}$	$\begin{pmatrix} -2 & -3 & -1 \\ -3 & -6 & 1 \\ -1 & 1 & -14 \end{pmatrix}$	$\begin{pmatrix} -3 & 2 & 1 \\ 2 & 10 & -6 \\ 1 & -6 & 7 \end{pmatrix}$	$\begin{pmatrix} -2 & 7 & 0 \\ 7 & 2 & -5 \\ 0 & -5 & 1 \end{pmatrix}$	$\begin{pmatrix} -8 & 7 & -4 \\ 7 & -9 & -5 \\ -4 & -5 & -8 \end{pmatrix}$	$\begin{pmatrix} -5 & 7 & 4 \\ 7 & 7 & -4 \\ 4 & -4 & 8 \end{pmatrix}$	$\begin{pmatrix} -6 & 5 & 0 \\ 5 & 7 & 9 \\ 0 & 9 & 6 \end{pmatrix}$
420	$\begin{pmatrix} 5 & -1 & 2 \\ -1 & 9 & -2 \\ 2 & -2 & -3 \end{pmatrix}$	$\begin{pmatrix} -31 & -1 & 1 \\ -1 & 17 & -1 \\ 1 & -1 & 3 \end{pmatrix}$	$\begin{pmatrix} -9 & 0 & 0 \\ 0 & 4 & 0 \\ 0 & 0 & -4 \end{pmatrix}$	$\begin{pmatrix} -4 & 4 & -2 \\ 4 & 0 & 3 \\ -2 & 3 & 3 \end{pmatrix}$	$\begin{pmatrix} -7 & 0 & 2 \\ 0 & 9 & 0 \\ 2 & 0 & -2 \end{pmatrix}$	$\begin{pmatrix} -14 & -2 & 1 \\ -2 & 8 & -2 \\ 1 & -2 & -1 \end{pmatrix}$	$\begin{pmatrix} -9 & -3 & -2 \\ -3 & 4 & 0 \\ -2 & 0 & 7 \end{pmatrix}$	$\begin{pmatrix} -3 & 4 & 5 \\ 4 & 6 & -1 \\ 5 & -1 & 2 \end{pmatrix}$

Table 6.37: Reflection average stress tensors, $\langle\sigma_{ij}\rangle^{hkl}$, for the 111, 200, 220, 311 and 420 reflections. The components of these tensors were obtained by averaging the particular average stress components, $\langle\sigma_{ij}\rangle_{i,\psi}$, (in the sample coordinates) of all grains for all ψ–tilts for each reflection.

$\langle\sigma_{ij}\rangle^{111}$ (MPa)	$\langle\sigma_{ij}\rangle^{200}$ (MPa)	$\langle\sigma_{ij}\rangle^{220}$ (MPa)	$\langle\sigma_{ij}\rangle^{311}$ (MPa)	$\langle\sigma_{ij}\rangle^{420}$ (MPa)
$\begin{bmatrix} 9 & 0 & -1 \\ 0 & -13 & 0 \\ -1 & 0 & 0 \end{bmatrix}$	$\begin{bmatrix} -7 & 0 & 0 \\ 0 & 4 & -1 \\ 0 & -1 & 0 \end{bmatrix}$	$\begin{bmatrix} -9 & 0 & -2 \\ 0 & 3 & 0 \\ -2 & 0 & 1 \end{bmatrix}$	$\begin{bmatrix} -3 & 1 & -1 \\ 1 & 2 & 1 \\ -1 & 1 & 3 \end{bmatrix}$	$\begin{bmatrix} 3 & -1 & 1 \\ -1 & 4 & -1 \\ 1 & -1 & -1 \end{bmatrix}$

6.4.2.4.2- Diffraction Strain/Stress Analysis

To simulate diffraction stress analysis for the gage section of our virtual Cu sample, we substituted the relevant average strain tensor components for each grain in the model, $\langle\varepsilon'_{11,\psi}\rangle_{i,\psi}$, into Eq. (1-11). This yielded the $\langle\varepsilon'_{11,\psi}\rangle_{i,\psi}^{Cu}$ $vs.\sin^2\psi$ plots shown in Fig. 6.24. The average response is oscillatory.

To obtain the reflection average stress $\langle\sigma_{33}^{D}\rangle^{hkl}$, we used Eq. (5-1-b), the slopes of least squares lines fitted to the $\langle\varepsilon'_{11,\psi}\rangle_{i,\psi}^{Cu}$ $vs.\sin^2\psi$ data for each reflection. We used diffraction elastic constants at Voigt, Reuss, Kröner, Neerfeld-Hill limits, shown in Table 5.8, and the simulation DEC values, S_1^{SP-Sim} and $\frac{S_2}{2}^{SP-Sim}$, shown in Table 6.24. These stress results are shown in Table 6.38. We observe that all reflections yield zero stress values within typical experimental limits. To test for oscillations, we removed the first two points from each plot and re-analyzed the data. The results are shown in Table 6.39.

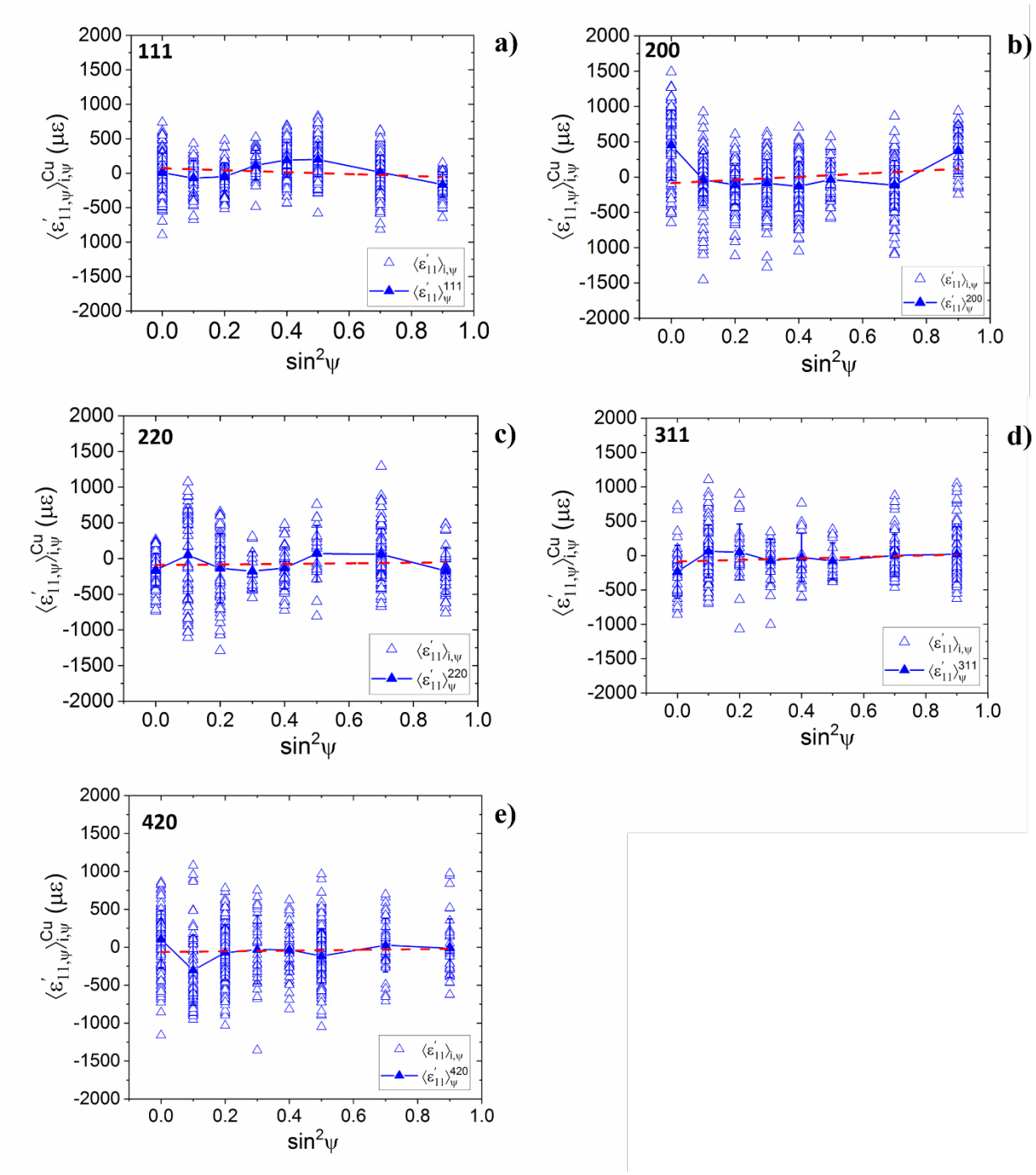

Figure 6.24: $\langle \varepsilon'_{11,\psi} \rangle^{Cu}_{i,\psi}$ *vs.* $sin^2\psi$ plots for all reflections of the gage section of Cu bar at zero external load after plastic flow.

Table 6.38: The average stresses, $\langle \sigma_{33}^{D} \rangle^{Cu-hkl}$, obtained from simulated diffraction analysis of the plots shown in Fig. 6.19. For comparison, $\overline{\sigma}_{ij} = 0\ MPa$.

$\langle \sigma_{33}^{D} \rangle^{hkl}$ (MPa)	Voigt	Reuss	Neer.-Hill	Kröner	$DEC_{Sim.}$
111	-15±18	-21±25	-18±21	-17±20	-14±17
200	24±30	10±13	15±18	16±21	23±29
220	4±16	4±14	4±15	4±16	4±16
311	12±23	8±8	9±10	10±11	11±12
420	5±16	3±10	4±12	4±13	5±15

Table 6.39: The average stresses obtained from simulated diffraction analysis of the plots shown in Fig. 6.24 after removal of first two ψ-ensemble points.

$\langle \sigma_{33}^{D} \rangle^{hkl}$ (MPa)	Simulated
111	-28±22
200	56±24
220	10±22
311	5±11
420	10±9

To further investigate this issue, we analyzed Fig 6.24 in terms of strain in the sample coordinates using Eq. (5.1-a). Table 6.40 lists the reflection average strain, $\langle \varepsilon_{11}^{D} \rangle^{hkl}$, $\langle \varepsilon_{33}^{D} \rangle^{hkl}$, obtained directly from the slopes and intercepts of these plots. We also list the arithmetic averages of these terms, $\langle \varepsilon_{11} \rangle^{hkl}$, $\langle \varepsilon_{33} \rangle^{hkl}$, computed from the average strains in the sample coordinates for

grains belonging to particular reflections. The averages obtained from diffraction analysis for reflections are not similar to the arithmetic averages in real space.

Table 6.40: The average strains in sample coordinates obtained from simulated diffraction analysis of the plots shown in Fig. 6.24. The averages for the reflection-ensembles in real space are also included, along with the model averages.

Reflection / Strain term	Isotropic (Eq. 6-3)	Model average	111	200	220	311	420
$\langle \varepsilon_{11}^{D} \rangle^{hkl} (\mu\varepsilon)$	-	-	71±86	-85±137	-92±72	-85±58	-62±72
$\langle \varepsilon_{33}^{D} \rangle^{hkl} (\mu\varepsilon)$	-	-	210±164	308±278	131±150	194±119	107±145
$\langle \varepsilon_{11} \rangle^{hkl} (\mu\varepsilon)$	0	0±32	-58±334	-58±288	1±339	-23±347	-55±306
$\langle \varepsilon_{33} \rangle^{hkl} (\mu\varepsilon)$	0	-2±33	212±416	-62±389	-103±370	-29±599	-82±364

In Table 6.41, we list the stresses in the sample coordinates obtained from these strain tensors. For this computation, we used the isotropic Hooke's law with (1) the elastic moduli of individual reflections, E^{hkl}, ν^{hkl}, computed from Tables 6.24 & 25, (2) the elastic moduli of the combined model, E, ν, computed from Tables 6.27.

Comparing Tables 6.37 & 41, we observe that 111 and 200 reflection average and computed stress tensors are quite different whereas the rest of the reflections have a reasonable agreement. In Table 6.33, we observe that computed reflection average stresses from E^{hkl}, ν^{hkl} are in reasonable agreement with the computed ones from E, ν. The difference in the axial stresses

between the two is up to % 11. Even though all reflections were considered as RVEs, the computed stress tensors for those reflections are not equal to real space reflection averages for 111 and 200 reflections. Diffraction stress formalism does not work for these reflections. We can conclude for diffraction stress formalism work, each ψ volume must be RVEs.

Table 6.41: The computed reflection average stresses from the average strain tensors listed in Table 6.32 and (1) E^{hkl}, ν^{hkl}, (2) E, ν.

(MPa)	E^{hkl}, ν^{hkl}	E, ν
111	$\begin{pmatrix} 45 & & \\ & 45 & \\ & & 61 \end{pmatrix}$	$\begin{pmatrix} 44 & & \\ & 44 & \\ & & 58 \end{pmatrix}$
200	$\begin{pmatrix} -11 & & \\ & -11 & \\ & & 9 \end{pmatrix}$	$\begin{pmatrix} 6 & & \\ & 6 & \\ & & 46 \end{pmatrix}$
220	$\begin{pmatrix} -13 & & \\ & -13 & \\ & & 8 \end{pmatrix}$	$\begin{pmatrix} -15 & & \\ & -15 & \\ & & 8 \end{pmatrix}$
311	$\begin{pmatrix} -6 & & \\ & -6 & \\ & & 22 \end{pmatrix}$	$\begin{pmatrix} -6 & & \\ & -6 & \\ & & 22 \end{pmatrix}$
420	$\begin{pmatrix} -8 & & \\ & -8 & \\ & & 9 \end{pmatrix}$	$\begin{pmatrix} -8 & & \\ & -8 & \\ & & 9 \end{pmatrix}$

Finally, we used all grains in the gage section of the unloaded Cu bar to obtain the $\langle \sigma_{33}^{D} \rangle^{hkl}$ from the slope of $\langle \varepsilon'_{11,\psi} \rangle_{I,\psi}^{Cu}$ vs. $\sin^2\psi$. We found, as expected, that the slope is zero and the calculated average stress is zero, satisfying force equilibrium.

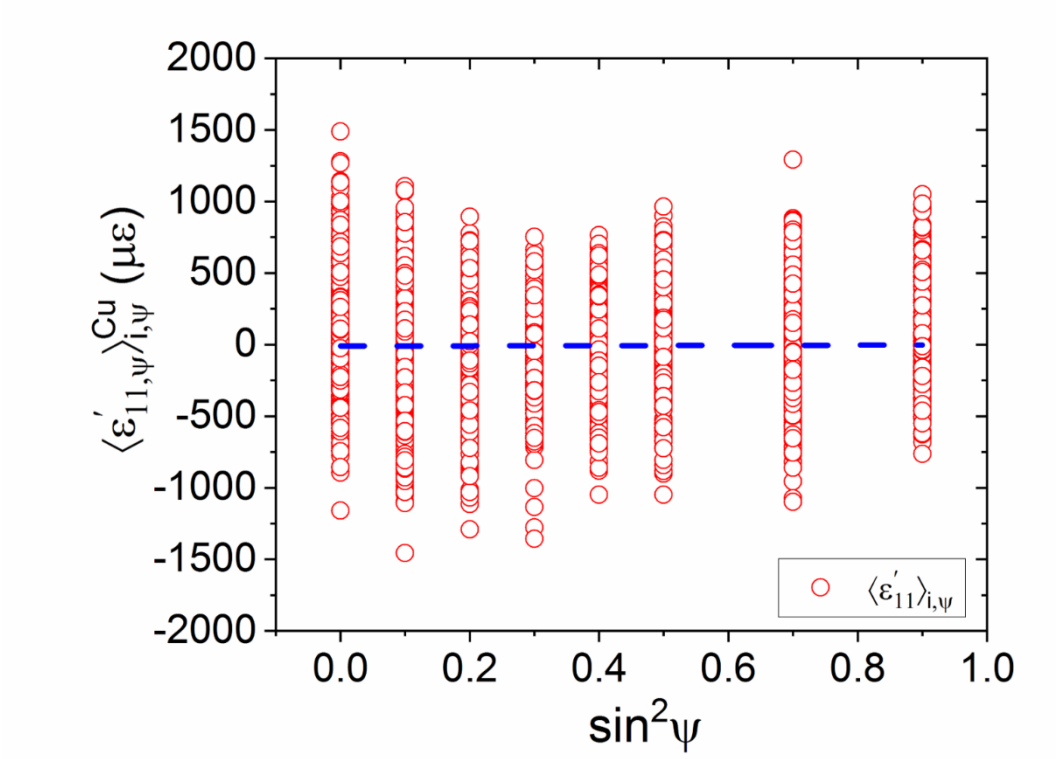

Figure 6.25: $\langle \varepsilon'_{11,\psi} \rangle^{Cu}_{i,\psi}$ *vs.* $sin^2\psi$ plot for all grains in the gage section of unloaded Cu bar.

6.4.2.5- Partitioning of Internal Stresses/Strains in a Two-phase, Cu – W sample

In this section, we will extend our simulations to the tensile loading of a two-phase, Cu – W, sample. For such a sample we will model, in order, (1) the determination of diffraction elastic constants, (2) the stress/strain distributions when the sample undergoes macroscopic plastic flow, with plasticity limited to the weaker, Cu, phase, and (3) the stress/strain distributions when it is unloaded after plastic deformation.

The two-phase sample consisted of 2500 grains, 1252 of which were in the gage section. In Tables 6.42 & 43, we list the # of grains for each ψ tilt and the volume fractions of the ψ–volumes for Cu and W phases in the gage section of the two-phase specimen. Overall 49%

of the volume contains Cu grains. Due to the random placement of grains, some ψ – volumes have very small populations, notably those at ψ=45° for the 110 reflection of W phase and ψ= 39.23° and 45° for 311 reflection of Cu phase. Still, the volume fractions of all ψ–volumes are comparable to those of the single-phase specimens treated previously.

In Fig. 6.26, we plot the uniaxial stress-strain curve of our two-phase specimen obtained from the finite element analysis. This plot was computed from the model where our input was single elastic compliances and single-phase yield responses of the W and Cu phases. In Table 6.44, we list the effective Young's modulus, E, Poisson's ratio, ν, and .2% offset yield stress of the two-phase sample determined from Figure 6.26. We also provide values for E and ν computed using Vegard's law. The differences show the presence of strong interaction between grains of the two-phases. The model can be considered elastic below 100 MPa applied load. It exhibits significant hysteresis when unloaded after plastic flow. As such, we expect a significant residual stress field to set up between the Cu and W grains after unloading.

Table 6.42: The population number and volume fraction for each ψ-ensemble N_{ψ}^{hkl} for the Cu phase in the gage section of the Cu – W sample.

ψ(°)	0	18.43	26.57	33.21	39.23	45	56.79	71.57	Total
$N_{\psi}^{111}, f_{\psi}^{111}$	37, 0.015	8, 0.003	12, 0.006	5, 0.003	24, 0.010	41, 0.015	44, 0.017	7, 0.004	178
$N_{\psi}^{200}, f_{\psi}^{200}$	11, 0.005	18, 0.007	29, 0.011	22, 0.009	29, 0.012	7, 0.003	24, 0.008	5, 0.002	145
$N_{\psi}^{220}, f_{\psi}^{220}$	20, 0.008	12, 0.005	10, 0.005	4, 0.002	5, 0.002	3, 0.001	17, 0.007	7, 0.002	78
$N_{\psi}^{311}, f_{\psi}^{311}$	6, 0.003	17, 0.005	5, 0.001	5, 0.003	2, 0.001	2, 0.001	11, 0.005	13, 0.006	61
$N_{\psi}^{420}, f_{\psi}^{420}$	32, 0.011	13, 0.005	44, 0.019	4, 0.002	12, 0.004	28, 0.011	9, 0.003	6, 0.003	148
N_{ψ}^{Total}	106	68	100	40	72	81	105	38	610

Table 6.43: The population number and volume fraction for each ψ-ensemble N_{ψ}^{hkl} for the W phase in the gage section of the Cu – W sample.

ψ(°)	0	18.43	26.57	33.21	39.23	45	56.79	71.57	Total
$N_{\psi}^{110}, f_{\psi}^{110}$	15, 0.006	15, 0.006	8, 0.003	16, 0.007	4, 0.002	1, 0.001	21, 0.008	5, 0.003	85
$N_{\psi}^{200}, f_{\psi}^{200}$	24, 0.009	6, 0.003	17, 0.007	31, 0.013	19, 0.008	24, 0.010	23, 0.010	16, 0.007	160
$N_{\psi}^{211}, f_{\psi}^{211}$	27, 0.011	12, 0.004	16, 0.006	16, 0.006	14, 0.006	10, 0.005	14, 0.006	22, 0.009	131
$N_{\psi}^{220}, f_{\psi}^{220}$	18, 0.007	4, 0.001	16, 0.006	16, 0.007	19, 0.007	17, 0.007	19, 0.007	14, 0.004	123
$N_{\psi}^{310}, f_{\psi}^{310}$	21, 0.010	18, 0.008	17, 0.005	16, 0.007	24, 0.009	20, 0.007	20, 0.008	7, 0.002	143
N_{ψ}^{Total}	105	55	74	95	80	72	97	64	642

Table 6.44: Young's Modulus, E, Poisson's ratio, ν, and yield strength of the two-phase Cu – W sample, computed from Fig 6.36 and Vegard's Law

	E (GPa)	ν	σ_Y (MPa)
Model (Fig. 6.26)	239	-	406
Vegard's Law	264	0.3	-

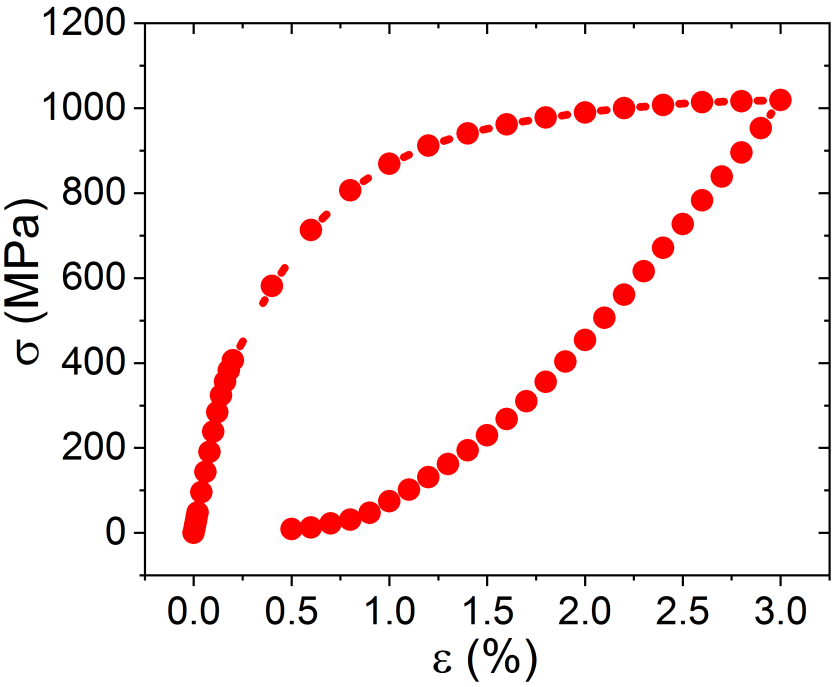

Figure 6.26: Refined stress-strain curve of the Cu – W by using single-phase compliances, yield response, and modified Voce parameters of the individual phases.

6.4.2.6- Determination of Diffraction Elastic Constants for Two-phase Cu – W Sample

In what follows we simulate the measurement of diffraction elastic constants (DECs). For this purpose, we employed the traditional procedure [19]. As before, these computations were performed only for the gage section of our virtual Cu – W sample.

For this purpose, the (virtual) Cu – W sample was loaded to 9.5, 19, 28.5, 38 and 47.5 MPa along $\vec{S}_3$. All of these loads are in the elastic region. (Fig. 6.25).

Diffraction elastic constants, S_1^{TP-Sim} and $\frac{S_2}{2}^{TP-Sim}$, of two-phases for the gage section of Cu – W bar, computed from the variation of the slopes and intercepts of the $\langle \varepsilon'_{11,\psi} \rangle_{I,\psi}^{W}$ vs. $\sin^2\psi$ $\langle \varepsilon'_{11,\psi} \rangle_{I,\psi}^{Cu}$ vs. $\sin^2\psi$ with applied load. DEC values computed from single-elastic compliances at the Voigt. Reuss, Neerfeld-Hill, Kröner limits, and simulated ones for single-phase W and Cu samples are also shown. For ease of comparison, we include the deviation of the simulation values from the Kröner limit.

6.4.2.6.1-Determination of Diffraction Elastic Constants for W Phase

The loads to which the Cu – W model was loaded, and the slopes, m_{hkl}, and intercepts, I_{hkl} of the $\langle \varepsilon'_{11,\psi} \rangle_{i,\psi}^{W}$ $vs. sin^2\psi$ plots for these loads (and their fit errors), are listed in Table 6.45. As expected, we obtain similar m_{hkl}, I_{hkl} for all reflections of the W phase.

Table 6.45: Slopes, m_{hkl}, and intercepts, I_{hkl} ,of regression fits of $\langle \varepsilon'_{11,\psi} \rangle_{i,\psi}^{W}$ $vs.$ $sin^2\psi$ plots for applied loads, 9.5, 19, 28.5, 38, 47.5 MPa.

$\sigma_{33}^{App.}$ (MPa)	9.5 MPa		19 MPa		28.5 MPa		38 MPa		47.5 MPa	
	m_{hkl}	I_{hkl}	m_{hkl}	I_{hkl}	m_{hkl}	I_{hkl}	m_{hkl}	I_{hkl}	m_{hkl}	I_{hkl}
(110)	39±1	-9±1	78±1	-18±1	117±1	-27±1	156±2	-36±1	195±2	-45±1
(200)	41±1	-9±1	81±2	-19±1	122±3	-28±1	162±3	-38±1	203±4	-47±2
(211)	41±1	-9±1	82±2	-19±1	123±3	-28±1	164±4	-37±1	205±5	-47±2
(220)	40±1	-9±1	80±1	-18±1	119±2	-27±1	159±3	-36±1	199±4	-46±1
(310)	40±1	-9±1	79±2	-18±1	119±2	-27±1	158±3	-36±1	198±4	-45±1

In Fig. 6.27, we plot the variation of these slopes and intercepts with applied load. Since $m_{hkl} = \frac{S_2}{2}\sigma_{33}^{App.}$ and $I_{hkl} = -S_1\sigma_{33}^{App.}$, these DEC, S_1^{TP-Sim} and $\frac{S_2}{2}^{TP-Sim}$ values for W in two-phase Cu – W sample can be obtained from the slopes of Figs. 15-a & b. These values are listed in Table 6.46.

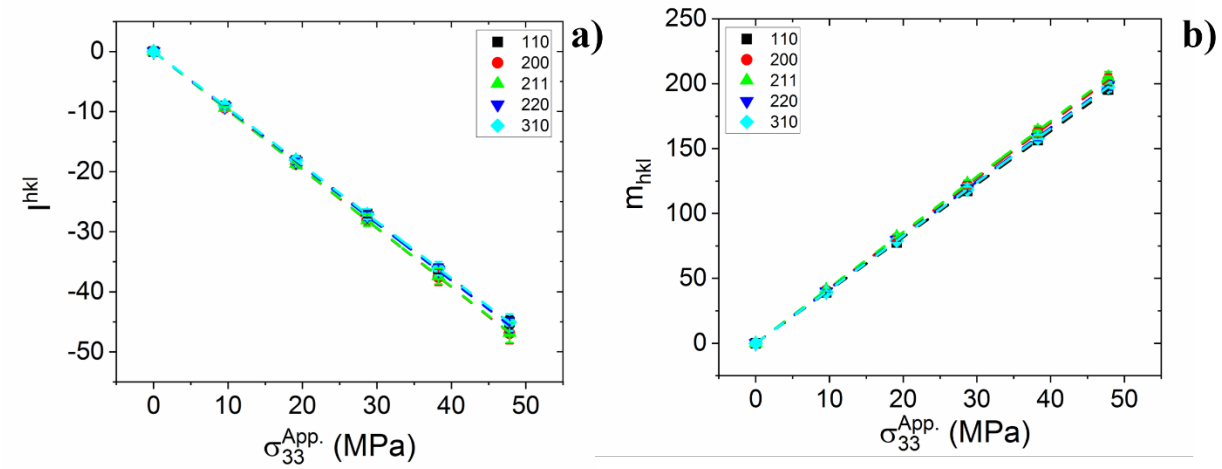

Figure 6.27: Variation of I_{hkl} and m_{hkl} with respect to $\sigma_{33}^{App.}$ for all W reflections in the gage section of two-phase Cu – W specimen.

Table 6.46: Diffraction elastic constants obtained from the FEA analysis of W phase for the gage section of two-phase Cu – W specimen. Values computed from single-elastic compliances at the Voigt. Reuss, Neerfeld-Hill and Kröner limits are also shown. Young's Modulus, E^{hkl}, and Poisson's ratio, ν^{hkl}, are calculated from S_1^{TP-Sim} and $\frac{S_2}{2}^{TP-Sim}$ values.

	Reuss/Voigt/Neer.-Hill/Kröner/DEC_{Sim}.		Simulation			
$(TPa)^{-1}$	S_1	$S_2/2$	S_1^{TP-Sim}	$\frac{S_2}{2}^{TP-Sim}$	E^{hkl} (GPa)	ν^{hkl}
(110)	-0.73	3.30	-0.94±0.01	4.09±0.01	318	0.30
(200)	-0.73	3.30	-0.98±0.01	4.25±0.01	306	0.30
(211)	-0.73	3.30	-0.98±0.01	4.28±0.01	303	0.30
(220)	-0.73	3.30	-0.95±0.01	4.15±0.01	313	0.30
(310)	-0.73	3.30	-0.94±0.01	4.13±0.01	314	0.30

We observe that S_1^{TP-Sim} and $\frac{S_2}{2}^{TP-Sim}$ values are similar for all reflections of the W phase. In fact, one can say that the W reflection volumes in the two-phase material exhibit reasonable isotropic elastic response. However, these DECs are higher than ones computed for single-phase W. Consequently, the presence of the more compliant Cu phase in the material causes a more compliant W elastic response. This is caused by the fact that the W phase carries significantly more load than the nominal applied stress.

6.4.2.6.2-Determination of Diffraction Elastic Constants for Cu Phase

In Table 6.47, we summarize the results of the stress analysis of the Cu phase of the combined model. The slopes, m_{hkl}, and intercepts, I_{hkl} obtained from regression fits to the $\langle \varepsilon'_{11,\psi} \rangle_{i,\psi}^{Cu}$ $vs. sin^2\psi$ plots and their fit errors are listed in Table 6.45. The m_{hkl}, I_{hkl} values for all reflections have a slightly tighter distribution compared to those for single-phase Cu (Table 6.22); the ratio of the slopes of the 111 and 200 reflections has dropped from 1.31 to 1.15.

Table 6.47: Slopes, m_{hkl}, and intercepts, I_{hkl} ,of regression fits of $\langle \varepsilon'^{Cu}_{11,\psi} \rangle_{i,\psi}$ $vs.\ sin^2\psi$ plots for applied loads, 9.5, 19, 28.5, 38, 47.5 MPa.

$\sigma_{33}^{App.}$ (MPa)	9.5 MPa		19 MPa		28.5 MPa		38 MPa		47.5 MPa	
	m_{hkl}	I_{hkl}	m_{hkl}	I_{hkl}	m_{hkl}	I_{hkl}	m_{hkl}	I_{hkl}	m_{hkl}	I_{hkl}
(111)	63±2	-15±1	124±4	-29±2	187±5	-44±2	249±8	-58±3	311±9	-73±4
(200)	71±4	-17±1	144±9	-34±3	216±13	-50±5	289±17	-67±6	360±21	-84±8
(220)	59±5	-13±1	120±10	-26±3	179±15	-40±5	241±20	-53±7	299±25	-66±8
(311)	69±3	-15±1	138±5	-30±3	206±8	-45±4	276±11	-60±5	345±13	-75±7
(420)	68±2	-15±1	136±4	-30±2	203±5	-46±2	271±7	-61±3	338±9	-76±4

In Fig. 6.28, we plot the variation of these slopes and intercepts with applied load. In Tables 6.48 & 49, we tabulate the DEC values obtained from these figures. S_1^{TP-Sim} and $\frac{S_2}{2}^{TP-Sim}$ are the DEC values of the Cu phase in two-phase Cu – W sample. S_1^{TP-Sim} and $\frac{S_2}{2}^{TP-Sim}$ values for all reflections are outside the interval bracketed by the Reuss and Voigt limits for single-phase polycrystalline Cu. As shown in Table 6.50, these diffraction elastic constants are very different from the DEC values, S_1^{SP-Sim} and $\frac{S_2}{2}^{SP-Sim}$, obtained for the single-phase Cu sample simulation. We note that, although grain populations are quite small in a few ψ-ensembles for the 220 and 311 reflections, all reflections show similar effects. Therefore, it is not likely that these effects are due to sampling[40].

[40] In the single-phase Cu model, increasing the diffracting population by 5x changed the DEC results by only 10% or less.

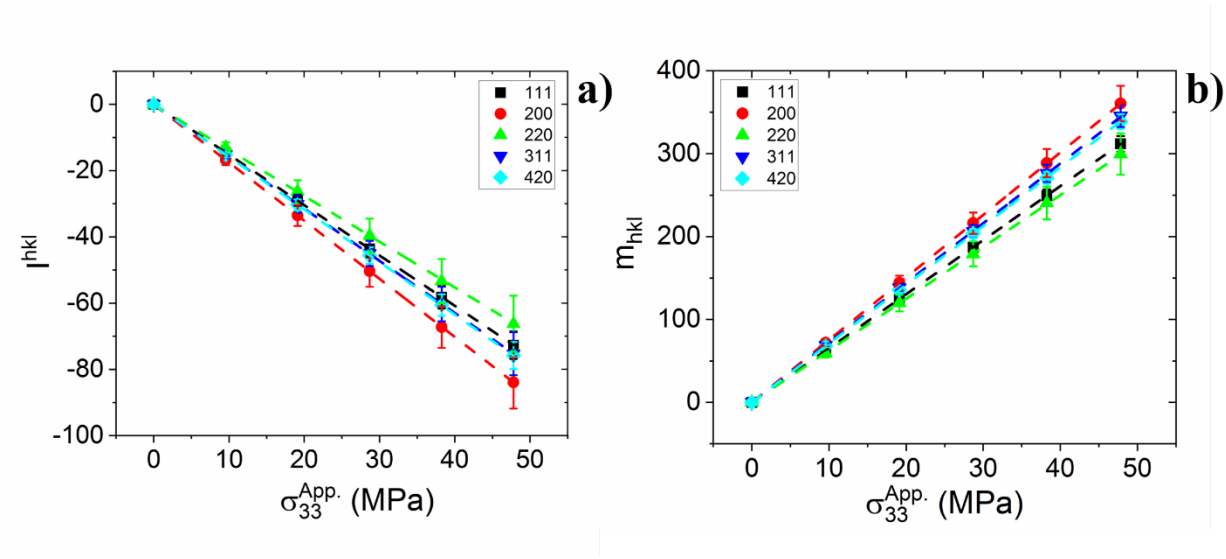

Figure 6.28: Variation of I_{hkl} and m_{hkl} with respect to $\sigma_{33}^{App.}$ for all Cu reflections in the gage section of Cu – W sample.

Table 6.50 shows that the mechanical response of the Cu phase appears to be stiffer in the two-phase sample. In Table 6.51, we tabulate Young's moduli, E^{hkl}, and Poisson's ratios, ν^{hkl}, for the grains diffracting in the Cu reflection volumes. These values were computed from the diffraction elastic constants shown in Table 6.50. The Young's moduli of all reflections are high and close to each other in magnitude.

Table 6.48: Diffraction elastic constant, S_1^{TP-Sim}, obtained from the FEA analysis of Cu phase for the gage section of two-phase Cu – W specimen. Values are computed from single-elastic compliances at the Voigt, Reuss, Neerfeld-Hill and Kröner limits. % Deviation of simulated S_1^{TP-Sim} from S_1^{SP-Sim} was also shown.

S_1 $(TPa)^{-1}$	Reuss	Voigt	Neer.-Hill	Kröner	S_1^{SP-Sim}	S_1^{TP-Sim}	% Dev. From S_1^{SP-Sim}
(111)	-1.40	-2.24	-1.83	-1.93	-2.17±0.01	-1.52±0.01	30
(200)	-6.28	-2.24	-4.26	-3.73	-2.92±0.01	-1.75±0.01	40
(220)	-2.62	-2.24	-2.43	-2.38	-2.76±0.01	-1.39±0.01	50
(311)	-3.98	-2.24	-3.11	-2.88	-2.62±0.01	-1.57±0.01	40
(420)	-3.94	-2.24	-3.09	-2.87	-2.75±0.01	-1.59±0.01	42

Table 6.49: Diffraction elastic constant, $\frac{S_2}{2}^{TP-Sim}$, obtained from the FEA analysis of Cu phase for the gage section of two-phase Cu – W specimen. Values are computed from single-elastic compliances at the Voigt, Reuss, Neerfeld-Hill and Kröner limits. % Deviation of simulated $\frac{S_2}{2}^{TP-Sim}$ from $\frac{S_2}{2}^{SP-Sim}$ was also shown.

$S_2/2$ $(TPa)^{-1}$	Reuss	Voigt	Neer.-Hill	Kröner	$\frac{S_2}{2}^{SP-Sim}$	$\frac{S_2}{2}^{TP-Sim}$	% Dev. From $\frac{S_2}{2}^{SP-Sim}$
(111)	6.65	9.17	7.91	8.24	8.78±0.01	6.51±0.01	26
(200)	21.28	9.17	15.23	13.63	10.90±0.01	7.54±0.01	31
(220)	10.31	9.17	9.74	9.58	10.82±0.01	6.30±0.01	42
(311)	14.39	9.17	11.78	11.09	9.87±0.01	7.23±0.01	27
(420)	14.26	9.17	11.72	11.04	10.14±0.01	7.09±0.01	31

Table 6.50: Diffraction elastic constants obtained from the FEA analysis of Cu phase for the gage section of single-phase Cu and two-phase Cu – W specimen.

Single-phase Cu (Table 6.24)		Cu phase in Cu – W sample	
S_1^{SP-Sim}	$\frac{S_2}{2}^{SP-Sim}$	S_1^{TP-Sim}	$\frac{S_2}{2}^{TP-Sim}$
-2.13±0.01	8.70±0.01	-1.52±0.01	6.51±0.01
-2.79±0.01	10.77±0.01	-1.75±0.01	7.54±0.01
-2.55±0.01	10.68±0.01	-1.39±0.01	6.30±0.01
-2.49±0.01	9.87±0.01	-1.57±0.01	7.23±0.01
-2.55±0.01	10.24±0.01	-1.59±0.01	7.09±0.01

Table 6.51: Young's moduli, E^{hkl}, and Poisson's ratios, ν^{hkl}, computed from DECs of Cu phase in Cu – W shown in Table 6.50.

Reflection	E^{hkl} (GPa)	ν^{hkl}
(111)	200	0.30
(200)	173	0.30
(220)	204	0.28
(311)	177	0.28
(420)	182	0.29

In the calculation of DECs for multiphase materials, we used $\sigma_{33}^{App.}$, following the standard practice in the field. This approach is, of course, not justified theoretically. The stiffer phase is expected to carry a larger share of the load. In Table 6.52, we list the global stress tensors for each phase in the Cu – W sample, the global stress tensor in the gage volume of the sample (taken over all grains for both phases), and the applied stress tensor computed using the tensile plot (Fig. 6.26) for all loads used for the calculation of the DECs for Cu and W phases. Consequently, the DEC values described in Tables 6.46 & 50 are "effective elastic constants". Since load partitioning within the phases of such a sample is not available in a routine experiment, these effective constants must be measured. They cannot be computed analytically from the first principles using

only the stiffness values of the individual phases. As a corollary, using single-phase DEC values in diffraction stress analysis of two-phase samples is not theoretically justified.

Table 6.52: Applied stress tensor and global average stress tensor of the entire Cu – W and each Cu and W phase elastically loaded. All values are in MPa.

$\sigma_{ij}^{App.}$	$\bar{\sigma}_{ij}$	$\bar{\sigma}_{ij}^{Cu}$	$\bar{\sigma}_{ij}^{W}$
$\begin{pmatrix} 0 & 0 & 0 \\ 0 & 0 & 0 \\ 0 & 0 & 9.5 \end{pmatrix}$	$\begin{pmatrix} 0 & 0 & 0 \\ 0 & 0 & 0 \\ 0 & 0 & 9.5 \end{pmatrix}$	$\begin{pmatrix} 0 & 0 & 0 \\ 0 & 0 & 0 \\ 0 & 0 & 7 \end{pmatrix}$	$\begin{pmatrix} 0 & 0 & 0 \\ 0 & 0 & 0 \\ 0 & 0 & 12 \end{pmatrix}$
$\begin{pmatrix} 0 & 0 & 0 \\ 0 & 0 & 0 \\ 0 & 0 & 19 \end{pmatrix}$	$\begin{pmatrix} 0 & 0 & 0 \\ 0 & 0 & 0 \\ 0 & 0 & 19 \end{pmatrix}$	$\begin{pmatrix} 1 & 0 & 0 \\ 0 & 1 & 0 \\ 0 & 0 & 14 \end{pmatrix}$	$\begin{pmatrix} -1 & 0 & 0 \\ 0 & -1 & 0 \\ 0 & 0 & 24 \end{pmatrix}$
$\begin{pmatrix} 0 & 0 & 0 \\ 0 & 0 & 0 \\ 0 & 0 & 28.5 \end{pmatrix}$	$\begin{pmatrix} 0 & 0 & 0 \\ 0 & 0 & 0 \\ 0 & 0 & 28.5 \end{pmatrix}$	$\begin{pmatrix} 1 & 0 & 0 \\ 0 & 1 & 1 \\ 0 & 0 & 22 \end{pmatrix}$	$\begin{pmatrix} -1 & 0 & 0 \\ 0 & -1 & -1 \\ 0 & 0 & 35 \end{pmatrix}$
$\begin{pmatrix} 0 & 0 & 0 \\ 0 & 0 & 0 \\ 0 & 0 & 38 \end{pmatrix}$	$\begin{pmatrix} 0 & 0 & 0 \\ 0 & 0 & 0 \\ 0 & 0 & 38 \end{pmatrix}$	$\begin{pmatrix} 1 & 0 & 0 \\ 0 & 2 & 0 \\ 0 & 0 & 29 \end{pmatrix}$	$\begin{pmatrix} -1 & 0 & 0 \\ 0 & -2 & -1 \\ 0 & -1 & 47 \end{pmatrix}$
$\begin{pmatrix} 0 & 0 & 0 \\ 0 & 0 & 0 \\ 0 & 0 & 47.5 \end{pmatrix}$	$\begin{pmatrix} 0 & 0 & 0 \\ 0 & 0 & 0 \\ 0 & 0 & 48 \end{pmatrix}$	$\begin{pmatrix} 2 & 0 & 0 \\ 0 & 2 & 0 \\ 0 & 0 & 37 \end{pmatrix}$	$\begin{pmatrix} -2 & 0 & 0 \\ 0 & -2 & -1 \\ 0 & -1 & 59 \end{pmatrix}$

6.4.2.7- Uniaxial Tension of Cu – W Bar at Plastic Regime

The final model utilizing the virtual three-dimensional polycrystalline specimen simulated the 3% extension (corresponds to 1019 MPa) of our two-phase Cu – W specimen. When such a specimen is loaded uniformly along $\vec{S}_3$ direction, the bar will extend this direction and contract in the transverse directions. However, since the isotropic Young's Modulus of Cu and W are very

different, 138 vs 387 GPa, respectively, grains belonging to the two-phases are expected to mutually constrain each other. In the direction of loading, $\vec{S}_3$, the W grains will constrain the elongation of Cu grains and place them in compression. Such constrain can result in plastic flow within the softer Cu grains. Concurrently, the Cu grains will pull the W grains (slightly) past their equilibrium lengths, placing them in tension. Even though the yield point of W is much higher than Cu, some W grains might also suffer from the plastic flow. There will also be transverse strains due to Poisson's contraction resulting in Heyn stresses due to elastic and plastic incompatibility. Overall, we expect triaxial stress states in the grains of both phases. The global averages of all stress components, $\bar{\sigma}_{ij}$, should be equal to the far-field stress, $\sigma_{ij}^{App.}$.

6.4.2.7.1- Stress Distribution in Sample Coordinates

Tables 6.53 & 54 list the global average stress and lattice strain tensors and their distribution parameters. These averages were computed over all grains, both Cu and W, in the model. The minimum and maximum values reflect the extrema in the relevant grain-average stresses/strains. We observe that, as expected, all $\bar{\sigma}_{ij} = \sigma_{ij}^{App.}$. However, all stress components exhibit wide distributions, the full widths of these stresses are quite large, indicating that some grains possess significant interaction stresses. The dispersion of the shear stresses, $\bar{\sigma}_{ij,i\neq j}$, are similar and are approximately 1/4th of the axial stress, $\bar{\sigma}_{33}$. Moreover, the minimum $\bar{\sigma}_{33}$ is -347 MPa, indicating that some grains are under compression even in the direction of loading.

Table 6.53: Global average stress tensor of the gage section of Cu – W bar extended 3 % and its dispersion parameters. The model contains 1252 grains, 610 Cu and, 642 W. All values are in MPa.

(MPa)	$\bar{\sigma}_{11}$	$\bar{\sigma}_{12}$	$\bar{\sigma}_{13}$	$\bar{\sigma}_{22}$	$\bar{\sigma}_{23}$	$\bar{\sigma}_{33}$
Average	**-20**	**6**	**11**	**-19**	**-45**	**1065**
Std. Dev	417	203	208	426	207	733
Maximum	1340	879	1103	1410	841	3650
Minimum	-1948	-969	-880	-1843	-1046	-347
Full Width	**3287**	**1848**	**1983**	**3253**	**1887**	**3996**

Table 6.54: Global average lattice strain tensor of the gage section of Cu – W bar extended 3 % and its dispersion parameters. The model contains 1252 grains, 610 Cu and, 642 W. All values are in microstrain (με).

(με)	$\bar{\varepsilon}_{11}$	$\bar{\varepsilon}_{12}$	$\bar{\varepsilon}_{13}$	$\bar{\varepsilon}_{22}$	$\bar{\varepsilon}_{23}$	$\bar{\varepsilon}_{33}$
Average	**-842**	**38**	**16**	**-856**	**-202**	**3467**
Std. Dev	1183	717	779	1201	762	1557
Maximum	2934	2963	3978	2766	2703	8677
Minimum	-5284	-3157	-2911	-4921	-3452	11
Full Width	8218	6120	6889	7687	6155	8666

Table 6.55 lists the average stress in the Cu phase and their dispersion parameters. All normal stresses $\bar{\sigma}_{ii}^{Cu}$, are finite, and $\bar{\sigma}_{11}^{Cu}$ and $\bar{\sigma}_{22}^{Cu}$ are much larger than $\bar{\sigma}_{11}$ and $\bar{\sigma}_{22}$ while the $\bar{\sigma}_{33}^{Cu}$ is smaller than the $\bar{\sigma}_{33}$. The shear stresses $\bar{\sigma}_{ij,i\neq j}^{Cu}$ are close to zero. The dispersion parameters for these shear stress components are much smaller than the corresponding values of the global stress tensor, $\bar{\sigma}_{ij}$.

Table 6.55: Average stress tensor for the Cu phase of the gage section of Cu – W bar extended 3 % and its dispersion parameters. This phase contains 610 grains. All values are in MPa.

(MPa)	$\bar{\sigma}_{11}^{Cu}$	$\bar{\sigma}_{12}^{Cu}$	$\bar{\sigma}_{13}^{Cu}$	$\bar{\sigma}_{22}^{Cu}$	$\bar{\sigma}_{23}^{Cu}$	$\bar{\sigma}_{33}^{Cu}$
Average	**224**	**5**	**1**	**225**	**-6**	**509**
Std. Dev	264	46	52	271	52	281
Maximum	1340	132	142	1410	185	1657
Minimum	-482	-118	-162	-674	-151	-347
Full Width	**1822**	**250**	**304**	**2084**	**236**	**2004**

Table 6.56: Average lattice strain tensor for the Cu phase of the gage section of Cu – W bar extended 3 % and its dispersion parameters. This phase contains 610 grains. All values are in microstrain (με).

(με)	$\bar{\varepsilon}_{11}^{Cu}$	$\bar{\varepsilon}_{12}^{Cu}$	$\bar{\varepsilon}_{13}^{Cu}$	$\bar{\varepsilon}_{22}^{Cu}$	$\bar{\varepsilon}_{23}^{Cu}$	$\bar{\varepsilon}_{33}^{Cu}$
Average	**-31**	**51**	**-31**	**-61**	**-103**	**2440**
Std. Dev	727	381	475	796	457	821
Maximum	2934	1680	1420	2766	1380	5480
Minimum	-1940	-1200	-1540	-2950	-1910	11
Full Width	4870	2880	2960	5716	3290	5469

Table 6.56 lists average lattice strain tensors in the Cu phase and its dispersion parameters. The average transverse normal strains of the Cu phase, $\bar{\varepsilon}_{11}^{Cu}$ *and* $\bar{\varepsilon}_{22}^{Cu}$, are almost zero, and much smaller than the global average strains of the entire model. The strain dispersions are also much smaller. In addition, the average equivalent plastic strain for the Cu phase is finite and the dispersion parameters of the equivalent plastic strain show that each grain experience a different but significant amount of plastic flow (Table 6.57). Some grains have negative equivalent plastic strains.

Table 6.57: Average equivalent plastic strain for the Cu phase of the gage section of Cu – W bar extended 3 % and its dispersion parameters. This phase contains 610 grains. All values are in microstrain (με).

(με)	$\bar{\varepsilon}^{eqpl,Cu}$
Average	**63650**
Std. Dev	36902
Maximum	212022
Minimum	-4181
Full Width	207842

Tables 6.58, 59 & 60 list the average stress, lattice strain tensors, and equivalent plastic strain in the W phase and their dispersion parameters. All normal stresses, $\bar{\sigma}_{ii}^{W}$, are finite, and $\bar{\sigma}_{11}^{W}$ *and* $\bar{\sigma}_{22}^{W}$ are compressive; opposite sign to the corresponding Cu phase-average stress terms. All shear stresses, $\bar{\sigma}_{ij,i\neq j}^{W}$, are close to zero. We calculate the average normal stress for the gage section of the Cu – W sample from the average normal phase stresses showed in Tables 6.55 & 58. We observe that the average normal phase stresses obey the average stress equilibrium condition shown in Eq. (5-8). The dispersion parameters for the phase-average W stress components are similar to the corresponding values for the global stress tensor, $\bar{\sigma}_{ij}$.

Table 6.58: Average stress tensor for the W phase of the gage section of Cu – W bar extended 3 % and its dispersion parameters. This phase contains 642 grains. All values are in MPa.

(MPa)	$\bar{\sigma}_{11}^{W}$	$\bar{\sigma}_{12}^{W}$	$\bar{\sigma}_{13}^{W}$	$\bar{\sigma}_{22}^{W}$	$\bar{\sigma}_{23}^{W}$	$\bar{\sigma}_{33}^{W}$
Average	**-253**	**6**	**21**	**-251**	**-83**	**1594**
Std. Dev	403	281	285	417	280	631
Maximum	836	879	1103	829	841	3650
Minimum	-1948	-969	-880	-1843	-1046	269
Full Width	**2784**	**1848**	**1983**	**2671**	**1887**	**3380**

Table 6.59: Average lattice strain tensor for the W phase of the gage section of Cu – W bar extended 3 % and its dispersion parameters. This phase contains 642 grains. All values are in microstrain (με).

(με)	$\bar{\varepsilon}_{11}^{W}$	$\bar{\varepsilon}_{12}^{W}$	$\bar{\varepsilon}_{13}^{W}$	$\bar{\varepsilon}_{22}^{W}$	$\bar{\varepsilon}_{23}^{W}$	$\bar{\varepsilon}_{33}^{W}$
Average	**-1613**	**25**	**60**	**-1610**	**-297**	**4446**
Std. Dev	1004	930	983	1022	958	1457
Maximum	854	2983	3978	799	2703	8677
Minimum	-5284	-3157	-2911	-4921	-3452	11
Full Width	6138	6140	6889	5720	6155	7906

Comparing Tables 54 & 59, we observe that the overall lattice strain tensor of the model is in the same form as the average lattice tensor of the W phase. This is expected since W is much stiffer than Cu. The amount of equivalent plastic strain in the W phase is much smaller than the one in the Cu phase (Table 6.60). In addition, several grains do not undergo plastic deformation.

Table 6.60: Average equivalent plastic strain for the W phase of the gage section of Cu – W bar extended 3 % and its dispersion parameters. This phase contains 642 grains. All values are in microstrain (με).

(με)	$\bar{\varepsilon}^{eqpl,W}$
Average	**9478**
Std. Dev	10458
Maximum	81005
Minimum	0
Full Width	81005

6.4.2.7.1.1- Phase-averaged Stress Components in Sample Coordinates Selected by Diffraction

In Figs. 6.29 & 30, we plot the grain averages of the stress terms, $\langle\sigma_{11}\rangle_{i,\psi}^{Ph}$, $\langle\sigma_{22}\rangle_{i,\psi}^{Ph}$, $\langle\sigma_{33}\rangle_{i,\psi}^{Ph}$, $(Ph = Cu, W)$and shear stress components of all grains for all ψ-tilts of 200 reflections of the Cu and W phases. The solid symbols in these plots are the corresponding ψ-volume average stress values, $\langle\sigma_{11}\rangle_{\psi}^{Ph}, \langle\sigma_{22}\rangle_{\psi}^{Ph}, \langle\sigma_{33}\rangle_{\psi}^{Ph}, \langle\sigma_{12}\rangle_{\psi}^{Ph}, \langle\sigma_{13}\rangle_{\psi}^{Ph}$ and $\langle\sigma_{23}\rangle_{\psi}^{Ph}$. We see that, for each reflection, the ψ-volume average stress values are close to each other for all ψ. The reflection average stresses, Table 6.61, are close to the phase-averaged stress tensors. Thus, the reflection volumes can be considered representative volume elements for specific phases. However, these volumes cannot be representative of the sample as a whole since these values are different than the global stress averages. Consequently, these phase-specific average stresses are not solely macro-stresses or far-field stresses. They also contain pseudo-macro stress components.

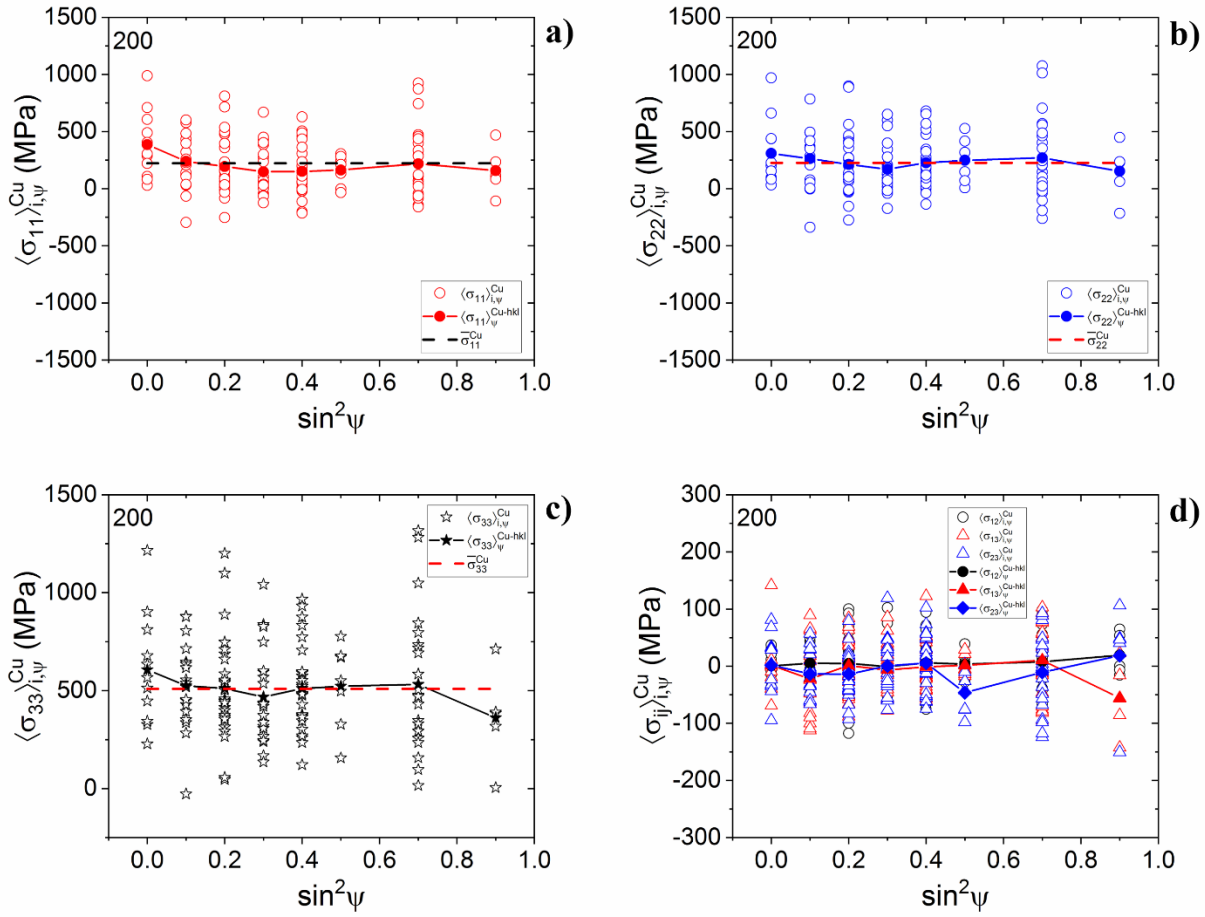

Figure 6.29: The phase-averaged grain stress values a) $\langle\sigma_{11}\rangle^{Cu}_{i,\psi}$, b) $\langle\sigma_{22}\rangle^{Cu}_{i,\psi}$, c) $\langle\sigma_{33}\rangle^{Cu}_{i,\psi}$ d) the shear stresses, for all grains as a function of $\sin^2\psi$.

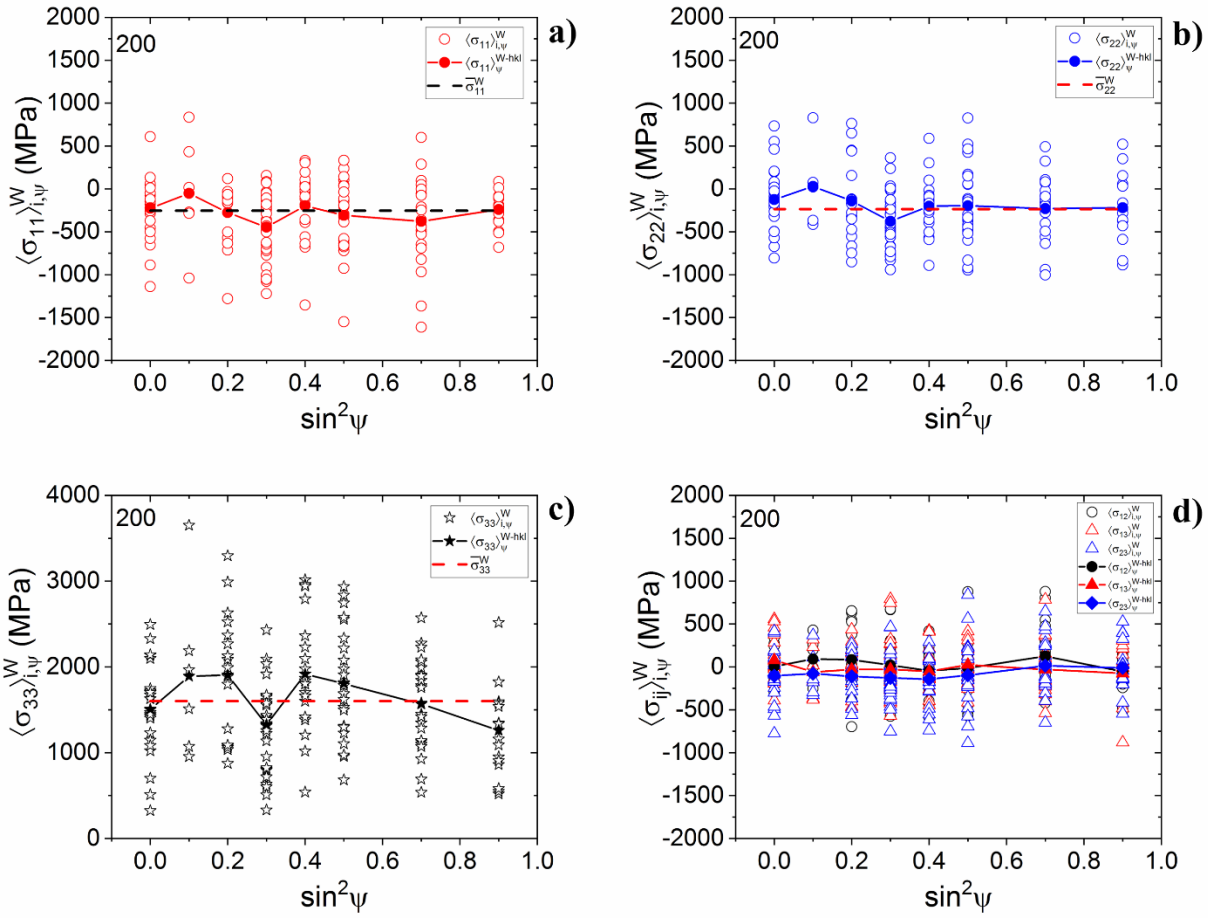

Figure 6.30: The phase-averaged grain stress values a) $\langle \sigma_{11} \rangle_{i,\psi}^{W}$, b) $\langle \sigma_{22} \rangle_{i,\psi}^{W}$, c) $\langle \sigma_{33} \rangle_{i,\psi}^{W}$ d) the shear stresses, for all grains as a function of $\sin^2\psi$.

Table 6.61: Reflection average stress tensors for the Cu and W phases of the gage section of the Cu – W bar extended 3 %. The phase-average stress tensor is also included for ease of comparison. All values are in MPa.

Cu	Cu-phase	W	W-phase
111	$\langle\sigma_{ij}\rangle^{Cu,111} = \begin{bmatrix} 264 & 3 & -2 \\ 3 & 216 & -6 \\ -2 & -6 & 512 \end{bmatrix}$	**110**	$\langle\sigma_{ij}\rangle^{W,110} = \begin{bmatrix} -222 & 36 & 66 \\ 36 & -250 & -79 \\ 66 & -79 & 1551 \end{bmatrix}$
200	$\langle\sigma_{ij}\rangle^{Cu,200} = \begin{bmatrix} 200 & 5 & -4 \\ 5 & 232 & -7 \\ -4 & -7 & 512 \end{bmatrix}$	**200**	$\langle\sigma_{ij}\rangle^{W,200} = \begin{bmatrix} -300 & 22 & -14 \\ 22 & -214 & -86 \\ -14 & -86 & 1606 \end{bmatrix}$
220	$\langle\sigma_{ij}\rangle^{Cu,220} = \begin{bmatrix} 255 & 1 & 7 \\ 1 & 268 & -11 \\ 7 & -11 & 547 \end{bmatrix}$	**211**	$\langle\sigma_{ij}\rangle^{W,211} = \begin{bmatrix} -158 & -11 & 9 \\ -11 & -208 & -79 \\ 9 & -79 & 1663 \end{bmatrix}$
311	$\langle\sigma_{ij}\rangle^{Cu,311} = \begin{bmatrix} 198 & 13 & -4 \\ 13 & 225 & 2 \\ -4 & 2 & 495 \end{bmatrix}$	**220**	$\langle\sigma_{ij}\rangle^{W,220} = \begin{bmatrix} -279 & -6 & 3 \\ -6 & -304 & -136 \\ 3 & -136 & 1579 \end{bmatrix}$
420	$\langle\sigma_{ij}\rangle^{Cu,420} = \begin{bmatrix} 195 & 4 & 7 \\ 4 & 205 & -6 \\ 7 & -6 & 486 \end{bmatrix}$	**310**	$\langle\sigma_{ij}\rangle^{W,310} = \begin{bmatrix} -282 & -1 & 59 \\ -1 & -287 & -40 \\ 59 & -40 & 1557 \end{bmatrix}$
	$\bar{\sigma}_{ij}^{Cu} = \begin{bmatrix} 224 & 5 & 1 \\ 5 & 225 & -6 \\ 1 & -6 & 509 \end{bmatrix}$		$\bar{\sigma}_{ij}^{W} = \begin{bmatrix} -253 & 7 & 21 \\ 7 & -251 & -83 \\ 21 & -83 & 1594 \end{bmatrix}$

6.4.2.7.2- Diffraction Stress/Strain Analysis

In Figs. 6.31 & 32, we plot the $\langle\varepsilon'_{11}\rangle_{i,\psi}^{Ph}$ $vs.\sin^2\psi$ data for all five reflections of the two-phases computed from the output of the FEpX model. Analysis of the slopes and intercepts of the linear regression fits were first used to compute the phase-averages of strains in the sample coordinate system by using Eq. (5-9).

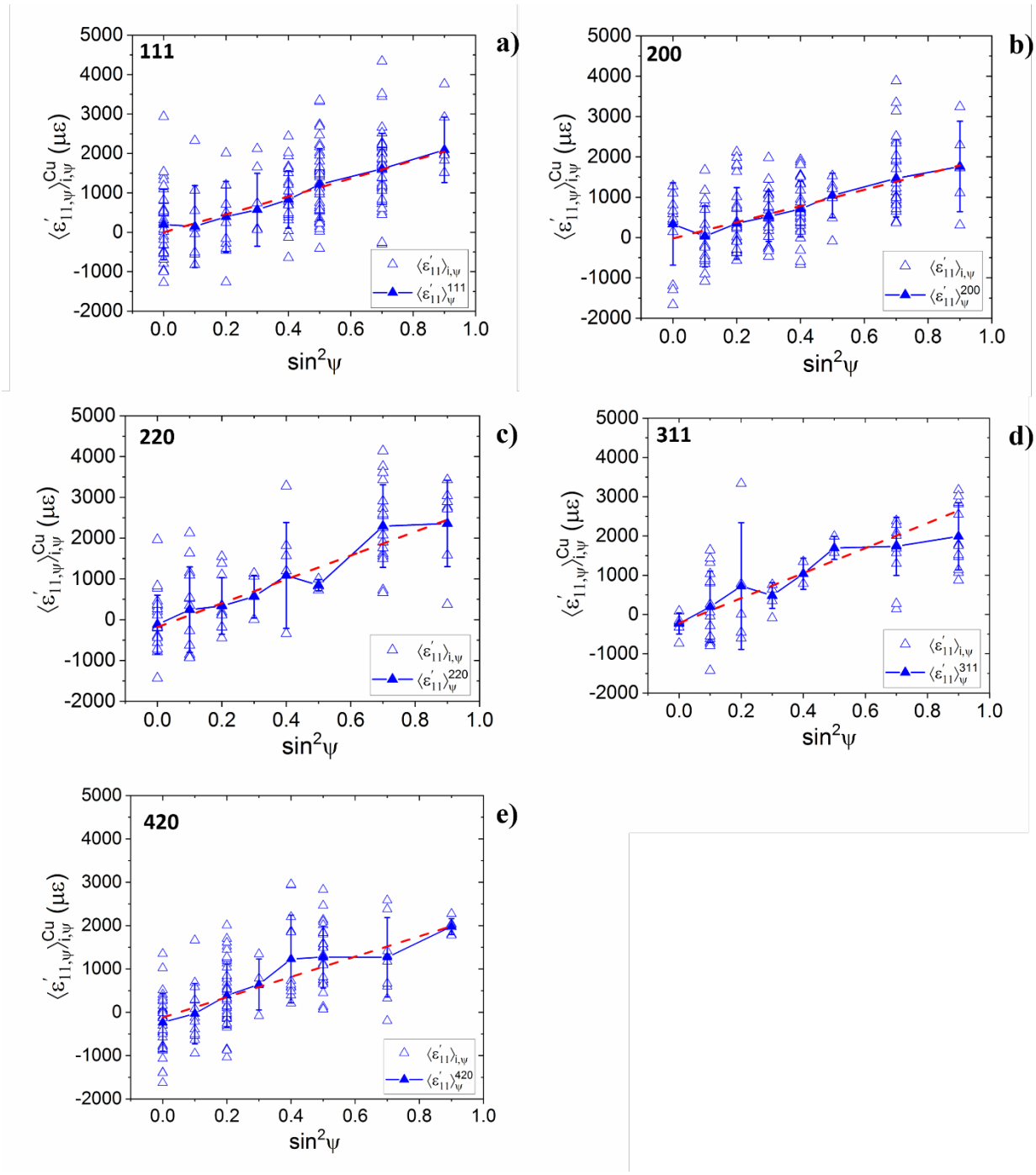

Figure 6.31: $\langle \varepsilon'_{11,\psi} \rangle^{Cu}_{i,\psi}$ *vs.* $sin^2\,\psi$ plots for studied reflections of the Cu phase in the Cu – W mesh after plastic flow.

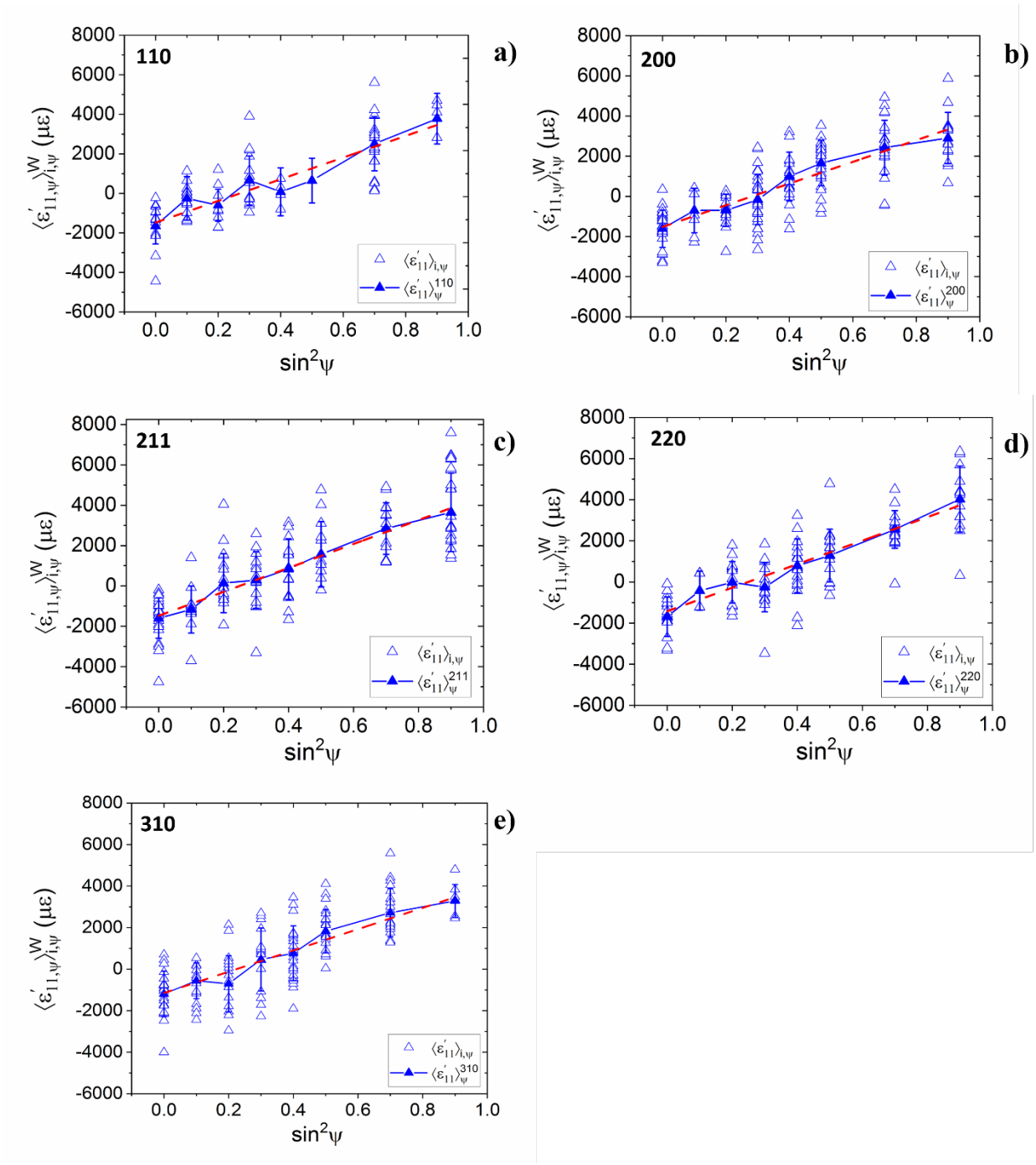

Figure 6.32: $\langle \varepsilon'_{11,\psi} \rangle^{W}_{i,\psi}$ $vs.$ sin^2 ψ plots for studied reflections of the W phase in the Cu – W mesh after plastic flow.

To obtain the reflection average stress $\langle\sigma_{33}^{D}\rangle^{hkl}$, we used Eq. (5-1-b), the slopes of least squares lines fitted to the $\langle\varepsilon'_{11,\psi}\rangle_{i,\psi}^{Cu}\ vs.\sin^2\psi$ and $\langle\varepsilon'_{11,\psi}\rangle_{i,\psi}^{W}\ vs.\sin^2\psi$ data for each reflection. We used diffraction elastic constants at Voigt, Reuss, Kröner, Neerfeld-Hill limits, shown in Table 5.8, and the simulation DEC values shown in Tables 6.46, 48 & 49. These stress results are shown in Tables 6.62 & 63. We observe that all reflections yield stress values different from the $\sigma_{33}^{App.}$ for the both phases. To test for oscillations, we removed the first two points from each plot and re-analyzed the data. The results are shown in Table 6.64.

Table 6.62: The average stresses, $\langle\sigma_{33}^{D}\rangle^{Cu-hkl}$, obtained from simulated diffraction analysis of the plots shown in Fig. 6.31. For comparison, $\bar{\sigma}_{ij} = 1019\ MPa$.

$\langle\sigma_{33}^{D}\rangle^{Cu-hkl}$ (MPa)	Voigt	Reuss	Neer.-Hill	Kröner	$DEC_{Sim.}$
111	248±15	342±21	287±18	276±17	349±21
200	219±24	95±10	132±14	148±16	267±29
220	319±36	284±32	300±34	305±35	464±53
311	347±44	221±28	271±34	287±37	440±56
420	255±14	164±9	200±11	212±12	330±19

Table 6.63: The average stresses, $\langle \sigma_{33}^{D} \rangle^{W-hkl}$, obtained from simulated diffraction analysis of the plots shown in Fig. 6.32. For comparison, $\bar{\sigma}_{ij} = 1019\ MPa$.

$\langle \sigma_{33}^{D} \rangle^{W-hkl}$ (MPa)	Voigt/Reuss/Neer.-Hill/Kröner	$DEC_{Sim.}$
110	1700±189	1371±152
200	1637±137	1270±107
211	1797±93	1386±71
220	1734±137	1379±109
310	1553±98	1241±79

Table 6.64: The average stresses obtained from simulated diffraction analysis of the plots shown in Figs. 6.31 & 32 after removal of first two ψ-ensemble points.

$\langle \sigma_{33}^{D} \rangle^{Cu-hkl}$ (MPa)	Simulated	$\langle \sigma_{33}^{D} \rangle^{W-hkl}$ (MPa)	Simulated
111	381±15	**110**	1477±214
200	289±19	**200**	1298±164
220	504±84	**211**	1268±80
311	437±135	**220**	1421±142
420	302±25	**310**	1263±147

The computed average stresses after the removal of the first two ψ-ensemble points yield that the change of the stresses can be up to 10 %. 200, 220 and 310 reflections of W, and 111, 200, and 311 reflections of Cu show linear behavior whereas the rest of the reflections show some oscillatory behavior.

From the slopes and intercepts of lines fitted to the data shown in Figs. 6.31 & 32, we obtain the phase-specific reflection average strains, $\langle \varepsilon_{ij}^{D} \rangle^{Ph-hkl}$, in sample coordinates. These results and their regression-fit errors are presented in Tables 6.65 & 66 for Cu and W phases, respectively. The reflection average strain tensors in the sample coordinates, computed from real space strain values, $\langle \varepsilon_{ij} \rangle^{Ph-hkl}$, obtained from the finite element analysis for each phase, as well as the overall phase average are also included.

Table 6.65: Slopes and intercepts of lines fitted to $\langle \varepsilon'_{11,\psi} \rangle_{i,\psi}^{Ph}$ $vs.$ $sin^2\,\psi$ data and the corresponding reflection average strain tensors for the Cu phase. The corresponding real space averages are also included. All values are in microstrain (με).

hkl	Intercept	Slope	$\langle \varepsilon_{ij}^{D} \rangle^{Ph-hkl}$	$\langle \varepsilon_{ij} \rangle^{Ph-hkl}$
111	1(68)	2274(139)	$\begin{bmatrix} 1 & 0 & 0 \\ 0 & 1 & 0 \\ 0 & 0 & 2273 \end{bmatrix}$	$\begin{bmatrix} 90 & 34 & -61 \\ 34 & -121 & -143 \\ -61 & -143 & 2460 \end{bmatrix}$
200	-23(96)	2014(219)	$\begin{bmatrix} -23 & 0 & 0 \\ 0 & -23 & 0 \\ 0 & 0 & 1991 \end{bmatrix}$	$\begin{bmatrix} -118 & 45 & -42 \\ 45 & -23 & 7 \\ -42 & 7 & 2419 \end{bmatrix}$
220	-181(161)	2925(334)	$\begin{bmatrix} -181 & 0 & 0 \\ 0 & -181 & 0 \\ 0 & 0 & 2744 \end{bmatrix}$	$\begin{bmatrix} 67 & 24 & 56 \\ 24 & 23 & -99 \\ 56 & -99 & 2529 \end{bmatrix}$
311	-219(155)	3184(404)	$\begin{bmatrix} -219 & 0 & 0 \\ 0 & -219 & 0 \\ 0 & 0 & 2965 \end{bmatrix}$	$\begin{bmatrix} -84 & 91 & -143 \\ 0 & 26 & -32 \\ 0 & 0 & 2308 \end{bmatrix}$
420	-119(110)	2341(131)	$\begin{bmatrix} -119 & 0 & 0 \\ 0 & -119 & 0 \\ 0 & 0 & 2222 \end{bmatrix}$	$\begin{bmatrix} -121 & 77 & 17 \\ 77 & -139 & -134 \\ 17 & -134 & 2428 \end{bmatrix}$
Phase average				$\begin{bmatrix} -31 & 51 & -31 \\ 51 & -61 & -103 \\ -31 & -103 & 2436 \end{bmatrix}$

Table 6.66: Slopes and intercepts of lines fitted to $\langle \varepsilon'_{11,\psi} \rangle^{Ph}_{i,\psi}$ $vs.\, sin^2\,\psi$ data and the corresponding reflection average strain tensors for the W phase. The corresponding real space averages are also included. All values are in microstrain (με).

hkl	Intercept	Slope	$\langle \varepsilon^D_{ij} \rangle^{Ph-hkl}$	$\langle \varepsilon_{ij} \rangle^{Ph-hkl}$
110	-1477(315)	5484(656)	$\begin{bmatrix} -1477 & 0 & 0 \\ 0 & -1477 & 0 \\ 0 & 0 & 4008 \end{bmatrix}$	$\begin{bmatrix} -1496 & 123 & 226 \\ 36 & -1595 & -291 \\ 66 & -79 & 4302 \end{bmatrix}$
200	-1522(190)	5400(453)	$\begin{bmatrix} -1522 & 0 & 0 \\ 0 & -1522 & 0 \\ 0 & 0 & 3878 \end{bmatrix}$	$\begin{bmatrix} -1769 & 75 & -68 \\ 75 & -1486 & -311 \\ -68 & -311 & 4480 \end{bmatrix}$
211	-1479(147)	5931(305)	$\begin{bmatrix} -1479 & 0 & 0 \\ 0 & -1479 & 0 \\ 0 & 0 & 4452 \end{bmatrix}$	$\begin{bmatrix} -1455 & -37 & 26 \\ -37 & -1620 & -260 \\ 26 & -260 & 4534 \end{bmatrix}$
220	-1423(196)	5721(450)	$\begin{bmatrix} -1423 & 0 & 0 \\ 0 & -1423 & 0 \\ 0 & 0 & 4298 \end{bmatrix}$	$\begin{bmatrix} -1638 & -17 & -1 \\ -17 & -1714 & -465 \\ -1 & -465 & 4469 \end{bmatrix}$
310	-1146(176)	5124(325)	$\begin{bmatrix} -1146 & 0 & 0 \\ 0 & -1146 & 0 \\ 0 & 0 & 3978 \end{bmatrix}$	$\begin{bmatrix} -1634 & 2 & 192 \\ 2 & -1654 & -162 \\ 192 & -162 & 4396 \end{bmatrix}$
Phase average				$\begin{bmatrix} -1613 & 25 & 60 \\ 25 & -1610 & -297 \\ 60 & -297 & 4446 \end{bmatrix}$

We observe that the strain tensors obtained from linear regression from all reflections agree quite well with the real space averages for both phases. On the other hand, the slopes of the $\langle \varepsilon'_{11,\psi} \rangle^{Ph}_{i,\psi}$ $vs.\sin^2\psi$ plots are quite different. Consequently, any computation which utilized only slopes would have yielded significantly different answers for each reflection.

In Table 6.67, we list the stresses in the sample coordinates obtained from $\langle \varepsilon^D_{ij} \rangle^{Ph-hkl}$ strain tensors for each phase. For this computation, we used the isotropic Hooke's law with the elastic moduli of individual reflections, E^{hkl}, ν^{hkl}, computed from Tables 6.46 & 49.

Comparing Tables 6.61 & 6.67, the computed reflection average stresses of reflections of Cu phase have similar results with the real space reflection average stresses. On the other hand, we do not observe similar behavior for the W phase. The real space reflection average stresses are *1.5x* larger than the computed ones for all reflections.

Table 6.67: The computed reflection average stresses from the average strain tensors listed in Tables 6.65 & 66 and E^{hkl}, v^{hkl}.

Cu	**Computed reflection average stresses**	**W**	**Computed reflection average stresses**
111	$\begin{pmatrix} 263 & & \\ & 263 & \\ & & 612 \end{pmatrix}$	**110**	$\begin{pmatrix} -167 & & \\ & -167 & \\ & & 1174 \end{pmatrix}$
200	$\begin{pmatrix} 286 & & \\ & 286 & \\ & & 544 \end{pmatrix}$	**200**	$\begin{pmatrix} -211 & & \\ & -211 & \\ & & 1060 \end{pmatrix}$
220	$\begin{pmatrix} 213 & & \\ & 213 & \\ & & 678 \end{pmatrix}$	**211**	$\begin{pmatrix} -83 & & \\ & -83 & \\ & & 1298 \end{pmatrix}$
311	$\begin{pmatrix} 192 & & \\ & 192 & \\ & & 632 \end{pmatrix}$	**220**	$\begin{pmatrix} -80 & & \\ & -80 & \\ & & 1297 \end{pmatrix}$
420	$\begin{pmatrix} 176 & & \\ & 176 & \\ & & 507 \end{pmatrix}$	**310**	$\begin{pmatrix} 28 & & \\ & 28 & \\ & & 1266 \end{pmatrix}$

6.4.2.8- Two-phase Cu – W Bar at Zero External Load after Tensile Plastic Flow

In this simulation, the virtual two-phase Cu – W bar was unloaded to $\sigma_{33}^{App.} = 9$ MPa tensile load[41] after being extended to 3% total strain. At this load, the retained tensile plastic strain in the Cu – W sample is approximately 0.5 % (Fig. 6.26). Most of the plastic deformation is in the softer Cu phase. In Tables 6.68 & 69, we show the equivalent plastic strains and their dispersion parameters for the Cu and W phases, respectively. The effective plastic strain in the copper phase is almost *7.5x* of that in W.

The tensile test plot (Fig. 6.26) of the virtual sample model shows that the sample starts macroscopic yielding when the applied load is ~406 MPa during the loading cycle. During the unloading cycle (Fig. 6.33) the stress-strain response of the specimen is linear for far-field stresses, 350 MPa< σ_{33}^{o} <1019 MPa, which corresponds to 1.8% < ε_{33}^{o} < 3%. Significant macroscopic flow in the sample occurs for lower stresses; For 9 MPa < σ_{33}^{o} < 350 MPa. If the sample had continued to unload elastically (dashed arrow in Figure 6.33), the specimen would have unloaded to 1.2% tensile plastic strain. We observe that at $\sigma_{33}^{o} = 9$ MPa, the retained plastic strain is 0.5% tensile. Thus, the sample yielded in compression 0.7%, at far-field loads, σ_{33}^{o} , much lower than the macroscopic yield stress during loading. Most of the plastic flow during unloading also occurred in the Cu phase. Comparing Tables 6.68 &.69 with Tables 6.57 & 60, respectively, we observe that while the equivalent plastic strain in W decreased ~3% after unloading, it went up by ~7% in the Cu phase.

[41] Since the model is being executed in strain control, unloading to exactly zero load was problematic. For the concepts we are concerned about $\sigma_{33}^{App.}$ =9 MPa is close enough to zero.

Table 6.68: Average equivalent plastic strain for the Cu phase of the gage section of Cu – W bar unloaded after extended 3 % and its dispersion parameters. This phase contains 610 grains. All values are in microstrain (με).

(με)	$\bar{\varepsilon}^{eqpl,Cu}$
Average	**68192**
Std. Dev	37969
Maximum	217680
Minimum	4487
Full Width	213194

Table 6.69: Average equivalent plastic strain for the W phase of the gage section of Cu – W bar unloaded after extended 3 % and its dispersion parameters. This phase contains 642 grains. All values are in microstrain (με).

(με)	$\bar{\varepsilon}^{eqpl,W}$
Average	**9181**
Std. Dev	10048
Maximum	81634
Minimum	0
Full Width	81634

The significant plastic flow of the overall specimen for 9 MPa < σ_{33}^{o} <350 MPa indicates that the local stresses at the grain scale are much higher than the yield point of Cu. This local stress enhancement is due to the Heyn stresses which form due to the compatibility conditions imposed on the Cu grains by the (deformation-free) W grains. The Cu grains, which had yielded in tension during the loading cycle are placed in compression by the (undeformed, hard) W grains trying to relax to their zero load configurations, and deform plastically. This would relax the local stress to the local yield stress of a particular Cu grain. Further decrease of the far-field load would cause the average grain stress, which is the sum of far-field and Heyn stress terms, to decrease as well,

but since σ_{33}^{o} is already quite low, we expect a significant inter-phase Heyn stress field to be finite after unloading, with Cu grains in compression and W grains in W. We will now examine these stress fields.

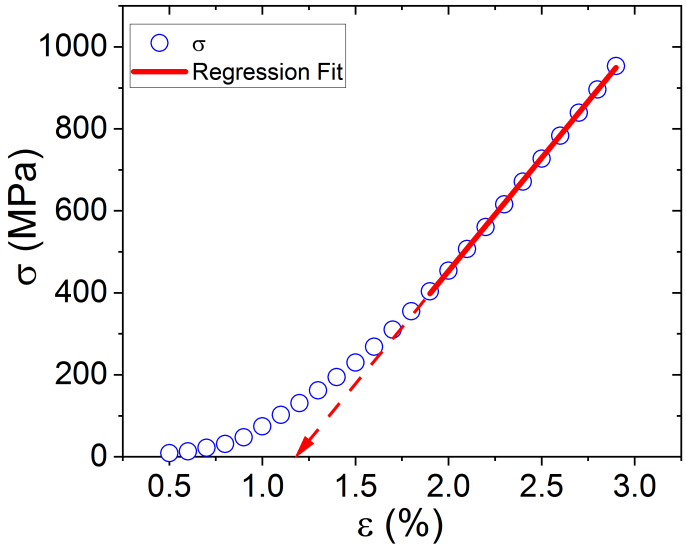

Figure 6.33: Unloading portion of the tensile plot in Fig. 6.26. We observe significant reverse yielding for far-field stresses, σ_{33}^{o}, below 350 MPa

6.4.2.8.1-Stress Distribution in Sample Coordinates

Tables 6.70 & 71 list the global average stress and lattice strain tensors and their distribution parameters in the gage section for both phases. These averages were computed over all grains, both Cu and W, in the model. We observe that, as expected, all $\bar{\sigma}_{33} = \sigma_{33}^{App.}$ within the error regime of a diffraction experiment. With the exception of $\bar{\sigma}_{23}$, all other $\bar{\sigma}_{ij}$ can be considered zero. However, all stress components exhibit wide distributions, the full widths are quite large,

indicating that some grains possess significant interaction stresses. The minimum $\bar{\sigma}_{33}$ value is -801 MPa, indicating that some grains are quite highly compressed. We observe similar behavior for the average lattice strains.

Table 6.70: Global average stress tensor of the gage section of Cu – W bar unloaded after extended 3 % and its dispersion parameters. The model contains 1252 grains, 610 Cu, and 642 W. All values are in MPa.

(MPa)	$\bar{\sigma}_{11}$	$\bar{\sigma}_{12}$	$\bar{\sigma}_{13}$	$\bar{\sigma}_{22}$	$\bar{\sigma}_{23}$	$\bar{\sigma}_{33}$
Average	**-9**	**4**	**5**	**-8**	**-25**	**13**
Std. Dev	282	150	146	285	149	343
Maximum	1073	645	861	906	675	1353
Minimum	-1297	-636	-796	-1328	-888	-801
Full Width	**2370**	**1280**	**1657**	**2234**	**1887**	**2154**

Table 6.71: Global average lattice strain tensor of the gage section of Cu – W bar unloaded after extended 3 % and its dispersion parameters. The model contains 1252 grains, 610 Cu, and 642 W. All values are in microstrain (με).

(με)	$\bar{\varepsilon}_{11}$	$\bar{\varepsilon}_{12}$	$\bar{\varepsilon}_{13}$	$\bar{\varepsilon}_{22}$	$\bar{\varepsilon}_{23}$	$\bar{\varepsilon}_{33}$
Average	**291**	**18**	**31**	**300**	**-65**	**-547**
Std. Dev	975	515	525	966	541	1489
Maximum	3442	2119	2934	2998	2205	3422
Minimum	-3020	-2122	-2612	-3146	-2917	-3636
Full Width	6462	4241	5546	6144	5122	7058

When we examine distributions of stresses and lattice strains in the individual phases we observe a very different case. Table 6.72 lists the average stress in the Cu phase and their dispersion parameters. All normal stresses $\bar{\sigma}_{ii}^{Cu}$, are finite, with tensile transverse stresses, $\bar{\sigma}_{11}^{Cu} \cong \bar{\sigma}_{22}^{Cu} \gg 0$, and compressive axial stress $\bar{\sigma}_{33}^{Cu} \ll 0$; the magnitudes of the average phase stress components,

$\bar{\sigma}_{kk}^{Cu}$ are an order of magnitude larger than the corresponding global average stresses $\bar{\sigma}_{kk}$. Average shear stress components, $\bar{\sigma}_{ij,i\neq j}^{Cu}$, are zero. The corresponding average lattice strains are tabulated in Table 6.73. If all Cu grains were contiguous and formed a continuous solid in Cartesian space, Tables 6.72 & 73 would indicate that this solid was under a normal tri-axial stress state, with isotropic tension in the cross-section of the gage section and compression along the axial, $\vec{S}_3$, direction.

Table 6.72: Average stress tensor for the Cu phase of the gage section of Cu – W bar unloaded after extended 3 % and its dispersion parameters. This phase contains 610 grains. All values are in MPa.

(MPa)	$\bar{\sigma}_{11}^{Cu}$	$\bar{\sigma}_{12}^{Cu}$	$\bar{\sigma}_{13}^{Cu}$	$\bar{\sigma}_{22}^{Cu}$	$\bar{\sigma}_{23}^{Cu}$	$\bar{\sigma}_{33}^{Cu}$
Average	**131**	**-2**	**-2**	**130**	**1**	**-190**
Std. Dev	179	31	34	178	34	169
Maximum	1073	90	94	906	107	623
Minimum	-414	-119	-94	-375	-88	-649
Full Width	**1487**	**209**	**188**	**1281**	**196**	**1272**

Table 6.73: Average lattice strain tensor for the Cu phase of the gage section of Cu – W bar unloaded after extended 3 % and its dispersion parameters. This phase contains 610 grains. All values are in microstrain (με).

(με)	$\bar{\varepsilon}_{11}^{Cu}$	$\bar{\varepsilon}_{12}^{Cu}$	$\bar{\varepsilon}_{13}^{Cu}$	$\bar{\varepsilon}_{22}^{Cu}$	$\bar{\varepsilon}_{23}^{Cu}$	$\bar{\varepsilon}_{33}^{Cu}$
Average	**1031**	**3**	**27**	**1038**	**47**	**-1893**
Std. Dev	541	225	312	506	325	509
Maximum	3442	957	1037	2998	1300	293
Minimum	-255	-1072	-962	-442	-1133	-3636
Full Width	3697	2029	1999	3440	2433	3929

Tables 6.74 & 75 list the average stress and lattice strain tensors in the W phase and their dispersion parameters. The stress state in the W phase is opposite to that of the Cu phase, with $\bar{\sigma}_{11}^{W} \cong \bar{\sigma}_{22}^{W} \ll 0$, and tensile axial stress $\bar{\sigma}_{33}^{Cu} \gg 0$. Interestingly, the average in-plane shear stress component, $\bar{\sigma}_{23}^{W}$, is finite for the W phase.

Table 6.74: Average stress tensor for the W phase of the gage section of Cu – W bar unloaded after extended 3 % and its dispersion parameters. This phase contains 642 grains. All values are in MPa.

(MPa)	$\bar{\sigma}_{11}^{W}$	$\bar{\sigma}_{12}^{W}$	$\bar{\sigma}_{13}^{W}$	$\bar{\sigma}_{22}^{W}$	$\bar{\sigma}_{23}^{W}$	$\bar{\sigma}_{33}^{W}$
Average	**-143**	**9**	**11**	**-140**	**-51**	**207**
Std. Dev	297	207	201	304	202	355
Maximum	609	645	861	649	675	1353
Minimum	-1297	-636	-796	-1328	-887	801
Full Width	**1806**	**1281**	**1657**	**1977**	**1562**	**2154**

Table 6.75: Average lattice strain tensor for the W phase of the gage section of Cu – W bar unloaded after extended 3 % and its dispersion parameters. This phase contains 642 grains. All values are in microstrain (με).

(με)	$\bar{\varepsilon}_{11}^{W}$	$\bar{\varepsilon}_{12}^{W}$	$\bar{\varepsilon}_{13}^{W}$	$\bar{\varepsilon}_{22}^{W}$	$\bar{\varepsilon}_{23}^{W}$	$\bar{\varepsilon}_{33}^{W}$
Average	**-413**	**32**	**35**	**-400**	**-171**	**731**
Std. Dev	749	685	667	754	669	849
Maximum	1627	2119	2934	1324	2205	3422
Minimum	-3020	-2122	-2612	-3146	-2917	-1681
Full Width	4647	4241	5546	4470	5122	5103

6.4.2.8.1.1- Phase-averaged Stress Components in Sample Coordinates Selected by Diffraction

In Figs. 6.34 & 35, we plot the grain averages of the stress and strain components, $\langle \sigma_{ij} \rangle_{i,\psi}^{Ph}$, $\langle \varepsilon_{ij} \rangle_{i,\psi}^{Ph}$, $(Ph = Cu, W)$for all ψ-tilts of the 200 reflections of the Cu and W phases. The solid symbols in these plots are the corresponding ψ-volume average stress and strain values, $\langle \sigma_{ij} \rangle_{\psi}^{Ph}$, $\langle \varepsilon_{ij} \rangle_{\psi}^{Ph}$. We see that the ψ-volume averages of the stress and strain components show little variation with ψ angle for both phases. We observed similar behavior for all reflections of all phases.

The reflection average stresses are tabulated in Table 6.76 for both W and Cu phases. For the W phase, all reflection volumes are under compression in the plane of the gage section and in tension along the axial direction, $\vec{S}_3$. The opposite stress state is observed for all reflection volumes of the Cu phase. The magnitudes of the reflection averages of the stress components, $\langle \sigma_{ij} \rangle_{i,\psi}^{Ph}$, are close to the relevant phase averages, $\bar{\sigma}_{ij}^{Ph}$ (Tables 6.72 & 74), however, they are different enough that they could not be considered representative volume elements.

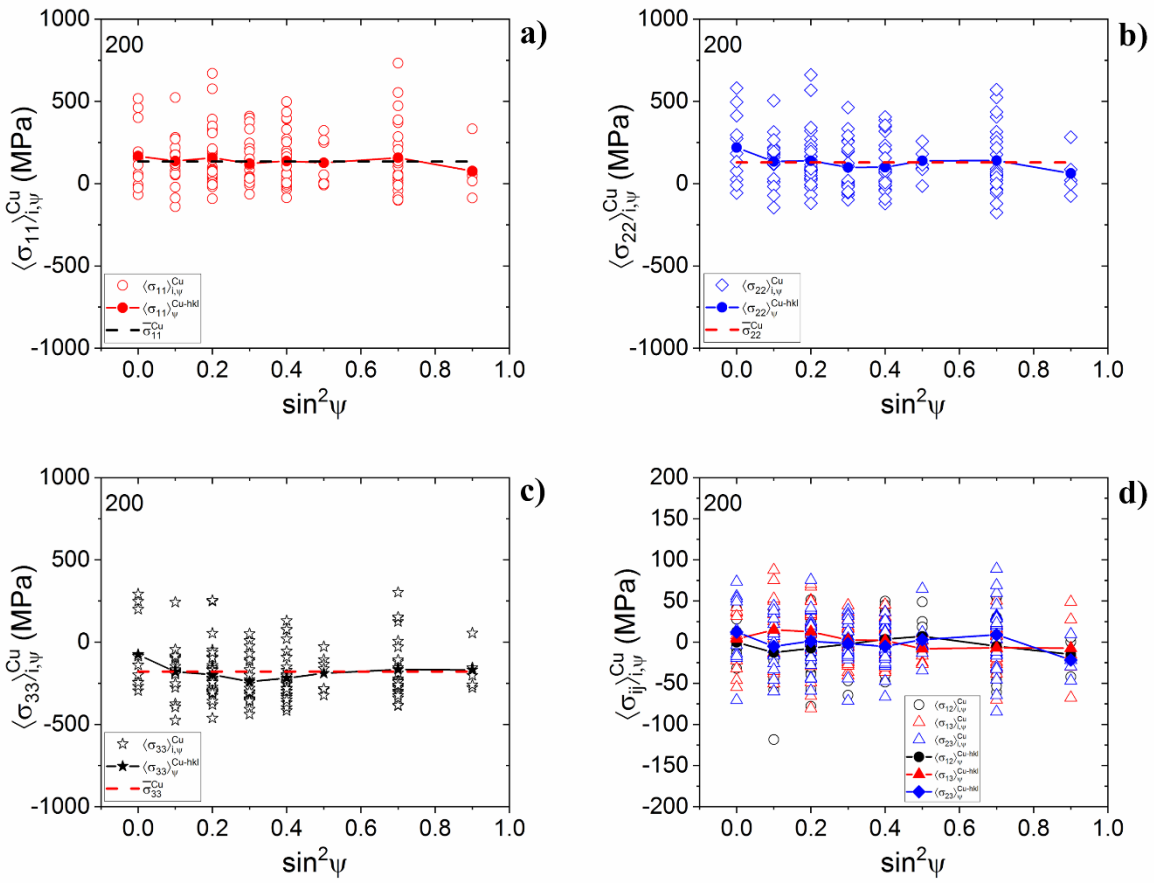

Figure 6.34: The phase-averaged grain stress values a) $\langle\sigma_{11}\rangle_{i,\psi}^{Cu}$, b) $\langle\sigma_{22}\rangle_{i,\psi}^{Cu}$, c) $\langle\sigma_{33}\rangle_{i,\psi}^{Cu}$ d) the shear stresses, for all grains as a function of $\sin^2\psi$.

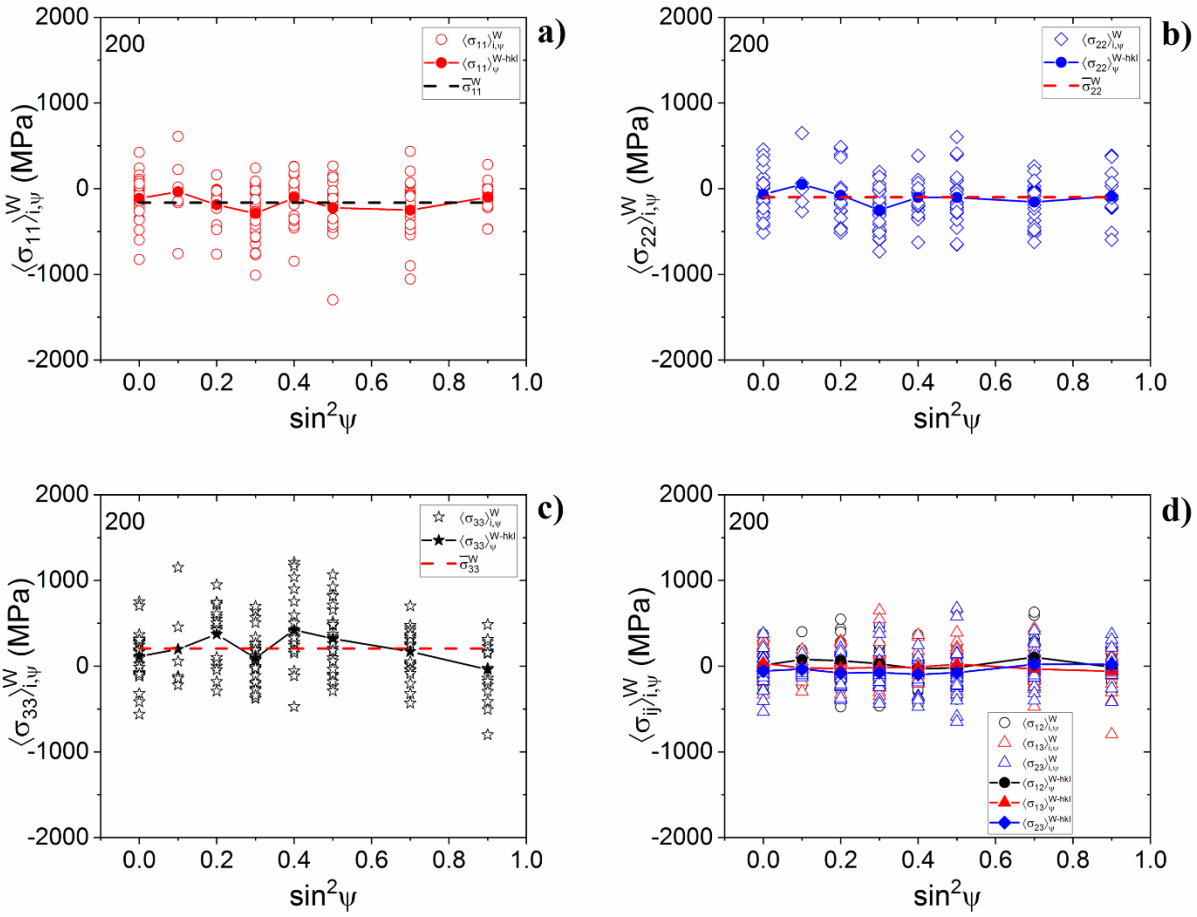

Figure 6.35: The phase-averaged grain stress values a) $\langle \sigma_{11} \rangle_{i,\psi}^{W}$, b) $\langle \sigma_{22} \rangle_{i,\psi}^{W}$, c) $\langle \sigma_{33} \rangle_{i,\psi}^{W}$ d) the shear stresses, for all grains as a function of $\sin^2\psi$.

Table 6.76: Reflection average stress tensors for the Cu and W phases of the gage section of the Cu – W bar unloaded after extended 3 %. The phase-average stress tensor is also included for ease of comparison. All values are in MPa.

Cu	Cu-phase	W	W-phase
111	$\langle\sigma_{ij}\rangle^{Cu,111} = \begin{bmatrix} 119 & 0 & -3 \\ 0 & 149 & 4 \\ -3 & 4 & -174 \end{bmatrix}$	**110**	$\langle\sigma_{ij}\rangle^{W,110} = \begin{bmatrix} -119 & 29 & 37 \\ 29 & -140 & -54 \\ 37 & -54 & 181 \end{bmatrix}$
200	$\langle\sigma_{ij}\rangle^{Cu,200} = \begin{bmatrix} 142 & -4 & 4 \\ -4 & 128 & 0 \\ 4 & 0 & -190 \end{bmatrix}$	**200**	$\langle\sigma_{ij}\rangle^{W,200} = \begin{bmatrix} -186 & 25 & -10 \\ 25 & -123 & -50 \\ -10 & -50 & 201 \end{bmatrix}$
220	$\langle\sigma_{ij}\rangle^{Cu,220} = \begin{bmatrix} 158 & -2 & 2 \\ -2 & 134 & -2 \\ 2 & -2 & -186 \end{bmatrix}$	**211**	$\langle\sigma_{ij}\rangle^{W,211} = \begin{bmatrix} -76 & -5 & 11 \\ -5 & -100 & -48 \\ 11 & -48 & 255 \end{bmatrix}$
311	$\langle\sigma_{ij}\rangle^{Cu,311} = \begin{bmatrix} 134 & -3 & -5 \\ -3 & 116 & 5 \\ -5 & 5 & -205 \end{bmatrix}$	**220**	$\langle\sigma_{ij}\rangle^{W,220} = \begin{bmatrix} -161 & 1 & -6 \\ 1 & -177 & -90 \\ -6 & -90 & 187 \end{bmatrix}$
420	$\langle\sigma_{ij}\rangle^{Cu,420} = \begin{bmatrix} 120 & 0 & -8 \\ 0 & 113 & -1 \\ -8 & -1 & -209 \end{bmatrix}$	**310**	$\langle\sigma_{ij}\rangle^{W,310} = \begin{bmatrix} -155 & 0 & 34 \\ 0 & -163 & -18 \\ 34 & -18 & 201 \end{bmatrix}$
	$\bar{\sigma}_{ij}^{Cu} = \begin{bmatrix} 131 & -2 & -2 \\ -2 & 130 & -1 \\ -2 & -1 & -191 \end{bmatrix}$		$\bar{\sigma}_{ij}^{W} = \begin{bmatrix} -143 & 9 & 11 \\ 9 & -140 & -51 \\ 11 & -51 & 207 \end{bmatrix}$

6.4.2.8.2- Diffraction Stress/Strain Analysis

In Figs. 6.36 & 37, we plot the $\langle\varepsilon'_{11}\rangle_{i,\psi}^{Ph}\ vs.\sin^2\psi$ data for all five reflections of the two-phases computed from the output of the FEpX model. To obtain the reflection average stress $\langle\sigma_{33}^{D}\rangle^{hkl}$, we used the slopes of linear regression fits to the $\langle\varepsilon'_{11}\rangle_{i,\psi}^{Ph}\ vs.\sin^2\psi$ data with diffraction elastic constants at Voigt, Reuss, Kröner, Neerfeld-Hill limits (Table 5.8), and the simulation DEC values (Tables 6.46, 48 & 49). These stress results are shown in Tables 6.77 & 78. We observe that all reflections yield stress values different from the far-field stress, σ_{33}^{o} for both phases.

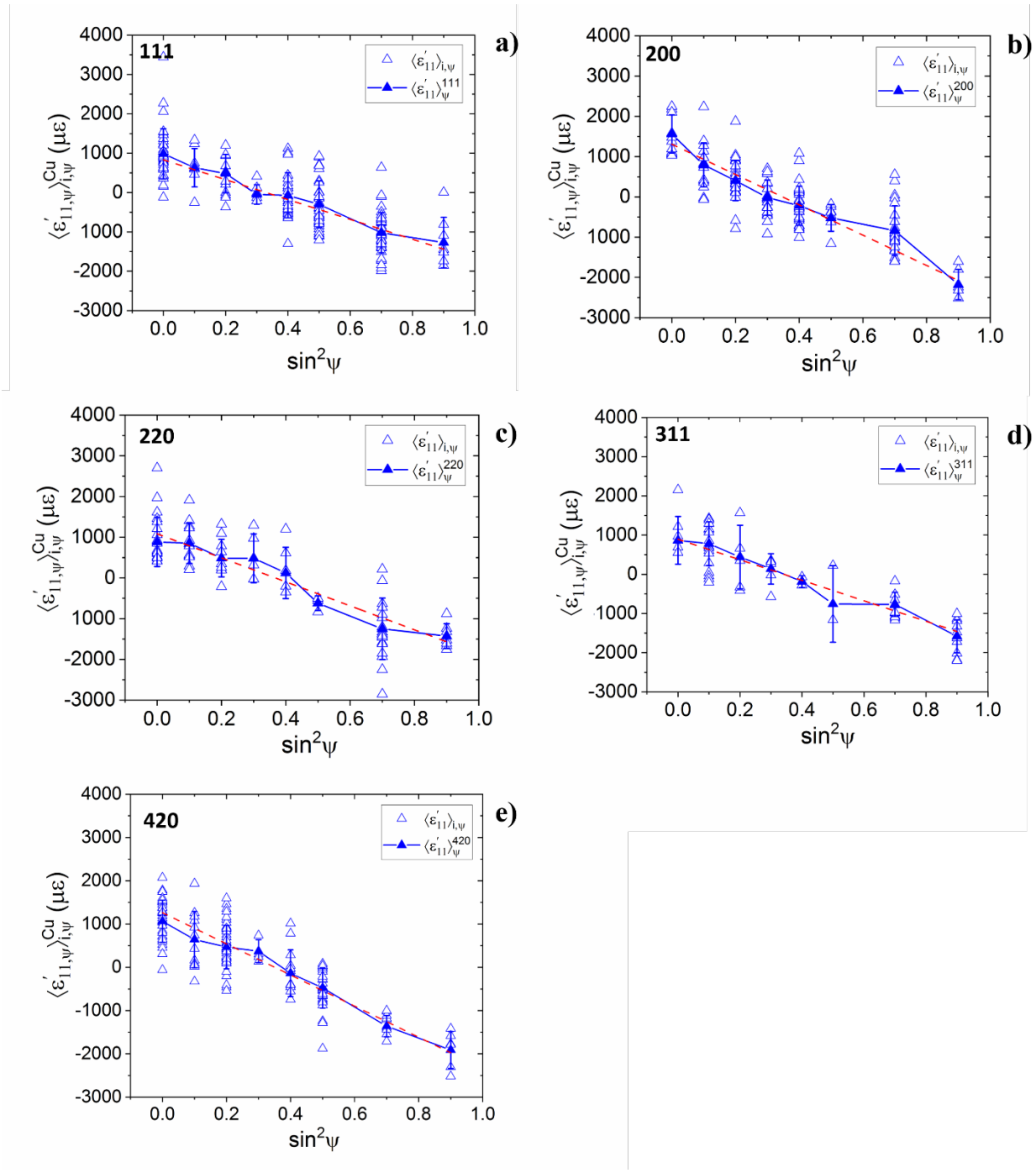

Figure 6.36: $\langle \varepsilon'_{11,\psi} \rangle_{i,\psi}^{Cu}$ *vs.* $sin^2\,\psi$ plots for studied reflections of the Cu phase of the unloaded the Cu – W model.

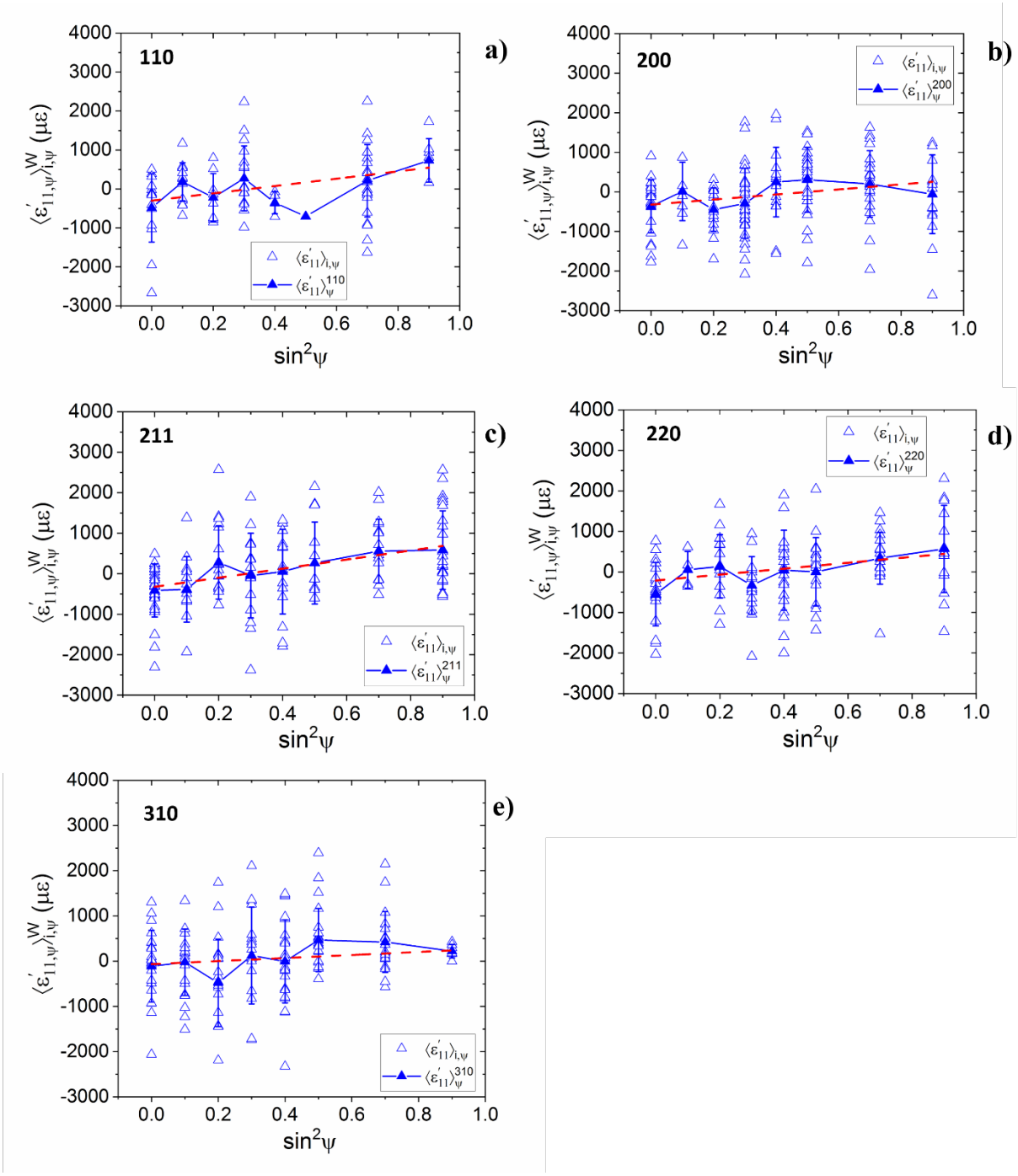

Figure 6.37: $\langle \varepsilon'_{11,\psi} \rangle^{W}_{i,\psi}$ *vs.* $sin^2\,\psi$ plots for studied reflections of the W phase of the unloaded the Cu – W model.

Table 6.77: The average stresses, $\langle \sigma_{33}^{D} \rangle^{Cu-hkl}$, obtained from simulated diffraction analysis of the plots shown in Fig. 6.35. For comparison, $\bar{\sigma}_{33} = 9\ MPa$.

$\langle \sigma_{33}^{D} \rangle^{Cu-hkl}$ (MPa)	Voigt	Reuss	Neer.-Hill	Kröner	$DEC_{Sim.}$
111	-227±8	-313±10	-253±8	-263±9	-320±11
200	-240±15	-104±6	-162±10	-145±9	-293±18
220	-190±25	-169±22	-182±24	-179±24	-277±37
311	-247±24	-158±15	-205±20	-193±18	-314±30
420	-238±9	-153±6	-198±8	-186±7	-308±12

Table 6.78: The average stresses, $\langle \sigma_{33}^{D} \rangle^{W-hkl}$ obtained from simulated diffraction analysis of the plots shown in Fig. 6.36. For comparison, $\bar{\sigma}_{33} = 9\ MPa$.

$\langle \sigma_{33}^{D} \rangle^{W-hkl}$ (MPa)	Voigt/Reuss/Neer.-Hill/Kröner	$DEC_{Sim.}$
110	285±123	230±100
200	194±110	151±85
211	340±70	262±54
220	221±98	176±78
310	101±56	81±45

The $\langle \varepsilon'_{11,\psi} \rangle_{i,\psi}^{Ph.}\ vs.\ sin^2\psi$ plots shown in Figs. 6.36 & 37 show deviations from linearity. To test if these deviations could be considered "oscillations" and influence the computed stress results, we removed the first two ψ-ensemble points and repeated the stress analysis. The results are summarized in Table 6.79 for both phases. For most reflections the removal of the first two ψ-ensemble points results in a significant change of the computed stress, $\langle \sigma_{33}^{D} \rangle^{Ph.-hkl}$. By inspection,

we conclude that all $\langle \varepsilon'_{11,\psi} \rangle_{i,\psi}^{Ph.}$ $vs. sin^2\,\psi$ plots are oscillatory and should not be analyzed by linear least-squares fitting.

Table 6.79: The average stresses obtained from simulated diffraction analysis of the plots shown in Figs. 6.31 & 32 after removal of first two ψ-ensemble points.

$\langle \boldsymbol{\sigma}_{33}^{D} \rangle^{Cu-hkl}$ (MPa)	Simulated	$\langle \boldsymbol{\sigma}_{33}^{D} \rangle^{W-hkl}$ (MPa)	Simulated
111	-362±46	**110**	275±136
200	-471±47	**200**	204±123
220	-502±69	**211**	183±69
311	-352±35	**220**	224±98
420	-547±32	**310**	75±86

From the slopes and intercepts of lines fitted to the data shown in Figs. 6.36 & 37, we obtain the phase-specific reflection average strains, $\langle \varepsilon_{ij}^{D} \rangle^{Ph-hkl}$, in sample coordinates. These results and their regression-fit errors are presented in Tables 6.80 & 81 for Cu and W phases, respectively. The reflection average strain tensors in the sample coordinates, computed from real space strain values, $\langle \varepsilon_{ij} \rangle^{Ph-hkl}$, obtained from the finite element analysis for each phase, as well as the overall phase average are also included.

We observe that the strain tensors obtained from linear regression from all reflections agree quite well with the real space averages for both phases. On the other hand, the slopes of the

$\langle \varepsilon'_{11,\psi} \rangle^{Ph}_{i,\psi}$ $vs. \sin^2 \psi$ plots are quite different. Consequently, any computation which utilized only slopes would have yielded significantly different answers for each reflection.

Table 6.80: Slopes and intercepts of lines fitted to $\langle \boldsymbol{\varepsilon'_{11,\psi}} \rangle^{\boldsymbol{Ph}}_{\boldsymbol{i,\psi}}$ $\boldsymbol{vs. sin^2 \psi}$ data and the corresponding reflection average strain tensors for the Cu phase. The corresponding real space averages are also included. All values are in microstrain (με).

hkl	Intercept	Slope	$\langle \boldsymbol{\varepsilon^D_{ij}} \rangle^{\boldsymbol{Ph-hkl}}$	$\langle \boldsymbol{\varepsilon_{ij}} \rangle^{\boldsymbol{Ph-hkl}}$
111	832(92)	-2525 (223)	$\begin{bmatrix} 832 & 0 & 0 \\ 0 & 832 & 0 \\ 0 & 0 & -1693 \end{bmatrix}$	$\begin{bmatrix} 1123 & 10 & 30 \\ 10 & 1019 & 69 \\ 30 & 69 & -1909 \end{bmatrix}$
200	1309(265)	-3765(265)	$\begin{bmatrix} 1309 & 0 & 0 \\ 0 & 1309 & 0 \\ 0 & 0 & -2456 \end{bmatrix}$	$\begin{bmatrix} 977 & -12 & 38 \\ -12 & 1071 & 17 \\ 38 & 17 & -1850 \end{bmatrix}$
220	1083(138)	-2946(386)	$\begin{bmatrix} 1083 & 0 & 0 \\ 0 & 1083 & 0 \\ 0 & 0 & -1863 \end{bmatrix}$	$\begin{bmatrix} 1071 & 0 & 33 \\ 0 & 1071 & 27 \\ 33 & 27 & -1881 \end{bmatrix}$
311	893(91)	-2613(186)	$\begin{bmatrix} 893 & 0 & 0 \\ 0 & 893 & 0 \\ 0 & 0 & -2394 \end{bmatrix}$	$\begin{bmatrix} 977 & 15 & 11 \\ 15 & 965 & 77 \\ 11 & 77 & -1828 \end{bmatrix}$
420	1262 (116)	-3596(216)	$\begin{bmatrix} 1262 & 0 & 0 \\ 0 & 1262 & 0 \\ 0 & 0 & -2334 \end{bmatrix}$	$\begin{bmatrix} 976 & 5 & 16 \\ 5 & 1039 & 49 \\ 16 & 49 & -1950 \end{bmatrix}$
Phase average				$\begin{bmatrix} 1032 & 3 & 27 \\ 3 & 1038 & 47 \\ 27 & 47 & -1893 \end{bmatrix}$

Table 6.81: Slopes and intercepts of lines fitted to $\langle \varepsilon'_{11,\psi} \rangle_{i,\psi}^{Ph}$ $vs.\ sin^2\psi$ data and the corresponding reflection average strain tensors for the W phase. The corresponding real space averages are also included. All values are in microstrain (με).

hkl	Intercept	Slope	$\langle \varepsilon_{ij}^{D} \rangle^{Ph-hkl}$	$\langle \varepsilon_{ij} \rangle^{Ph-hkl}$
110	-302(214)	1049(449)	$\begin{bmatrix} -302 & 0 & 0 \\ 0 & -302 & 0 \\ 0 & 0 & 747 \end{bmatrix}$	$\begin{bmatrix} -328 & 99 & 129 \\ 99 & -398 & -185 \\ 129 & -185 & 642 \end{bmatrix}$
200	-353(117)	628(283)	$\begin{bmatrix} -353 & 0 & 0 \\ 0 & -353 & 0 \\ 0 & 0 & 275 \end{bmatrix}$	$\begin{bmatrix} -529 & -83 & -36 \\ -83 & -322 & -172 \\ -36 & -172 & 734 \end{bmatrix}$
211	-281(145)	1219(302)	$\begin{bmatrix} -281 & 0 & 0 \\ 0 & -281 & 0 \\ 0 & 0 & 938 \end{bmatrix}$	$\begin{bmatrix} -306 & -14 & 34 \\ -14 & -385 & -159 \\ 34 & -159 & 782 \end{bmatrix}$
220	-195(134)	720(324)	$\begin{bmatrix} -195 & 0 & 0 \\ 0 & -195 & 0 \\ 0 & 0 & 525 \end{bmatrix}$	$\begin{bmatrix} -420 & 4 & -24 \\ 4 & -469 & -296 \\ -24 & -296 & 723 \end{bmatrix}$
310	-40(153)	350(185)	$\begin{bmatrix} -40 & 0 & 0 \\ 0 & -40 & 0 \\ 0 & 0 & 310 \end{bmatrix}$	$\begin{bmatrix} -422 & 2 & 112 \\ 2 & -445 & -67 \\ 112 & -67 & 741 \end{bmatrix}$
Phase average				$\begin{bmatrix} -412 & 32 & 35 \\ 32 & -401 & -171 \\ 35 & -171 & 731 \end{bmatrix}$

In Table 6.82, we list the stresses in the sample coordinates obtained from $\langle \varepsilon_{ij}^{D} \rangle^{Ph-hkl}$ strain tensors for each phase. For this computation, we used the isotropic Hooke's law with the elastic moduli of individual reflections, E^{hkl}, ν^{hkl}, computed from Tables 6.46 & 49.

Comparing Tables 6.76 & 82, the computed reflection average stresses of reflections of Cu and W phase do not agree with the real space reflection average stresses in magnitude, even though we do obtain the correct sign for all cases.

Table 6.82: The computed reflection average stresses from the average strain tensors listed in Tables 6.80 & 81 and E^{hkl}, v^{hkl}.

Cu	Computed reflection average stresses	W	Computed reflection average stresses
111	$\begin{pmatrix} 125 & & \\ & 125 & \\ & & -264 \end{pmatrix}$	**110**	$\begin{pmatrix} -47 & & \\ & -47 & \\ & & 209 \end{pmatrix}$
200	$\begin{pmatrix} 190 & & \\ & 190 & \\ & & -310 \end{pmatrix}$	**200**	$\begin{pmatrix} -159 & & \\ & -159 & \\ & & -11 \end{pmatrix}$
220	$\begin{pmatrix} 203 & & \\ & 203 & \\ & & -266 \end{pmatrix}$	**211**	$\begin{pmatrix} 0 & & \\ & 0 & \\ & & 284 \end{pmatrix}$
311	$\begin{pmatrix} 70 & & \\ & 70 & \\ & & -385 \end{pmatrix}$	**220**	$\begin{pmatrix} -23 & & \\ & -23 & \\ & & 151 \end{pmatrix}$
420	$\begin{pmatrix} 197 & & \\ & 197 & \\ & & -311 \end{pmatrix}$	**310**	$\begin{pmatrix} 32 & & \\ & 32 & \\ & & 117 \end{pmatrix}$

6.4.2.9- Deformation Distributions of Virtual Cu Sample

In previous sections, we observe that some grains in the virtual Cu sample might be under larger triaxial stress (Figs. 6.11 & 12). Thus, we decided to investigate the distributions of the trace, $tr(\sigma_{ij})$, of the stress tensors for all grains in the gage section of the Cu sample, and their corresponding Von Mises stress values. These are scalar parameters, similar to the equivalent plastic strain, and are given by:

$$tr(\sigma_{ij}) = \sigma_{kk} \qquad \text{Eq. (6-3-a)}$$

$$\sigma_{VM} = \sqrt{\frac{3}{2}\sigma_{ij}\sigma_{ij} - \frac{1}{2}(\sigma_{kk})^2} \qquad \text{Eq. (6-3-b)}$$

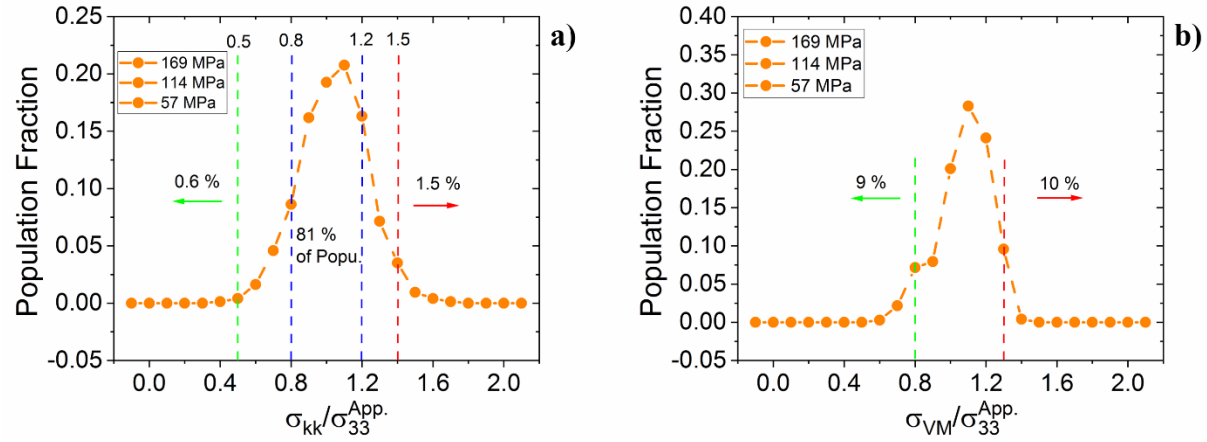

Figure 6.38: The distribution of a) the trace and b) Von Mises stresses of 3 elastic loadings for virtual Cu. Trace and Von Mises stresses are normalized by the applied stress to aid in plotting.

Fig. 6.37 shows the distribution of normalized $tr(\sigma_{ij})$ and σ_{VM} parameters for the elastic region of our virtual sample. The distribution of $tr(\sigma_{ij})/\sigma_{33}^{App.}$ for 57, 114, and 169 MPa show that for 0.8% of the grain population (~5 grains), the trace is less than 50% of the ideal homogeneous value. 10 grains or so have traces greater than *1.4x* of the ideal value. The distribution of $\sigma_{VM}/\sigma_{33}^{App.}$ for the same loads is much narrower. We note that the grains with the lowest trace values did not correspond to those with the lowest VM stress values. The shape of the distribution for these loads is very similar for all elastic loading steps.

The shape of the $tr(\sigma_{ij})/\sigma_{33}^{App.}$ distribution changes markedly for 222 MPa applied load. This is due to the onset of local plastic flow. With the increasing applied load and resultant plastic strain, the $tr(\sigma_{ij})/\sigma_{33}^{App.}$ distribution keeps changing. At $\sigma_{33}^{App.} = 304\ MPa$, the distribution has changed dramatically from its shape in the elastic region: Only 4% of the grains are at 50% of the ideal trace ratio, with some grains having zero trace values. In addition, approximately 9% of the grains are *1.5-2x* of the ideal trace value. After large-scale plastic flow, the distribution stabilizes. The distribution at $\sigma_{33}^{App.} = 320\ MPa$ applied load is very similar to that at $\sigma_{33}^{App.} = 304\ MPa$. We also observe similar distributions at $\sigma_{33}^{App.} = 329, 333\ \&\ 334.5\ MPa$ (Fig. 6.38-a). The changes of the distribution profiles for $\sigma_{VM}/\sigma_{33}^{App.}$ Are similar to those for the normalized trace parameter (Fig. 6.38-b).

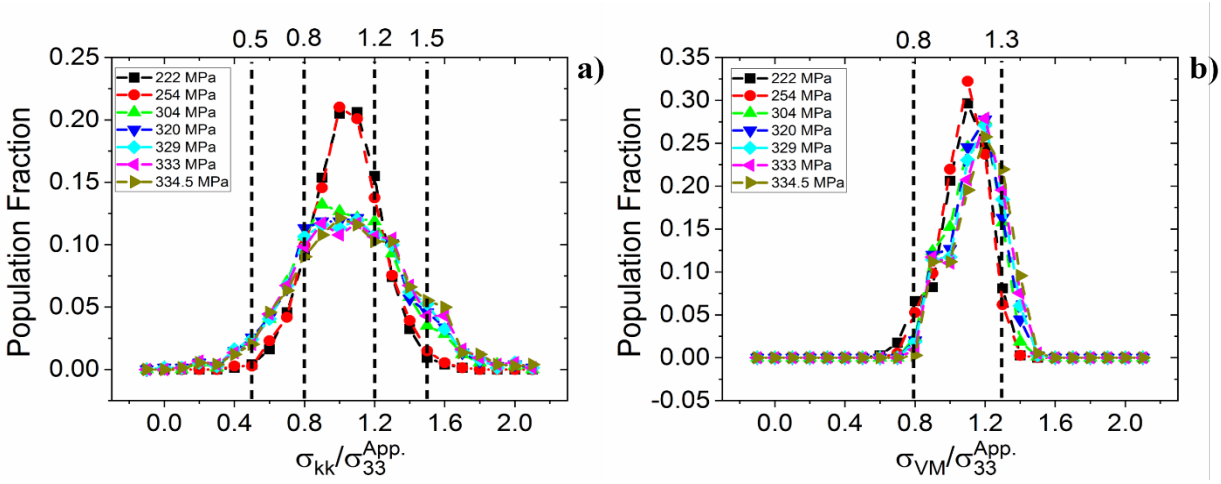

Figure 6.39: The distribution of a) the trace and b) Von Mises stresses of seven elastoplastic loading steps for the single-phase Cu model. Trace and Von Mises stresses are normalized by the applied stress.

We tested the normality of all distributions using the conventional Shapiro-Wilk (SW) and Kolmogorov-Smirnov (KS) tests [134, 135, 136]. Both SW and KS tests showed that the trace ratio is not normally distributed in the elastic regime. With increasing plastic flow under increasing applied load, the KS test starts to accept normality, whereas the SW test rejects normality for these distributions. The situation changes gradually during unloading: In the first unloading step where $\sigma_{33}^{App.} = 269\ MPa$, the SW test rejects normality whereas the KS test cannot reject normality. For the next two unloading steps, $\sigma_{33}^{App.} = 169\ \&\ 72\ MPa$, normality is rejected by both tests. At approximately zero external load[42], the distribution satisfies both normality tests and the profile is well fitted with a Gaussian function (Figure 6.40-a). This profile shows that, while the unloaded material has a normal stress distribution centered at 6 MPa, it has a very wide stress distribution; the FWHM is 200 MPa, and 30% of the grain population will have stresses larger than ±100 MPa. We note that, in contrast to the trace ratio, the distribution of the von Mises ratio did not approach normality after unloading (Fig. 6.40-b).

[42] We relaxed the applied stress to 1 MPa so that the trace ratio, $tr(\sigma_{ij})/$, was finite. In the absence of Heyn stresses, $tr(\sigma_{ij})$ should be equal to $\sigma_{33}^{App.}$.

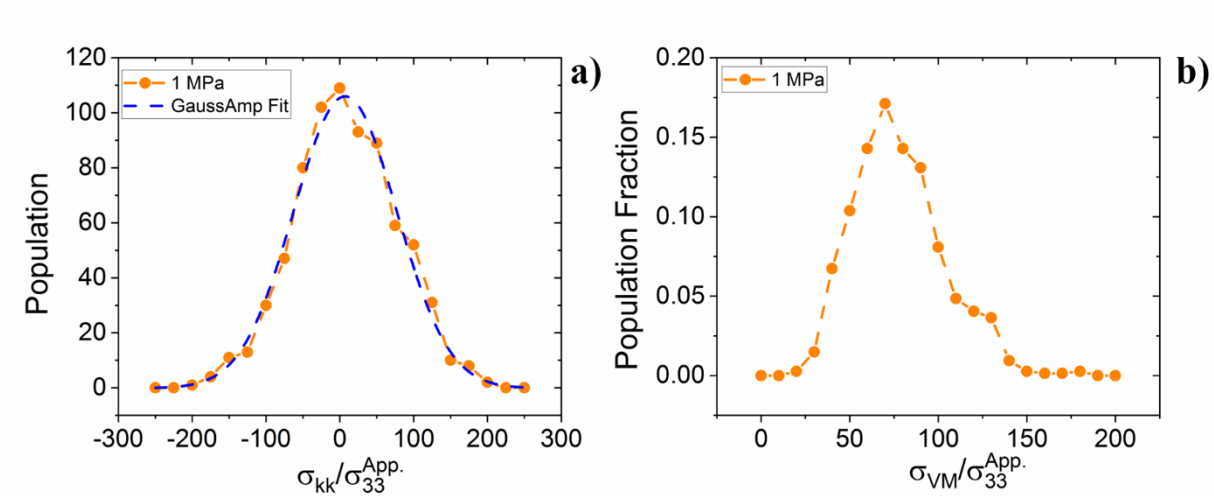

Figure 6.40: Trace (a) and von Mises (b) ratio distributions in the Cu sample after unloading from the plastic flow.

As in the case of single-phase Cu, to avoid a sampling issue, we performed a larger simulation. The population distribution of grains in the gage section of the combined model, with a total of 6260 grains. All populations have increased approximately five-fold. There are at least 12 grains in each ψ – volume for both phases. The smallest populated ψ – volumes are ψ= 26.57°, 39.23° and 45° for 311 reflection of Cu phase. The results of the combined model are within 10% of the results of the model consisting of 1252 grains in the gage section. Therefore, we decided to show the results belong to smaller simulations.

6.4.2.10- Effect of Sampling on Results of Two-phase Cu – W Simulations

In the two-phase Cu – W simulations containing 2500 diffracting grains, some ψ – volumes had very small populations due to the random placement of grains. Thus, we wanted to check the effect of sampling on the results of Cu – W simulations. To investigate these issues,

we performed a larger simulation by modeling the stress-strain responses of four additional (random) models, each with 2500 grains, and analyzing the results together with the original model.

The population distribution of grains for Cu and W phases in the gage section of the combined model, with a total of 6260 grains, is shown in Tables 6.83 & 84. All populations have increased approximately five-fold. The ψ-ensemble with the smallest population, 12 grains, belongs to the 311 reflection at ψ=26.57° in the Cu phase.

Table 6.83: The population distribution for the Cu phase in the gage section of the Cu – W sample.

ψ(°)	0	18.43	26.57	33.21	39.23	45	56.79	71.57	Total
$N_{\psi}^{111}, f_{\psi}^{111}$	199	46	66	30	107	226	225	47	946
$N_{\psi}^{200}, f_{\psi}^{200}$	65	106	135	140	148	32	118	31	775
$N_{\psi}^{220}, f_{\psi}^{220}$	66	58	46	17	36	23	67	27	340
$N_{\psi}^{311}, f_{\psi}^{311}$	18	86	12	25	16	14	48	82	301
$N_{\psi}^{420}, f_{\psi}^{420}$	137	59	196	36	45	141	45	29	688
N_{ψ}^{Total}	485	355	455	248	352	436	503	217	3050

Table 6.84: The population distribution for the W phase in the gage section of the Cu – W sample.

$\psi(°)$	0	18.43	26.57	33.21	39.23	45	56.79	71.57	Total
$N_{\psi}^{110}, f_{\psi}^{110}$	75	56	49	66	17	25	87	30	405
$N_{\psi}^{200}, f_{\psi}^{200}$	83	68	112	130	123	136	77	59	788
$N_{\psi}^{211}, f_{\psi}^{211}$	149	69	101	84	92	64	103	106	768
$N_{\psi}^{220}, f_{\psi}^{220}$	97	23	79	53	64	87	87	68	558
$N_{\psi}^{310}, f_{\psi}^{310}$	109	81	91	70	97	101	87	55	691
N_{ψ}^{Total}	513	297	432	403	393	413	441	318	3210

We compared DEC values, $S_1^{TP-Sim-Com.}$ and $\frac{S_2}{2}^{TP-Sim-Com.}$, of the combined model with those for the original (small) model, respectively. These results are shown in Tables 6.85, 86 & 87. We observe that a five-fold population increase has changed the S_1^{TP-Sim} and $\frac{S_2}{2}^{TP-Sim}$ values for all reflections by 20% or less for both phases. The DEC values for the 220 reflection of the Cu phase have the largest deviation, 18 to 20 %. This change is not the result of sampling because the lowest populated reflection belonged to 311 reflection of the Cu phase in the original model. We observe smaller changes in DEC values obtained from the combined model for the reflections of both phases except 220 reflection of Cu phase between 1 to 9 %.

Table 6.85: Diffraction elastic constants obtained from the FEA analysis of W phase for the gage section of the combined model. % Deviation of simulated $S_1^{TP-Sim-Com.}$ & $\frac{S_2}{2}^{TP-Sim-Com.}$ from S_1^{TP-Sim} & $\frac{S_2}{2}^{TP-Sim}$ was also shown.

(TPa)$^{-1}$	$S_1^{TP-Sim-Com.}$	$\frac{S_2}{2}^{TP-Sim-Com.}$	S_1^{TP-Sim}	$\frac{S_2}{2}^{TP-Sim}$	%Dev. From S_1^{TP-Sim}	%Dev. From $\frac{S_2}{2}^{TP-Sim}$
(110)	-0.96±0.01	4.26±0.01	-0.94±0.01	4.09±0.01	2	4
(200)	-0.97±0.01	4.22±0.01	-0.98±0.01	4.25±0.01	2	1
(211)	-0.96±0.01	4.21±0.01	-0.98±0.01	4.28±0.01	2	2
(220)	-1.01±0.01	4.29±0.01	-0.95±0.01	4.15±0.01	6	3
(310)	-0.96±0.01	4.19±0.01	-0.94±0.01	4.13±0.01	2	2

Table 6.86: Diffraction elastic constant, $S_1^{TP-Sim-Com.}$, obtained from the FEA analysis of Cu phase for the gage section of the combined model. % Deviation of simulated $S_1^{TP-Sim-Com.}$ from S_1^{TP-Sim} was also shown.

S_1 (TPa)$^{-1}$	$S_1^{TP-Sim-Com.}$	S_1^{TP-Sim}	% Dev. From S_1^{TP-Sim}
(111)	-1.47±0.01	-1.52±0.01	3
(200)	-1.73±0.01	-1.75±0.01	1
(220)	-1.69±0.01	-1.39±0.01	18
(311)	-1.56±0.01	-1.57±0.01	1
(420)	-1.74±0.01	-1.59±0.01	9

Table 6.87: Diffraction elastic constant, $\frac{S_2}{2}^{TP-Sim-Com.}$, obtained from the FEA analysis of Cu phase for the gage section of the combined model. % Deviation of simulated $\frac{S_2}{2}^{TP-Sim-Com.}$ from $\frac{S_2}{2}^{TP-Sim}$ was also shown.

$S_2/2$ (TPa)$^{-1}$	$\frac{S_2}{2}^{TP-Sim-Com.}$	$\frac{S_2}{2}^{TP-Sim}$	% Dev. From $\frac{S_2}{2}^{TP-Sim}$
(111)	6.38±0.01	6.51±0.01	2
(200)	7.35±0.01	7.54±0.01	3
(220)	7.58±0.01	6.30±0.01	20
(311)	6.90±0.01	7.23±0.01	5
(420)	7.34±0.01	7.09±0.01	4

Finally, we compared the global average stress and lattice strain tensor of gage section of the combined model shown in Tables 6.88 & 89 and the original model extended 3% which was shown in Tables 6.70 & 71. We observe that a five-fold population increase has changed the average stress and lattice strain values and their standard deviation parameters by 5% or less for both phases. The full width of stress and lattice strain tensor components for the combined model is much larger than the original model.

Table 6.88: Global average stress tensor of the gage section of the Cu – W bar extended 3 % and its dispersion parameters. The model contains 6260 grains, 3050 Cu, and 3210 W. All values are in MPa.

(MPa)	$\bar{\sigma}_{11}$	$\bar{\sigma}_{12}$	$\bar{\sigma}_{13}$	$\bar{\sigma}_{22}$	$\bar{\sigma}_{23}$	$\bar{\sigma}_{33}$
Average	**-18**	**6**	**12**	**-15**	**-47**	**1065**
Std. Dev	425	203	207	423	207	730
Maximum	1505	959	1237	1494	848	4126
Minimum	-2333	-994	-934	-1843	-1205	-347
Full Width	**3835**	**1953**	**2271**	**3337**	**2053**	**4473**

Table 6.89: Global average lattice strain tensor of the gage section of the Cu – W bar extended 3 % and its dispersion parameters. The model contains 6260 grains, 3050 Cu, and 3210 W. All values are in microstrain (με).

(με)	$\bar{\varepsilon}_{11}$	$\bar{\varepsilon}_{12}$	$\bar{\varepsilon}_{13}$	$\bar{\varepsilon}_{22}$	$\bar{\varepsilon}_{23}$	$\bar{\varepsilon}_{33}$
Average	**-838**	**35**	**24**	**-840**	**-197**	**3460**
Std. Dev	1200	710	774	1190	760	1540
Maximum	3550	3110	4290	2870	2700	9970
Minimum	-6310	-3290	-3110	-5020	-4020	-1280
Full Width	**9860**	**6400**	**7400**	**7890**	**6720**	**11250**

Consequently, increasing diffracting grains 5 times does not change results drastically. We concluded that the sampling does not play an important role in our simulations. Therefore, we presented the results of the original model of the two-phase Cu – W specimen in this thesis. However, we also need to acknowledge that the increase of full-width also shows us that we need to have more grains in virtual samples in order to have a representative polycrystalline sample.

6.5- Summary

In this chapter, we used an advanced crystal-based polycrystalline FEM program, FEpX, to obtain local stress and strain distribution in three-dimensional virtual, untextured, polycrystalline bars deformed in tension through plastic flow and unloaded. These values were, then, used to conduct virtual diffraction experiments for the determination of lattice strains and stresses, and the determination of diffraction elastic constants (DECs). We modeled, in sequence, an isotropic material, two single-phase materials (Cu and W), and one two-phase material (Cu – W).

We used the isotropic material, with a unity Zener index, to check for St. Venant effects due to boundary conditions. Our results showed that the central ~3/8 of the bar was under uniform uniaxial tension, while the ends had triaxial stresses and strong stress/strain gradients. We named the central portion the “gage” section of our virtual tensile test.

In the W sample, with the Zener index equal to 0.99, $\varepsilon'_{hkl}\ vs.\ \sin^2\psi$ plots were linear in the gage section and standard diffraction formalism yielded excellent results, with computed stresses exactly equal to the applied stresses. On the other hand, we observed oscillatory

$\varepsilon'_{hkl}\ vs.\sin^2\psi$ in the regions closer to the edges due to grip boundary conditions. For our Cu and Cu – W samples we only analyzed the gage region. We observed the following:

a) Interaction stresses arising to constrain incompatible displacements across grain boundaries cause oscillations in $\varepsilon'_{hkl}\ vs.\sin^2\psi$ plots.

b) Stresses computed from the slopes of lines fitted to oscillatory $\varepsilon'_{hkl}\ vs.\sin^2\psi$ plots can yield large errors.

c) It is not possible to study stresses in two-phase materials using $\varepsilon'_{hkl}\ vs.\sin^2\psi$ plots with single-phase elastic constants.

d) In single-phase or two-phase samples which underwent plastic flow, the distribution of Heyn stresses complicates diffraction analysis. In such samples, multiple reflections must be measured and the results compared to each other before stresses are reported.

e) In two-phase samples, multiple reflections from both phases must be measured.

f) Even for untextured samples stress and lattice strain dispersions caused by Heyn effects cannot be assumed to be Gaussian in nature. These dispersions can become Gaussian after unloading from the plastic flow.

7- CONCLUSIONS & FUTURE WORK

In this dissertation, we presented a rigorous analysis of diffraction stress measurement via computation simulations. We introduced a detailed literature review of residual stress and stress determination techniques based on measurement of lattice strains through diffraction and showed that, even though the basic approach has been in use for almost a century, there are still cases where the results are suspect. There are cases where the reported stress states violate equations of equilibrium or other cases where diffraction results show stress where sectioning methods do not. To formulate an adequate answer to these issues we started with a rigorous analysis of basic theory. The equations used in these techniques are valid only at geometric points. Therefore, their utilization in analyzing data using strains measured over volumes sampled by diffraction is possible only when the material and the stress/strain state within this volume are homogeneous. Consequently, the extension of the diffraction formalisms to stress/strain determination in polycrystalline materials is not straightforward since such materials are quasi-homogeneous unless the single crystals constituting the material are, themselves, isotropic. To address these issues, we provided a more appropriate set of definitions based on solid mechanics and performed series of rigorous finite element modeling as follows:

a) We used a homogeneous solid cylinder sample compressed by a C-clamp as an ideal model with a simple residual stress state. We saw that:

   i. The stress/strain state within the sample can change with position depending on the deformation history and boundary conditions of the system. We suggested, for the first time, the use of proper free-body diagrams for the volume of interest.

ii. Representative volume elements in real space and diffraction space might be different.

iii. Heterogeneous stress/strain distributions in the volume of interest can cause oscillatory ε'_{hkl} vs. $sin^2\psi$ plots.

iv. It is possible to define three types of residual stresses which are compatible with both real and diffraction spaces, respectively.

b) We tested these concepts further by modeling inclusions within a matrix in several geometries.

i. We observed that our expanded definitions work well in such systems. We were also able to clearly define the macrostresses, microstresses, and pseudo-macro stresses in such systems.

ii. We showed that the scale-dependent definitions used in the literature, first proposed by Macherauch, fail to describe these stress states.

iii. We cannot always define a proper representative volume element when there are stresses within a sample that exhibited highly localized distributions with strong gradients. In such cases, the beam size used in the experiment must be selected taking into account the grain sizes in the ROI and any St. Venant effects.

Our simple models showed that experimenters need to be very careful preparing for the measurements: significant metallographic material characterization and modeling may be necessary for real samples.

c) We simulated a virtual diffraction stress experiment in ideal polycrystalline thin films using ABAQUS CAE. Models were constructed such that no St. Venant stresses existed in the

region of the interests. We then compared the real space and diffraction average stresses/strains in our ideal samples (this is NOT possible in real experiments).

i. We observed that sub-volumes sampled by diffraction during different parts of the experiment, which we term ψ-volumes, volumes are not necessarily representative volume elements, consequently, they can cause non-linearities in ε'_{hkl} vs. $sin^2\psi$ plots.

ii. ε'_{hkl} vs. $sin^2\psi$ can show linear behavior if and only if ψ-ensembles of the particular hkl reflections are representative volume elements.

iii. In addition, we found out that even though calculated average strains from linear least square of fitting of ε'_{hkl} vs. $sin^2\psi$ plots are in agreement with the real space values, any computation of stresses utilizing only slopes of these plots would have yielded significantly different answers in two-phase materials.

d) We extended our analysis in Chapter 6 into a more realistic simulation where three-dimensional polycrystalline single and two-phase materials were used. In this simulation, we performed a virtual in-situ diffraction experiment where the sample was pulled along the axial direction.

i. We first used an isotropic material to check for St. Venant effects. By using free-body diagrams, we partitioned the sample into two regions: a) gage sections b) grip sections.

ii. We found out that in tungsten (W), oscillatory ε'_{hkl} vs. $sin^2\psi$ plots were observed in the grip sections due to St. Venant effects, whereas in the gage section, linear ε'_{hkl} vs. $sin^2\psi$ plots were observed under homogeneous uniaxial stress.

iii. In Cu and two-phase Cu – W samples, we observed that interaction stresses arising to constrain incompatible displacement across grain boundaries cause oscillations in ε'_{hkl} vs. $sin^2\psi$ plots, and stresses calculated from the linear least square of fitting of these plots can yield large errors.

iv. It is not possible to study stresses in two-phase materials using ε'_{hkl} vs. $sin^2\psi$ plots with single-phase elastic constants.

v. It was found that more grains must be sampled in a material under plastic loading because the number of interaction strains/stresses increases significantly compared to elastic loading. Multiple reflections must be measured.

vi. After unloading from plastic flow, the dispersions of stress and lattice strain caused by the Heyn effect can be assumed to be Gaussian.

Within this information, we would like to provide a recipe for the users wishing to perform an accurate experiment:

a) Since we cannot know exactly the history of the specimen under investigation, significant preliminary material characterization must be performed. For example, a phase analysis, grain size measurement, hardness test, and tensile test are necessary to have ideas about the history of the sample. Additional measurements can be done if the user thinks that it is necessary.

b) Since the local stress/strain distribution of the sample can be different depending on microstructure, loading type, presence of the second phase, etc. crystal-based finite element analysis must be performed in order to have an idea about the stress/strain of the material. The model results can, then, be used to guide beam location and size on the sample.

c) To maximize sampling and minimize bias introduce by Bragg selectivity of diffraction, the time of flight neutron diffraction experiment with at least 3 detectors would be the best approach for residual stress measurements. This type of system enables us to determine the principal stresses using all reflections. In other words, the strain will be calculated over a much larger volume which includes at least 4 and 5 reflections. Also, the number of detectors helps the experimenter to perform $\sin^2\psi$ analysis. If this technique is not possible, experimenters must use at least three or four reflections in CW-neutron or monochromatic XRD systems.

d) For all samples, diffraction elastic constants should be determined experimentally for all reflections used before a systematic study of residual stresses in actual components is attempted.

e) We recommend the use of advanced crystal-based finite element modeling software. Even in simple sample geometries, the stress/strain state can be complicated.

FUTURE WORK

In our simulations, we only simulated the measurement volume, and also, all of the grains positioned in the virtual sample diffracted at certain reflections and –tilts. However, in real-life measurement, the majority of the grains do not diffract. We want to verify our observations using much larger models with at least 10000 grains or more. Ideally, these should have real grain boundary structures. Instead of using strain values from the FEM Mesh, we should use these local strain values to calculate the intensity vs. sin2θ for each ψ-volume and reflections by employing the kinematic theory of diffraction. Strain will be calculated by single peak and profile fitting of

the simulated diffraction profiles in order to compare results. Hooke's Law will then be used to calculate the average stress.

A further extension of this work is to validate our expanded definitions with 3D diffraction microscopy. The grain-scale measurement allows users to find out the residual stress state of individual grains. In this way, the stress state of the sample can be mapped easily and new definitions can be tested.

Further basic analysis, just like in this thesis, a fiber and Goss textured sample must be simulated and tested. The oscillations will be more visible because of the incomplete sampling of the non-textured reflections.

References

[1] Noyan, I. C., Huang, T. C. and York, B. R., "Residual Stress/Strain Analysis in Thin Films by X-ray Diffraction," *Critical Reviews in Solid State and Materials Science,* vol. 20, no. 2, pp. 125-177, 1995.

[2] Mura, T., Micromechanics of Defects in Solids, Martinus Nijhoff, 1982.

[3] G. S. Schajer and C. O. Ruud, "Overview of Residual Stresses and Their Measurement," in *Practical Residual Stress Measurement Methods*, West Sussex, John Wiley & Sons, 2013, p. 1.

[4] Macherauch, E., "Residual Stresses," *Application of Fracture Mechanics to Materials and Structures,* pp. 157-192, 1984.

[5] Zoetelief, W. F., Douven, L. F. A. and Ingen Housz, A. J., "Residual Thermal Stresses in Injection Molding Products," *Polymer Engineering and Science,* vol. 36, no. 14, pp. 1886-1896, 1996.

[6] Msallem, Y. A., Jacquemin, F. and Poitou, A., "Residual Stresses Formation During the Manufacturing Process of Epoxy Matrix Composites: Resin Yield Stress and Anisotropic Chemical Shrinkage," *Internation Journal of Material Forming,* vol. 3, pp. 1363-1372, 2010.

[7] F. M. D'Heurle, "Metallurgical Topics in Silicon Device Interconnections," *International Materials Reviews,* vol. 34, pp. 53-68, 1989.

[8] I. C. Noyan, "Defining Residual Stresses in Thin Film Structures," *Advances in X-ray Analysis,* vol. 35, pp. 461-473, 1992.

[9] Gibbs, J. W., "On the Equilibrium of Heteregeneous Substances," *Transactions of the Connecticut Academy,* vol. III, pp. 108-198, 1874.

[10] Kelvin, W. T. and Tait, P. G., Treatise on Natural Philosophy, Oxford: Clarendon Press, 1867.

[11] Wu, X. and Yuntian, Z., "Heterogeneous Materials: A New Class of Materials which Unprecedented Mechanical Properties," *Materials Research Letters,* vol. 5, no. 8, pp. 527-532, 2017.

[12] V. Kafka, "On Constitutive Equations of Quasihomogeneous Materials," *Zeitschrift für angewandte Mathematik und Mechanik ,* vol. 59, pp. 423-430, 1979.

[13] Macherauch, E., Wohlfahrt, H. and Wolfstieg, U., "Zur Zwechmabigen Definition von Eigenspannungen," *HTM,* vol. 28, p. 201, 1973.

[14] Cullity, B. D., "Some Problems in X-ray Stress Measurements," *Advances in X-ray Analysis,* vol. 20, pp. 259-271, 1977.

[15] Garrod, R. I. and Hawkes, G. A., *Journal of Applied Physics,* vol. 14, p. 422, 1963.

[16] B. D. Cullity, "Sources of Error in X-ray Measurement of Residual Stress," *Journal of Applied Physics,* vol. 35, pp. 1915-1917, 1964.

[17] Ricklefs, R. E. and Evans, W. P., "Anomalous Residual Stresses," *Advances in X-ray Analysis,* vol. 10, p. 273, 1967.

[18] Cullity, B. D., "Residual Stress after Plastic Elongation and Magnetic Losses in Silicon Steel," *Transactionds of the Metallurgical Society of AIME,* vol. 227, no. 2, p. 356, 1963.

[19] Noyan, I. C. and Cohen, J. B., Residual Stress: Measurement by Diffraction and Interpretation, New York: Springer, 1987.

[20] Baczmanski, A., Braham, C. and Seiler, W., "Evolution of Plastic Incompatibility Stresses in Duplex Stainless Steel Determined by X-ray Diffraction," *Physics Status Solid A,* vol. 201, no. 13, pp. 2886-2899, 2004.

[21] A.-J.-C. d. Saint-Venant, "Memoire sur la flexion des prismes," *Journal de Mathematiques Pures et Appliquees,* vol. 1, pp. 89-189, 1856.

[22] Boussinesq, J., Application des potentiels a l' etude de l'equilibre et des mouvements des solides elastiques, Paris: Gauthier-Villars, 1885.

[23] A. Love, A Treatise on the Mathematical Theory of Elasticity, New York: Dover, 1944.

[24] R. Toupin, ""Saint-Venant's principle"," *Archive for Rational Mechanics and Analysis,* vol. 18, pp. 83-96, 1965.

[25] R. Von Mises, ""On Saint-Venant's Principle"," *Bulletin of American Mathematical Society,* vol. 51, p. 555, 1945.

[26] C. Horgan, "On Saint-Venant's principle in plane anisotropic elasticity," *Journal of Elasticity,* vol. 2, pp. 169-180, 1972.

[27] C. Horgan, "On Saint-Venant's Principle in the two-dimensional linear theory of elasticity," *Archive for Rational Mechanics and Analysis,* vol. 21, pp. 1-22, 1966.

[28] J. Zhao, "Toupin-Type Decay and Saint-Venant's Principle," *Applied Mechanics Review,* vol. 63, pp. 1-20, 2010.

[29] T. Davis, D. Healy, A. Bubeck and R. Walker, "Stress concentrations around voids in three dimensions: The roots of failure," *Journal of Structural Geology,* vol. 102, pp. 193-207, 2017.

[30] ASTM, "Standard Test Method for Determining Residual Stresses by the Hole-Drilling Strain-Gage Method," American Society for Testing and Materials, West Conshohocken, 2008.

[31] Shadley, J. R., Rybicki, E. F. and Shealy, W. S., "Application Guidelines for the Parting out in a Through Thickness Residual Stress Measurement Procedure," *Strain,* pp. 157-166, 1987.

[32] Tebedge, N., Alpsten, G. and Tall, L., "Residual Stress Measurement by the Sectioning Method," *Experimental Mechanics,* vol. 13, no. 2, pp. 88-96, 1973.

[33] Prime, M. B., "Residual Stress Measurement by Successive Extension of a Slot: The Crack Compliance Method," *Applied Mechanics Review,* vol. 52, no. 2, pp. 75-96, 1999.

[34] Cheng, W. and Finnie, I., Residual Stress Measurement and the Slitting Method, New York: Springer, 2007.

[35] Theiner, W. and Holler, P., "Magnetische Verfahren zur Spannungsermittlung," *Harteri-Tech. Mitt.,* pp. 157-163, 1982.

[36] Jiles, D. C., "Review of Magnetic Methods for Nondestructive Evaluation," *NDT International,* vol. 21, no. 5, pp. 311-319, 1988.

[37] E. Schneider, "Ultraschallverfahren zur Spannungsermittlung," *Harteri-Tech. Mitt,* pp. 164-169, 1982.

[38] Leon-Salamanca, T. and Bray, D. E., "Residual Stress Measurement in Steel Plates and Welds Using Criticall Refracted Longitudinal (LCR) Waves," *Reseearch in Nondestructive Evaluation,* vol. 7, no. 4, pp. 169-184, 1996.

[39] Wong, A. K., Dunn, S. A. and Sparrow, J. G., "Residual Stress Measurement by Means of the Thermoelastic Effect," *Nature,* vol. 332, no. 6165, pp. 613-615, 1988.

[40] M. Hetenyi, Handbook of Experimental Stress Analysis, New York: Wiley, 1950.

[41] Chiang, S. S., Marshall, D. B. and Evans, A. G., "The Response of Solids to Elastic/Plastic Indentations I: Stress and Residual Stresses," *Journal of Applied Physics,* vol. 50, no. 1, pp. 298-311, 1982.

[42] Barret, C. S. and Massalski, T. B., Structure of Metals, New York: McGraw-Hill, 1966.

[43] Cullity, B. D., Elements of X-ray Diffraction, Reading: Addison-Wesley, 1978.

[44] M. J. Hytch and A. M. Minor, "Observing and measuring strain in nanostructures and devices with transmission electron microscopy," *MRS Bulletin,* vol. 39, pp. 138-147, 2014.

[45] Dölle, H. and Hauk, V., *Zeitsschrift für Metallkunde,* vol. 68, pp. 725-728, 1977.

[46] C. M. Brakman, "Residual Stresses in Cubic Materials with Orthorhombic or Monoclinic Specimen Symmetry: Influence of Texture on ψ Splitting and Non-linear Behaviour," *Journal of Applied Crystallography,* vol. 16, no. 3, pp. 325-340, 1983.

[47] "Residual Stress Analysis Using Overlapping Diffraction Peaks. Case of Textured Cubic Materials," *Journal of Applied Crystallography,* vol. 20, no. 6, pp. 479-487, 1987.

[48] Baczmanski, A., Wierzbanowski, K., Haije, W. G., Helmholdt, R. B., Ekambaranathan, G. and Pathiraj, B., "Diffraction Elastic Constants for Textured Materials - Different Methods of Calculation," *Crystal Research & Technology,* vol. 28, no. 2, pp. 229-243, 1993.

[49] Dölle, H., "Influence of Multiaxial Stress States, Strain Gradients and Elastic Anisotropy on the Evaluation of Residual Stresses with X-rays," *Journal of Applied Crystallography,* vol. 12, pp. 489-501, 1979.

[50] J. F. Nye, Physical Properties of Crystals, Oxdord: Clarendon Press, 1976.

[51] H. Dölle and V. Hauk, "Systematik Moglicher Gitterdehnungs-verteilungen bei Mechanischen Beanspruchten Metallischen Werkstoffen," *Zeitschrift für Metallkunde,* vol. 68, pp. 725-728, 1977.

[52] J. B. Cohen, H. Dölle and M. R. James, "Determining Stresses from X-ray Powder Patterns," *NBS Special Publication,* vol. 567, pp. 453-477, 1980.

[53] Shiraiwa, T. and Sakamoto, Y., "The X-ray Stress Measurement of the Deformed Steel Having Preferred Orientation," in *13th Japan Congress on Material Research*, Kyoto, 1970.

[54] F. Bollenrath, Hauk, V. and Muller, E.H., "Zur Berechnung der Vielkristallinen Elastizitatskonstanten aus den Werten der Einkristalle," *Zeitschrift fur Metallkunde,* pp. 76-82, 1967.

[55] A. C. Vermeulen, "An Elastic Constants Database and XEC Calculator for Use in XRD Residual Stress Analysis," *Advanced X-ray Analysis,* vol. 44, pp. 128-133, 2001.

[56] K. Perry, *Experimental Determination of X-ray Elastic Constants,* Evanston: Northwestern University, 1982.

[57] Noyan, I. C., "Equilibrium Conditions for the Average Stresses Measured by X-rays," *Metallurgical Transactions A,* vol. 14A, pp. 1907-1914, 1983.

[58] van Baal, C. M., "The Influence of Texture on the X-ray Determination of Residual Stresses in Ground or Worn Surfaces," Delft University of Technology, Rotterdamsburg, 1982.

[59] H. Dölle, "Evaluation of (Residual) Stresses in Textured Cubic Metals," *Metallurgical and Materials Transactions A,* Vols. 11-A, pp. 831-836, 1980.

[60] H. Dölle and V. Hauk, "Einfluss der Mechanischen Anisotropie des Vielkristalls (Textur) auf die Rontgenographische Spannunugs-ermittlung," *Zeitschrift fur Metallkunde,* vol. 69, pp. 410-417, 1978.

[61] Lode, W and Peiter, A, "Numerik Rontgenographischer Eigenspannungsanalysen Oberflachennaher Schichten," *Härterei technische Mitteilungen,* vol. 32, pp. 235-240, 1977.

[62] Lode, W. and Peiter, A, "Grundsatzliche Erweiterungsmoglichkeiten der Rontgen-Verformungstechnik," *Metallkunde,* vol. 35, pp. 227-230, 1977.

[63] I. C. Noyan, "Residual Stress Distributions in Plastically Surface Deformed Two-Phase Materials," Northwestern University, Evanston, 1984.

[64] R. Marion, "X-ray Stress Analysis of Plastically Deformed Metals," Northwestern University, Evanston, 1972.

[65] Haase, A., Klatt, M., Schafmeister, A., Stabenow, R. and Ortner, B., "The Generalised sin2psi Method: An Advanced Solution for X-ray Stress Analysis in Textured Materials," *Powder Diffraction,* vol. 29, no. 2, pp. 133-136, 2014.

[66] Morawiec, A., "On Accounting for Preferred Crystallite Orientation in Determination of Average Elastic Strain by Diffraction," *Journal of Applied Crystallography,* vol. 51, pp. 148-156, 2018.

[67] Greenough, G. B., "Residual Lattice Strains in Deformed Polycrystalline Metal Aggreagates," *Proceedings of Royal Society,* vol. A197, pp. 556-567, 1949.

[68] Faninger, G., "Lattice Strains in Deformed Cubic Metals," *Japanese Society of Material Science,* vol. 19, pp. 42-56, 1970.

[69] Faninger, G., "Uber Vielkristallverfestigungskurven und Einkristalldaten von Aluminium, Kupfer und Nickel," *Acta Physica Austriaca,* vol. 27, pp. 122-143, 1968.

[70] Hauk, V., "Rontgenographische Gitteronnstantenmessungen on plastisch verformten Stahlproden," *Naturwiss,* vol. 40, pp. 507-508, 1953.

[71] Hauk, V., "Zum gegenwartigen Stande dez Spannungsmessung mit Rontgenstrahlen," *Archiv für das Eisenhüttenwesen,* vol. 25, pp. 273-278, 1954.

[72] Marion, R. H. and Cohen, J. B., "Anomalies in Measurement of Residual Stress by X-ray Diffraction," *Advanced X-ray Analysis,* vol. 18, pp. 466-501, 1975.

[73] W. Weidemann, "Ph.D. Thesis," Technische Hochschule, Aachen, 1966.

[74] Chidambarrao, D., Song, Y. C. and Noyan, I. C., "Numerical Simulation of the X-ray Stress Analysis Technique in Polycrystalline Materials under Elastic Loading," *Metallurgical and Materials Transactions A,* vol. 28, no. 12, pp. 2515-2525, 1997.

[75] Peiter, A. and Lode, W., "Strain Field Analysis with the X-ray Integration Method," *Strain,* pp. 69-75, 1983.

[76] Lode, W. and Peiter, A., "Theorie des Rontgen-Integralverfahrens," *Haerterei-Technische Mitteilungen,* vol. 35, pp. 148-155, 1980.

[77] Wagner, C. N. J., Eigenmann, B. and Boldrick, M. S., "The Phi-Integral Method for X-ray Residual Stress Measurements," University of California, Los Angeles, 1986.

[78] Eigenmann, B., "Computer-aided X-ray Residual Stress Analysis in High Strength Aluminum Alloys for Production Control during the Manufacturing Process," Universitat Karlsruhe, West Germany.

[79] Wagner, C. N. J. and Boldrick, M. S., "The Psi-differential and Integral Methods for Residual Stress Measurements by X-ray Diffraction," University of California, Los Angeles, 1983.

[80] Willemse, P. F., Naughton, B. P. and Verbraak, C. A., "X-ray Residual Stress Measurements on Cold - drawn Steel Wire," *Material Science and Engineering,* vol. 56, pp. 25-37, 1982.

[81] Hauk, V. and Vaessen, G., "Eigenspannungen in Kristallitgruppen Texturierter Stahle," *Zeitschrift für Metallkunde,* vol. 76, pp. 102-107, 1988.

[82] V. Hauk, "Evaluation of Macro- and Micro-Residual Stresses on Textured Materials by X-ray, Neutron Diffraction and Deflection Measurements," *Advances in X-ray Analysis,* vol. 29, pp. 1-15, 1986.

[83] H. U. Baron and V. Hauk, "Rontgenografische Ermittlung der Eigenspannungen in Kristallitegruppen von fasertexturierten Werkstoffen," *Zeitschrift für Metallkunde,* vol. 79, pp. 127-131, 1988.

[84] Gergaud, P., Labat, S. and Thomas, O., "Limits of Validity of the Crystallite Group Method in Stress Determination of Thin Film Structures," *Thin Solid Films,* vol. 319, pp. 9-15, 1998.

[85] De Buyser, L., Van Houtte, P. and Aernoudt, E., "X-ray Measurement of Residual Stresses in Textured Thin Coatings," *Textures and Microstructures,* vol. 14, no. 18, pp. 73-78, 1991.

[86] Quaeyhaegens, C., Knuyt, G. and Stals, L. M., "Residual Macroscopic Stress in Highly Preferentially Oriented Titanium Nitride-Coatings Deposited on Various Steel Types," *Journal of Vacuum Science & Technology A,* vol. 14, p. 2462, 1996.

[87] Perry, A. J., Valvoda, V. and Rafaja, D., "X-ray Residual Stress Measurement in TiN, ZrN and HfN films using Seemann-Bohlin Method," *Thin Solid Films,* vol. 214, pp. 169-174, 1992.

[88] Serruys, W., Van Houtte, P. and Aernoudt, E., "Residual Stresses in Science and Technology," DGM, Oberursel, 1986.

[89] Quaeyhaegens, C., Knuyt, G. and Stals, L. M., "Stury of Residual Macroscopic Stress in TiN Coatings Deposited on Various Steel Types (TuSA1)," *Surface and Coating Technology,* vol. 74, no. 75, pp. 104-109, 1995.

[90] Ortner, B., "Why We Should Give Up the Sin2Psi Method," *Advanced X-ray Analysis,* vol. 52, pp. 763-772, 2009.

[91] Ortner, B., "The Matrix Method for Data Evaluation and its Advantages in Comparison to the Sin2Psi and Similar Methods," *Materials Science Forum,* vol. 681, pp. 7-12, 2011.

[92] B. Ortner, "Matrix Method for X-ray Stress Measurement in Single Crystals, and the Rational Planning of the Measurements," *Advanced Materials Research,* vol. 996, pp. 58-63, 2014.

[93] B. Ortner, "Symmetry Properties and Transformation Behaviour of the X-ray Stress Factors," *Journal of Applied Crystallography,* vol. 39, pp. 401-409, 2006.

[94] Welzel, U., Ligot, J., Lamparter, P., Vermeulen, A. C. and Mittemeijer, E. J., "Stress Analysis of Polycrystalline Thin Films and Surface Regions by X-ray Diffraction," *Journal of Applied Crystallography,* vol. 38, pp. 1-29, 2005.

[95] Vermeulen, A. C., "Assumptions in Thin Film Residual Stress Methods," *Material Science Forum,* Vols. 404-407, pp. 35-42, 2002.

[96] Ballard, B. L., Predecki, P. K., Watkins, T. R., Kozaczek, K. J., Braski, D. N. and Hubbard, C. R., "Depth Profiling Biaxial Stresses in Sputter Deposited Molybdenum Films: Use of the cos2theta Method," *Advanced X-ray Analysis,* vol. 39, pp. 363-370, 1997.

[97] Taira, S., Tanaka, K. and Yamazaki, T., "A Method of X-ray Microbeam Measurement of Local Stress and its Application to Fatigue Crack Growth Problems," *Japanese Society of Materials Science,* vol. 27, pp. 251-256, 1978.

[98] S. Kaldor and I. Noyan, "Effects of boundary conditions and anisotropy on elastically bent silicon," *Experimental Mechanics,* vol. 42, pp. 353-358, 2002.

[99] R. P. Scully, "Medical Republic," 11 December 2020. [Online]. Available: https://medicalrepublic.com.au/how-an-ingenious-vaccine-design-became-its-downfall/38391. [Accessed 2021 May 2021].

[100] H. Conway, "The Axially Loaded Circular Cylinder," *Transactions of the ASME,* pp. 318-320, 1962.

[101] V. O. F. Fischer, "Naherungslosung zur Ermittlung der wirklichen Spannungsverteilung and konzentriert belasteten Zylinderenden," *Ingeniur-Archiv,* pp. 178-189, 1931.

[102] J. R. Barber, Elasticity, Springer Netherlands, 2010.

[103] J. Bauschinger, "Ueber die Veranderung der Elasticitatsgrenze und des Elasticitatsmoduls verschiedener Metalle," *Zivilingenieur,* vol. 27, 1881.

[104] J. Hadamard, Lectures on Cauchy's Problem in Linear Partial Differential Equations, Yale University Press, 1923.

[105] I. C. Noyan and L. T. Nguyen, "Effect of Plastic Deformation on Oscillations in "d" vs. sin2psi Plots - A FEM Analysis," *Advances in X-ray Analysis,* vol. 32, pp. 355-364, 1989.

[106] I. C. Noyan and L. T. Nguyen, "Oscillations in Interplanar Spacing vs. sin2Psi - A FEM Analysis," *Advances in X-ray Analysis,* vol. 31, pp. 191-204, 1988.

[107] Y. Song and I. C. Noyan, "Variation of the Effective Elastic Constants in the Sample Coordinate System with tilt angle for X-ray Strain-stress Analysis," *Philosophical Magazine A,* vol. 4, pp. 1105-1112, 1996.

[108] H. F. Poulsen, "An introduction to the three-dimensional X-ray diffraction microscopy," *Journal of Applied Crystallography,* vol. 45, pp. 1084-1097, 2012.

[109] H. O. Sorensen, S. Schmidt, J. P. Wright, G. B. M. Vaughan, S. Techert, E. F. Garman, J. Oddershede, J. Davaasambu, K. S. Paithankar, C. Gundlach and H. F. Poulsen, "Multigrain Crystallography," *Crystalline Materials,* vol. 227, pp. 63-77, 2012.

[110] "ABAQUSCAE," SIMULIA, [Online]. Available: https://www.3ds.com/products-services/simulia/products/abaqus/abaquscae/. [Accessed September 2016].

[111] P. R. Dawson and D. E. Boyce, "FEpX - Finite Element Polycrystals: Theory, finite element formulation, numerical implentation and illustrative examples," *arXiv:1504.03296 [cond-mat.mtrl-sci],* 2015.

[112] M. Handbook, Vol. 1 - Properties and Selection: Irons, Steels and High-Performance Alloys, 10th Ed., ASM International, 1990.

[113] M. Handbook, Vol. 2 - Properties and Selection: Nonferrous Alloys and Special-Purpose Materials, 10 Ed., ASM International, 1990.

[114] M. De Graef and M. E. McHenry, Structure of Materials: An Introduction to Crystallography, Diffraction, and Symmetry, Cambridge: Cambridge University Press, 2012.

[115] E. B. Marin and P. Dawson, "Elastoplastic finite element analyses of metal deformations using polycrystal constitutive models," *Computer Methods in Applied Mechanics and Engineering,* vol. 165, no. 14, pp. 23-41, 1998.

[116] E. B. Marin and P. R. Dawson, "On modelling elasto-viscoplastic response of metals using polycrystal plasticity," *Computer Methods in Applied Mechanics and Engineering,* vol. 165, no. 14, pp. 1-21, 1998.

[117] R. Quey, "Neper: Polycrystal Generation and Meshing," [Online]. Available: https://neper.info/. [Accessed March 2020].

[118] H. -J. Bunge, Texture Analysis in Materials Science, Berlin: Akademie-Verlag, 1969.

[119] R. Quey, P. Dawson and F. Barbe, "Large-scale 3D random polycrystals for the finite element method: Generation, meshing and remeshing," *Computer Methods in Applied Mechanics and Engineering,* vol. 200, no. 17-20, pp. 1729-1745, 21 October 2020.

[120] T. Kanit, S. Forest, I. Galliet, V. Mounoury and D. Jeulin, "Determination of the size of the representative volume element for random composites: statistical and numerical approach," *International Journal of Solids and Structures,* vol. 40, no. 13-14, pp. 3647-3679, 2003.

[121] W. J. Drugan and J. R. Willis, "A micromechanics-based nonlocal constitutive equation and estimates of representative element size for elastic composites," *Journal of the Mechanics and Physics of Solids,* vol. 44, no. 4, pp. 497-524, 1996.

[122] J. N. Goodier, and S. Timoshenko, Theory of Elasticity, India: Mc Graw Hill, 1934.

[123] R. A. Toupin, "Saint-Venant and a Matter of Principle," *Transactions of the New York Academy of Sciences,* vol. 28, pp. 221-232, 1965.

[124] O. Zanaboni, "Dimonstrazione generale del Principio del de Saint-Venant," *Atti Della Academia Nazionale Dei Lincei,* vol. 25, pp. 117-120, 1937.

[125] R. Batra, "Saint-Venant's principle in linear elasticity with microstructure," *Journal of Elasticity,* vol. 13, pp. 165-173, 1983.

[126] P. Vafeades and C. Horgan, "Exponential decay estimates for solutions of the von Karman equations on a semi infinite strip," *Archive for Rational Mechanics and Analysis,* vol. 104, pp. 1-25, 1988.

[127] J. Zhao, "Toupin-Berdichevskii Theorem Can't be Considered as a Mathematical Expression of Saint-Venant's Principle," *Applied Mathematics and Mechanics,* vol. 7, pp. 971-974, 1986.

[128] M. Whittaker, "Considerations in fatigue lifing of stress concentrations in textured titanium 6-4," *International Journal of Fatigue,* vol. 33, no. 10, pp. 1384-1391, 2011.

[129] N. Hardiman, "Elliptic elastic inclusion in an infinite elastic plate," *The Quarterly Journal of Mechanics and Applied Mathematics,* vol. 7, no. 2, pp. 226-230, 1954.

[130] S. Gong and S. Meguid, "Interacting circular inhomogeneities in plane elastostatics," *Acta Mechanica,* vol. 99, pp. 49-60, 1993.

[131] R. Hertzberg, Deformation and Fracture Mechanics of Engineering Materials, Hoboken: Wiley & Sons, 1976.

[132] P. Subramanian, D. Chakrabarti and D. Laughlin, Phase Diagrams of Binary Copper Alloys, Materials Park: ASM International, 1994.

[133] ASM International, Atlas of Stress-Strain Curves, United States of America: ASM International, 2002.

[134] Kolmogorov, A., "Sulla determinazione empirica di una legge di distribuzione," *Giornale dell'Istituto Italiano degli Attuari,* vol. 4, pp. 83-91, 1933.

[135] Smirnov, N., "Table for estimating the goodness of fit of empirical distributions," *Annals of Mathematical Statistics,* vol. 19, no. 2, pp. 279-281, 1948.

[136] Shapiro, S. S. and Wilk, M. B., "An analysis of variance test for normality," *Biometrika,* vol. 52, no. 3-4, pp. 591-611, 1965.

[137] Totten, G., Howes, M. and Inoue, T., "Handbook of Residual Stress and Deformation of Steel," ASM International, Ohio, 2002.

[138] Gitman, I. M., Askes, H., Sluys, L. and Valls, O. L., "The Concept of Representative Volume for Elastic, Hardening and Softening Materials," in *Advanced Problems in Mechanics*, Saint Petersburg, 2004.

[139] Z. Hashin, "Analysis of Composite Materials," *Journal of Applied Mechanics,* vol. 50, pp. 481-505, 1983.

[140] R. Hill, "Elastic Properties of Reinforced Solids: Some Theoretical Principles," *Journal of the Mechanics and Physics of Solids,* vol. 11, pp. 357-372, 1963.

[141] Noyan, I. C. and Schadler, L. S., "Characterization of Inhomogeneous Elastic Deformation with X-ray Diffraction," *Metallurgical and Materials Transactions A,* vol. 25A, pp. 341-347, 1994.

[142] Noyan, I. C., "Determination of Elastic Constants of Inhomogeneous Materials with X-ray Diffraction," *Materials Science and Engineering,* vol. 75, pp. 95-103, 1985.

[143] Baczmanski, A., Wierzbanowski, K. and Lipinski, P., "Determination of Residual Stresses in Plastically Deformed Polycrystalline Materials," *Trans Tech Publications,* vol. 2051, pp. 157-162, 1994.

[144] R. A. Winholtz and J. B. Cohen, "Generalised Least-squares Determination of Triaxial Stress States by X-ray Diffraction and the Associated Errors," *Australian Journal of Physics,* vol. 41, pp. 189-199, 1988.

[145] T. Imura, S. Weissmann and J. J. J. Slade, "A study of age-hardening of Al-3.85% Cu by the divergent X-ray beam method," *Acta Crystollagraphy,* vol. 15, pp. 786-793, 1977.

[146] M. Handbook, Vol.1 - Properties and Selection: Irons, Steels, and High-Performance Alloys, 10th ed., ASM International, 1990.

[147] M. Handbook, Vol. 2 - Properties and Selection: Nonferrous Alloys and Special-Purpose Materials, 10th ed., ASM International, 1990.

[148] [Online]. Available: http://www.matweb.com/search/DataSheet.aspx?MatGUID=41e0851d2f3c417ba69ea0188fa570e3.

[149] A. Scheinker and R. Pokharel, "Adaptive 3D convolutional neural network-based reconstruction method for 3D coherent diffraction imaging," *Journal of Applied Physics,* vol. 128, no. 184901, 2020.

[150] D. Denkova, M. Ploschner, M. Das, L. M. Parker, X. Zheng, Y. Lu., A. Orth, N. H. Packer and J. A. Piper, "3D sub-diffraction imaging in a conventional confocal configuration by exploiting super-linear emitters," *Nature Communications,* vol. 10, no. 3695, 2019.

[151] H. Lester and R. Aborn, *Army Ordnance 6,* pp. 120, 200, 283, 364, 1925-1926.